DESIGN, DEVELOPMENT, AND EVALUATION OF MESO-SCALE ROBOTIC SYSTEM FOR DEEP INTRACRANIAL TUMOR REMOVAL

A Dissertation
Presented to
The Academic Faculty

By

Shing Shin Cheng

In Partial Fulfillment
of the Requirements for the Degree
Doctor of Philosophy in
Robotics

Georgia Institute of Technology

August 2018

DESIGN, DEVELOPMENT, AND EVALUATION OF MESO-SCALE ROBOTIC SYSTEM FOR DEEP INTRACRANIAL TUMOR REMOVAL

Approved by:

Dr. Jaydev P. Desai
Wallace H. Coulter Department of Biomedical Engineering
Georgia Institute of Technology

Dr. Jun Ueda
George W. Woodruff School of Mechanical Engineering
Georgia Institute of Technology

Dr. Frank L. Hammond III
Wallace H. Coulter Department of Biomedical Engineering
Georgia Institute of Technology

Dr. Jonathan Rogers
George W. Woodruff School of Mechanical Engineering
Georgia Institute of Technology

Dr. John N. Oshinski
Wallace H. Coulter Department of Biomedical Engineering
Georgia Institute of Technology

Date Approved: June 12, 2018

ACKNOWLEDGMENTS

I would like to express my deepest gratitude to my PhD advisor, Professor Jaydev P. Desai, for giving me the opportunity and believing in me who came to the lab without any Master's experience, giving me the financial support for a technically challenging and socially meaningful project, providing me advice, feedback, and encouragement, being available every time I need more attention and guidance, and finally providing strong support for my future career pursuit. He has given me opportunities after opportunities and I could not say enough thank you.

I would like to thank everyone at University of Maryland School of Medicine, including Dr. Rao Gullapalli, Steve Roys, Dr. Mahamadou Diakite, Dr. J. Marc Simard, Dr. Matt Kole, and Dr. Jiachen Zhuo. The radiologist team had been able to work closely with us and provided us the MRI facility to perform robot evaluation. Despite his busy schedule, Dr. Gullapalli stayed up past midnight to work with us. I am also very grateful to my PhD reading committee members, Dr. Jun Ueda, Dr. Frank Hammond, Dr. Jonathan Rogers, and Dr. John Oshinski for their commitment, time, and very constructive advice given during my proposal and defense presentation. I would like to thank National Institute Of Biomedical Imaging And Bioengineering of the National Institutes of Health for sponsoring the MINIR-II project under the Award Number R01EB015870.

I would like to thank many staffs at University of Maryland, College Park (UMCP) and Georgia Institute of Technology, who provided a helping hand throughout the years. They are the technical and administration staffs in the machine shops, clean room, UMCP Department of Mechanical Engineering and Georgia Tech Department of Biomedical Engineering. I would like to dedicate special appreciation to two wonderful staffs that I had the pleasure to work with, Coral-Gean Abel and Karine Avagian.

It has been an incredibly gratifying experience in a lab (RAMS lab at University of Maryland, College Park and RoboMed lab at Georgia Institute of Technology) full of students and post-docs who have become more like friends than colleagues to me, including Jun Sheng, Kihan Park, Yeongjin Kim, Xuefeng Wang, Yash Chitalia, Phillip Tran, Chad Kessens, Elif Ayvali, Wenxue Zhao, Carolyn Adkins, Bo Yang, and Nahian Rahman. I really appreciate the collaboration and teamwork that I formed with the two post-docs, Yeongjin Kim and Xuefeng Wang, who had guided me throughout my research work. Jun Sheng and Kihan Park are two close friends who have shared ideas, advice, assistance, and encouragement throughout the four years during which our times in the lab have overlapped. I also had the honor to witness some important milestones in their lives.

I would like to thank my parents, especially my mother, who has been a constant moral support for me. Despite not being able to spend much time with her during this time, she has been a Facetime away and she is always be my best listener. Her love and support mean a lot to me. I would like to thank my brother and his family for being who they are and supportive of every one of my decision. Simply, without my family, I will not be where I am today.

Last but not least, I would like to make a special mention to my wife, Su Cheun Oh, who is herself a gifted engineer and a disciplined researcher. I would not forget the nights she stayed up with me just to encourage me to tackle the seemingly unsolvable problems and overcome the insurmountable pressure, the brainstorming and idea explaining sessions we had together, and the correct positive mindset she instilled in me. She has always been there for me through thick and thin and is always the first person that I want to share my best and worst moments.

I would like to dedicate this dissertation to both my parents and my fiancée.

TABLE OF CONTENTS

LIST OF TABLES

LIST OF FIGURES

SUMMARY

It remains a challenging procedure to remove deep brain tumor due to its location around critical brain structures, the limitations in existing surgical tools, and the lack of real-time image guidance. The Minimally Invasive Neurosurgical Intracranial Robot (MINIR-II) project aims at combining flexible robotic technology, minimally invasive approach, and magnetic resonance imaging (MRI) to achieve more precise and complete removal of brain tumor.

MINIR-II is a spring-based 3-D printed flexible robot that is tendon-driven and equipped with electrocautery, suction and irrigation capabilities. A novel central tendon routing mechanism has been employed to enable independent segment control in a tight workspace. To improve stability of the surgical procedure, a stiffness-tunable MINIR-II with shape memory alloy (SMA) spring segments has also been developed and characterized to investigate the effect of tendon locking and SMA segment stiffening on the stiffness of individual segment. SMA springs have also been used as a proof-of-concept MRI-compatible actuator for MINIR-II. To improve the actuation bandwidth, cooling module-integrated SMA springs have been developed together with a new actuation mechanism involving the alternate passage of water and compressed air. A phenomenological model and a heat transfer model were developed and verified to model the actuator behavior in antagonistic configuration. With the robot developed and tested for its performance and MRI-compatibility, ultrasonic motors were used instead of SMA springs to provide a more reliable actuation solution. A remote actuation strategy with three different transmission designs was implemented due to the interference of ultrasonic motors and drivers with the MR image quality when they are in close proximity to the MR isocenter. The inefficiency in force transmission in the first flexible Bowden cable transmission led to the development of the second rigid transmission as well as the third improved version of the rigid transmission. The robotic system was finally evaluated in terms of its workspace, segment coupling effectiveness,

precision, repeatability, and hysteresis behavior.

A compact MRI-compatible robotic system used to actuate a multi-DoF skull-mounted flexible robot has been presented. Research innovation could be found in the 3-D printed flexible robot design, compact SMA spring cooling module development, stiffness modulated robot design, and transmission design in the MR environment. Intrinsic sensor integration and more user-friendly control interface are two important future works that would take the robotic system one step closer to being clinically evaluated.

CHAPTER 1
INTRODUCTION

1.1 Motivation

Brain tumors can occur at any age and are found in 20-40% of adult cancer patients [1]. Surgery remains the most common first-step treatment option for operable brain tumors and traditional open surgery (craniotomy) requires the removal of a significant piece of the skull and/or facial musculature over the brain tumor. Minimally invasive approach with keyhole access is quickly gaining popularity in all types of surgeries, including brain tumor resection, to reduce post-surgery pain, encourage rapid recovery, and minimize complications associated with craniotomy. Maximal tumor removal while minimizing collateral manipulation of critical brain structures are the two main objectives of a brain tumor resection procedure.

Neurosurgery can benefit from improvement in continuous imaging technology, especially the magnetic resonance imaging (MRI). MRI provides excellent soft-tissue contrast and is suitable for imaging of non-bony parts of the body. This makes it the best imaging modality for brain and will allow clear delineation of brain tumor boundary. MR-guided neurosurgery can tremendously improve the chance of complete tumor removal with minimal removal of healthy surrounding tissues without exposing patients to the ionizing radiation of X-rays. Intraoperative MRI procedure therefore is envisioned to be the future of image-guided neurosurgery. The design of the robotic system, including the choices of actuators, has to fulfill the MRI-compatibility requirements. The materials available to build up the robotic system are thus limited to those that are non-ferrous and non-magnetic. In general, the use of metals should be minimized as well.

Straight rigid surgical tools have been reliable intruments for surgeons for decades.

Even in this era of keyhole surgeries, straight slender rigid laparoscopic tools, evidently with well-thought-out design, are used. Each rigid tool usually can perform multiple functions such as grasping and cauterizing or dissecting and probing. In body parts such as torso, abdomen and pelvis, carbon dioxide gas is pumped into the cavity to inflect and create the surgical space. The laparoscopic surgical tools are inserted through multiple holes and the end-effectors of the different tools meet at the surgical site to work in tandem with each other. However, the gas cannot be pumped into the brain cavity since it is filled with soft tissues. It is also extremely risky to create multiple dime-sized holes in the brain for different straight rigid surgical tools to be inserted. Therefore, a flexible meso-scale robot is envisioned to be the perfect substitute for multiple rigid surgical tools. One robot is inserted into the brain and has the flexibility to interact safely with the soft brain tissue while carrying multiple surgical accessories.

Given the high medical cost that patients often have to shoulder and the limited accessibility to robotic surgery due to the high capital investment that only well-off hospitals can afford, we also attempt to build a more affordable and single-use neurosurgery robot. It has been shown that the da Vinci surgical robots do not increase the quality of surgery by as much as its cost compared to traditional laparoscopic surgery in fields such as cardiovascular surgery, gynecological surgery and others, except urological surgery. Columbia University published a study that shows that it costs $3000 more to perform a robotically assisted adnexal surgery compared to traditional laparoscopic surgery [2]. Therefore, 3-D printing is used extensively in this research to produce medical-grade robots that are disposable after single use. More affordable smart actuator options are also investigated and improved in terms of its design and actuation mechanism to produce superior performance.

While high flexibility of a continuum robot is useful for various surgical procedures, the robot may lack the stability or rigidity that rigid tools provide, which is desirable for certain surgical procedures. While navigating in the brain tissue or around the brain tumor, certain segments of the flexible robot that are not being actuated may need to be stiffened to accomplish certain surgical tasks. The ability to independently modulate the stiffness of a specific robot segment therefore becomes important to improve the maneuverability and manipulation of a flexible robot.

The quality of MR images is critical to the success of an MR image-guided surgical procedure. Actuators such as piezoelectric motors, despite being MRI-compatible, would lead to artifacts in the MR images when they are placed close to the MR isocenter. By placing the actuators far from the MR isocenter, it has been shown in the literature to produce much cleaner MR images [3]. Remote actuation of the robot using cable-driven mechanism and novel transmission modules therefore is needed to ensure high robot performance in terms of accuracy and repeatability during tumor resection under MR image guidance.

It has been almost three decades since the first robot-assisted surgery took place and neurosurgery remains one of the most challenging surgical procedures for robotics to be adopted. This is due to various reasons, including the lack of operational space, our incomplete understanding of the brain, the limitations in the surgical end effectors that interface with the brain tissues, and the proximity of the problematic areas to critical neural structures and vessels. The contributions from this work, especially in terms of the MRI-compatible flexible robot design, actuator improvement, and transmission design, hopefully provide a firm research foundation for MRI-compatible robotic systems with flexible end-effectors, taking us one step closer to a safer and more precise intraoperative MRI-guided robotic neurosurgery.

1.2 Related Work

1.2.1 Neurosurgical Robots

The PUMA 200 robot [4], originally an industrial robot and widely acknowledged as the first robot ever to be used in a surgical application, was employed to perform a tumor biopsy procedure in the brain based on pre-operative computer tomography (CT) images in 1988. The robotic-assisted procedure was completed faster and with higher accuracy than a manual procedure. The PUMA robot with an interactive 3-dimensional display of CT images was later used to hold and control a surgical retractor to remove deep benign astrocytomas in children in 1991 [5].

After taking into consideration safety, geometry, and rigidity required for a surgical robot inside a CT scanner, the industrial robot is abandoned and a custom-designed surgical robot was developed, namely Minerva [6]. It is a 7-degree of freedom (DoF) neurosurgical robot first developed in 1993 to increase the accuracy and precision of stereotactic neurosurgery under CT guidance. It was used with a Brown-Robert-Wells (BRW) reference system and performed an entire operation, including skin incision, bone drilling, dura perforation, and probe manipulation. It was then updated in 1995 [7] with sterilization features, force sensors, nonlinear electrostimulation probe, and ability to perform several procedures including hematoma evacuation, cyst aspiration, and living cell implantation.

In 2005, a master-slave microsurgical robotic system was developed to improve the dexterity of the surgeons in deep surgical fields through a narrow corridor [8]. The slave system consists of two manipulators with six-DoFs while the master system can control movements in seven DoFs. Visualization is provided through a high definition video camera system with a microscope lens.The system was used to perform artery suturing in rats as well as in cadavers. Several challenges were reported, including the further miniaturization of the manipulator and the inclusion of multi-DoF force sensing.

NeuroMate robot system (Renishaw Ltd., UK, previously licensed by Integrated Surgical Systems, California) is a commercially available CT or MRI-guided passive robotic system that can achieve intraoperative patient registration using a stereotactic frame or in a frameless mode and optimal localization [9]. It is also the first FDA-approved neurosurgical robotic system and has been used for a variety of procedures including tumor biopsy, functional neurosurgery, stereotactic neurosurgery, and deep brain stimulation [10]. The high application accuracy of the NeuroMate robotic system has recently been validated in in-vivo procedures [11].

Teleoperated micromanipulator system (NeuRobot) was developed specifically for neurosurgery with three microrobot arms/microinstruments and a straight rigid neuroendoscope. It contains a safety feature that constrains the end effector motion to a region that is defined by its simulator, ROBO-SIM based on pre-operative MR images [12]. It is made up of a slave micromanipulator, a master manipulator, a supporting device, and a 3-D monitor. It has been used to perform surgical simulation on a cadaver head [13] and completed basic gestures such as dissecting, tying, and coagulating. In 2012, it was used to perform four complex surgical procedures on a cadaver and ventriculostomy in a clinical trial on a patient upon approval by the Ethical Committee of Shinshu University School of Medicine [14]. The patient does not suffer post-operative complication but the ventricle size was not reduced after the surgery.

The Robot and Sensor integration for Computer Assisted Surgery and Therapy (ROBOCAST) project is a multi-national effort in Europe to advance surgical robotics research. It involves communication and information transfer, software development, preoperative and intraoperative image segmentation and surgical planning [15], robot control and manipulation, and visual and tactile information feedback [16]. It consists of a PathFinder robot (a 6-DoF robot arm on a wheeled platform acting as a gross positioner), a hexapod MARS robot (acting as a fine positioner), and a linear actuator to allow a large range of motion, precise positioning, and insertion of a surgical probe. The robotic system is targeted towards several surgical applications including but not limited to tumor biopsy, localized tumor therapy, cyst drainage, and deep brain stimulation. A flexible probe has also been developed to be integrated as an end effector of the PathFinder robot [17].

Medtech ROSA® Brain (France) is an FDA-approved neurosurgical robotic system developed by Medtech (France). The system consists of a robot arm with six DoFs and is equipped with assisted neuronavigation that displays surgical instruments in real time on patient images as well as haptic feedback. According to its official website, it can be used for a wide range of medical applications, including tumor biopsy [18], electrode implantation for stimulation [19], laser interstitial ablation of tumor [20], endoscopic neurointervention, open skull surgery, and keyhole surgery. It has been used to address conditions such as hydrocephalus, dystonia, Parkinson's Disease, and Cavernoma. One of the most important advantages of the system is the patented non-invasive, contactless patient registration system that removes the use of a stereotactic frame or fiducials [18].

Robotic NeuroNAvigation (RONNA) system is a neurosurgical robot developed in Croatia under an European Union (EU) fund. It consists of two robot arms; one of which is the main robot to perform precise manipulation and the other one acts as a compliant robotic assistant [21]. Two industrial robots, the 6-DoF KUKA KR6 (master robot) and the 7-DoF KUKA LWR 4+ (assistant robot), were used in the first phase of the project while mobile platforms were added in the second phase. More recently, the third generation, namely RONNA G3 has been developed consisting of robotic arms on a mobile platform, global optical tracking system (Polaris Spectra, NDI), and a planning and navigation system [22]. A clinical study involving tumor biopsy and cyst removal using the RONNA G3 system has been performed on a patient successfully.

1.2.2 Flexible Surgical Robots

Flexible robots have been of interest to researchers in a diverse of fields. There have been several review articles that provide complete overview of a variety of flexible robots with different geometrical structures and actuation mechanism [23]. Most surgical robots are composed of rigid components that are not preferred in a surgical environment that is filled with critical tissues. Increasing the degrees of freedom (DoF) increases the dexterity of a robot and a continuum robot can be defined as one that has infinite number of joints (DoFs). A soft continuum robot does not have rigid and discrete joints and thus provides the structural compliance highly desired when interfacing with body tissues. Its flexibility provides dexterous movement in a restricted surgical space and their simple structural design usually permits a smaller geometrical construct than the rigid joint counterparts.

Several recent review papers on the role of continuum robots in medical application can be found in [24, 25, 26].

While rigid surgical robots consist of discrete joints with negligible impedance, a flexible robot articulates the entire body structure as a continuum. Thus, the body material of flexible robots should have relatively low elastic modulus. Plastic and metal are the most common choices for surgical robot fabrication. Due to their much higher modulus than the surrounding tissues, they need to be made into flexible geometrical structures, such as a spring, a thin tube, or a thin rod.

As the operational space in biological environments (e.g. brain) is usually very limited, several smart actuation mechanisms have also been developed, including the flexible catheter with a slave micromanipulator [27], bevel-tipped needle [28], the concentric tube robot [29, 30], tendon-driven robot [31, 32], tendon-driven with follow-the-leader mechanism [33], and the SMA torsion spring actuated robot [34]. More recently, researchers have made use of closed loop elastic structures [35, 36] and notched joints [37, 38, 39, 40] to develop small-scale continuum robots.

Since we envision a meso-scale neurosurgical robot which uses electrocautery to remove the tumor, it needs to have space for suction and irrigation tube as well as routing the hardware for electrocauterization and sensing. As the number of segments increases, coupling between the segments also gets more complex. Thus, we need a simple design that provides just enough lumen space and at the same time allows independent control between segments.

Simaan $et\ al.$ [41] have developed a flexible robot for minimally invasive surgery (MIS) on the throat and upper airways. The robot is composed of flexible plastic rods that pass through supporting disks on their rim and can be pushed and pulled on. It can exert larger than 1 N force at its tip and bend to a curvature of more than 70 mm. It is designed to perform functional reconstruction of tissues and suturing inside the larynx, which have been difficult to perform via conventional MIS appproach.

Okazawa et al. were the early developers of a hand-held motorized steerable needle device using a locally pre-curved needle inside a rigid straight cannula [42]. The sliding of the pre-curved needle along the longitudinal direction of the device allows the lateral steering motion of the tip. The steering direction and the bending magnitude can be controlled at the tip during a percutaneous intervention. A path planning algorithm has also been developed that provides autonomous steering of the device towards a desired target.

Sears and Dupont propose a continuum robot made of pre-curved concentric tubes [30]. The position and orientation of the tip of the device are determined by rotating and extending multiple tubes with respect to one other at the base of the system. Different from conventional needle steering method based on the tissue reaction force and the shape of the needle tip, concentric precurved tubes allow active control of the needle motion. Webster et al. also developed a similar device separately from Sears and Dupont, which is an active cannula that consists of several pre-curved superelastic tubes [43, 44]. Depending on the length of each tube that is exposed, the cannula bends to minimize the stored elastic potential energy of the system. The potential of concentric tube robots have led to research interest in modeling its motion behavior, designing appropriate actuation systems [45, 29], motion planning in constrained body anatomy, and applying the technology for various types of surgery [46].

Zaneti $et\ al.$ developed a highly articulated robotic surgical system (CardioARM) that is composed of fifty serially connected rigid cylindrical links, for minimally invasive intrapericardial therapeutic delivery [47, 33]. The CardioArm can be introduced percutaneously through a subxiphoid access in the chest and bypass around the heart until it reaches the target region. The device utilizes the ”follow the leader” mechanism in which the user provides control inputs for the distal end effector of the robot. The other links then follow the leader’s location as it moves forward. Epicardial ablation in a porcine model has been demonstrated using this device.

The Medrobotics Flex® Robotic system, evolved from the research at Carnegie Mellon

University, is a commercially available surgical platform with a flexible robotic scope [48]. It allows the surgeon to navigate through a non-linear path to improve access and visualization of the desired target. Similar to the follow the leader approach, the robotic scope consists of an inner and outer mechanisms, both of which derived from numerous mechanical linkages. The outer mechanism is advanced, steered and locked in place before the inner mechanism follows, creating a rigid, stable surgical platform to insert flexible instruments through a single access site. The system comes with an on-board high definition camera to provide a clear view of the navigation path and surgical site as well as a complete set of flexible instruments, including laser holder, grasper, scissors, needle driver, spatula, needle knife and dissector. It had been cleared by FDA for transoral and colorectal surgery in 2017.

Zuo $et\ al.$ developed a flexible meso-scale robot for gastroinstestinal (GI) surgery, inspired by an earthworm [49]. The robot has a diameter of 7.5 mm and a length of 120 mm, and is screw-driven by an electrical motor. The authors have presented the locomotion mechanism of the robot which creeps along a rubber tube. The robot can turn approximately 50° in any direction. The robot can also move horizontally and along inclined tubes with controlled velocity during its operation.

The continuum robot developed by Yamada $et\ al.$ [35] consists of a thin elastic spirally-cut outer tube and an elastic inner arm in the form of a belt-shaped strip. The inner arm can exist in two different configurations: 1) bent only and 2) bent and twisted. Either one of the two free ends of the inner arm can be linearly pushed or pulled into and out of the elastic tube by two movable shafts at the proximal end, allowing the robot to be bent into different curved shapes. It has also been evaluated as MR-compatible and could potentially be used in MR-guided minimally invasive surgery. Remirez and Wesbter [36] proposed an innovation that allows direct and real-time control over the cross-over point caused by the twisting inner strip, thus creating more variety of curved shapes achievable.

Recently, flexibility in small-scale dexterous surgical robots has been achieved via notch making in a solid tube. The notch manufacturing methods vary among research groups. The notches for the dexterous continuum manipulators (DCMs) are extruded using the EDM process from a cylinder that consists of two concentric nitinol tubes nested tightly together [39, 50, 51]. In another example, a dexterous wrist has been developed by making asymmetric cutouts in a nitinol tube and integrated into a concentric tube robot as its end effector [38]. A 1.16mm diameter prototype has been developed using a tabletop CNC milling machine while an even smaller prototype of 0.46mm diameter was developed using microEDM to validate its potential for scalability. Steerable needles are also developed by carving a series of small notches on the standard brachytherapy needle shaft [40] with the notch design parameters optimized through a finite element model. These prototypes achieve up to 70% smaller radius of curvature than the standard needles without the notches and reach targets with a 1.2mm accuracy error.

Choi $et\ al.$ [52] have developed continuum robotic endoscope using a spring backbone separated into different modules at regular intervals by cylinders. Three wires were routed along the periphery of the device to produce 3-DoF motion including compression and the 2-DoF steering motion. Flexibility and backdrivability of the spring were cited as the major advantages of the device to ensure safe interaction of the endoscope with human anatomy.

Hwang $et\ al.$ [53] developed the K-NOTES system, which comprises of an overtube, two surgical robot arms, and an endoscopic camera. The overtube functions as an outer sheath that provides 2-DoF steernig function at its tip and provides a stable surgical platform when manipulation force is exerted. It had the limitation of being too bulky and exerting too little tip force. Portable Endoscopic Tool Handler (PETH) was therefore introduced to improve the system practicality and allow integration of conventional endoscope and instruments. The flexible scope part of the system is able to endure up to 6 N force at its tip [53].

The Viacath system [54] developed by Hansen Medical consists of an electronically controlled flexible instrument with a diameter of 4.5 mm. Its shaft is made of stainless steel spring wrapped in Teflon and has seven DoFs controlled by 14 cables. It has fixed end effector that can produce a tip force up to 3 N but this design decision makes instrument change difficult.

Boston Scientific Corporation, Natick, MA developed the direct drive endoscopic system (DDES) to perform intralumenal and translumenal procedures. The system consists of a steerable guide sheath with a 16 mm visualization lumen and two 4 mm instrument channels for insertion of graspers, scissors, needle drivers, and cautery probes. The flexible instruments are traction cable controlled and can produce up to five-DoF motion. Some limitations include hysteresis and low force transmission due to long flexible cable and a relative parallel instrument axis with respect to the optical axis [55, 56].

In collaboration with Karl Storz Endoskope, IRCAD-EITS (Strasbourg, France) developed Anusbiscope [57], which is a four-way articulated flexible endoscope with an optics source and an advanced vision (imaging) system, and an insertion lumen of 16 mm diameter. Two movable robot arms can be inserted to enable triangulation of surgical instruments at the distal end. Peroral transluminal and intraluminal surgery, including procedures such as dissection and suturing have been performed on a porcine model without injury to the internal organs.

Suzuki $et\ al.$ developed a scorpion-shaped endoscopic surgical robot [58] that consists of two robotic arms mounted on an endoscope with forceps at the distal tips of the arms. The robot arms and forceps are actuated by step motors via the tendon mechanism. The robot can produce tip force of more than 3 N to grab a 6 mm-diameter object. It is also equipped with haptic feedback and augmented reality technology.

TransEnterix Inc. developed the SPIDER Surgical System [59] that performs laparoendoscopic single-site surgery (LESS). Instead of inserting rigid straight instruments via multiple small incision, it allows insertion of multiple flexible laparoscopic instruments through one incision.

Sensei [60] and Megellan developed by Hansen Medical are commercialized robotic catheter systems. Sensei robotic system incorporates the Artisan® Extend Control Catheter, which is a steerable sheath that allows access to all areas of the atrium. It provides motion scaling up to 4:1 ratio to enable fine control of the catheter motion and force feedback to ensure constant stable tissue contact. The Magellan system[61, 62, 63] is used to navigate through the peripheral blood vessels in an vascular intervention procedure. It enables precise steering and and distal tip control of standard guidewires and robotic catheters of various french gauge sizes from 6 Fr to 10 Fr.

1.2.3 MRI-Compatible Surgical Robots

In the industry, the ClearPoint® System has been developed by MRI Interventions, Inc. to perform MRI-guided stereotactic neurosurgery procedure such as biopsy and electrode insertion. It consists of a compact, single-use SmartFrame trajectory device, a head fixation frame, and a controller that can be manually controlled from just outside the MRI bore. The head-mounted trajectory device is connected to the controller using a Bowden Cable system. The NeuroBlate® System has been developed by Monteris Medical Corporation to perform neurosurgical ablation. It delivers laser energy via a fiber optic probe to provide volumetric ablation to traditionally inoperable lesions in the brain. A 2-DoF needle drive can be cable-driven to perform insertion and rotation of the straight laser probe [64]. Medtronic also developed the Visualase® Thermal Therapy System to monitor and perform laser ablation of soft tissue in a neurosurgery. It employs the smallest laser catheter with a diameter of 1.65 mm and requires a small incision of 3.2 mm diameter.

NeuroARM [65] is a teleoperated neurosurgical robotic system consisting of two robotic arms that are capable of manipulating microsurgical tools. The robotics arms are driven by piezoelectric motors (HR2-1N-3, Nanomotion Ltd., Yokneam, Israel). It is connected to a workstation that has a human-machine interface where the surgeon interacts with the surgical sites. The system is equipped with haptic feedback as well as intraoperative MR image and 3-dimensional high definition display of the surgical site from the surgical microscope.

Surgical tools that can be placed in the two robotic arms are selected from bipolar forceps, tissue forceps, needle driver, suction and irrigation tubes, and microscissors. Currently, procedures within a closed-bore MRI allow only one neuroARM manipulator.

In 1995, Masamune *et al.* developed the first robotic manipulator to perform needle insertion in a neurosurgical procedure in the MRI environment [66]. The framework of the system was constructed from polyethylene terephthalate (PET) while other transmission parts (e.g. bearings, gears, lead screws) were machined from non-magnetic steel, brass, aluminum, Delrin, and ceramics. All six DoFs of the robot were actuated by ultrasonic motors (Shinsei Corporation). Positioning accuracy and backlash errors were identified experimentally to be in the 10s of μm and 100s of μm for all DoFs. The evaluation of MRI compatibility in the MRI scanner (MRH-500 Hitachl Co., Japan) shows that the maximum distortion error was 4 mm.

ROBITOM (Robotic system for biopsy and interventional therapy of mammary lesions) [67] was another early prototype that was developed to allow breast biopsy in an MR scanner. The 6-DoF robot consists of a control unit, trocar, biopsy needle, laser applicator, a driving unit, and a gripper. In-vitro experiments were conducted in pig liver with the robot achieving high precision in a 1.5 Tesla MR.

An MRI-compatible robotic system was developed through the collaboration between the National Institute of Advanced Industrial Science and Technology (AIST), Japan and the Harvard Medical School [68]. It is designed to assist the surgeons in minimally invasive procedures, such as biopsy, by providing more precise positioning of the catheter, laser pointer, and other lightweight instruments. Every part of the robot were made of paramagnetic materials, including aluminum alloys and plastics, to ensure its MRI compatibility.The robot was designed to have its mechanical main body above the surgeon's head with two rigid arms hang down to the surgical workspace. The actuation of all degrees of freedom is provided by ultrasonic motors with optical encoders. Placing the main body away from the surgical field clears the space for surgeons and improves MR compatibility but reduces its precision and dynamic response. It was tested in an intraoperative MR scanner (Signa SP/i, GE Medical Systems, 0.5 Tesla) with parallel facing magnets.

A master-slave robotic system was developed using conventional motors in the control room and hydrostatic transmission for a power transfer over up to 10 m [69, 70]. Compared to pneumatic actuation, it is claimed that hydraulic connection would provide a much stiffer transmission and thus faster response. The system consists of a steel master cylinder and a slave cylinder made of non-magnetic and non-conducting materials. Fiber optic-based force and torque sensors and optical position encoders have also been developed to be MRI compatible. Evaluation in an fMRI MR scanner (Marconi Magnex Eclipse 1.5 Tesla Power Drive 250) with a human subject shows that the brain activity is similar with and without the robotic system, thus confirming that the presence of the hydrostatic transmission does not interfere with the fMRI scanner.

Larson $et\ al.$ develoepd a 5-DoF robotic stereotactic device with telescoping shaft transmission for minimally invasive MR-guided intervention in the breast [71]. The device mainly has two functions: 1) stabilize the breast via compression and 2) define the trajectory along which the interventional probe will be inserted. The actuation of all degrees of freedom, including the breast stabilization, is controlled by ultrasonic piezoelectric motors. A graphical user interphase has also been developed for planning and monitoring of the procedure. The breast is stabilized by moving a stabilization plate towards another fixed plate via a Delrin lead screw. The MR compatibility of the device was tested and confirmed on a human 4 Tesla magnet with minor main magnetic field inhomogeneity. High positioning repeatability of less than 1° and backlash in the probe angle of 4° was achieved.

A 5-DoF MR-image guided robot was developed at Imperial College London to perform prostate lesion biopsy [72, 73]. A master-slave configuration was developed to resolve the problems of space constraint in the MR bore and limit exposure of the operators to magnetic field strength. A shielded aluminum enclosure that houses a 24 V battery and the motor driver electronics, was placed 1-2 m away from the MR isocenter and grounded.

Shielded twisted pair cables were used to connect the electronics in the enclosure to the control room via a low pass filter. Upon evaluation in the MR scanner (Siemens Magnetom Vision, 1.5-T), the signal-to-noise ratio (SNR) dropped by 2.6% when the encoder was powered and 13.7% when the motor was actuated at maximum speed.

Fisher *et al.* [74] developed an MRI-compatible pneumatically-controlled robot for transperineal needle placement in a prostate intervention procedure. The robot uses custom-made pneumatic cylinders, proportional pressure regulator and pneumaticaly operated brakes. The cylinder is made of glass, graphite and brass to ensure low friction, MR compatibility, and more stable operation while the brake was developed to lock the piston in its position to provide a stable needle insertion platform. The robot controller is placed inside the MR scanner room to minimize the distance valves and the robot. Containing an embedded computer, pressure sensors and various servo valves, the controller is placed 3m from the edge of the scanner bore and has an electromagnetic interference shielder enclosure. The low-level embedded PC communicates with the planning and control workstation in the MRI control room via a fiber-optic Ethernet connection. The system was tested on the MR scanner (Philips Achieva, 3T) and there was an SNR loss of 5.5% with T1 weighted imaging.

A teleoperated master-slave surgical robotic system was developed [75] to perform biopsy and RF ablation of breast tumor. It consists of an MRI-compatible slave robot with a 1-DoF piezoelectric motor actuated needle driver, a 3-DoF pneumatically actuated parallel mechanism to orient the needle, and a 2-DoF pneumatically actuated X-Y positioning stage. All electronics and valves were placed in the control room and long transmission lines were used to connect these parts with the slave robot through the waiveguide. The system was evaluated on the MR scanner (Tim Trio, Siemens Medical Solutions, 3T) and less than 8% drop in SNR was observed. It has also been used for both ex-vivo and in-vivo targeting under MR guidance. The time delay due to the long transmission lines and the more complex control for smooth and precise positioning are some of the limitations observed.

Krieger *et al.* [76] developed a transrectal prostate intervention robot with actuated needle alignment and manual needle insertion. The needle insertion task was made manual to maintain a more direct surgeon control and ensure a quicker path to clinical trials. The robot consists of a rotation stage and a translation stage fully integrated in a motor box and the actuation is provided by piezoelectric motors (HR1, Nanomotion Ltd., Yokneam, Israel) placed about 30 cm from the MRI isocenter. A biopsy gun is integrated at an angle to the transrectal probe at the front of the motor box. The aluminum controller box containing the motor amplifiers and motion controller is placed inside the MRI room and connected to a filtered 24V DC power supply through the penetration panel. An SNR reduction of up to 60% was reported and significant improvement could be achieved when the robot was covered in radiofrequency (RF) shielding.

Goldenberg *et al.* [77] developed a 5-DoF robot (MRI-P) for prostate intervention. The robot has a modular trocar to mount different surgical tools for different intervention procedures including thermal ablation, brachytherapy, and biopsy. The robot, placed between the patient's legs and about 20 cm from the MR isocenter, consists of two horizontal and vertical linear joints and three rotational joints, all of which actuated via short transmission by ultrasonics motors (either USR60-E3N or USR30-E3N, Shinsei Corporation). Most parts of the robot is made out of aluminum 60601, brass, and plastic while the surgical tools are made of titanium. The robot controller, shielded in an aluminum enclosure, is placed in a low magnetic field fringe area in the MRI room. Power supply and communication with the human control interface are provided to the robot controller by cables passing through the filtered waveguide. Upon the MRI compatibility evaluation, an SNR drop of 38% was observed when the motor was running at 75% load without significant deviation in the targeting accuracy.

Oliver [3] developed an MRI-guided Endoscopic Retrograde Cholangio-Pancreatography (ERCP) system with a remote actuation unit. A novel miniature pneumatic clutch represented a key innovation that is integrated into the design to reduce the number of parallel motors and provide a reliable and efficient transmission. There is also a catheter feed module that drives the catheter into and out of the duodescope control handle. Ultrasonic motors (USR-60, Shinsei Corporation) are used to actuate the six DoFs of the duodenoscope. The motor drivers, pneumatic valves, batteries, and other electronics of the endoscope remote actuation system are stored in an aluminum box. SNR drop was found to be less than 20% when the unshielded motor is placed beyond 30 cm from the MR isocenter of a 1.5T GE Sigma Excite closed bore MRI scanner. The MR compatibility results show that the active components of the actuation system must be shielded and the power source must be isolated from the scanner room shield.

Li $et\ al.$ [78] developed an MRI-guided stereotactic neurosurgery robot designed to be kinematically equivalent to the Leksell stereotactic frame and to perform electrode placement for deep brain stimulation. It combines a 3-DoF prismatic Cartesian motion base module and a 2-DoF remote center of motion (RCM) mechanism module. In particular, parallel mechanism design is employed for the RCM linkage, which is made of the high strength plastic Ultem, to provide sufficient stiffness to the robot. Custom motor controllers are used to control the linear piezomotors (PiezoLegs LL1011C) and rotary piezomotors (PiezoLegs, LR80) at the various robot joints. SNR drops of 13.6% and 12.5% in T1 and T2 images were observed during simultaneous actuation of the robot and MR imaging.

The first MRI-compatible concentric tube robot was developed by Su $et\ al.$ [79] and is claimed to be suitable for a variety of applications including neurosurgery, percutaneous interventions, and other procedures requiring a curved trajectory. Completely residing inside the MRI bore, the 6-DoF robot is connected to a customized robot controller placed at the fringe area inside the MRI room. The robot supports three concentric tubes with a 3-DoF cannula driver and a 3-DoF Cartesian positioning stage, all of which are actuated by piezoelectric motors from PiezoMotor. The customized motor drivers, that use four class AB linear amplifiers, generate less high frequency noise and therefore cleaner driving signals, thus lowering the interference of the driving electronics with the MR imaging. The customized driver boards are claimed to support both harmonic and non-hormonic piezoelectric motors from four major piezoelectric motor suppliers: Nanomotion, PiezoMotor, Shinsei, and PCB Motor. More details on the customized drivers can be found in [80]. Positioning errors of less than 2.24 mm were reported for three different trajectories upon evaluation inside a 3 Tesla Philips Achieva scanner.

The innovative continuum robot developed by Yamada $et\ al.$ [35] based on elastic tube and elastic strips is MRI-compatible since the material used is purely polyethylene resin and it is tendon-driven. Besides manual actuation, the actuator that was implemented was not specified but shape memory alloy was mentioned as a potential actuator. Based on preliminary MRI compatibility evaluation, the artifact obtained was similar for the proposed continuum robot and for a clinically-used biopsy needle, confirming its potential for intraoperative MRI-guided procedures.

An MR-compatible surgical manipulator has been designed developed for intraoperative MRI-guided minimally invasive liver surgery [81]. Be-Cu was chosen as the material to build the tip while aluminum, brass, and titanium were were used for the structure. These materials were specifically selected to ensure MR compatibility of the device. Ultrasonic motors placed far from the MRI bore are used to generate hydraulic power in the hydraulic bilateral cylinder for manipulation of the forceps. The problem of cavitation and fluid leakage is dealt with through the development of a fluid leakage compensation mechanism that refills fluid when the hydraulic pressure drops below a threshold. Besides, an RCM mechanism has also been developed and actuated by an ultrasonic motor (USR60-S4, Shinsei Corporation). Upon evaluation of the system in a conventional MR scanner (MRH-500, HITACHI Medical Co.), it was observed that there was an almost 50% reduction in SNR when the system was placed inside the bore and actuated. However, the range of affected area is limited to 10 mm radius around the system. It is also proven that the system was operational during MR scanning.

”MRI Steath” robot [82] is an MRI-compatible robot developed for prostate intervention. It is actuated by a new type of pneumatic motor called PneuStep, where step motion is achieved by sequentially pressurizing the three pneumatic ports. No electricity is therefore involved. The robot is also exclusively made of nonmagnetic and dielectric materials such as Polyetherimide (Ultem 1000), Delrin, Nylon 6/6, Peek 1000, Garolite G-11, Polyimide, high- alumina ceramic, glass, sapphire, PTFE (Teflon), and Silicone rubber. The robot control unit, containing the electronics and solenoid valves, is placed in the control room and connected to the robot through 6 m long hoses. The robot can achieve positioning error of less than 0.315 mm and a repeatability of 0.060 mm. The less than 1% passive image deterioration factor, E_P coefficient, and active image deterioration factor, E_A coefficient, proved that there was minimal or unperceivable artifacts on the MR images during evaluation of the robot in an MR scanner.

An MRI-safe robot was developed to perform direct MRI-guided endorectal prostate biopsy [83]. The robot is basically an assistive device to help surgeons automatically orient a needle-guide and control the needle insertion depth. Two PneuStep motors are integrated into the robot body to control two DoFs of the robot, namely the angle of the endorectal extension and the angle of the needle guide relative to the endorectal extension. The evaluation of the robot in the MRI shows that the E_P coefficient and E_A coefficient are extremely low and the SNR change due to robot motion is –0.71%.

A four-DoF origami-enabled robotic end effector, including a parallel foldable structure and a gripper, has been developed for minimally invasive surgery [84]. Origami principle was applied to allow the device to shrink to a very small size and yet maintain the mechanism complexity that promotes tool dexterity. The foldable structure consists of a 3-DoF parallel platform while the gripper is a compliant structure connected to a linear SMA actuator via a cable. Even though the device was not evaluated for its MR compatibility, it was claimed that SMA was chosen as the actuator due to its MR compatibility, showing the device’s potential as an MR compatible surgical tool in the future.

Ho *et al.* have developed the first and second prototypes of the Minimally Invasive Neurosurgical Robot (MINIR) that are MRI-compatible from brass [85] and plastic, respectively. The first prototype was a multi-rigid-link robot made of brass with SMA wires forming antagonistic local actuator at each revolute joint. SMA wires were installed in the joints of the robot made of brass links to perform local actuation. Due to the artifacts introduced by the electric current passing through the SMA wires, local actuation method was abandoned and SMA springs were used to actuate a 4-DoF serial robot made of plastic links via tendon sheath mechanism [31]. It was found that SNR dropped by 0.7% during robot actuation and 1.4% during electrocautery procedure.

1.2.4 MRI-Compatible Actuators

Magnetic resonance imaging is an imaging modality that provides much superior soft tissue imaging than many other imaging technologies including CT, conventional X-ray, and ultrasound due to its high spatial resolution and soft tissue contrast. For many decades since the emergence of MRI, pre-operative MRI has been used to allow neurosurgeons to identify the brain tumor in 3D space within the brain and plan the surgical path to reach the tumor. However, the anatomical location of the tumor and its surrounding tissues may change between the time the preoperative imaging takes place and the actual surgical time due to reasons such as brain shift. Organ deformation may also happen when the robot is being inserted along a certain path in the soft tissue environment. It would be highly desirable to have real-time imaging available to the surgeon during navigation of the surgical robot to adapt the trajectory to the soft tissue in real time [86] and to avoid multiple entry of the robot or constant repositioning, increasing safety and accuracy of the surgical procedure and reducing patient trauma. However, the high magnetic field environment and switching magnetic field gradients pose various challenges to the design of any mechatronic or robotic system [87], including magnetically induced eddy current and the resulting force effect, magnetically induced elevated forces and torques, radiofrequency-induced thermal effect, affect on the proper operation of sensors and actuators especially during MR scanning, and lastly artifact formation and SNR deterioration on the MR images. Various methods could be used to verify the effect of presence and actuation the robotic system on the MR images, namely geometric distortion, SNR reduction, and qualitative assessment on the artifact by a surgeon/radiologist [78]. Defined by the NEMA standard, SNR is the signal in the center of a homogeneous phantom, divided by the noise intensity in the periphery [88]. The signal is defined as the mean pixel intensity in the region of interest (ROI) while the noise is defined as the root mean square (RMS) signal intensity in an ROI outside of the phantom. The type of actuators that are compatible with MRI technology is limited due to the interference that the strong magnetic field on the regular electromagnetic motors. In the past decades, ultrasonic piezomotors, hydraulic actuators, pneumatic motors, and shape memory alloy have been the mainstay actuators used for MRI-compatible surgical robots.

Hydraulic actuation

An ultrasonic motor-hydraulic actuation system [81] was used to manipulate a gripper for minimally invasive liver surgery. Bilateral hydraulic cylinders and a remote center of motion (RCM) mechanism were used to make the robotic setup compact. High fluidic pressure was used to reduce the air bubble effect while automatic refilling mechanism was built to prevent the drop of fluid pressure beneath a desired level due to fluid leakage.

Hydrostatic transmission was used in [69] to transmit force between the electromagnetic motors in the control room to the end effector in the MR scanner. The system was tested in an fMRI scanner and it was shown that a human brain activity was not disturbed by the presence of the system.

Despite the fact that hydraulic actuators are completely MRI-safe, there have not been many research in the past decade that make use of it for MRI-compatible surgical robotics. Fluid leakage and cavitation are still major concerns that need to be addressed before hydraulic actuation become a major actuation method of choice for MRI applications.

Pneumatic actuation

Pneumatic actuation [89, 90, 91, 92] is a fully MRI compatible actuation method that does not pose the risk of interference of magnetic field by EM signals from any electronics when the electrically activated valves are placed in the control room and air transmission is passed through the waveguide [89].

A CT- and MR-compatible light puncture robot (LPR) was developed to target lesions larger than 1 cm in 2004 [86] that is intrinsically compliant. Information from the MR images is used to complete the control loop to verify the LPR's position and orientation. The 5-DoF robot is strapped to the patient's body to account for the physiological movements during the procedure. The two rotation joints are actuated by pneumatic cylinders pressurized at 3.5 bar. 7m long plastic tubes are used to connect the actuators to their valving system in the control room. Preliminary results show that the robot could achieve targeting precision with errors less than 2 mm.

Fisher $et\ al.$ [74] developed an MRI-compatible transperineal needle placement robot for prostate intervention using custom-made pneumatic cylinders made of glass, graphite and brass to ensure low friction, MR compatibility, and more stable operation. They were able to achieve SNR loss of less than 5% in a standard 3 Tesla MRI. A pneumatically actuated needle insertion robot was developed [93] to perform biopsy and RF ablation of breast tumor. However, the time delay and complex control for smooth and precise positioning are some of the limitations for the pneumatic actuators.

A novel pneumatic step motor called PneuStep was developed to actuate the various joints of the "MRI Steath" robot [82]. Pneumatics actuation allows complete decoupling from electromagnetism, allowing the robot to operate inside the MRI bore under real-time MR imaging feedback. Precise step motion is achieved by pressuring three pneumatic ports sequentially and a fiber optic encoder allows closed-loop control. The motor also includes an integrated gearhead and a fiber optic quadrature encoder for closed-loop control of the motor. Similar step motor design with a different working principle has been proposed by

Sajima $et\ al.$ [94] and Chen $et\ al.$ [95]. Their pneumatic stepper motors have simplified design and smaller diameter but at the expense of reduced precision and torque.

Besides the heavy infrastructure involved, pneumatic actuation possesses some intrinsic drawbacks such as actuation delay and difficulty to produce smooth motion. Researchers have been trying to tackle these problems from both control and design perspectives.

Ultrasonic and piezoelectric motors

Piezoelectric motors use the reverse piezoelectric effect to convert electrical energy in the form of high frequency (around 40 kHz) voltage to mechanical energy in the form of vibration. This in turn drives the piezoelectric ceramic plates to move a ceramic bearing structure to generate either linear or rotary motion. On the other hand, ultrasonic motors use the same form of piezoceramic materials as the piezoelectric motors but use resonant vibration to induce the motion.

Ultrasonic motors (USR30-N4, Shinsei Corporation, Japan) [66] are used in a 6-DoF needle insertion robot in a low-field 0.5 Tesla MRI machine. It was found that the ultrasonic motors which was placed very close to the isocenter, when being powered on, caused significant distortion. Therefore, the motors were powered down during MRI scan. A higher MRI image resolution was found to be required to improve the positioning error of the needle placement. Chinzei $et\ al.$ [68] used ultrasonic motors (USR60-S3N, Shinsei Corporation, Japan) placed above the surgeon's head and two long rigid arms to solve the problems of small workspace in closed-bore MRI and reduced SNR ratio of MR images. Tsekos $et\ al.$ [96] also used the motors from Shinsei Corporation and placed them 1 m from the iscocenter of a 4 Tesla MR scanner. Telescopic acrylic shafts were used to transmit the force from the remotely-placed motors. They achieved sub-millimeter accuracy of the probe tip and the largest error was due to backlash in the rotation joint. Elhawary $et\ al.$ [72] used piezomotor (PiezoLegs, Piezomotor, Sweden) near the MRI isocenter to perform prostate biopsy and found there was a reduction of under 28% in signal-to-noise

(SNR) when position control was implemented to operate the motor. Krieger $et\ al.$ [76] developed a prostate intervention robot using piezoelectric motors (HR1, Nanomotion Ltd., Yokneam, Israel) placed about 30 cm from the MRI isocenter. An SNR reduction of up to 60% was reported and significant improvement could be achieved when the robot was covered in RF shielding. The drive eletronics and control boards were placed in a Faraday cage in the MRI room in these applications. Su $et\ al.$ [79] actuated an MRI-compatible concentric tube robot using piezoelectric motor (PiezoMotor, Uppsala, Sweden) using a custom-made driver to further eliminate the artifacts deemed to be caused by the driving signals from commercial piezomotor drivers. Li $et\ al.$ [78] used linear (PiezoLegs LL1011C) and rotary piezomotors (PiezoLegs, LR80) from PiezoMotor, Uppsala, Sweden for a neurosurgical robot that is kinematically equivalent to the Leksell stereotactic frame. Using their custom-made motor driver, an SNR reduction of less than 14% was reported, compared to the 28% maximum drop reported in [72] that used commercial driver. Oliver [3] developed an MRI-guided Endoscopic Retrograde Cholangio-Pancreatography (ERCP) system using ultrasonic motors (USR-60, Shinsei Corporation, Japan) and found that the SNR drop improved to less than 5% when the robot's distance from the isocenter was 90 cm.

Due to reasons such as the use of electrical cables in the motor, it is advisable to keep the motor at least 30 cm from the MR isocenter. Various research has also showed that the motor driver/controller should be placed around 1-2m from the MR isocenter. Any closer distance will prevent the motor from being operational properly. The critical distance also depends on the size of the MR scanner (60 cm or 70 cm bore size) and the magnetic field strength (1.5 T or 3 T).

Various experiments have been performed to investigate the effect of piezoelectric motors on the MR images. Fischer $et\ al.$ conducted an experimental evaluation and comparison for the effect of different MRI-compatible actuators, namely an ultrasonic motor (Shinsei Corporation), an piezoelectric motor (Nanomotion Ltd.), and a pneumatic cylinder (Airport, Norwalk), on MR imaging in a 3T Achieva scanner (Philips Medical Systems) and 1.5T Signa scanner (GE Healthcare) [97]. Placing the controllers in the scanner room reduces the SNR drop and the pneumatic cylinders generated practically no drop in SNR, compared to the other two motors. The Shinsei ultrasonic motor caused a larger drop in SNR during its motion, compared to the Nanomotion piezoelectric motor. The SNR drop due to the presence of actuators and controllers was greater on the 1.5T scanner than on the 3T scanner but this could be due to the better shielding of the scan room for the newer 3T MR scanner. Despite the less favorable results for the Shinsei motors, they continue to be the most used motors in MRI-compatible robotic systems throughout the recent decade, most likely due to the superior torque and reliability. Moreover, other research [3, 71, 77, 81] using the ultrasonic motors from Shinsei Corporation produced significantly more promising results than in [97].

Electrostatic linear motor

Dual Excitation Multiphase Electrostatic Drive (DEMED) is an example of electrostatic actuators, driven by high three-phase AC voltage [98]. A non-magnetic prototype, fabricated from only paramagnetic materials, consists of a pair of stator and slider that move relative with respect to each other during voltage excitation. The power source, connected to the motor via an 8 m shielded cable, and the function generator were placed outside the MR room. Evaluation in an fMRI scanner shows that there was maximum detectable thrust force of 10 N on the robotic system at applied voltage of 1.5kV and the SNR started to drop when the applied voltage exceeded 1.2 kV. SNR, however, is independent of the driving frequency and any distance beyond 60cm from the MR scanner.

Electrostrictive polymer actuators (EPAM)

Binary polymer based actuators, called Electrostrictive Polymer Actuators (EPAM) [99] has been used to reconfigurable MRI surface imaging coil (RMIC). It consists of a dielectric polymer film stretched in a plastic body and compliant electrodes on either side of the film.

When a potential difference is applied across the dielectric, the film is compressed and expands in its area, thus producing a mechanical motion. The binary nature of the actuator fixes the position that the device would be moved into, thus removing the need for any sensor to provide real-time feedback. The MRI compatibility evaluation shows no RF noise in the images and the image quality is comparable to that achieved using commercial imaging coils.

Electro-rheological fluid (ERF)

Electro-rheological fluid, that changes its rheological properties such as viscosity or yield stress upon application of electric field, is used as the actuator for an MRI-compatible hand rehabilitation device [100]. Its properties of quick response and ability to reduce system complexity make it very attractive. The device consists of the ERF resistive element, gearbox, handles and sensors. The resistive element has an inner rotating electrode cylinder and a outer stationary cylinder electrode, separated by a thin layer of ERF. The actuation of the ERF generates a torque on the rotating shaft attached to the rotating electrode. The power supply for the ERF was placed in the control room. The device was evaluated in a 3T MR scanner and it was found that the loss in SNR was not significant.

Shape memory alloy (SMA)

Shape memory alloy (SMA) actuators, mostly made of NiTiNOL (Nickel Titanium discovered at Naval Ordinance Lab by Buehler and Wiley [101]), exhibits two smart behaviors: shape memory effect (SME) and superelastic property. It also exists in two fundamental phases: martensite and austenite (parent/memorized phase). Under SME, the material can be trained to have a specific memorized shape. At a low temperature under the austenite start temperature, SMA can undergo a large deformation. Upon thermal activation, SMA recovers a large deformation and returns to its parent phase and shape after reaching austenite finish temperature. When it is cooled down below martensite finish temperature under no load, it converts to the martensite phase and thus can be easily deformed again. Nitinol can experience a recoverable strain of up to approximately 7-8% and more than 200% in its elastic modulus during conversion between its low-temperature martensite phase and high-temperature austenite phase [102]. Other alloys such as Cu-Al-Ni, Mn-Cu, and Au-Cd also exhibit similar properties with recoverable strain between 3% and 8% but NiTi exhibits superior mechanical properties in tensile strength, corrosion and abrasion resistance and ductility.

SMA has the advantages of having large power density, large stroke length, high corrosion resistance, biocompatibility, and compact footprint as well as being silent during its operation. It can also be attractive economically since it is orders of magnitude cheaper compared to ultrasonic/piezoelectric motors. It usually requires very simple design architecture and integration into the overall robotic design without the need for speed reduction or motion amplification.

SMA has been used in several surgical instruments such as an SMA-actuated active endoscop [103], surgical forceps in a laparoscopic surgery [104], and a steerable probe for percutaneous intervention [105]. These devices, however, have not been tested for MRI compatibility. A NiTi stent with an internal expanded diameter of 9 mm has been developed [106] and was evaluated for its MRI compatibility. The results show that NiTi stent induces minor artifacts on the MR images and allowed for visualization of signals from within the stent lumen. SMA wires and springs [31] have been used to actuate two versions of a meso-scale multi-link neurosurgical robot. SMA wires were installed in the joints of the robot made of brass links to perform local actuation. Due to the artifacts introduced by the electric current passing through the SMA wires, SMA springs were used outside the robot and used to actuate a robot made of plastic links via tendon sheath mechanism. An SMA torsion spring has also been used as an actuator in the Neurosurgical Intracerebral Hemorrhage Evacuation Robot (NICHE) [107]. The robot has recently integrated a fiber optic rotation sensor and its MRI compatibility has been verified in a 7-Tesla small bore

MR scanner.

1.3 Research Objectives

The use of flexible robots in surgical procedure is an emerging trend and will continue to play a bigger role in the coming decades. As for the appropriate imaging modality, MRI is clearly the best imaging technique for brain lesions. Based on our literature review, there are a lot of innovations in flexible robots and MRI-compatible surgical robots. Most MRI-compatible robots are used for needle targeting with actuation mechanisms developed to position a 1-DoF insertion probe/needle that can be inserted or retracted. The straight rigid probe limits the workspace it covers and therefore the tumor size that can be targeted. On the other hand, most flexible surgical robots are not MRI-compatible due to their robot body being made out of magnetic materials or their actuators being not MRI-compatible. To the best of our knowledge, there are only two MRI compatible flexible robots, namely the concentric tube robot [29, 79] and the elastic strip-based continuum robot [35], which has been barely evaluated for any surgical procedure. The size of the concentric tube robot is very small, thus limiting the number and type of instruments that can be integrated. It is targeted towards needle-based percutaneous procedures. Our research objective is therefore to design, develop, and evaluate a robotic system that actuates a flexible robot in the MR scanner. The robot has to be fully MRI-compatible with the ability to integrate multiple instruments and yet small enough to fit inside an existing surgical speculum. It should have a range of motion large enough to aspirate tumor up to the 4 cm diameter. The robotic system needs to have a compact footprint that would fit in the MR bore so that real-time visualization, tracking, and guidance of the flexible robot can take place.

1.4 Thesis Overview

Chapter 1 presents the motivation behind our research to develop a neurosurgical robotic system to remove deep brain tumor. It also includes a comprehensive review of the existing neurosurgical robots, flexible surgical robots, MRI-compatible surgical robots, and MRI-compatible actuators. Chapter 2 introduces the design, development, modeling, and experimental evaluation of a 3-D printed, tendon-driven flexible robot (MINIR-II) that has independent segment motion due to its unique tendon routing configuration. Chapter 3 presents the development, modeling, and evaluation of the compact cooling module-integrated SMA springs as the proof-of-concept actuators for MINIR-II while Chapter 4 describes the development and evaluation of a new actuation mechanism to operate the cooling module-integrated SMA springs. A stiffness modulated robot prototype has also been developed and modeled in Chapter 5. Three attempts to develop a remote-actuated robotic system with MINIR-II as the end effector are described in Chapter 6, 7, and 8, with the final setup, of which the hysteresis performance has been modeled, being the most reliable. Last but not least, in Chapter 9, we make some concluding remarks and discuss potential future work for the project.

CHAPTER 2

3-D PRINTED SPRING-BASED FLEXIBLE ROBOT

2.1 Introduction

The goal of this research was to develop a minimally invasive neurosurgical robot to remove brain tumor under continuous MRI guidance. Based on preoperative MR images such as diffusion tensor imaging (DTI), a trajectory from the brain surface to the tumor, which may not be the shortest but with ”the least transgression of white matter fascicles” [108], can be identified. A speculum such as the BrainPath system is then inserted gently, displacing the brain tissues along the sulcus, to create the pathway for the MINIR robot.

In the initial work, a brass alloy 360 MINIR prototype with nine revolute joints was developed. Each joint was actuated by antagonistic SMA wires [109]. This was followed by a rapid prototyped MINIR actuated by tendon-sheath mechanism [31, 110]. The work explained in this chapter is an improvement, especially in terms of robot design, over our previous effort [31]. A spring-based backbone with three independently actuated segments, named the second generation of MINIR (MINIR-II), was used to replace the rigid links to provide a more compliant interface and to maneuver within the tumor for complete tumor removal. The important problem of decoupling continuum segments was resolved through smart tendon routing configuration. Part of the work described in this chapter was done in collaboration with the former post-doc in the lab, Dr. Yeongjin Kim.

2.2 Robot Design

The robot was designed to have the workspace to cover deep brain tumors which have average diameter of less than 40 mm [111] and each segment should achieve a bending angle of at least 45°. It is important to note that the bending angle is relative to the orientation (surface normal vector) of the prior disk. Hence the change in bending angle causes twice the change in the surface normal of the following disk. For example, a bending angle of 45° results in a 90° orientation change of the following disk as illustrated in Fig. 2.1(e). Divided into three segments, the robot has a 60 mm length and a diameter of 12.6 mm. The diameter was selected to fit inside existing endoports (11-13 mm) used in microsurgical resection of deep-seated brain tumor [112, 113]. The lumen through the center of the robot has to be at least 3 mm to have enough room for electrocautery wires, and suction and irrigation tubes. The electrocautery probes are embedded at the tip of the end segment of the robot. There is not a required target end effector force to navigate in a brain tumor or human brain tissue (human brain tissue has a stiffness of 0.1-3 kPa [114]) since it depends on variables such as the shape and size of the tool tip, the navigation velocity, and the robot configuration. The robot motion experiment in gelatin would serve as preliminary verification of the motion capability of the robot inside the brain.

Our continuum robot has a snake-like body made of four disks (Disk 1, Disk 2, Disk 3, and Disk 4) supported by interconnected inner plastic springs. It has three segments (base, middle, and end segments), maintained in a cylindrical shape by a long continuous outer spring, as shown in Fig. 2.1. This spring structure provides the robot with a flexible and compliant main body that allows smooth maneuverability in a soft tissue environment. At the same time it improves robot dexterity by allowing 2 DoFs at a single point (like a universal joint) using two pairs of tendons terminated at four locations on each segment disc spaced 90° apart. The two antagonistic pairs of tendons enable back and forth motion of a robot segment in two independent DoFs (pitch and yaw). We explored different materials and dimensions for the springs to achieve the desired stiffness, defined by its ability to maintain its elasticity after being bent by at least 45° using SMA spring actuators without breaking. We excluded all metallic material to avoid noise in MRI images (even MRI-compatible metals can create distortion in the MRI images if placed in the imaging plane) and ended up choosing VeroWhite, a material used in the rapid prototyping machine (Objet

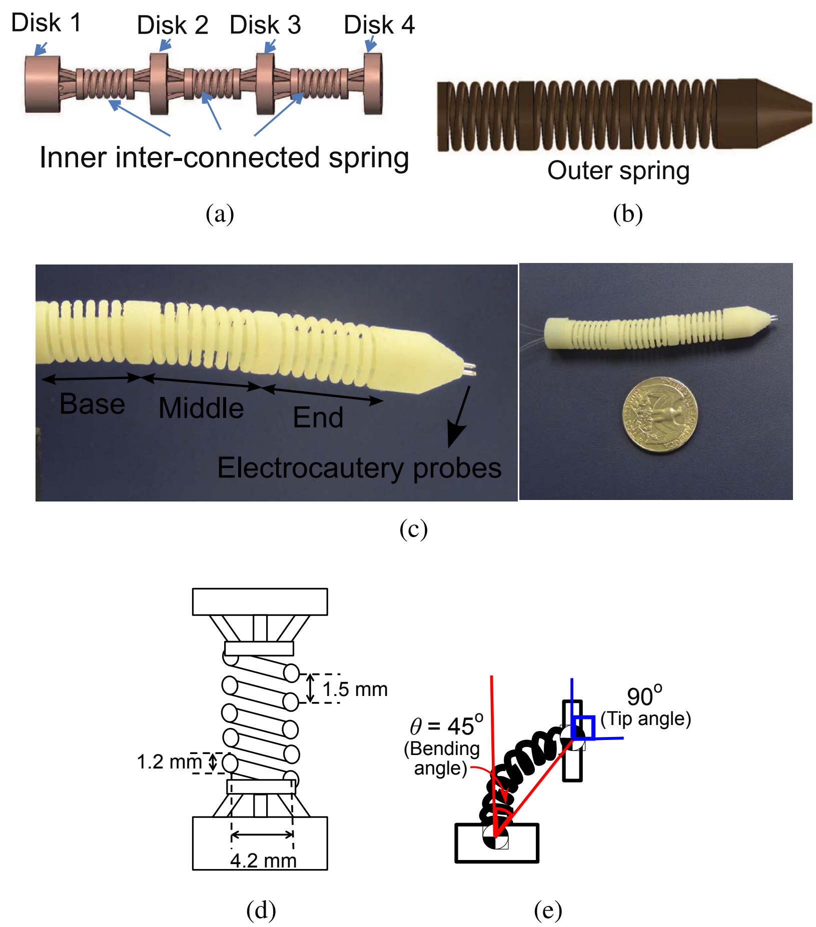

Figure 2.1: (a) CAD illustration of the inner spring (b) CAD illustration of the outer spring (c) Actual picture of the MINIR-II equipped with cautery probes (d) Schematic of one robot segment with dimensions (e) Schematic showing the surface normal of the segment disk has an orientation change (i.e. 90°) that is twice the bending angle (i.e. 45°)

350V, Stratasys, USA) that has a stiffness of 2495 MPa and a 20% elongation at break. For higher spring constant and thus a higher stiffness, a large spring wire diameter was used. The outer spring, which is parallel to the inner spring, contributes slightly to the spring constant. It is primarily intended to prevent contact between the tendons and the environment and to preserve the curved shape of the robot during its motion. The selection of the plastic spring pitch, wire diameter, and spring coil diameter was done after several trials, given the spatial limitations due to the maximum allowable robot diameter and the minimum lumen diameter. The combination of 1.5 mm pitch, 1.2 mm spring wire diameter, and 4.2 mm spring coil diameter, as shown in Fig. 2.1(d), led to a robot segment that has flexural rigidity of $3.7\times10^{-5}\ Nm^2$ and axial stiffness of 46.6 N/m. The complete three-segmented robot has flexural rigidity of $1.9\times10^{-4}\ Nm^2$.

In most of the existing continuum robots with tendon driven mechanism [115, 116], tendons/alternate force transmission mechanisms are routed along the periphery of the robot, as seen in the 1^{st} configuration in Fig. 5.2(a). Motion coupling between segments in a continuum robot has also been traditionally resolved by simultaneous use of multiple actuators and an appropriate control model [117]. However, we attempt to handle the problem in the design stage so as to minimize the number of actuators that need to be activated for a desired robot configuration. Inspired by the central tendon routing configuration in rigid joint robot [118] and combined continuum-rigid robot [119], we applied similar design concept on our completely flexible robot that has no pulleys at the robot joints. Different from Hirose's design [118] which had one tendon routed around a pulley at every robot joint, pulleys are not used in the main robot body in our design to keep the robot diameter small and two sets of tendons are used at each joint to provide active back and forth motion as well as 3-dimensional motion capability for each segment. As shown in the 2^{nd} configuration, tendons for each segment are routed through the central axis of the inter-connected springs and branch out only at the base of the target segment. When tendon pulling generates moment at the end segment, it only generates normal compression at the two other proximal segments, as shown in Fig. 5.2(b). We can also compensate the gravitational load on the robot body by varying the stiffness of the inter-connected spring during the design stage. Due to its elastic characteristics, the robot stays in its straight home configuration when no tension is exerted. This innovative tendon routing configuration in our robot marks a unique improvement over other continuum robots in previous research [115, 116, 120].

Finally, we manufactured our robot in a single piece so that in a practical application, the individual segments would not be easily separated. The lack of an assembling process also saves manufacturing time and cost, as well as allows customizable robot to be more easily produced.

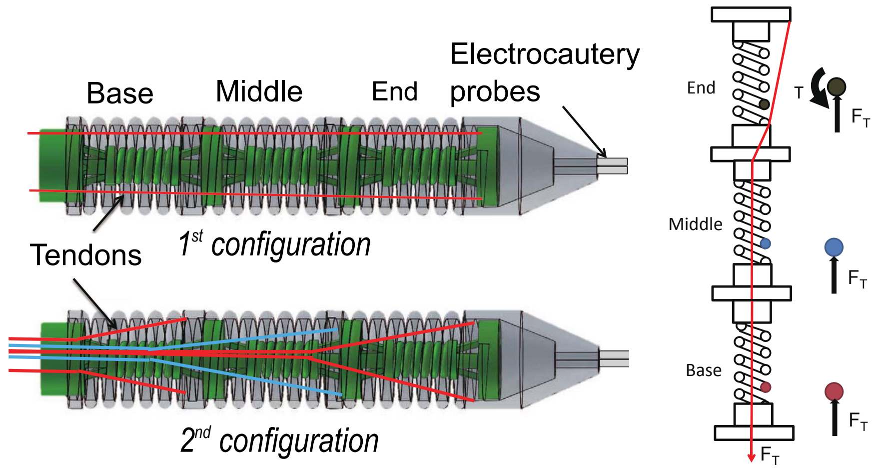

(a) (b)

Figure 2.2: (a) Two configurations of tendon routing mechanism (b) Schematic showing the forces exerted in the spring wire of each segment when the 2^{nd} tendon configuration is used

2.3 Kinematics and Jacobian

2.3.1 Relationship between Tendon Displacement and Joint Variables

The discussion in this section focuses on a single segment, more specifically the base segment. Since the central tendon routing configuration allows independent segment motion, the kinematics framework developed here can be applied directly for the middle segment and the end segment. As discussed in Section II, since our design differs from that in [115, 116, 120], we developed a new forward kinematic framework, based in part on the prior work of [120]. It is important to note that due to the tendons being routed along the central axis, there is a fundamental difference in the kinematics between the tendon displacement and the bending angle. Derivation of the kinematic relationship relies on the assumptions that the robot bends along a circular arc and the arc length, S, is assumed to be constant at all times due to the compliance of the inner inter-connected spring between the disks. As shown in Fig. 5.9, each segment has two disks: Disk 'a' (the stationary or proximal disk) and Disk 'b' (the bending or distal disk). Bending of a robot segment in any direction is a result of pulling of at most two tendons. In a general case, the robot segment

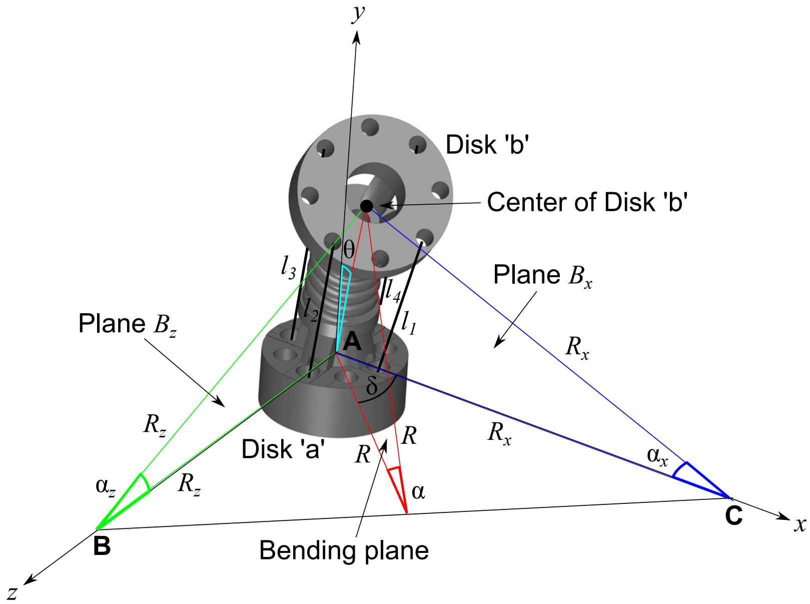

Figure 2.3: Schematic showing geometrical relationship between the radius of the bending arc, R, and the radius of the bending arc to the x-axis, R_x and that to the z-axis, R_z. R and δ can be expressed in terms of R_x and R_z. Note that the bending angle, $\theta = \frac{\alpha}{2}$.

would bend by bending angle θ, which is equal to $\alpha/2$ or $S/2R$, where R is the radius of the bending arc in the bending plane, due to pulling of tendon l_1 and tendon l_2, as shown in Fig. 5.9. α is in the the bending plane which is highlighted in red. Plane B_x is the plane that intersects both the x-axis and tendon l_1 whereas plane B_z is the plane that intersects both the z-axis and tendon l_2.

Analyzing plane B_x, as shown in Fig. 2.4(a), a triangle can be observed, namely △A'CD'. r_1 and r_2 are the radii of the disk from A to A' and D to D', respectively. Given l_1, r_1, r_2, and S, we can determine the radius of the arc, R_x by forming a geometrical relationship between the aforementioned parameters through the law of cosines:

$$l_1 = \sqrt{(R_x - r_1)^2 + (R_x - r_2)^2 - 2(R_x - r_1)(R_x - r_2)cos(S/R_x)} \quad (2.1)$$

and solve it through numerical computation. l_1 can be replaced by l_3 for the opposite bending motion in plane B_x. Similarly, in plane B_z, R_z can be determined from the following

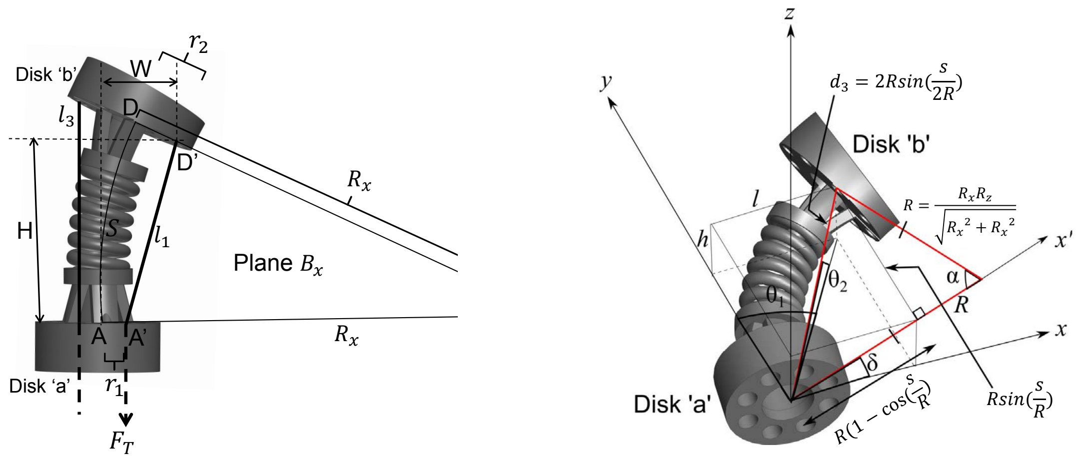

(a) (b)

Figure 2.4: (a) Schematic showing relationship between the tendon length, l_1 and radius of bending arc to the x-axis, R_x (b) Geometric relationship between R and δ, and the joint variables used in the kinematics model, θ_1, θ_2, and d_3

relationship:

$$l_2 = \sqrt{(R_z - r_1)^2 + (R_z - r_2)^2 - 2(R_z - r_1)(R_z - r_2)cos(S/R_z)} \tag{2.2}$$

and l_2 can be replaced by l_4 for the opposite bending motion in plane B_z.

For 3-dimensional bending motion involving both R_x and R_z as shown in Fig. 5.9, the radius of the bending arc, R, and the angle, δ, of the bending plane to the horizontal plane can be calculated by making use of the area of $\triangle$ABC and therefore can be expressed as follows:

$$R = \frac{R_x R_z}{\sqrt{R_x^2 + R_z^2}} \text{ and } \delta = tan^{-1}(\frac{R_x}{R_z}) \tag{2.3}$$

R and δ are used to relate to the joint variables, θ_1, θ_2, and d_3, as shown in Fig. 2.4(b). θ_1 is the joint angle with the axis of rotation along the z-axis; θ_2 is the joint angle with the axis of rotation along the x-axis; d_3 is the displacement between the centers of Disk 'a' and Disk 'b'. The position coordinate of Disk 'b' in the bending plane (highlighted with a red outline in Fig. 2.4(b)), can be expressed as:

$$(x', y) = (R[1 - cos(\frac{s}{R})], Rsin(\frac{s}{R})) \tag{2.4}$$

As shown in Fig. 2.4(b), l and h can then be expressed as:

$$l = R(1 - cos(s/R))cos(-\delta) \tag{2.5}$$

$$h = R(1 - cos(s/R))sin(-\delta) \tag{2.6}$$

The joint variables for forward kinematics can be calculated as follows:

$$\theta_1 = tan^{-1}(\frac{Rsin(\frac{s}{R})}{l}) - \frac{\pi}{2} = tan^{-1}(\frac{1}{tan(\frac{s}{2R})cos(\delta)}) - \frac{\pi}{2} \tag{2.7}$$

$$\theta_2 = sin^{-1}(\frac{h}{2Rsin(\frac{s}{2R})}) = sin^{-1}(-sin(\frac{s}{2R})sin\delta) \tag{2.8}$$

$$d_3 = 2Rsin(\frac{s}{2R}) \tag{2.9}$$

In our kinematics model, each robot segment consists of five joints, θ_1, θ_2, $\theta_3 = d_3$, θ_4, and θ_5. Since the rigid body kinematics model does not account for continuous bending behavior of a flexible robot segment, θ_4 and θ_5 are the two virtual joints added to correct the orientation of Disk 'b' of each segment [120] and are related to θ_1 and θ_2 due to the characteristic of the continuum robot such that $\theta_4 = \theta_1$ and $\theta_5 = \theta_2$. All joint variables are clearly defined in Fig. 2.5.

2.3.2 Derivation of Forward Kinematics using the Twist Method

As mentioned earlier, each robot segment has five joints: two orthogonal revolute joints with intersecting axes at Disk 'a', a prismatic joint that connects Disk 'a' and Disk 'b', and two other orthogonal revolute joints with intersecting axes at Disk 'b'. To solve the forward

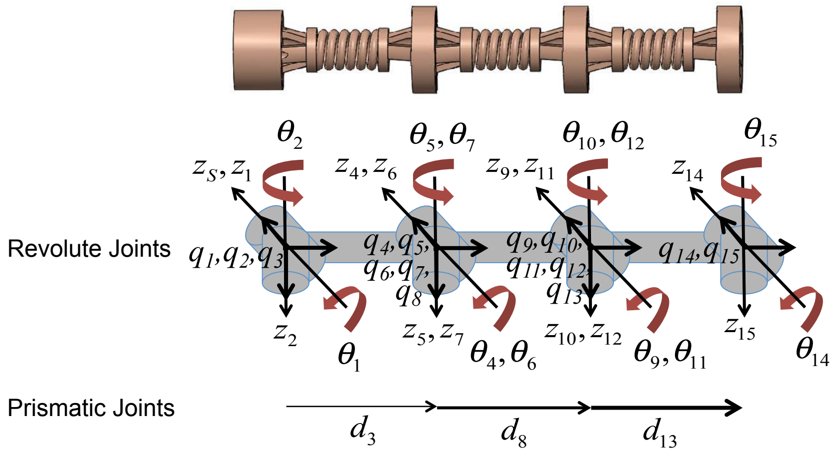

Figure 2.5: Schematic of MINIR-II with all joints and coordinate axes defined (Subscript 'S' represents the base frame which coincides with the first frame.)

kinematics for the base segment using twist coordinates, we need to obtain the product of the exponential mapping of the twists for all the joints in the segment, as expressed below:

$$g_{st}(\theta) = e^{\hat{\xi}_1\theta_1} e^{\hat{\xi}_2\theta_2} e^{\hat{\xi}_3\theta_3} e^{\hat{\xi}_4\theta_4} e^{\hat{\xi}_5\theta_5} g_{st}(0) \tag{2.10}$$

where $g_{st}(0)$ is the initial position and orientation of Disk 'b' of the base segment. The exponential mapping function for revolute joints is expressed as Eq. (2.11).

$$e^{\hat{\xi}_i\theta_i} = \begin{bmatrix} e^{\hat{w}_i\theta_i} & [(I - e^{\hat{w}_i\theta_i})\hat{w}_i + w_i w_i^T \theta_i] v_i \\ 0 \quad 0 \quad 0 & 1 \end{bmatrix} \tag{2.11}$$

for $i = 1, 2, 4, 5$ in the base segment

where $\hat{w}$ is skew symmetric matrix of the angular velocity vector and θ is the joint variable. v_i is the linear velocity of each joint i. The exponential mapping function for prismatic joint is expressed as Eq. (2.12).

$$e^{\hat{\xi}_i\theta_i} = \begin{bmatrix} & e^{\hat{w}_i\theta_i} & & v_i\theta_i \\ & & & \\ 0 & 0 & 0 & 1 \end{bmatrix} \quad \text{for } \; i = 3 \text{ in the base segment} \tag{2.12}$$

We first determine the angular velocity, w and link length, q for each joint with respect to the frame of the 1^{st} joint, as seen in Eq. (2.13) and (2.14).

$$w = \begin{bmatrix} w_1 & w_2 & w_3 & w_4 & w_5 \end{bmatrix} = \begin{bmatrix} 0 & 1 & 0 & 0 & 1 \\ 0 & 0 & 0 & 0 & 0 \\ 1 & 0 & 0 & 1 & 0 \end{bmatrix} \tag{2.13}$$

Since d_3 in Fig. 2.5 has to be obtained from Eq. (2.9), it is treated as zero during derivation of the forward kinematics. This results in the following q matrix.

$$q = \begin{bmatrix} q_1 & q_2 & q_3 & q_4 & q_5 \end{bmatrix} = \begin{bmatrix} 0 & 0 & 0 & 0 & 0 \\ 0 & 0 & 0 & d_3 & d_3 \\ 0 & 0 & 0 & 0 & 0 \end{bmatrix} \tag{2.14}$$

Linear velocity, v, is then determined from Eq. (2.15).

$$v = \begin{bmatrix} -w_1 \times q_1 & -w_2 \times q_2 & -w_3 \times q_3 & -w_4 \times q_4 & -w_5 \times q_5 \end{bmatrix} \tag{2.15}$$

Therefore, the twist for the base segment can be written as follows:

$$\xi = \begin{bmatrix} \xi_1 & \xi_2 & \xi_3 & \xi_4 & \xi_5 \end{bmatrix} = \begin{bmatrix} v_1 & v_2 & v_3 & v_4 & v_5 \\ w_1 & w_2 & w_3 & w_4 & w_5 \end{bmatrix} \tag{2.16}$$

The exponential mapping of w for revolute joints i with its rotation axis along the z-axis and x-axis are respectively expressed as:

$$e^{\hat{w}_i\theta_i} = \begin{bmatrix} C_i & -S_i & 0 \\ S_i & C_i & 0 \\ 0 & 0 & 1 \end{bmatrix} \; ; \; e^{\hat{w}_i\theta_i} = \begin{bmatrix} 1 & 0 & 0 \\ 0 & C_i & -S_i \\ 0 & S_i & C_i \end{bmatrix} \tag{2.17}$$

where C_i and S_i refer to cosine of θ_i and sine of θ_i. The exponential mapping of w for the prismatic joint is a 3x3 identity matrix. Substituting Eqs. (2.13), (2.15), and (2.17) into Eqs. (2.11) and (2.12), we obtain the expression for the exponential mapping of twists for revolute and prismate joints, respectively. The position and orientation matrix relative to the frame of the 1^{st} joint, $g_{st}(0)$ can be expressed as:

$$g_{st}(0) = \begin{bmatrix} 1 & 0 & 0 & 0 \\ 0 & 1 & 0 & d_3 \\ 0 & 0 & 1 & 0 \\ 0 & 0 & 0 & 1 \end{bmatrix} \tag{2.18}$$

Substituting Eqs. (2.11), (2.12), and (2.18) into Eq. (2.10), we obtain the final position and orientation matrix of Disk 'b' of the base segment, which is a 4x4 homogeneous transformation matrix, all entries of which are listed in Eq. (2.19).

$$g_{st} = \begin{bmatrix} C_1\,C_4 - C_2\,S_1\,S_4 & S_1\,S_2\,S_5 - C_5\,(C_1\,S_4 + C_2\,C_4\,S_1) & S_5\,(C_1\,S_4 + C_2\,C_4\,S_1) + C_5\,S_1\,S_2 & -C_2\,S_1\,d_3 \\ C_4\,S_1 + C_1\,C_2\,S_4 & -C_5\,(S_1\,S_4 - C_1\,C_2\,C_4) - C_1\,S_2\,S_5 & S_5\,(S_1\,S_4 - C_1\,C_2\,C_4) - C_1\,C_5\,S_2 & C_1\,C_2\,d_3 \\ S_2\,S_4 & C_2\,S_5 + C_4\,C_5\,S_2 & C_2\,C_5 - C_4\,S_2\,S_5 & S_2\,d_3 \\ 0 & 0 & 0 & 1 \end{bmatrix} \tag{2.19}$$

The model can easily be expanded for the complete three-segmented robot to obtain the position and orientation of the true end effector (Disk 'b' of the end segment or Disk 4, as shown in Fig. 2.1(a)):

$$g_{st}(\theta) = e^{\hat{\xi}_1\theta_1} e^{\hat{\xi}_2\theta_2} \dots e^{\hat{\xi}_{15}\theta_{15}} g_{st}(0)$$

where $g_{st}(0)$ is the initial position and orientation of Disk 'b' of the end segment.

2.3.3 Derivation of Jacobian

We can derive Jacobian in the spatial coordinates from the exponential mapping of the twists prime, ξ' such that $J = \begin{bmatrix} \xi'_1\ \xi'_2 \dots \xi'_{15} \end{bmatrix}$, where $\xi'_1 = \xi_1$, which is obtained from Eq. (2.16). The rest of the twist primes are expressed as $\xi'_i = \begin{bmatrix} v'_i\ w'_i \end{bmatrix}^T$, where $i = 2, 3, \dots 15$.

For prismatic joints (i = 3, 8, 13), $v'_i = \prod_{j=1}^{i-1} e^{\hat{w}_j\theta_j} = \begin{bmatrix} 0\ 1\ 0 \end{bmatrix}^T$, where θ's are the joint angles while $w' = \begin{bmatrix} 0\ 0\ 0 \end{bmatrix}^T$. For revolute joints, $\begin{bmatrix} v'_i \\ w'_i \end{bmatrix} = \begin{bmatrix} -w'_i \times q'_i \\ w'_i \end{bmatrix}$, where

$$w'_i = \prod_{j=1}^{i-1} e^{\hat{w}_j\theta_j} w_i\ ;\ q'_i = \prod_{j=1}^{i-1} e^{\hat{w}_j\theta_j} q_i \tag{2.20}$$

where $i = 2, 4, 5, 6, 7, 9, 10, 11, 12, 14$, and 15. Again, θ's are the revolute joint angles. $e^{\hat{w}_j\theta_j}$ can be derived using Eq. (2.17). Angular velocity, w is defined with respect to the frame of the 1^{st} joint. q for the entire three-segmented robot are listed as follows:

$$q_1 = q_2 = \begin{bmatrix} 0\ 0\ 0 \end{bmatrix}^T \tag{2.21}$$

$$q_4 = q_5 = q_6 = q_7 = \begin{bmatrix} 0\ d_3\ 0 \end{bmatrix}^T \tag{2.22}$$

$$q_9 = q_{10} = q_{11} = q_{12} = \begin{bmatrix} 0\ d_3 + d_8\ 0 \end{bmatrix}^T \tag{2.23}$$

$$q_{14} = q_{15} = \begin{bmatrix} 0 \; d_3 + d_8 + d_{13} \; 0 \end{bmatrix}^T \tag{2.24}$$

Jacobian for one robot segment can be written as:

$$J = \begin{bmatrix} 0 & 0 & -C_2\, S_1 & d_3\, C_1 & -d_3\, C_1\, S_1\, S_2 \\ 0 & 0 & C_1\, C_2 & d_3\, S_1 & d_3\, {C_1}^2\, S_2 \\ 0 & 0 & S_2 & 0 & -d_3\, C_1\, C_2 \\ 0 & C_1 & 0 & S_1\, S_2 & {C_1}^2 - C_2\, {S_1}^2 \\ 0 & S_1 & 0 & -C_1\, S_2 & c_1\, S_1 + C_1\, C_2\, S_1 \\ 1 & 0 & 0 & C_2 & S_1\, S_2 \end{bmatrix} \tag{2.25}$$

Since θ_4=θ_1 and θ_5=θ_2, there are really only three independent virtual joints in one segment. The joint parameter vector can thus be defined as $\psi = [\theta_1 \; \theta_2 \; d_3]^T$ and the joint parameter velocity would be $\dot{\psi} = [\dot{\theta_1} \; \dot{\theta_2} \; \dot{d_3}]^T$. Velocity vector at the task space can be related to the joint parameter velocities via $\begin{bmatrix} v \; \omega \end{bmatrix}^T = J\dot{\psi}$, where the Jacobian matrix is formed by combining the 1^{st} and 4^{th} columns and combining the 2^{nd} and 5^{th} columns in Eq. (2.25).

$$J = \begin{bmatrix} d_3\, C_1 & -d_3\, C_1\, S_1\, S_2 & -C_2\, S_1 \\ d_3\, S_1 & d_3\, {C_1}^2\, S_2 & C_1\, C_2 \\ 0 & -d_3\, C_1\, C_2 & S_2 \\ S_1\, S_2 & C_1 + {C_1}^2 - C_2\, {S_1}^2 & 0 \\ -C_1\, S_2 & S_1 + C_1\, S_1 + C_1\, C_2\, S_1 & 0 \\ 1 + C_2 & S_1\, S_2 & 0 \end{bmatrix} \tag{2.26}$$

2.3.4 Forward Kinematics: Simulation and Experiments

We performed MATLAB simulations of the motion of the MINIR-II robot comprised of three segments. Fig. 2.6 shows the simulation results of the three segments when bending angles, θ's, of the base, middle, and end segments are equal to $\pi/4$, $\pi/4$ and $\pi/4$, and the bending plane rotates about the y-axis of the individual segment in intervals of $\pi/20$ for

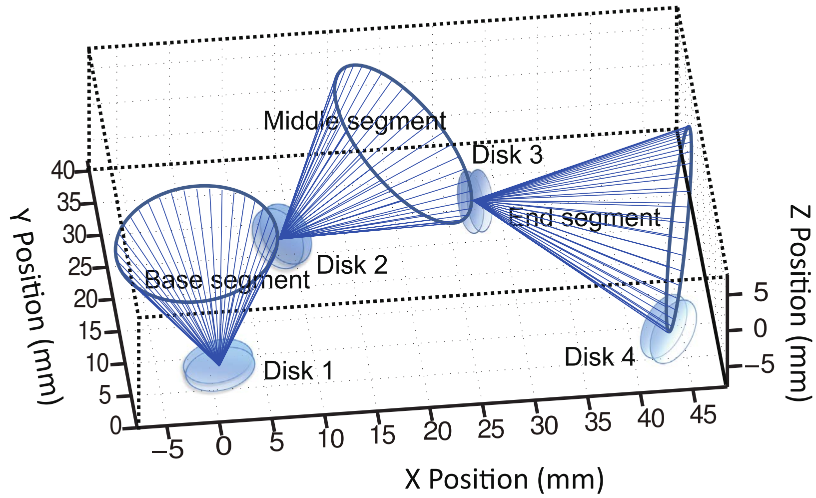

Figure 2.6: Simulation result ($\theta_{base} = 45°, \theta_{mid} = 45°, \theta_{end} = 45°$)

forty different δ angles. Each blue line indicates attachment between the positions of Disk 1, Disk 2, Disk 3, and Disk 4. We also performed verification experiment of our forward kinematics model. We used antagonistic SMA springs as actuators and the individual tendon was connected to each SMA spring assembly as shown schematically in Fig. 2.7(a). A marker was attached to the end of each SMA spring to measure the change in the tendon length. Four markers were attached to the discs of the robot segments to form three vectors for the three segments. They were constantly being tracked by a stereo camera that has a 15 fps resolution. The bending angle of a robot segment is defined as the relative angle of a vector formed by a robot segment with respect to the vector formed by its proximal segment. A Proportional-Integral (PI) controller monitored the difference between the real-time SMA spring displacement and the desired tendon (or SMA spring) displacement, and determined the voltage to be supplied to the SMA spring. The pulse-width modulation (PWM) signal from the Arduino board was calculated based on the voltage input (PWM signal (0-255) = voltage input/ 5 V) and used to heat the SMA spring. Seven tendon displacement from 1 mm to 7 mm with 1 mm interval were tested for the bending of each segment. We compared the simulation results from the kinematics model with the experimental results. Figs. 2.7(b), 2.7(c) and 2.7(d) show the positions of Disk 'a' and Disk 'b'

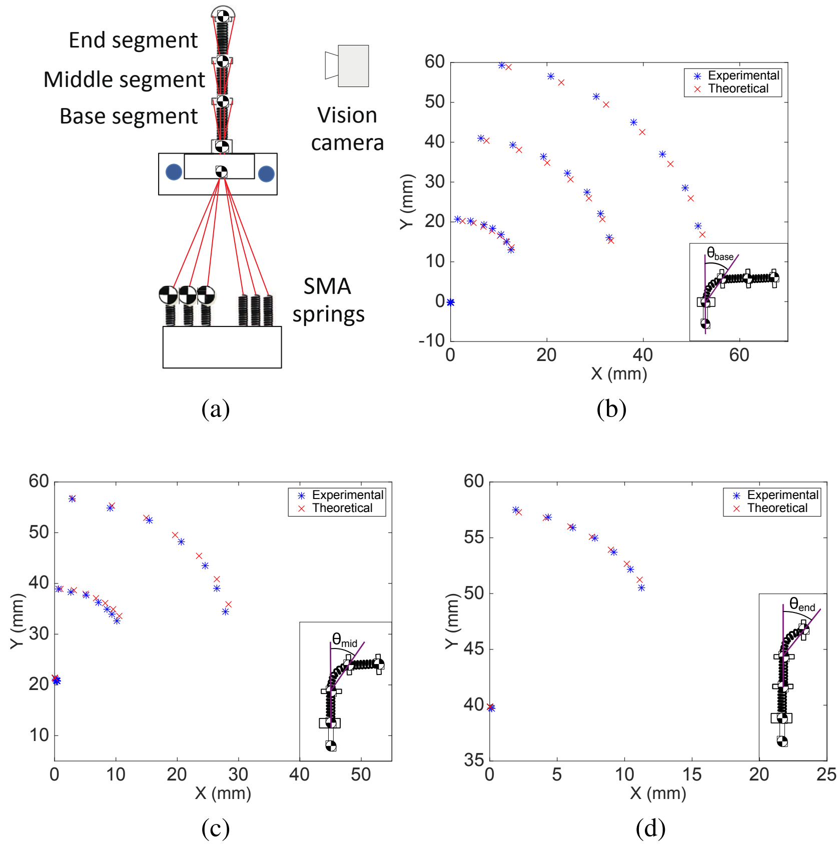

Figure 2.7: (a) Experimental setup of forward kinematics verification (b) Position of the base, middle and end segments when the tendon connected to the base segment was pulled in 1 mm increment until 7 mm (c) Position of the base, middle and end segment when the tendon connected to the middle segment was pulled in 1 mm increment until 7 mm (d) Position of the middle and end segment when the tendon connected to the end segment was pulled in 1 mm increment until 7 mm

of the robot segment being actuated as well as Disk 'b' of other segments distal to it given seven different tendon displacements. The predicted positions of the robot segments reasonably match the experimental data. The positions of Disk 'b' of the actuated segment, be it base, middle or end, are very well matched by the model. There are however noticeably more discrepancies in the position of the segments that are farther away from the actuated segment. This error could be due to the bending motion that was not perfectly parallel to the camera. The assumptions of constant spring length and constant spring curvature would also have contributed to modeling errors, especially at larger bending angles. To minimize the error caused by potential compression of the springs, we designed spring segments to have no gaps between the coils. An MRI-compatible passive magnetic field sensor would be integrated in the robot to provide position and orientation feedback to compensate for the predicted error in the real application.

2.3.5 Force Analysis

Neglecting gravitational influence, the elastic potential energy of a single robot segment due to pure bending can be expressed as [121, 122]:

$$E_e = \int_S \frac{\beta}{2}(\frac{d(2\theta)}{ds})^2 ds \tag{2.27}$$

where β is the flexural rigidity of a spring (a robot segment). θ, which is $S/2R$, is the bending angle and can be expressed in terms of θ_1 and θ_2 by solving Eqs. (7) and (8). When bending in a single plane, the xy-plane, θ is replaced by θ_1. $\beta = \frac{2SEIG}{\pi n R(2G+E)}$ [123], where S, E, I, G, R, and n are the spring length, the Young's modulus, area moment of inertia, shear modulus, mean radius of the spring coil, and number of spring coil, respectively. $E = 300 \times 10^6\ Pa$; $I = 1.02 \times 10^{-13}\ m^4$; $G = \frac{E}{2(1+\nu)}$; $\nu = 0.3$; $R = 2.1 \times 10^{-3}\ m$; $n = 5$.

In the current work, we assumed the middle and base segments of the robot would be constrained during the electrocautery process and only the end segment would be actuated. Therefore, the relationship between the actuator torque on the three independent virtual joints in a single segment, τ and the tip force perpendicular to the d_3 vector, F_k are related by $\tau = J^T F_k + \nabla E_e$ [121, 122], where J is the Jacobian for a single segment from Eq. (2.26) and ∇E_e is the gradient of the elastic energy with respect to the joint parameters, θ_1, θ_2 and d_3.

For bending in xy-plane, τ can be written as follows:

$$\begin{pmatrix} \tau_1 \\ \tau_2 \\ F_3 \end{pmatrix} = \begin{pmatrix} d_3\, C_1 & -d_3\, C_1\, S_1\, S_2 & -C_2\, S_1 \\ d_3\, S_1 & d_3\, {C_1}^2\, S_2 & C_1\, C_2 \\ 0 & -d_3\, C_1\, C_2 & S_2 \\ S_1\, S_2 & C_1 + {C_1}^2 - C_2\, {S_1}^2 & 0 \\ -C_1\, S_2 & S_1 + C_1\, S_1 + C_1\, C_2\, S_1 & 0 \\ 1 + C_2 & S_1\, S_2 & 0 \end{pmatrix}^T \begin{pmatrix} F_{k_x} \\ F_{k_y} \\ F_{k_z} \\ M_{k_x} \\ M_{k_y} \\ M_{k_z} \end{pmatrix} + \begin{pmatrix} \frac{4\beta}{S}\theta_1 \\ 0 \\ 0 \end{pmatrix} \tag{2.28}$$

where τ_1, τ_2, and τ_3 are the torques provided by the three virtual joints in our forward kinematics model. F and M are the force and moment at the end disc of the single segment. To verify the model, a blocked test was performed to measure the tip force of a single segment when tension was supplied by the actuator of the first joint and the robot was in its home configuration. Therefore, Eq. (2.28) can be reduced to the following:

$$\tau_1 = (F_{T_x} H + F_{T_y} W) = d_3 C_1 F_{k_x} + d_3 S_1 F_{k_y} + \frac{4\beta}{S}\theta_1 = d_3 F_k + \frac{4\beta}{S}\theta_1 \tag{2.29}$$

The angle that the tendon forms with respect to the vertical y-axis (long axis of the robot) is approximated to be the same as θ_1. Therefore, F_{T_x} and F_{T_y} are calculated as $F_T sin\theta_1$ and $F_T cos\theta_1$, respectively. H and W can be observed in Fig. 2.4(a).

To experimentally determine the relationship between tension in the tendon and tip force, we performed blocked test with a single segment of the robot for three different bending angles, θ_1's, namely 0°, 15° and 30° (see Fig. 2.8(a)). A pair of SMA spring actuators were connected to the robot segment. SMA spring 1 was heated to generate the pullling force while SMA spring 2 acted as a passive spring. The tendon connecting SMA spring 2 and the robot segment was completely slack. During the experiments, forces were recorded by the three forces sensors shown in Fig. 2.8(a). The segment disk was attached to force sensor 3 via a solid wire to form a rigid connection and ensure good force transmission. Tension, F_T can be calculated as the difference between forces recorded by

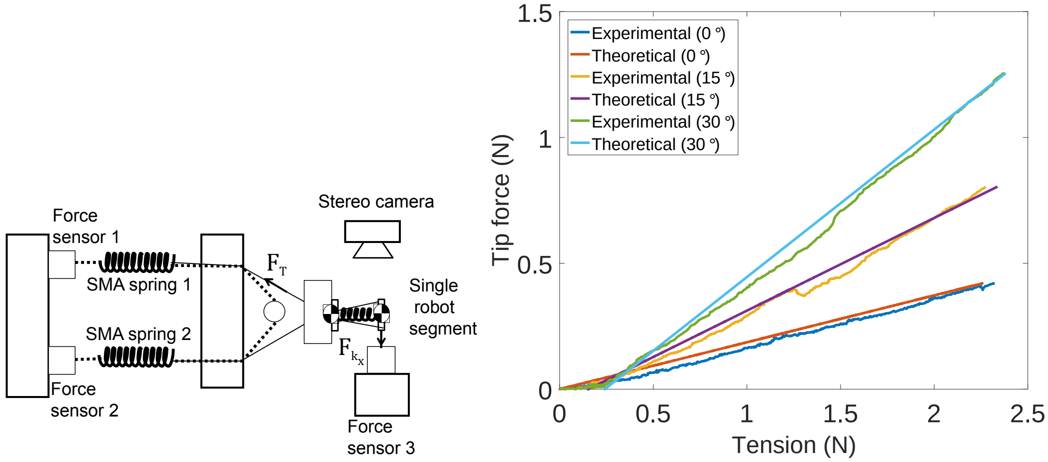

(a) (b)

Figure 2.8: (a) Experimental setup schematic to determine relationship between tension and tip force; (b) Experimental results

force sensor 1 and force sensor 2 while tip force, F_{k_x} was directly measured by force sensor 3.

The relationship between tension and tip force is plotted in Fig. 2.8(b). It can be observed that the tip force exerted was 0.19 times, 0.37 times, and 0.59 times the tension applied in the tendon when θ_1s were 0°, 15° and 30°, respectively. The theoretical data from Eqs. (2.29) matched the experimental data well (R^2=0.9890, 0.9653 and 0.9934).

2.4 Independent Segment Control

Our novel central tendon routing configuration provides better control over the motion of each robot segment than the peripheral tendon routing configuration in continuum robots [115, 116]. To verify independent segment control, we utilized the three-segment robot as shown in Fig. 5.11(a). Vision markers were attached to the disks of all segments. We tracked the position of each marker while a tendon was being pulled to actuate a single segment. Figures. 5.11(b), 5.11(c), and 5.11(d) show the bending angles of all segments during actuation of the end, middle and base segments, respectively. The results show that minimal angle changes were observed in the segments proximal to the actuated segment. When the

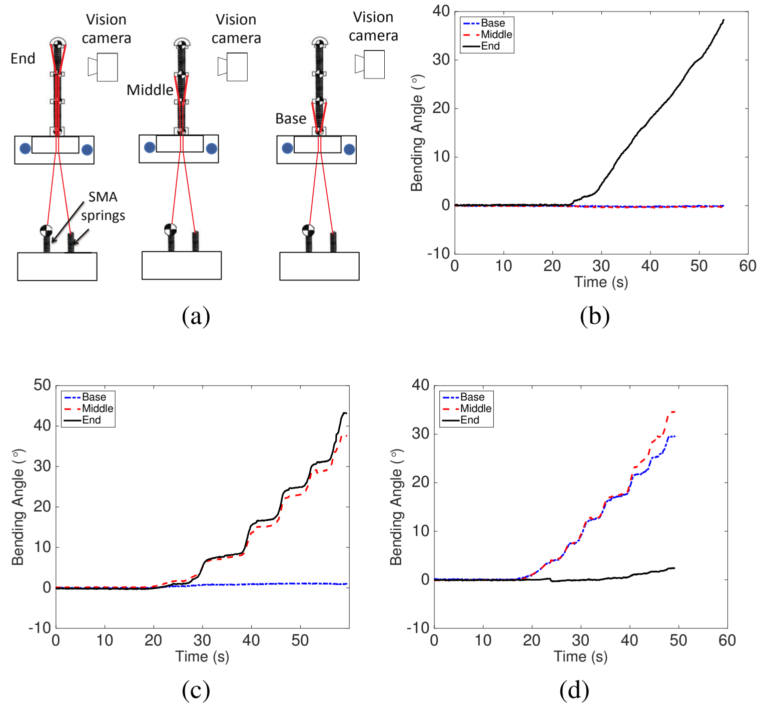

Figure 2.9: (a) Experimental setup schematic to determine independent segment motion by actuating only one segment; Results from the independent segment control experiments for (b) end segment, (c) middle segment and (d) base segment

end segment was moved, as shown in Fig. 5.11(b), the maximum absolute angle changes for the base and middle segments were 0.16°, and 0.48°, respectively. When the middle segment was bent, as shown in Fig. 5.11(c), the maximum absolute angle change for the base segment was 1.1°. Due to the characteristics of continuum robots, the segment actuated and its neighboring distal segment have almost identical bending angles, as shown in Figs. 5.11(c) and 5.11(d). We also moved the end robot segment in the yz-plane after the middle segment was moved and held fixed in the xy-plane at 0°(home configuration), 10°, 20°, and 30°(which correspond to 0°, 20°, 40°, and 60° change in the segment disk orientation-representative motion in Fig. 1(e)). As seen in Fig. 2.10 , the maximum angle changes for the non-actuated robot segments are minimal and less than 2.1° in all cases. The slight motion in the non-actuated segments was due to friction/stiction in the overall actuation mechanism.

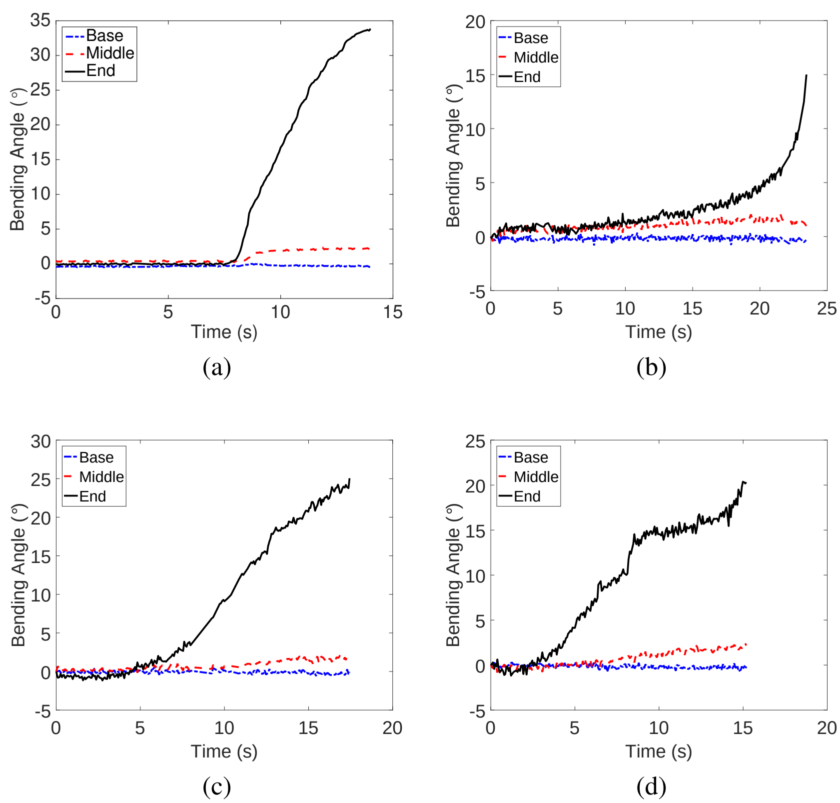

Figure 2.10: Bending motion of all segments when the end segment was actuated in the z-direction after the middle segment was moved independently for (a) 0°(b) 10°(c) 20°and (d) 30° in the xy-plane

We also performed experiments for bending motion of multiple segments in the same plane: (1) bending of the base segment followed by the middle segment and (2) bending of the base segment followed by the end segment. From the results shown in Fig. 2.11(a), the bending of the middle segment caused a slight drop in the bending angle of the base segment which was already in a bent position in the same plane. The small drop with a maximum of 4° happened only at the beginning stage of the actuation of the middle segment and would not increase further. It was caused by the compression of the base segment spring backbone as the tendon for the middle segment was pulled to actuate the middle segment. Fig. 2.11(b) shows the same trend with the already bent proximal segments (base and middle) both experiencing slight drop in their bending angles as the end segment was actuated. However, for the most parts, each segment can be independently actuated even when its proximal segment is already in a bent configuration, which would not be possible using the common peripheral tendon routing configuration.

Fundamentally our design allows independent motion of each segment covering an even larger bending angles than demonstrated above. However, due to the 3-D printing plastic material, bending angles significantly beyond 45° are yet to be investigated and beyond the scope of our requirement. As the angle increases beyond 45°, we can expect more coupling due to geometrical non-linearity and possibly friction from lack of sheath around the tendons. The slight coupling between robot segments currently being displayed could be compensated through a control mechanism that introduces more tension into the proximal segments. A thin sheath could be added to each tendon to minimize the contact friction among them.

2.5 Vision-Based Control with Cooling Strategy

We developed a compact actuator setup and implemented the forced air cooling strategy, as seen in Fig. 2.12(a). To resolve the problem of slow response of the SMA springs, we used compressed air at 50 psi to cool the SMA spring actuators by blowing it into each

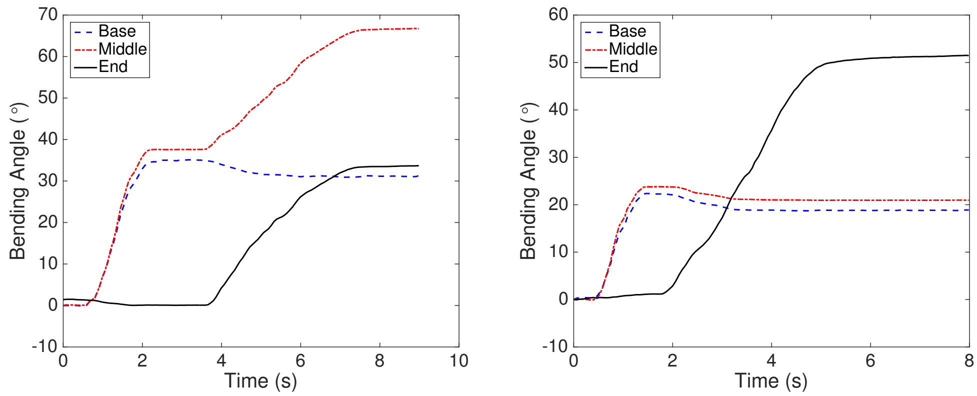

(a) (b)

Figure 2.11: Bending motion of the base, middle, and end segments (a) when the base segment was moved independently, followed by independent actuation of the middle segment (b) when the base segment was moved independently, followed by independent actuation of the end segment

cooling channel that has a width and height of 12 mm each. The length of the channel is 30 cm, which is more than the maximum length that the SMA spring would be extended to. Our goals were to increase the SMA cooling speed and to make the cooling mechanism as compact as possible. Higher cooling speed leads to increased actuation bandwidth and a compact cooling mechanism allows control over individual SMA spring actuators, leading to a more practical robotic setup for brain surgery. The cooling unit, as shown in Fig. 2.12(a), consists of acrylic plates with channels where SMA springs are located. The air tubes are connected to the channels through the holes drilled on one side of the plate. Compressed air is passed into the channels through the tubes and allowed to leave from the far end of each air channel. Figs. 2.12(b) and 2.12(c) show schematically the actuation mechanism employed in our system. As the compressed air is supplied to the non-heated SMA springs, the antagonistic SMA spring gets heated and contracts, bending the robot to one direction.

To ensure MRI compatibility, all components of the robot were made of plastic, except the electrocautery probes and SMA springs. The SMA springs were placed approximately 20 cm away from the robot part that was to be inserted into the brain. Thus, the actu-

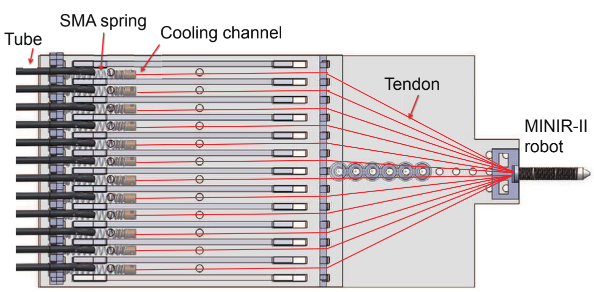

(a)

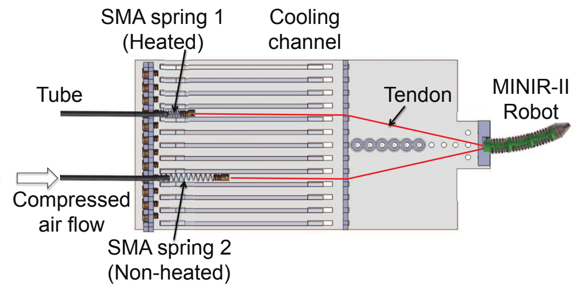

(b)

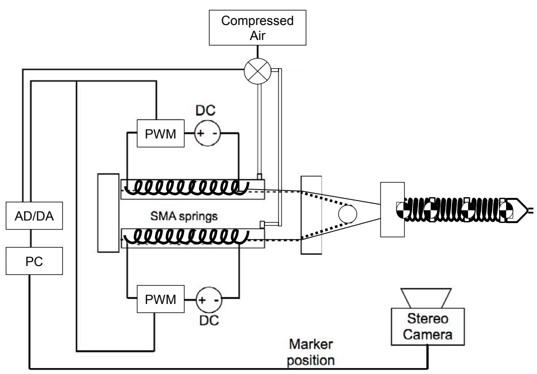

(c)

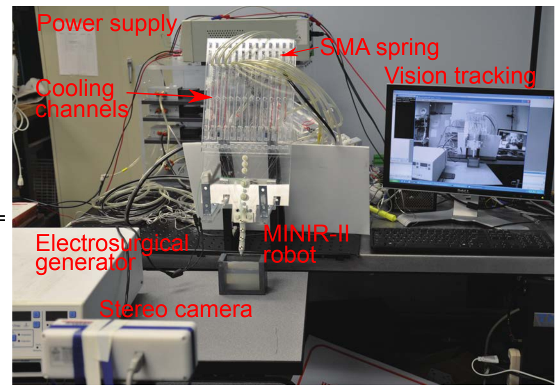

(d)

Figure 2.12: (a) CAD model of overall system consisting of 6-DoF robot, six pairs of SMA springs, and their corresponding cooling channels; (b) CAD models showing air flow direction during left bending motion; (c) Schematic of resistive heating and forced air cooling strategy for single pair of antagonistic SMA springs that relates to one-DoF robot motion; (d) Complete experimental setup for vision control of MINIR-II

ators did not enter the brain and are away from the imaging region of the MRI scanner, avoiding heat damage to the brain tissue and distortion in MRI images. The entire continuum robotic system was composed of the robot, SMA spring actuators, the driving circuit, the cooling units, the automatic valves, a stereo camera, an electrosurgical generator (Aaron 2250, Bovie Medical Corporation, USA), and a computer with an analog-to-digital-converter (ADC) board and an Arduino board, as shown in Fig. 2.12(d). Vision feedback was used to control the motion of the robot. Vision markers were attached to each disk and tracked by the stereo camera to calculate vectors between the disks. A PI controller was used to calculate control signal until the desired angle was achieved. The signal indicates the time whether to heat the SMA springs or to open the valves to flow the compressed air

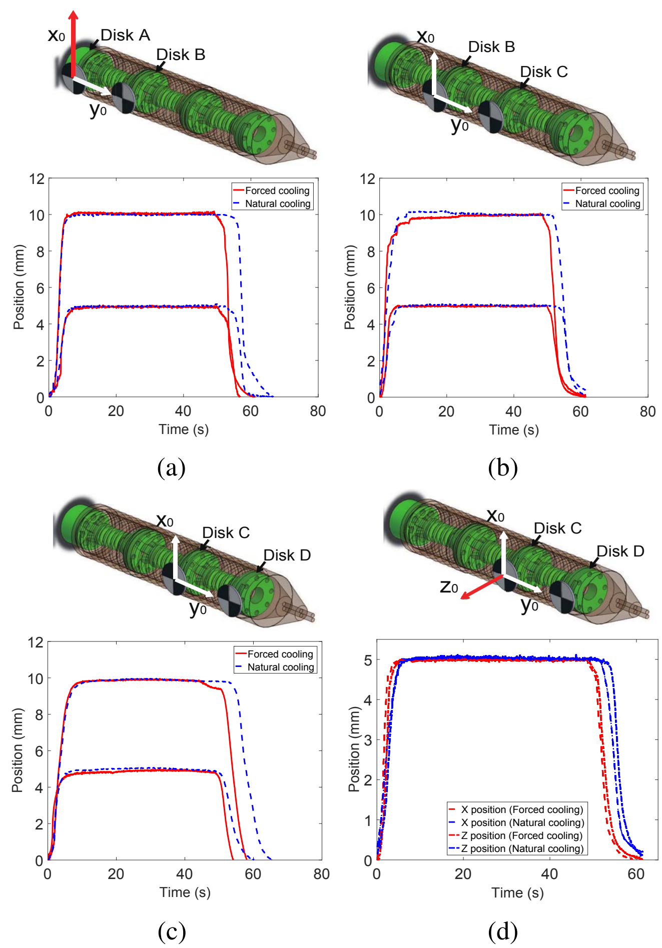

Figure 2.13: Step input tracking in the x-direction for: (a) base segment, (b) middle segment and (c) end segment of MINIR-II; (d) Step input tracking of end segment in x- and z-directions

to cool them. The Arduino board was utilized to generate PWM signals to heat the SMA actuators.

In the vision control experiment, we compared the robot tracking performance under natural cooling and forced air cooling. The experiment was repeated to demonstrate 1-DoF motion of each robot segment as well as simultaneous 2-DoF motion of the end segment. For the 1-DoF experiments, we provided 5 mm and 10 mm step inputs in the x-direction. For the 2-DoF experiment, 5 mm step inputs in both x- and z-directions were used. For sinusoidal input experiment, a wave of 5 mm amplitude with 40 s period was assigned to the middle segment of the robot. We also tested continuous motion of the middle segment at different amplitudes with 20 s time interval.

Figs. 2.13(a), 2.13(b) and 2.13(c) show the x position changes of Disk 2 (base segment), Disk 3 (middle segment) and Disk 4 (end segment), respectively, when desired inputs of 5 mm and 10 mm were provided under natural cooling and forced cooling. Fig. 2.13(d) shows the 2-DoF motion of Disk 4 when desired inputs of 5 mm in the x- and z-direction were provided simultaneously under natural cooling and forced cooling. Once the SMA springs were heated to reach the desired step input position, it took 6s and 10s to return from 5 mm position to the original configuration under forced cooling and natural cooling, respectively. It took 8s and 15s to return from 10 mm position, respectively. The slower return of the robot segment in the case of natural cooling was due to the resistance provided by the previously heated SMA spring in the antagonistic configuration, which still possessed some residual heat. The forced air cooling, on the other hand, allowed faster dissipation of residual heat in the previously heated SMA spring which therefore provided minimum resistance to its antagonistic SMA spring that was being heated. The difference in cooling time between the 5 mm and 10 mm inputs was due to the range of motion over which the SMA springs contracted and relaxed. A larger range of motion requires the SMA temperature to rise much higher and therefore more time is required to cool down. Furthermore, the temperature of the SMA spring, which had just been heated, did not drop immediately after resistive heating stopped. The position of the disk did not change until the spring force of the antagonistic SMA spring, generated by heating, became larger than the force exerted by the residual heat in the previously heated SMA spring.

Results from the sinusoidal input experiment are shown in Fig. 2.14(a). Forced air cooling of the SMA spring actuators led to successful tracking of the sinusoidal trajectory ($R^2 = 0.9144$). Under natural cooling, the robot could follow reasonably well in the first period but started to fail in the second period ($R^2 = 0.1760$). The residual heat built up in the SMA spring without forced cooling and created a strong resistive force that hindered the sinusoidal trajectory tracking. The result for the continuous step motion experiment is shown in Fig. 2.14(b). We stopped heating the initially heated SMA spring after 60 s. The most significant difference between the effect of cooling methods happened between 60-80s, during which the previously heated SMA spring underwent either natural cooling or forced cooling. These trajectory following experiments confirmed the beneficial effects of forced air cooling in improving the actuation bandwidth of the robot. More experiments will be performed in our future works to determine the maximum actuation bandwidth and speed that this robot actuated by SMA springs is capable of and to investigate the various parameters that could affect its actuation bandwidth.

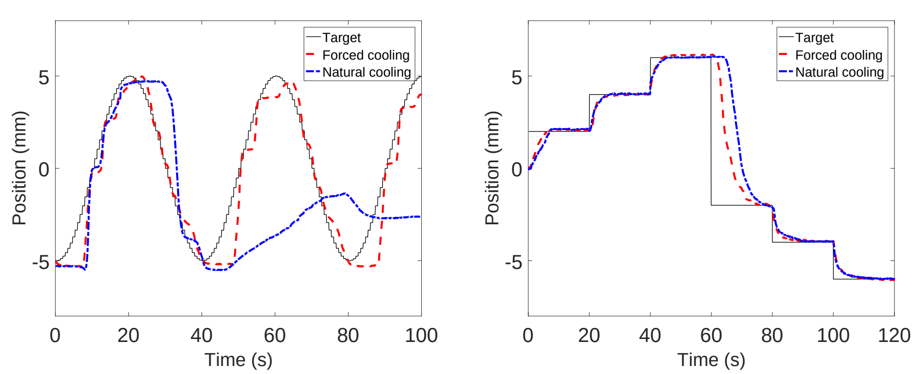

(a) (b)

Figure 2.14: Motion tracking of middle segment of MINIR-II in response to (a) sinusoidal input and (b) step inputs

2.6 Motion Test in Gelatin and MRI Compatibility Test

To verify motion capability of the robot in a brain-simulated environment, we inserted the robot into a gelatin (Knox, USA) slab. We then actuated the robot segment to move it back and forth while electrocauterizing the gelatin. Figure 2.15 shows the ability of our robot to move in a gelatin slab (2% by weight) to create electrocauterized cavities. As for the MRI-compatibility experiment, we used a gelatin slab in a cantaloupe to simulate the brain tissue in the skull. The pulp of the cantaloupe was removed and it was filled with gelatin. As shown in Fig. 2.16, fiber optic sensor (FU-77V, Keyence, Belgium), instead of the vision camera, was used to measure the displacement of the SMA spring during the robot motion under MRI. The entire setup was placed under a head coil at the center of an MRI scanner. Automatic valves and an air compressor are located outside the MRI room. Before actuating the robot, we took 200 high-resolution MRI images in 1000 seconds to evaluate the degree of image distortion caused by the robot and determine the signal-to-noise ratio (SNR) changes of MRI images during MRI scanning. The average SNR of the 200 images with non-actuated MINIR-II is 77.8. We then actuated the end segment of the robot and took 20 MRI images during the actuation process. The MR images and SNR changes, shown in Fig. 8.21(a), shows that the end segment has been moved to the left. During actuation, the average SNR of the 20 images was 72.7, which resulted in a 6.4% SNR drop. Fig. 8.21(b) shows the MRI images of each robot segment being bent in the gelatin.

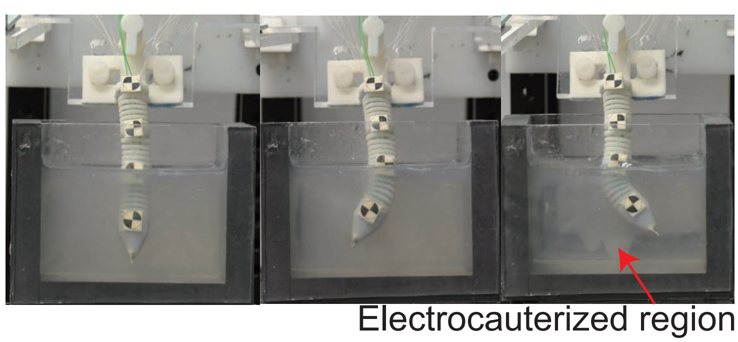

Figure 2.15: Motion test in a gelatin slab

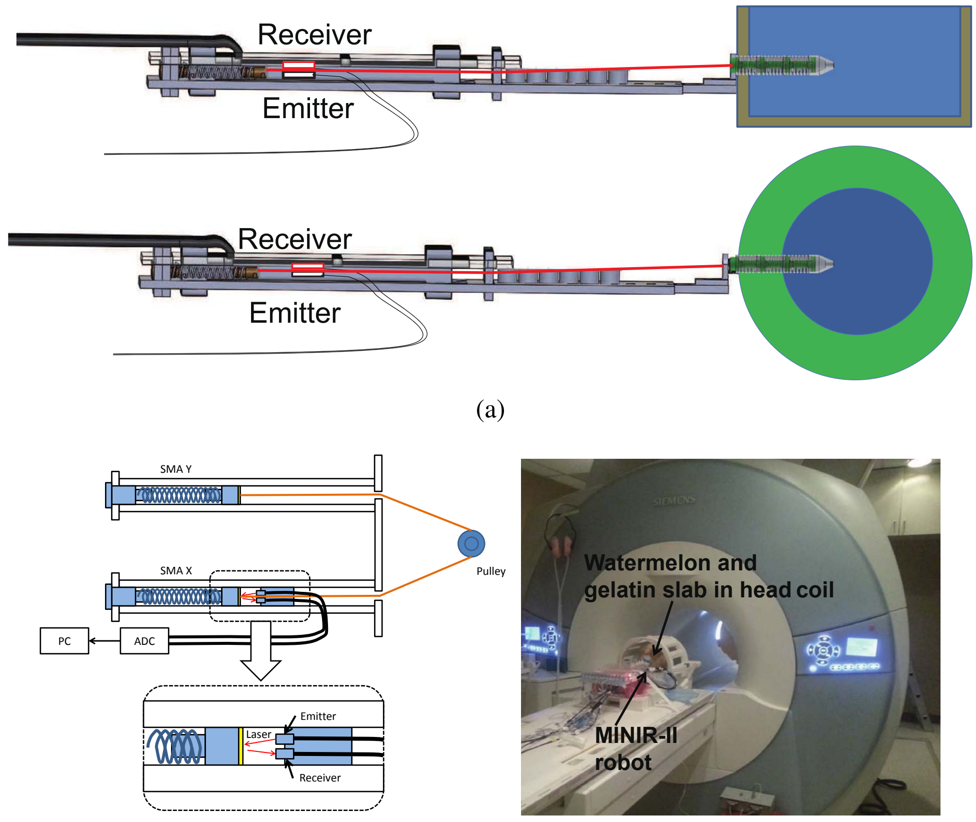

(a) (b) (c)

Figure 2.16: (a) Schematic of the MRI compatibility experiment in gelatin slab and cantaloupe (b) Detailed schematic of the laser setup to provide SMA spring displacement feedback for control (c) Actual photo of the experimental setup in the MRI room

2.7 Summary

We developed an MRI-compatible flexible meso-scale neurosurgical continuum robot, consisting of three segments of inter-connected spring backbone and a continuous outer spring. It offers independent segment control by routing of the tendons near the central axis of the robot. This feature was verified through a series of experiments to test both planar and orthogonal motion between segments. The flexible robot actuated by centrally routed tendons requires a distinct kinematic model, which was derived and verified through comparison between experimental and theoretical data. We also developed the SMA cooling system using compressed air to address the concern of limited actuation bandwidth in the neuro-

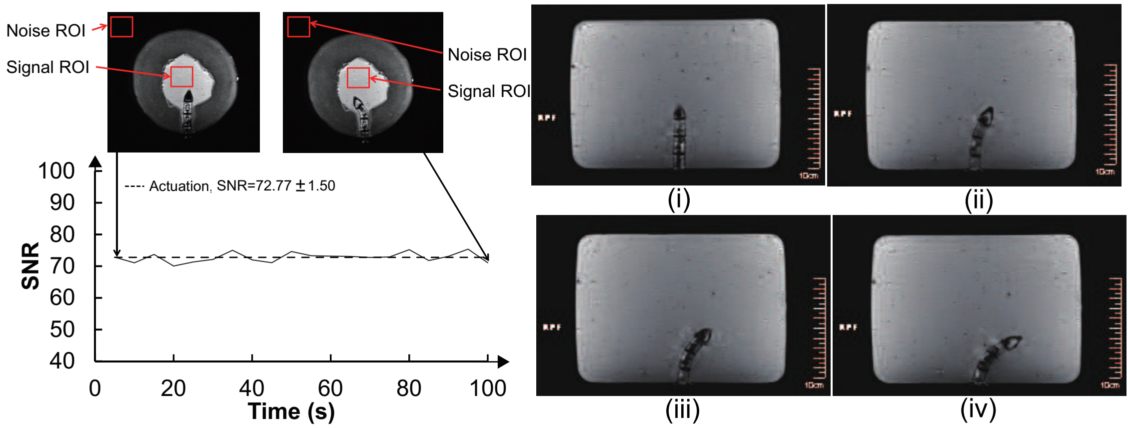

(a) (b)

Figure 2.17: (a) High resolution MR images of MINIR-II in a watermelon and SNR changes when the robot was actuated (b) High resolution MR images of MINIR-II in a gelatin slab: (i) Home configuration (ii) End segment bending (iii) End and middle segments bending (iv) End, middle and base segments bending

surgical robot. Finally, we verified the MR compatibility and motion capability of the robot in gelatin. At this point, there was a limit on the range of motion due to degradation of the VeroGrey material which becomes brittle over time. Other material such as the Extreme Frost Detail from Shapeways and VisiJet CR-CL 200 from 3D Systems would be tested in the experiments in the later chapters. We were also planning to add robot stiffness tuning to the prototype to improve robot manipulation of the flexible robot.

CHAPTER 3
DEVELOPMENT OF COOLING MODULE-INTEGRATED SMA SPRING ACTUATOR

3.1 Strengths and Drawbacks of SMA

Among the many MRI-compatible actuators, we opted for SMA springs during the initial robot development stage (Chapter 3, Chapter 4, and Chapter 5). It has many excellent properties that allow it to be integrated into a robotic application and at the same time SMA presents an interesting research topic since it poses the problem of real-time control. Ultrasonic motors are the other type of actuator that we employed due to its excellent reliability and resolution. They were used to replace the SMA in Chapter 7 and beyond. There are tradeoffs in employing either SMA or ultrasonic motors with the SMA having the problem of low actuation bandwidth and the ultrasonic motors posing the problem of creating interference with MR images when placed in close proximity to the MRI. In our work, novel solutions have been developed to minimize the drawbacks of both actuators. Pneumatic and hydraulics are the two other potentially feasible and reliable alternatives but we chose not to engage with the problem of leakage, cavitation, time delay, and uncontrolled motion, associated with these actuation methods, which could be fatal in a surgical robotic system.

Some of the advantages of using SMA spring in a neurosurgical robotic application are that it possesses high power density, exhibits high strain, and is compact and MRI-compatible. It can be used as linear actuators directly without any complicated gearing setup for speed reduction or motion amplification [124]. SMA has been researched in the past thirty years with various constitutive models being proposed to simulate its behavior and improve its control. The more commonly used SMAs have one-way shape memory effect and are thus used in antagonistic configuration. Creative applications have made use of the SMA's shape memory effect and superelastic behavior in various geometric forms such as wires [125], strips [126], rods [127], films [128], springs [129] and tubes [130]. Both academia and industry have made use of the SMA's inherent properties such as lightweight, low-cost and high power density in several product applications. Additive manufacturing, such as selective laser sintering (SLS) and electron beam melting (EBM), also allows the production of porous NiTi structures which are used as implants in orthopedic surgery [131]. The low cost involved in developing an SMA actuator allows the product to be disposable, leading to increased interest from the medical and industrial communities. Despite the multiple advantages of the SMA, there are a few drawbacks that need to be addressed so that the SMA can be fully taken advantage of as an actuator for a neurosurgical robot. These include the non-linear properties during phase transformation, the effect of thermomechanical cycles on the resultant stress and strain, and most importantly slow response time. The low actuation frequency stems from the fact that heat transfer and thus temperature change required for the thermally activated SMA takes time, be it the time required for the SMA to heat up and contract (transforms from martensite to austenite) or to cool down and relax (transform from austenite to martensite).

3.2 Background on Heating and Cooling of SMA

There are a number of different ways to heat SMA actuators, such as conductive (Peltier effect) [132], radiative [133], inductive [134].The most common convenient, and efficient heating method was Joule/resistive heating [135] and depending on the power supplied, the heating rate can be controlled. There were research that focused on improving the heating rate of SMA by introducing capacitors with low parasitic resistance [136] and inducing rapid heating below a threshold SMA resistance [137]. High current pulse actuation was also used to heat the SMA at a higher frequency, leading to small increase in temperature and thus a significantly reduced response time [138]. The more interesting challenge lies with addressing the low cooling rate under natural/passive cooling especially when the

SMA is heated to a high temperature (e.g. 60°-90°). Work has been done to optimize the PID controller gain to generate overshoot during the heating phase for the SMA to operate at the point on the hysteresis curve where faster cooling can be induced [139]. There was also research that divided SMA wires into segments and the hysteresis loop was exploited to improve the SMA response time and reduce power consumption [140]. Forced cooling strategies were also introduced to speed up heat transfer and thus improve the overall actuation speed. SMA wire was embedded in closed-system water channels to provide active cooling and adaptive hysteresis control was employed to further improve the actuation frequency. SMA wires have also been embedded/covered with other materials with high thermal conductivity such as silicone [141, 142, 143]. Fan cooling is one of the simplest and effective choices when individual SMA does not need to be cooled separately. It has been used to create a controlled convective cooling environment to predict the SMA behavior under external airflow [144]. The water-jet cooling of a moving SMA was investigated to explore its potential use in the field of microelectromechanical system (MEMS) and it was found that the shape deformation of the actuator increases with increased jet speed and decreases with increased nozzle-to-surface distance [145]. Peltier effect was also used to perform localized cooling to create an SMA actuator with high frequency response. The SMA wire cooled down within 1s (0.5 A current supplied) to 3s (1.5 A current supplied) after getting heated for 1s [146]. A light-weight heat sink, consisting of an outer metal tube coated with silicone grease was constructed to cool the SMA [138]. A mobile heat sink [147] equipped with a switching mechanism was developed to improve the actuation speed of an antagonistic pair of SMA wires in one-dimension without an increase in energy loss or power consumption that heat sinking would normally be associated with. Extensive experiments to investigate the convective cooling of SMA wires in various cooling environments such as air, oil, water, mineral oil, and thermally conductive grease [148]. All the cooling media investigated were in the static state except air. Distilled water provides the best cooling effect with the highest convective coefficient but is corrosive and requires good sealing. Oil provides an intermediate level of convective coefficient and does not cause corrosion. However it is hard to manage and requires good sealing as well. Forced air is less messy compared to the other media but requires additional bulky components for constant supply. Tadesse $et al.$ [149] investigated various active cooling methods as well and found forced water cooling to be superior to heat sinking and forced air cooling. An SMA spring actuated robotic hand exoskeleton for rehabilitation of stroke patients was developed using compressed air as the cooling factor to improve the exoskeleton's actuation frequency [129]. Investigations by Lara-Quintanilla and Bersee [150] using forced air cooling showed the influence of several parameters such as SMA size, applied stress, strain interval, and strain ratio on amplifying the actuation frequency of SMA. Smaller wire diameter has a much larger effect than higher stress in improving the actuation frequency due to the significantly greater surface-to-volume ratio of the wire. When the full working range of SMA is not required, smaller strain amplitude obviously would lead to higher actuation frequency. The nonlinear strain behavior of SMA with respect to temperature also allows the SMA to attain the maximum frequency when it is operated around the middle working range. In a more recent work, a smart soft composite (SSC) bending actuator was developed by embedding multiple SMA wires with small diameter in a polydimethylsiloxane (PDMS) matrix and acrylonitrile butadiene styrene (ABS) layered reinforcement structure [151]. Large bending deformation of around 50°can be achieved when the actuation speed matches the resonant frequency of the actuator which can be configured based on the configuration of the reinforcement structure and the actuator length. The actuator was found to still produce large bending deformation at actuation frequency as high as 35 Hz.

3.3 Actuation Bandwidth of Neurosurgical Robots

The MINIR-II robot used electrocautery to coagulate the brain tumor which can then be aspirated. Generally, an electrocauterization procedure in neurosurgery is carried out at a relatively slow pace. There is not a specific minimum required actuation speed or bandwidth required for a neurosurgical robot. The linear piezoelectric actuator on the ROBOCAST system advanced the biopsy probe at a velocity of 2 mm/s [152]. The neuroArm, also actuated by piezoelectric motors, had a tip speed of 0.5-5 mm/s [153]. In a robot-assisted ventriculostomy, the endoscope is moved at speeds between 0.5-2 mm/s [154]. A piezoelectric-motor actuated needle designed for neurosurgery was inserted and manipulated at speeds between 0.5-2 mm/s and it was found that an increase in speed would increase resistant force but reduce tissue deformation [155]. It is important to recognize that the actuation frequency of the piezoelectric motor can reach thousands of Hz but it is not required during neurosurgery. A concentric tube robot was reported to move at 2mm/s in a simulated procedure in gelatin to aspirate hemorrhage [156]. We can conclude that both the movement speed of a cautery probe in brain tissue and the speed of electrocauterization process are in the range between 0.5 and 5 mm/s. Surgeons normally use different current intensity, electrocautery application duration and cutting speeds during an electrocautery procedure to ensure a near complete removal of the target tumor and minimize undesired damage on adjacent tissues [157]. Thus, it is important to ensure that the neurosurgical robot actuated by the SMA spring actuators can be manipulated at sufficiently high bandwidth.

Since a compact design that integrated the cooling mechanism with the SMA was still not available, the focus of this chapter was to address this particular shortcoming by building upon the wet actuator concept [158] of using water as the cooling medium and applying it to the SMA spring instead of the SMA wire. We were able to maintain the compactness of the spring actuator through routing of a soft tube over each spring coil. Electrical heating was used to actuate the SMA spring so that power was not wasted on maintaining the hot water temperature in a wet actuator system.

3.4 Design of an SMA Spring Cooling Module

The wet SMA actuator introduced by Ertel and Mascaro [158] was an SMA wire placed in a compliant tube that changed its longitudinal shape with the SMA when it was heated by flowing hot water through the tube [158]. Cold water was then passed through the tube to cool the SMA wire. Similarly, our proposed cooling strategy uses water as the cooling medium. The main design objectives of our cooling strategy for the SMA springs were to improve the available actuation frequency of the SMA spring, and to maintain the compactness and portability of the actuator. Therefore, we proposed a flexible channel that consists of a soft silicone tube being threaded carefully through each SMA spring coil, forming a compact SMA spring with integrated cooling module [135], as shown in Figure 3.1(a). Other materials needed in making the cooling-module integrated SMA actuator are shown in Figure 3.1(b), including two moisture-resistant Acetal Barbed Tube Tee Fitting for $\frac{3}{32}$" tube ID (McMaster Carr, USA), two silicone rubber tapered stopper plugs (Powder Plug Coating Supply, USA) with dimensions of 1.5mm bottom diameter X 4.7mm top diameter X 15.8mm long, and a micro resistance temperature detector (RTD) (Alpha Technics, CA, USA). Before the threading process started, we straightened the two ends of the spring to allow easy entry of spring wire into the tube. The length of each straightened end was about 35 mm. The RTD sensor was then tied to one of the SMA spring coils using a thin strip of wire and bonded to the surface using high-temperature resistant superglue. Two pieces of electrical wires were soldered using tin solder with high percentage of silver to the last SMA spring coils, respectively, before the two straight ends of the SMA spring inside the tube. This ensures that the straight ends would not curve into a helical shape when current was applied. Sharp ends of the spring were trimmed and made blunt to prevent cracks from forming in the generally thin tube while the tube was being threaded.

Once the SMA spring was completely wrapped in the tube, T-barbed fittings were connected to the tube at both its ends. The fittings were sealed using rubber plugs, through

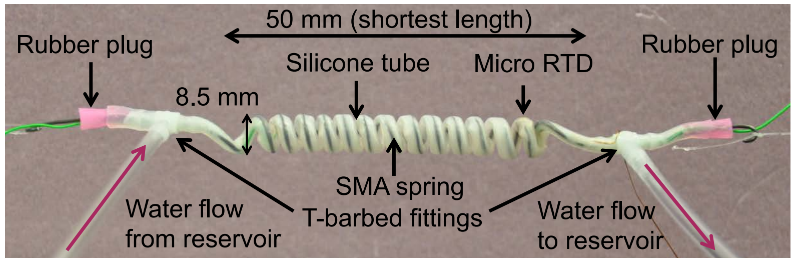

(a)

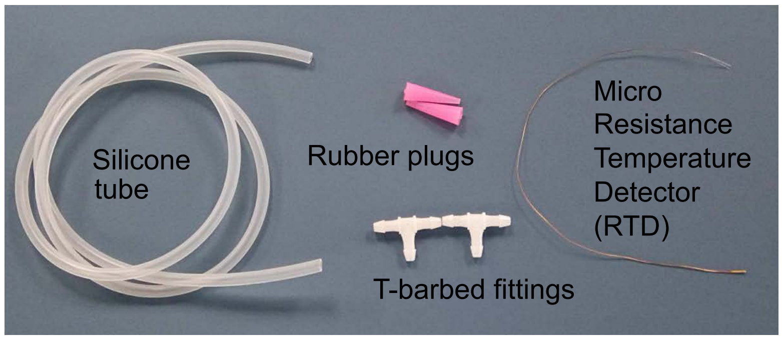

(b)

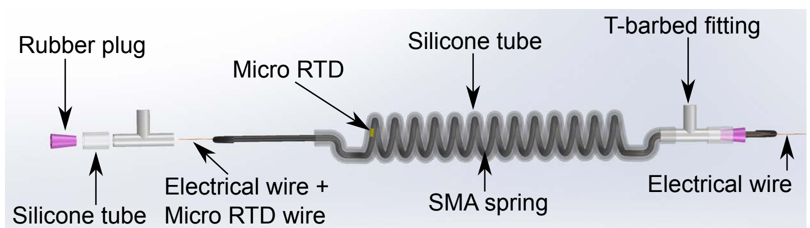

(c)

Figure 3.1: (a) SMA spring coils covered in a continuous silicone tube (b) Materials needed to make the SMA spring with cooling module (c) CAD schematic of the cooling module-integrated SMA spring with detailed illustration of the connection and arrangement of each component

which the straight ends of the SMA spring were inserted. Electrical wires were threaded through the rubber plugs using a needle to prevent any water leakage and led to the circuit board. Strong fish wires acting as tendons were connected mechanically to the two ends of the straight sections of the spring during the experiments. Figure 3.1 shows a magnified view of the SMA spring actuator integrated with the cooling channel.

3.5 Phenomenological Model of SMA Spring in an Antagonistic Configuration

3.5.1 Model Derivation

In antagonistic actuation configuration, the SMA spring actuator can be coupled with either a passive spring or another SMA spring. In the current work, we used a pair of SMA springs to allow the neurosurgical robot to begin at the home (center) position and perform back and forth motion. A constitutive model representing the behavior of the SMA springs in antagonistic configuration was therefore required to predict the actual motion which can then be used in a control framework. Through the model, we were able to obtain a relationship between the applied axial force, axial deflection and martensite volume fraction around the SMA transformation temperatures obtained from the heat transfer model in section 4. The state variables in our model are therefore axial force (F), axial spring deflection (δ), and martensite volume fraction (ξ). Tanaka [159], Liang and Rogers [160], Brinson [161], Boyd and Lagoudas [162], and Frémond [163] initially proposed constitutive models for SMA wire. Tobushi and Tanaka [164], Liang and Rogers [165], Aguiar et al. [166], Hadi et al. [167], and Ma et al. [168] used the wire models to derive those for the SMA helical spring. An et al. [169] also proposed a static two-state design model for the SMA spring.

The model described here was built upon Brinson's work on SMA wire [161] and the work by Ho and Desai [31, 170], which was based on Tobushi and Tanaka's [164], and Liang and Roger's [165] models. As stated in the work of Aguiar et al. [171], Brinson model was originally used for describing one-dimensional tension and compression and it would be valid to describe pure shear stress of an SMA spring by replacing the tensile properties with the shear properties. This is due to the fact that the torsion test has generated qualitatively similar stress-strain curve as the tension test [172, 173]. Even though there are previous works [174, 175] that show opposite results for SMA in the superelastic regime, it has generally been accepted in a significant amount of literature [164, 165, 171, 176, 177] that Eq. (3.1) is an appropriate constitutive model for an SMA spring. The governing equation in terms of shear stress in the SMA spring is expressed as [165]:

$$\tau - \tau_0 = G(\xi)(\gamma - \gamma_0) + \frac{\Theta}{\sqrt{3}}(T - T_0) + \frac{\Omega(\xi)}{\sqrt{3}}(\xi - \xi_0) \tag{3.1}$$

where $\tau, G, \gamma, \Theta, T, \Omega$, and ξ are shear stress, shear modulus, shear strain, coefficient of thermal expansion, temperature, phase transformation coefficient and martensite volume fraction, respectively. Subscript '0' denotes the initial conditions. In this work, we assume that the coefficient of thermal expansion, Θ, is negligible because of the relatively unsubstantial thermal strain compared to the strain due to phase transformation.

Ignoring the pitch and curvature effect, and assuming that the shear strain is linearly distributed in the spring wire cross section, the spring coil diameter is constant throughout the spring length, and phase transformation is homogeneous across the spring wire cross section, shear strain can be related to axial spring deflection by the following expression [178]:

$$\gamma = \frac{d_s}{\pi N D_s^2}\delta \tag{3.2}$$

where d_s, D_s and N are the SMA spring wire diameter, mean diameter of the spring, and the number of spring coils, respectively. Assuming that phase transformation is homogeneous along the SMA spring wire cross section, the maximum shear stress at the outer surface of the SMA spring wire, $\tau_{max} = \tau$, can be related to axial force by the following expression [165, 171, 178]:

$$\tau = \frac{8W_c D_s}{\pi d_s^3}F \tag{3.3}$$

where W_c is the Wahl's correction factor ($W_c = \frac{4R-1}{4R-4} + \frac{0.615}{R}$, where $R = \frac{D_s}{d_s}$). Shear stress is linearly distributed across the spring wire cross section when W_c is unity. Substituting Eqs. (3.2) and (3.3) into Eq. (3.1) leads to

$$C_1(F - F_0) = C_2 G(\xi)(\delta - \delta_0) + \frac{\Omega(\xi)}{\sqrt{3}}(\xi - \xi_0) \tag{3.4}$$

where $C_1 = \frac{8W_c D_s}{\pi d_s^3}$ and $C_2 = \frac{d_s}{\pi N D_s^2}$. It should be noted that the homogeneous phase transformation assumption is not the most realistic representation of the shear stress and phase distribution in the SMA spring wire cross section. However, it is useful to be employed in a simplified modeling approach to simulate the antagonistic SMA behavior in a practical robotic actuation setup. Models with more realistic non-homogeneous phase distribution in different annular regions of the SMA cross section have been proposed and investigated in the literature [164, 166, 179, 180].

By applying a material restriction, we can form a relationship between the shear modulus and the phase transformation coefficient [161]. We consider a case where an SMA spring in its fully austenite state (no initial deflection) is loaded until all the austenite is converted into detwinned martensite. The deflection that remains upon unloading is assumed to be the maximum recoverable deflection, δ_L. In this scenario, the initial conditions are $F_0 = \delta_0 = \xi_0 = 0$ and the final conditions are $F = 0, \delta = \delta_L, \xi = 1$. Replacing these variables in Eq. (3.4) leads to the relationship:

$$\Omega(\xi) = -\sqrt{3}C_2 G(\xi)\delta_L = -\frac{\sqrt{3}G(\xi)d_s}{\pi N D_s^2}\delta_L \tag{3.5}$$

Substituting Eq. (3.5) into Eq. (3.4), we obtain

$$C_1(F - F_0) = C_2 G(\xi)(\delta - \delta_0) - C_2 \delta_L G(\xi)(\xi - \xi_0) \tag{3.6}$$

The shear modulus can be expressed as [159, 161]:

$$G(\xi) = \xi G_M + (1 - \xi)G_A \tag{3.7}$$

where G_M and G_A are the elastic shear moduli of temperature-induced martensite and austenite, respectively. Brinson proposed that martensite volume fraction, ξ, that varies from 0 to 1, consists of two components: twinned martensite or temperature-induced martensite (TIM), ξ_T, and detwinned martensite or stress-induced martensite (SIM), ξ_S [161], and hence:

$$\xi = \xi_T + \xi_S \tag{3.8}$$

Having gone through the derivation in Brinson's work [161], we can express the constitutive model of an SMA spring that relates the axial force on the spring, F, and the spring deflection, δ, as:

$$C_1(F - F_0) = C_2[G(\xi)\delta - G(\xi_0)\delta_0] - C_2\delta_L[G(\xi)\xi_S - G(\xi_0)\xi_{S0}] \tag{3.9}$$

Based on Eq. (3.9), we can differentiate between twinned and detwinned martensite phases, and thus take into account the non-linear stress-strain behavior for the entire temperature range. We assume that the tendon that connects the SMA springs is always in tension and any stretch in the tendon is negligible.

We observed, through our characterization experiment, that an SMA spring, in its martensite phase, has a distinct force-deflection relationship. It can be divided into a linear region for $\tau < \tau_s^{cr}$ and a non-linear transformation region for $\tau_s^{cr} < \tau < \tau_f^{cr}$, where τ_s^{cr} and τ_f^{cr} are critical start shear stress and critical finish shear stress, respectively. G_M is the shear modulus of the SMA spring when it remains in the twinned martensite phase and behaves linearly like a passive tension spring within its elastic limit. The non-linear region is reflected in the Brinson model through the detwinned martensite volume fraction, ξ_S, that is modeled as a cosine function, ranging from 0 to 1 as the SMA martensite detwins.

When two SMA springs are configured antagonistically, and are heated and cooled alternately, we can model the force-deflection relationship as the non-heated SMA spring in its martensite phase getting stretched by the heated SMA spring during its actuation in either direction. We assume the starting position of the spring is always at or under the characteristic martensite graph. Therefore, we write the initial detwinned martensite volume fraction as follows:

$$\xi_{S0} = \frac{\delta_0 - \frac{C_1 F_0}{C_2 G_M}}{\delta_L} \tag{3.10}$$

We can then substitute Eq. (3.10) and the initial conditions for each heating and cooling process into Eq. (3.9) to obtain the equation governing each SMA in the antagonistic pair, in terms of force and displacement. More detailed descriptions of the steps taken to simulate the antagonistic SMA behavior will be discussed in Section 6: Results and Discussion.

Based on the above model, we need to know the change in martensite volume fraction of both the heated and non-heated SMAs. During the heating phase, martensite volume fraction components, ξ_S and ξ_T, are functions of temperature and shear stress and can be written as follows [161]:

$$\xi = \frac{\xi_0}{2}\left\{cos[\frac{\pi}{A_F - A_S}(T - A_S - \frac{\tau}{C_A})] + 1\right\} \tag{3.11a}$$

$$\xi_S = \xi_{S0} - \frac{\xi_{S0}}{\xi_0}(\xi_0 - \xi) \tag{3.11b}$$

$$\xi_T = \xi_{T0} - \frac{\xi_{T0}}{\xi_0}(\xi_0 - \xi) \tag{3.11c}$$

where C_A is the martensite to austenite transformation constant. A_F and A_S are the austenite finish and austenite start temperatures, respectively. The martensite volume fraction of the non-heated spring that is stretched from twinned martensite to detwinned martensite can be expressed as follows [161]:

For $T<M_S$ and $\tau_s^{cr}<\tau<\tau_f^{cr}$:

$$\xi_S = \frac{1-\xi_{S0}}{2} cos\left\{\frac{\pi}{\tau_s^{cr}-\tau_f^{cr}} \times (\tau - \tau_f^{cr})\right\} + \frac{1+\xi_{S0}}{2} \tag{3.12a}$$

$$\xi_T = \Delta_{T\xi} - \frac{\Delta_{T\xi}}{1-\xi_{S0}}(\xi_S - \xi_{S0}) \tag{3.12b}$$

where, if $M_F<T<M_S$ and $T<T_0$

$$\Delta_{T\xi} = \frac{1-\xi_{S0}-\xi_{T0}}{2} cos\left\{\frac{\pi}{M_S-M_F}(T-M_F)\right\} \tag{3.12c}$$

$$+\frac{1-\xi_{S0}+\xi_{T0}}{2} \tag{3.12d}$$

otherwise

$$\Delta_{T\xi} = \xi_{T0} \tag{3.12e}$$

The change in martensite volume fraction of the originally heated spring that, upon cooling, transforms from austenite to detwinned martensite is given by:

$$\xi_S = \frac{1-\xi_{S0}}{2} cos\left\{\frac{\pi}{\tau_s^{cr}-\tau_f^{cr}} \times [\tau - \tau_f^{cr} - C_M(T-M_S)]\right\} + \frac{1+\xi_{S0}}{2} \tag{3.13a}$$

$$\xi_T = \xi_{T0} - \frac{\xi_{T0}}{1-\xi_{S0}}(\xi_S - \xi_{S0}) \tag{3.13b}$$

where C_M is the austenite to martensite transformation constant and M_S is the martensite start temperature. Detailed work on how to determine both C_M and C_A will be described in subsection 3.2.

It is important to note that the spring does not transform into pure twinned martensite phase upon cooling because it is not cooled down in stress-free state. There is always stress from the antagonistic spring at all times.

3.5.2 Determination of Parameters for the SMA Spring Constitutive Model

Table 3.1: SMA Spring Parameters

Parameters	Symbols	Units	Values
Number of spring coil	N		13
Wire diameter	d_s	mm	0.75
Spring diameter	D_s	mm	8.5
Twinned martensite shear modulus	G_M	GPa	16.36
Austenite shear modulus	G_A	GPa	25.06
Austenite start temperature	A_S	$^{\circ}C$	45.87
Austenite finish temperature	A_F	$^{\circ}C$	49.12
Martensite start temperature	M_S	$^{\circ}C$	42.37
Martensite finish temperature	M_F	$^{\circ}C$	38.17
Martensite constant	C_M	MPa/ $^{\circ}C$	17.25
Austenite constant	C_A	MPa/ $^{\circ}C$	12.81
Critical start shear stress	τ_s^{cr}	MPa	69.25
Critical finish shear stress	τ_f^{cr}	MPa	164.8
Maximum recoverable deflection	δ_L	m	0.08

All the parameters required for the SMA phenomenological model in Section 3.1 are listed in Table 3.1. The four stress-free transformation temperatures of the SMA were obtained from a differential scanning calorimetry (DSC) test, in which a small sample of 18 mg of the SMA was heated and cooled in the temperature range of 25 °C to 100 °C. The heat flow rate results obtained from the test is plotted in Figure 3.2. To determine the martensite and austenite shear moduli of the SMA spring, we stretched the SMA spring and obtained the relationship between force and displacement of the spring at T = 25 °C (T<A_S) and T = 60 ° (T>A_F). In both experiments, we fixed one side of the SMA spring to a force sensor (MDB-2.5, Transducer technology, USA) attached to a fixed wall and the other side to a DC motor load shaft, as shown in Figure 3.3. We used Proportional+Integral (PI) control to maintain the SMA temperature before actuating the motor to stretch the spring for 95 mm. The force and spring deflection data are shown in Figure 3.4(a), where analytical data from the SMA model were shown to match the experimental data. The force data was converted into shear stress using Eq. (3.3) while the displacement data was

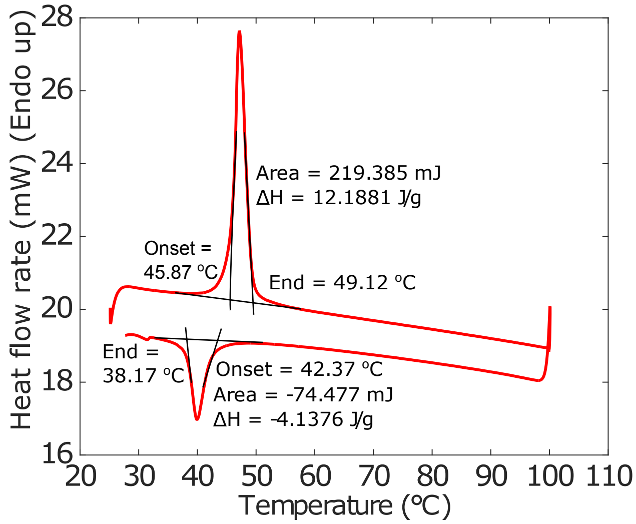

Figure 3.2: Transformation temperatures obtained from raw data of differential scanning calorimetry (DSC) test

converted into shear strain using Eq. (3.2). Shear stress is then plotted against shear strain in Figure 3.4(b). Two lines of best fit were used to determine slopes in the linear regions during austenite and martensite phases. The critical shear stress for conversion of twinned martensite to detwinned martensite (τ_s^{cr}) can be determined from the highest shear stress in the linear region of the characteristic martensite graph for T$<A_S$, as shown in Figure 3.4(b).

We performed block test at two different pre-stress levels to determine the transformation constants, C_M and C_A. The SMA spring was connected to a force sensor attached to a fixed wall on one side and to a moveable wall on the other side, as shown by the schematic in Figure 3.5(a). The wall was moved farther from the SMA spring to create the higher pre-stress level. During each of the two experiments, the two walls were fixed and hence the strain of the SMA spring was assumed zero. We first heated the SMA spring using a heat gun and once the force reached a plateau, the heat gun was removed and the SMA spring was left to cool down to room temperature. Force and temperature data were recorded throughout the experiment. We determined four transformation temperatures at each stress level from the force-temperature plot and connected two data points representing the same transformation temperature with a line. The four lines, as shown in Figure 3.5(b), rep-

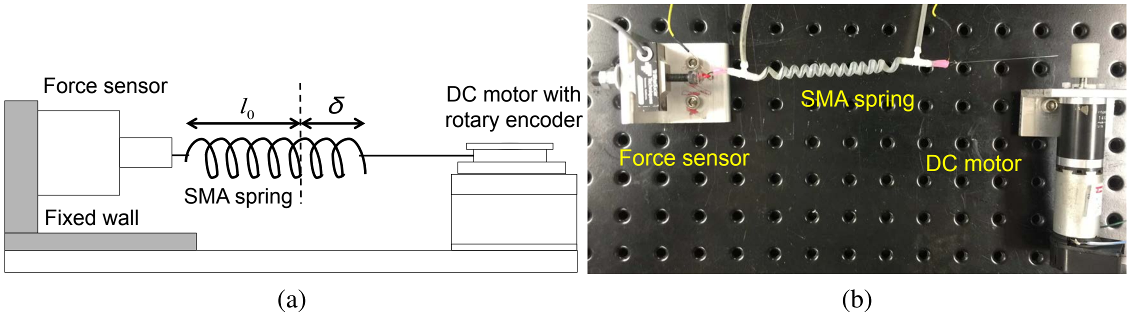

Figure 3.3: (a) Schematic and (b) actual experimental setup to stretch SMA spring at T <A$_S$ and T>A$_F$ (l_0 is the initial non-stretched length of the SMA spring and δ is the axial deflection)

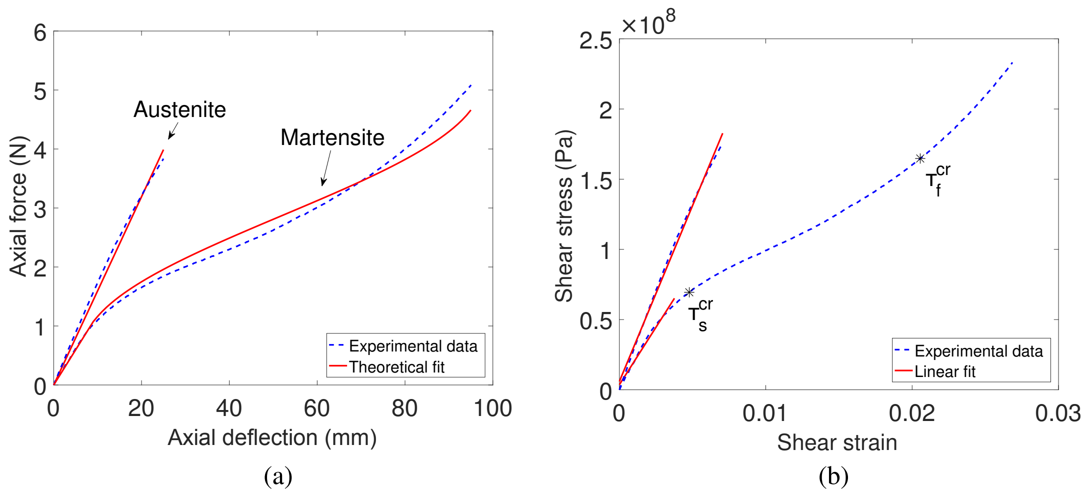

Figure 3.4: (a) Experimental and theoretical data comparison for T $>A_F$ (characteristic austenite graph) and for T $<A_S$ (characteristic martensite graph) (b) Experimental result and linear fit to determine the elastic shear moduli for T $>A_F$, G_A and for T $<A_S$, G_M

resented the relationship between critical shear stress and each of the four transformation temperatures. They provided us with the constant, C_M, which was the average of the slopes for the M_S and M_F lines and C_A, which was the average of the slopes for the A_S and A_F lines.

3.6 Heat Transfer Model

3.6.1 Model Derivation

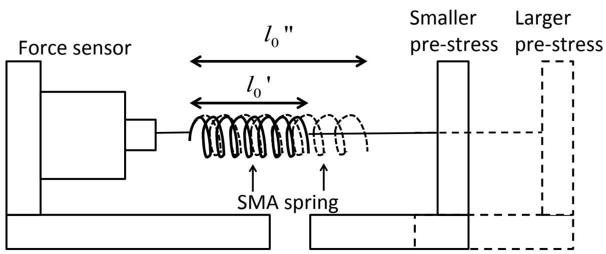

(a)

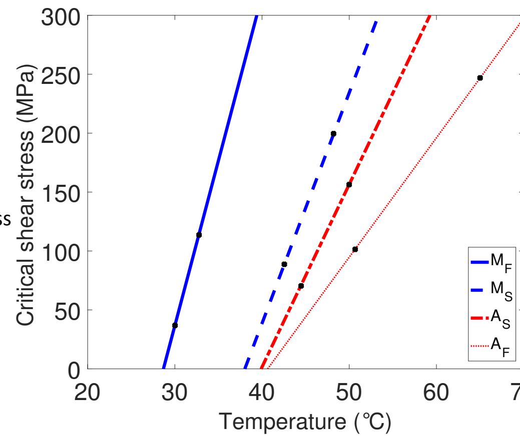

(b)

Figure 3.5: (a) Schematic of block test (l_0' and l_0'' represent two different initial lengths (prestrains) due to the two pre-stresses) (b) Experimental results from block tests done at 2 different pre-stresses (represented by the two markers on each line) for four transformation temperatures

SMA is a smart material that responds to temperature changes. In our work, we increased the temperature of the SMA springs using resistive heating and reduced it using forced convection of water. A thermal model is hereby developed to predict the temperature profile of SMA for the transient process. It can be combined with the SMA phenomenological model to simulate the SMA displacement during its actuation period.

We related the variation of temperature in the SMA spring wire with time under four assumptions. Firstly, heat is purely removed from the SMA into its environment via convection. When compared with the heat removed by forced convection, that removed via conduction and radiation is negligible and therefore is not considered significant. Secondly, Biot number, Bi, can be defined as follows:

$$Bi = \frac{h_w d_s}{k_s} \tag{3.14}$$

where h_w and k_s are the convective heat transfer coefficient of water and thermal conductivity of SMA, respectively. If $Bi \ll 1$, then we can assume the resistance to conduction in the SMA is much smaller than the resistance to convection across its boundary layer with water. Using the convective heat transfer coefficient of water (discussed later in this paper), Biot number during forced convection ranges from 0.05 to 0.1 throughout the entire operational temperature range. Since $Bi \leq 0.1$, we can apply the lumped capacitance method which assumes that the temperature within SMA is spatially uniform. Thirdly, geometrical changes in the radial direction is negligible during the heating and cooling process, leading to the assumption that SMA spring wire diameter stays unchanged at all times, including during phase transformation. Fourthly, material properties such as heat capacity, as well as temperature distribution are homogeneous throughout the entire spring length and across its cross-section. SMA resistance changes in a hysteretic form [181] during phase transformation but its negligible changes were not taken into account in our analysis.

In our model, we made use of a control volume of a small cylindrical section, Δx, of the SMA spring wire. In the subsequent discussion, subscript 's' denotes the SMA wire and subscript 'w' denotes water in the coiled tube. Applying energy balance to the control volume [182], the heat transfer model for the SMA spring wire can be represented as follows:

$$\frac{\beta_s I^2 \Delta x}{A_c} - A h_w (T_s - T_w) - m_s L_s \dot{\xi} = m_s C_s \dot{T}_s \tag{3.15}$$

where $\beta_s, I, A_c, A, h_w, T_s, T_w, L_s, m_s$ and C_s are SMA resistivity, current, cross-sectional area of the SMA spring wire, surface area of the SMA spring wire, heat convection coefficient of water, surface temperature of SMA, water temperature, latent heat of transformation, mass of SMA, and the specific heat capacity of SMA, respectively.

The first term on the left side of Eq. (3.15) describes resistive heating using electric current. The second term refers to the heat transfer between the SMA wire and its fluid environment. The heat convection coefficient is smaller during heating because it only involves free convection. It increases during cooling due to forced convection. The third term describes the heat energy changes during phase transformation of SMA between martensite and austenite phases. Martensite volume fraction is a function of both temperature and shear stress. Its derivative is obtained by differentiating Eq. 3.11a and Eq. 3.13a for the heating and cooling phases, respectively. For the simulation, shear stress and its derivative were obtained and derived from the experimental force measured by the force sensor. The term on the right side of Eq. (3.15) represents the heat energy storage in the SMA control volume. Mass, surface area, and cross-sectional area of a small section, Δx, of the SMA spring can be written as:

$$m_s = \rho_s \pi \frac{d_s^2}{4} \Delta x; \quad A = \pi d_s \Delta x; \quad A_c = \pi \frac{d_s^2}{4} \tag{3.16}$$

where ρ_s is the SMA density. Substituting m_s, A and A_c into Eq. (3.15), we obtain:

$$\dot{T}_s - \frac{16\beta_s I^2}{\pi^2 \rho_s d_s^4 C_s} + \frac{4h_w}{\rho_s d_s C_s}(T_s - T_w) + \frac{L_{sh}\dot{\xi}}{C_s} = 0 \tag{3.17}$$

where L_{sh} is the latent heat of transformation during the heating phase (see Table 4.2). During cooling phases (A $\rightarrow$ detwinned M), heating stops and I = 0. Equation (3.17) thus becomes:

$$\dot{T}_s + \frac{4h_w}{\rho_s d_s C_s}(T_s - T_w) + \frac{L_{sc}\dot{\xi}}{C_s} = 0 \tag{3.18}$$

where L_{sc} is the latent heat of transformation during the cooling phase (see Table 4.2).

SMA resistivity can be obtained experimentally by measuring voltage across the SMA spring and current passing through it in series. Specific heat capacity and latent heat of transformation of the SMA spring were determined using the differential scanning calorimeter, as shown in Figure 3.2 and as mentioned in Table 4.2. Assuming that the SMA spring wire is perfectly centered in the silicone tube, convection coefficient of the water flow, h_w, is defined as [183]:

$$h_w = \frac{k_w Nu}{D_h} \tag{3.19}$$

where the hydraulic diameter (D_h) is expressed as D_h = $d_t - d_s$ [183], and d_t, d_s, Nu and k_w are the silicone tube inner diameter, SMA spring wire diameter, Nusselt number, and thermal conductivity of water, respectively.

For determining the Nusselt number, we modeled the SMA spring wire as a horizontal cylinder. During the transition from cooling to heating, water flow was stopped. Water is therefore retained in the silicone tube during the SMA heating phase, which also enables the actuator to be uniformly heated throughout. SMA spring thus experiences free convection by static water during the heating phase and forced convection due to flowing water during the cooling phase.

For *free convection* (water is static in the silicone tube during the SMA heating phase), we applied the equation for Nusselt number based on [184], in which a general empirically determined equation suitable for all types of fluid for a large range of Raleigh number (Ra) was provided. Thus,

$$Nu = [0.60 + 0.387 \frac{Ra}{[1 + (0.56/Pr)^{9/16}]^{16/9}}^{1/6}]^2 \qquad (3.20)$$

$$for \quad 10^{-5} \leq Ra \leq 10^{12}$$

Ra is defined as:

$$Ra = Gr \cdot Pr = \frac{g\beta_w(T_s - T_w)D_h^3}{\nu_w \alpha_w} \qquad (3.21)$$

The Grashof number, Gr, and the Prandtl number, Pr, are defined as follows:

$$Gr = \beta_w(T_s - T_w)\frac{gD_h^3}{\nu_w^2}; \qquad Pr = \frac{\mu_w C_w}{k_w} \qquad (3.22)$$

while α_w is the thermal diffusivity (α_w = $\frac{k_w}{\rho_w C_w}$). β_w, C_w, ν_w, μ_w, and ρ_w are the volumetric coefficient of thermal expansion, specific heat capacity under constant pressure, kinematic viscosity ($\nu_w = \frac{\mu_w}{\rho_w}$), dynamic viscosity and density, respectively, of water. The differential equation for free convection is therefore expressed as:

$$\dot{T}_s - \frac{16\beta_s I^2}{\pi^2 \rho_s d_s^4 C_s} + \frac{\frac{4k_w}{D_h}[0.60 + 0.387 \frac{Ra}{[1+(0.56/Pr)^{9/16}]^{16/9}}^{1/6}]^2}{\rho_s d_s C_s}(T_s - T_w) + \frac{L_{sh}\dot{\xi}}{C_s} = 0 \qquad (3.23)$$

For *forced convection* (water flows continuously through the tube during the SMA cooling phase), we implemented the following equation [185]:

$$Nu = (0.255 + 0.699Re^{1/2})Pr^{0.29} \tag{3.24}$$

The Reynolds Number, Re, is defined as:

$$Re = \frac{u_w D_h}{\nu_w} \tag{3.25}$$

where u_w is the water velocity. The maximum water flow-rate (at 12 V power supply to the brushless submersible water pump) through the coiled tube was measured to be 131.9 mm^3/s. Using water properties at 300 K, the Reynolds Number was calculated to be 84.23. The differential equation for forced convection is therefore expressed as:

$$\dot{T}_s + \frac{\frac{4k_w}{D_h}(0.255 + 0.699Re^{1/2})Pr^{0.29}}{\rho_s d_s C_s}(T_s - T_w) + \frac{L_{sc}\dot{\xi}}{C_s} = 0 \tag{3.26}$$

Below is a list of water properties required for the thermal model and their respective equations defined in terms of the film temperature, T_f, where $T_f = \frac{T_s+T_w}{2}$ as an approximation and $T_w = 300$ K [183]:

Dynamic viscosity: $\mu_w = 4.8 \times 10^{-8}T_f^2 - 3.9 \times 10^{-5}T_f + 0.0081$

Thermal conductivity:$k_w = -2.3 \times 10^{-6}T_f^2 + 0.0021T_f + 0.17$

Prantl number: $Pr = 0.00039T_f^2 - 0.3T_f + 63$

Water density: $\rho_w = -0.2T_f + 1.1 \times 10^3$

Volumetric coefficient of thermal expansion: $\beta_w = -0.049T_f^2 + 39T_f - 7 \times 10^3$

Using the heat transfer model, we were able to simulate the change in SMA spring temperature when it is heated during free convection in static water and cooled under forced convection in flowing water in a tube. We used numerical simulation in MATLAB to derive the theoretical relationship between temperature of the SMA wire, T_s, over a period of time, t, since Eqs. (3.23) and (3.26) are both nonlinear.

3.6.2 Determination of Parameters for Heat Transfer Model

Table 3.2: Heat Transfer Parameters

Parameters	Symbols	Units	Values
SMA spring wire			
Resistivity	β_s	$\mu\Omega$·m	0.44
Density	ρ_s	kg/m^3	6450 [186]
Thermal conductivity	k_s	W/(m·K)	18 [158]
Specific heat capacity	C_s	J/(kg·K)	466 (heating)
			-260 (cooling)
			refer to Figure 3.6
Latent heat of transformation (heating)	L_{sh}	J/kg	12188.1
Latent heat of transformation (cooling)	L_{sc}	J/kg	-4137.6
Water			
Temperature	T_w	K	300
Specific heat capacity	C_w	J/(kg·K)	4179 [183]
Convection coefficient	h_w	W/(m^2 °C)	refer to Section 4.1
Acceleration of gravity	g	m/s^2	9.81

All the parameters required for the heat transfer model in Section 4.1 are listed in Table 4.2. Resistivity of the SMA wire, β_s, changed slightly during the thermal cycle and was treated as a constant in our model. It was derived from resistance, R measured at room temperature using Eq. (3.27).

$$\beta_s = R\frac{A_c}{L_s} = R\frac{d_s^2}{4D_sN} \tag{3.27}$$

where L_s is the length of the entire SMA spring. Specific heat capacity, in the unit of $\frac{J}{kg\ ^\circ C}$, was derived from the heat flow rate, H, in mW, through Eq. (3.28). It is important to note that the heat flow rate, as shown in Figure 3.2, needs to have its baseline data subtracted before being substituted in Eq. (3.28). The heating rate used during the DSC test, denoted as R_T, was 5 $°C/min$ and the mass of the SMA sample, denoted as m_s, was 18 mg.

$$C_s = \frac{1000\ H}{R_T \times m_s} \tag{3.28}$$

The plot of specific heat capacity against temperature can be seen in Figure 3.6. Based on Figure 3.6, two average values were stated for the heating and cooling phases, respectively, in Table 4.2. The entire dataset from Figure 3.6, however, was used for the simulation. Latent heat of transformation for the heating and cooling phase are obtained from the areas under the two peaks, referred to as 'ΔH', in Figure 3.2.

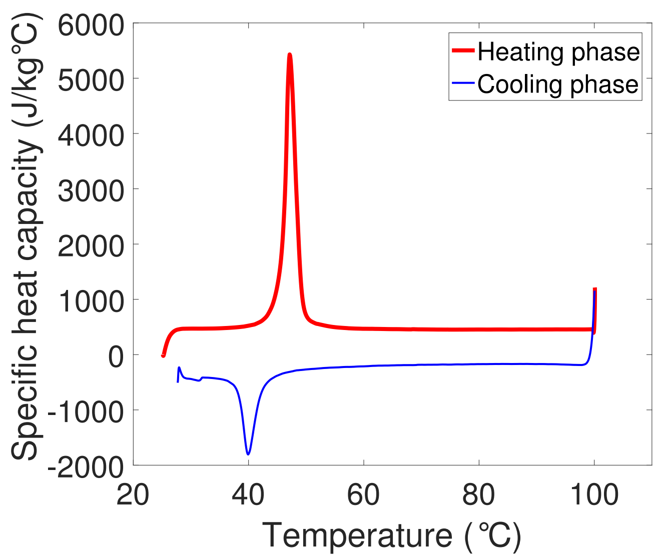

Figure 3.6: Specific heat capacity of SMA spring for temperatures between 25°C and 100°C

3.7 Experimental Setups

3.7.1 Verification of Antagonistic SMA Model and Heat Transfer Model, and Determination of Maximum Actuation Frequency

The experimental setup, shown in Figure 3.7 was used to determine the experimental behavior of SMAs in antagonistic configuration. In the setup, the tendon connecting the an-

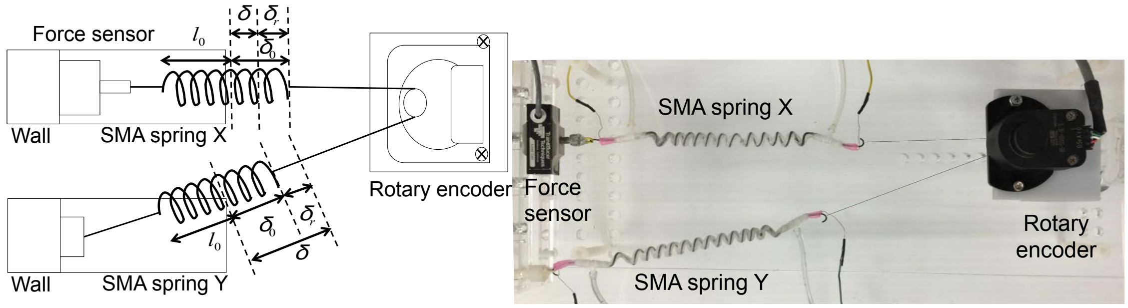

(a) (b)

Figure 3.7: (a) Experimental setup at its initial configuration, where l_0, δ_0, δ, and δ_r are the non-stretched length of each SMA spring, initial displacement, final displacement, and stretched/recovered length during each actuation step (b) Actual characterization setup to evaluate the effect of cooling module on the performance of antagonistic SMAs as well as to determine experimental behavior of antagonistic SMAs

tagonistic SMA springs was wound around the shaft of a rotary encoder. We ensured that the tendon and the encoder shaft were in contact at all times so that the spring deflection could be determined through the angle change measured by the encoder. The two SMAs were loaded to the same initial displacement and force at the beginning of the experiment. SMA X is the SMA spring that is heated initially and SMA Y is the SMA spring that is not heated initially. Step inputs of ± 10 mm were provided as the control reference while displacement and force data were collected by the rotary encoder and the force sensor, respectively. The experimental data were then compared with the theoretical simulation based on the work in section 3.1. Furthermore, the temperature changes over time during the heating and cooling phases of the SMAs in antagonistic configuration were experimentally determined using identical setup. Force and temperature data were collected while SMA spring X was heated from room temperature to 322 K (49 °C). The effectiveness of the cooling mechanism we proposed was also evaluated through similar experimental setup. A maximum constant current of 4 A was provided to heat the SMA using a motor driver through its current controller. The performance of SMAs was evaluated for sinusoidal references of various amplitudes, including 2 mm, 4 mm, 6 mm, 8 mm, 10 mm, and 12 mm.

3.7.2 Implementing Antagonistic SMA Spring Actuators on MINIR-II

The SMA spring actuators with integrated cooling modules were configured in an antagonistic configuration and set up as shown in Figure 3.8 to move a robot segment in one plane. We tested our actuators with the end segment of MINIR-II that consists of parallel springs: a flexible inner-spring backbone comprising of three segments and an outer spring for maintaining the robot shape. Each segment of the robot has a length of 19 mm. The robot is 3-D printed and is made of verowhite plastic. Each spring actuator has an unstretched length of approximately 50 mm and was pre-stretched by 25 mm. The two springs were connected to each other directly by a fish wire. The wire was routed around the rotary encoder to ensure the tension of the unactuated spring on the robot segment was always zero. Each of the antagonistic springs was then connected through tendon driven mechanism to the robot end segment by a fish wire to move it back and forth. The first two segments of the robot were constrained during the experiment. We used the rotary encoder to measure the displacement of the SMA springs during the experiment. This allows us to provide step inputs in terms of SMA displacement in both directions and therefore enables the robot to move at a specified frequency. We used a vision system with markers to track the angular displacement of the end segment of MINIR-II.

3.8 Results and Discussion

The SMA model was verified by comparing the theoretical simulation with the experimental result. Both antagonistic SMA springs have the same parameters, as seen in Table 3.1. They also started with the same initial displacement and force during the experiment. We provided step inputs of ± 10 mm and recorded the change in force and displacement. The experimental setup is shown in Figure 3.7.

The simulation begins with the same initial displacement, δ_0 = 25 mm, and force, F_0 = 1.24 N, as the experiment. The initial condition is indicated with '*' in Figure 3.9. Then,

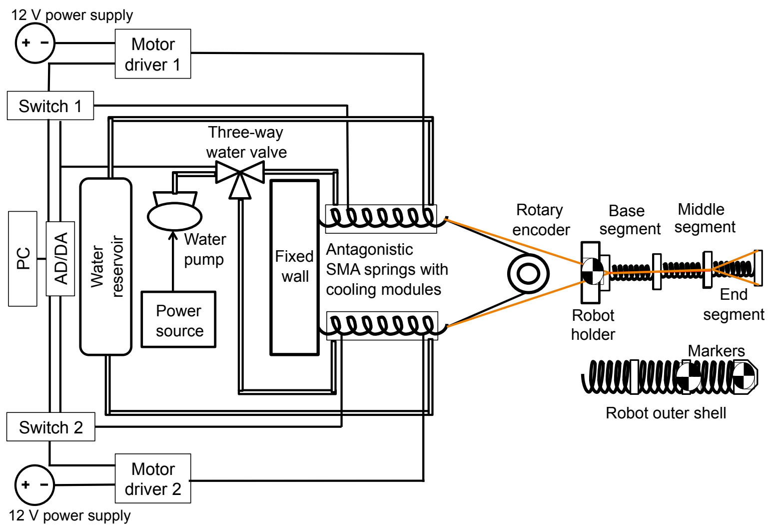

(a)

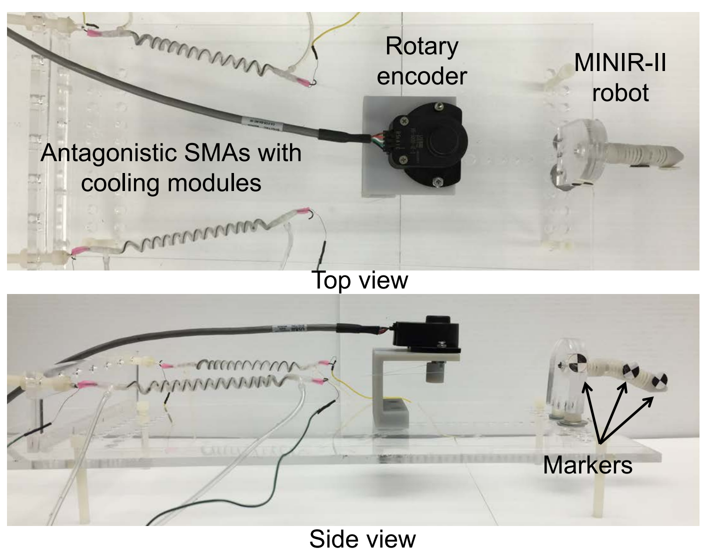

(b)

Figure 3.8: (a) Schematics and actual arrangement of the experimental setup involving antagonistic pair of SMA springs to move only the end segment (b) SMA springs in antagonistic configuration for actuating single robot joint (Tendons in the top view are highlighted in black for clarity)

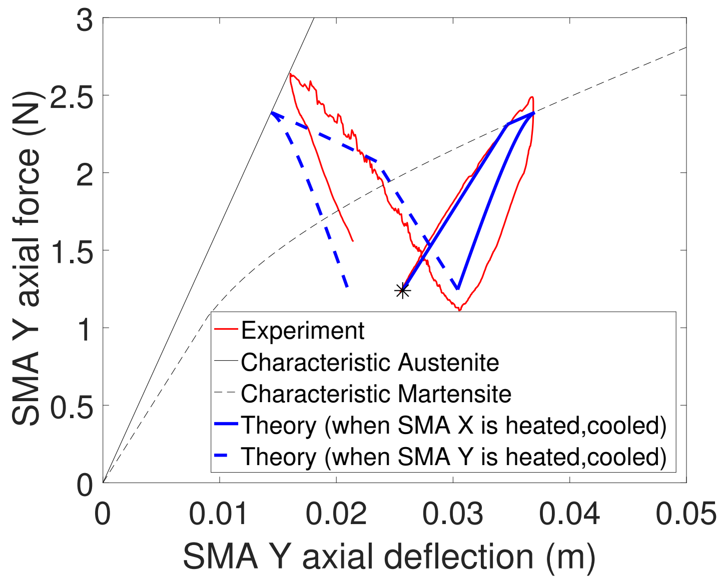

Figure 3.9: Experimental data and theoretical simulation of the behavior of SMA spring Y, starting from initial position '$*$'. When its antagonistic spring, SMA X, is heated, SMA Y is stretched for +10 mm (solid blue). SMA Y then unloads upon cooling of SMA X. When SMA Y is heated, its displacement trajectory (dotted blue) goes towards negative direction until it intersects with its characteristic austenite graph. It then unloads upon cooling.

we followed the following four steps to complete the simulation of one motion cycle of the antagonistic SMA springs (Subscript 'X' denotes SMA X while subscript 'Y' denotes SMA Y):

Step 1: Since the SMA's initial displacement is under the martensite graph and is such that $\delta_s^{cr} < \delta < \delta_f^{cr}$, where δ_s^{cr} and δ_f^{cr} are the axial deflections that correspond to τ_s^{cr} and τ_f^{cr} (see Figures 3.4 and 3.9), the initially non-heated SMA, SMA Y, would be loaded in such a way that the net force and displacement increase linearly with the stiffness slope of G_M. It should be noted that the general force-displacement equation for each SMA spring is stated in Eq. (3.9). During the simulation, the equation governing SMA X, which is heated initially, is obtained by substituting Eq. (3.10) into Eq. (3.9) and is expressed as:

$$C_1 F_X = C_2[\xi_X G_{M_X} + (1 - \xi_X) G_{A_X}][\delta_X - \delta_{L_X} \xi_{S_X}] \tag{3.29}$$

ξ_{S_Y} is equal to ξ_{S0_Y} in Eq. (3.9) for SMA Y. Therefore, the equation governing SMA Y is expressed as:

$$C_1(F_Y - F_{0_Y}) = C_2 G_{M_Y}(\delta_Y - \delta_{0_Y}) \tag{3.30}$$

Since we pre-strain both SMA springs to the same deflection, hence $\delta_{0_X} = \delta_{0_Y} = \delta_0$. The relationship between δ_X and δ_Y is described by:

$$\delta_X = -\delta_Y + 2\delta_0 \tag{3.31}$$

Combining Eq. (3.29), Eq. (3.30) and Eq. (3.31), we obtain:

$$F = \frac{\frac{C_2}{C_1} G_{M_Y}(\delta_0 - \delta_{L_X}\xi_{S_X}) + F_0}{1+\alpha} \tag{3.32}$$

where $\alpha = \frac{G_{M_Y}}{\xi_X G_{M_X} + (1-\xi_X) G_{A_X}}$ in Eq. (3.32). Using Eq. (3.11a) and Eq. (3.11b) to simulate the change in martensite volume fraction in SMA X, we can solve numerically Eq. (3.32). In this case, ξ_X drops from 1 to 0.27 when the linear increase of the non-heated SMA Y trajectory intersects the characteristic martensite graph.

Step 2: Once the force-displacement trajectory of SMA Y reaches the characteristic martensite graph, it would follow the martensite path while being loaded by the heated SMA. SMA X is governed by the same equation as Eq. (3.29). SMA Y has the same governing equation as SMA X, except that $\xi_Y G_{M_Y} + (1-\xi_Y) G_{A_Y} = G_{M_Y}$, since $\xi_Y = 1$. The equation of SMA Y is expressed as:

$$C_1 F_Y = C_2 G_{M_Y}(\delta_Y - \delta_{L_Y}\xi_{S_Y}) \tag{3.33}$$

The relationship between δ_X and δ_Y is now:

$$\delta_X - \delta_{0_X} = -(\delta_Y - \delta_{0_Y}) \tag{3.34}$$

Combining Eq. (3.29), Eq. (3.33) and Eq. (3.34), we obtain:

$$F = \frac{\frac{C_2}{C_1} G_{M_Y}(\delta_{0_Y} + \delta_{0_X} - \delta_{L_X}\xi_{S_X} - \delta_{L_X}\xi_{S_1} - \delta_{L_Y}\xi_{S_Y})}{1+\alpha} \tag{3.35}$$

While solving Eq. (3.35), we use Eq. (3.11a) and Eq. (3.11b) to simulate the change in martensite volume fraction in SMA X, and Eq. (3.12a) to simulate the change in detwinned martensite volume fraction in SMA Y. This behavior can be simulated for $0 < \xi_X < 0.27$. Temperature from the beginning of step 1 to the end of step 2 is between the austenite start and austenite finish temperatures, adjusted to match the stress levels.

Step 3: The heated SMA X trajectory at this point should have intersected with the characteristic austenite plot. The cooling process for SMA X then follows, allowing SMA Y to unload. The equations for SMA X and SMA Y are the same as those from Step 1, namely Eq. (3.29) and Eq. (3.30). ξ_{S0_X} and ξ_{0_X} are both 0 since it is initially in the austenite phase. ξ_{S_Y} remains unchanged (ξ_{S_Y} = ξ_{S0_Y}) because a non-heated SMA does not change its phase during its unloading. The relationship between δ_X and δ_Y are, however, not the same as in Step 1. They are instead the same as Eq. (3.34) in Step 2. Combining Eq. (3.29), Eq. (3.30) and Eq. (3.34), we obtain:

$$F = \frac{\frac{C_2}{C_1} G_{M_Y}(\delta_{0_X} - \delta_{L_X}\xi_{S_X}) + F_0}{1+\alpha} \tag{3.36}$$

We use Eq. (3.13a) to simulate the change in detwinned martensite volume fraction in SMA X in Eq. (3.36).

Step 4: SMA X currently becomes the non-heated SMA spring while SMA Y gets heated. We will repeat step 1 since SMA X has a displacement under the characteristic martensite graph as well. Therefore, steps 1 to 3 are repeated to complete one motion cycle.

Figure 3.9 shows the theoretical and experimental results of SMA Y that was actuated over one motion cycle of ±10 mm. Both results showed similar trend and covered the same value range. The interaction between the silicone tube and the SMA spring during its motion, and the loading history of the SMA could have contributed to the discrepancy between the theoretical and experimental data.

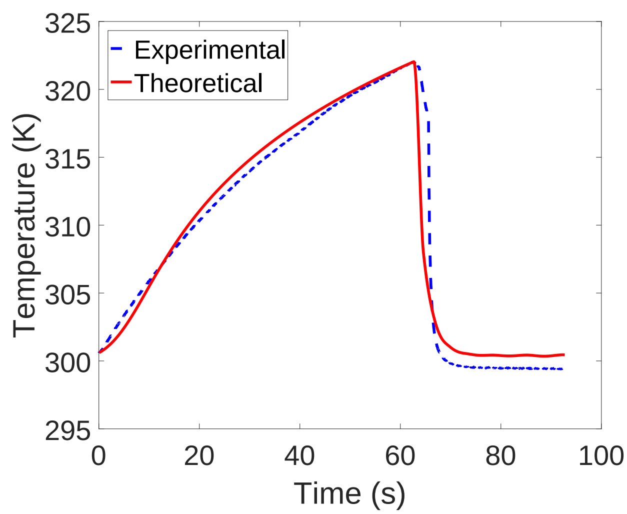

Figure 3.10: Comparison of theoretical and experimental data for temperature vs time during the heating and cooling periods

We verified the heat transfer model by comparing the simulation of temperature change of SMA over time with the experimental data. The experimental setup is shown in Figure 3.7 and a current of 1 A was supplied to heat the SMA spring so that it reached the desired temperature at 322 K. Once the desired temperature was reached, the current was turned off and water was allowed to flow through the cooling channel to cool the SMA. The temperature change in the SMA spring was recorded during its heating and cooling phases. Experimental data that include strain change, Reynolds Number of the water flow and current applied were used in the heat transfer model to simulate the temperature profile. The results are shown in Figure 3.10, that shows that the model matches the experiment well in both heating and cooling phases with an R^2-value of 0.946.

The maximum frequency of the antagonistic SMA spring actuators is determined by the coefficient of determination (R^2-value) > 0.9 between the the sinusoidal reference and the actual data. As shown in Figure 3.11, the cooling module provided significant improvement over natural cooling by air in terms of the SMA's ability to actuate at higher frequency.

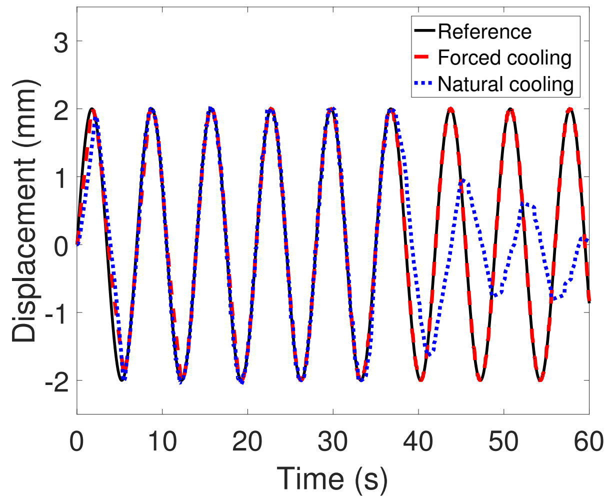

Figure 3.11: Tracking of sinusoidal trajectory of 2 mm amplitude and 7 s period under natural cooling by surrounding air (without cooling module) and forced convection by flowing water (with cooling module)

Forced convection by water in the tube allowed the SMA spring to follow a sinusoidal input with frequency of 0.143 Hz (7 s period) for an amplitude of 2 mm (R^2-value = 0.9927). Under natural cooling by air, the trajectory was well tracked for the initial 5 periods (R^2-value = 0.9585). After that, the residual heat remaining in either SMA spring built up and eventually resisted the motion in either direction, causing the discrepancy between the reference and the actual data. We did not observe such degradation in performance when the SMA was actuated under forced water cooling. We also performed the same experiment using the cooling module-integrated SMA springs for several motion amplitudes, ranging from 2 mm to 12 mm. The result is shown in Figure 3.12, where we observe that an increase in motion amplitude corresponds to a decrease in maximum actuation frequency. Besides that, at high amplitudes, the effect of low heating efficiency due to the static water retained in the cooling module can be observed. Hence, in our future work, we need to remove water from the cooling module during the heating phases to obtain a more satisfactory system performance and improve its efficiency.

We implemented our cooling module-integrated SMA springs on MINIR-II robot to move its end segment back and forth along the vertical axis. By contracting the SMA by

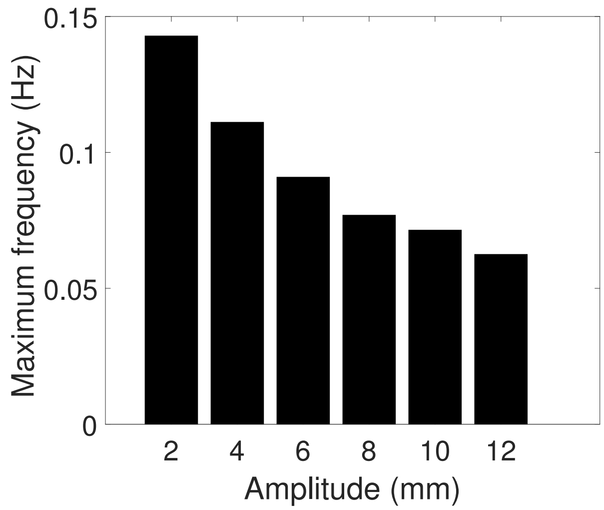

Figure 3.12: Maximum frequencies that can be achieved by antagonistic SMA springs with integrated cooling modules in response to sinusoidal inputs of different amplitudes

± 4 mm, shown in Figure 3.13(a), we were able to move the end segment of the robot by approximately $\pm 25°$, as shown in Figure 3.13(b). The back and forth motion of the end segment of the robot is shown in Figure 3.14. In our future work, we envision using an imaging modality to achieve a more precise control of the configuration of the robot in the workspace.

3.9 Summary

We proposed a cooling module that was integrated with an SMA spring to form a compact actuator. We presented our work on the SMA spring model in an antagonistic setup, simulated it based on various initial conditions for one motion cycle, and verified the simulation with the experimental results. We also presented the heat transfer model that simulated the temperature change of SMA over time. The model was compared with the experimental data for one heating and cooling cycle of the SMA spring. The proposed cooling module integrated SMA spring actuator significantly improved the actuation frequency and we were able to achieve it over a sustained period of time. We also implemented the actuators on a single segment of MINIR-II and commanded the SMAs to move over ± 4 mm, which

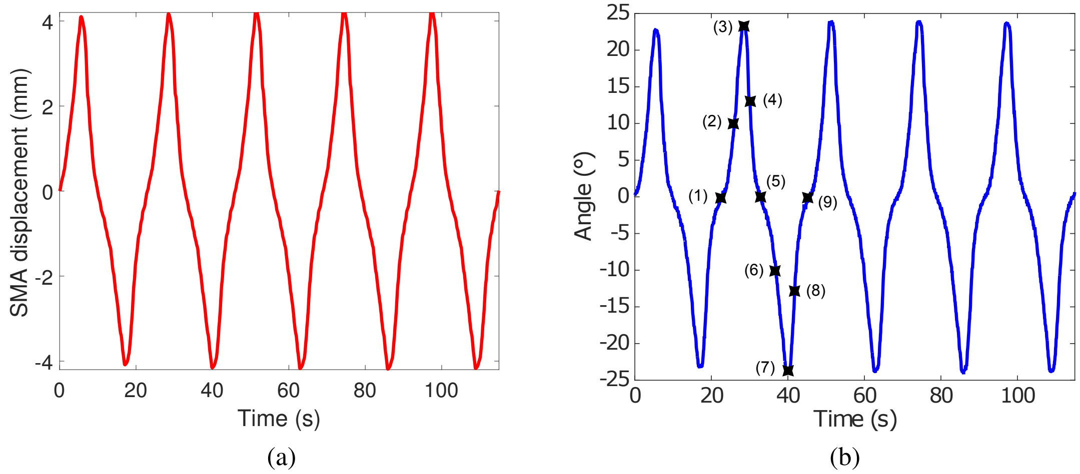

Figure 3.13: (a) SMA displacement and (b) the corresponding angular displacement of the end robot segment (Actual positions of the end robot segment at stages labeled (1) through (9) are shown in Fig. 3.14.)

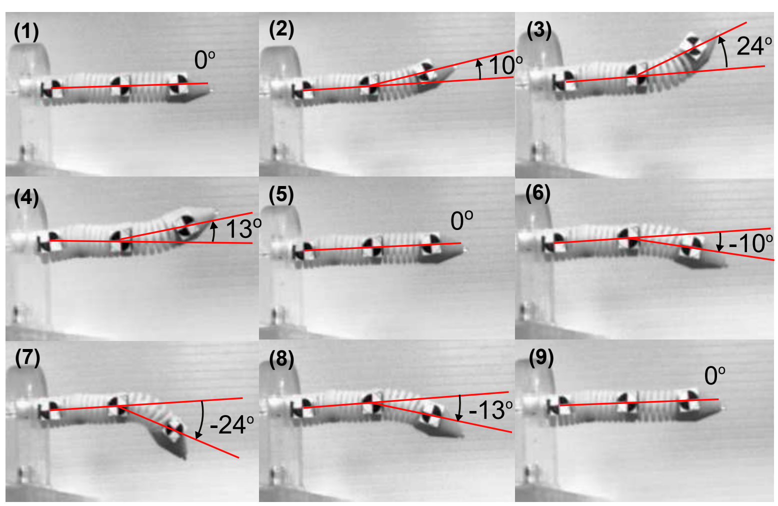

Figure 3.14: The end segment of MINIR-II robot moves back and forth under active cooling of SMA actuators (Base and middle segments were constrained). The red lines are superimposed in the figure for clarity.

corresponds to an angular displacement of approximately $\pm$ 25° in the robot. In the next chapter, we would try to remove the static water from the cooling module during the heating phases, create a better seal to prevent water leakage and investigate more tube dimensions to achieve a smoother water flow. These improvements would be critical to improving the maximum actuation frequency of the SMA especially for large ranges of motion. The work presented was the first step towards our eventual goal of developing a near real-time SMA actuated actively cooled multi-degree-of-freedom MINIR-II for MRI-guided neurosurgery.

CHAPTER 4

DEVELOPMENT OF AN ACTUATION MECHANISM FOR COOLING MODULE-INTEGRATED SMA SPRINGS

4.1 Introduction

In the previous chapter [135], we proposed a compact cooling module-integrated SMA spring actuator that consists of a flexible tube threaded through each SMA spring coil. As a continuation to the work, we present a new actuation mechanism whereby water was used to cool the SMA spring actuators that completed actuation and air was introduced to remove the water from the system prior to the next actuation cycle. The originality of our approach lies in the combination of two fluids using a single set of apparatus to achieve both fast cooling and efficient heating of SMA springs while keeping the compact configuration of the actuators. Extensive modeling and characterization work was done to investigate the effect of several parameters that directly influence the SMA thermal behavior and the actuation mechanism. This is, to our knowledge, the first time that SMA springs were used to actuate a robot end effector back and forth at more than 1 mm/s, comparable to existing neurosurgery robot speed.

4.2 Cooling Module and Actuation Mechanism for Antagonistic SMA Springs

In this work, we attempted to address one particular issue with SMA, its slow response. An interesting prototype introduced by Mascaro and Asada in 2003 [187] was a wet actuator which was an SMA wire enclosed in a compliant tube that changed its longitudinal shape with the SMA when it was heated by flowing hot water through the tube. Cold water was then passed through the tube to cool the SMA wire and return the SMA to its low-stiffness martensite phase. Inspired by the idea and intending to apply it on SMA spring, we proposed a cooling module-integrated SMA spring [135]. It involved the threading of a flexible tube through the SMA spring and sealing of the two ends by rubber plugs, as shown in Fig. 3.1. For the idea to work well, the flexible tube needed to have the right amount of softness, flexibility, and wall thickness. Different from [135], where our idea was first introduced and tested, the work in this chapter involved rigorous selection process of the best available silicone tube (McMaster-Carr) to be used as the cooling module for the SMA spring of our choice (Flexmet, Belgium). Tubes with different parameters were tested on the SMA spring that has a spring coil diameter, D_s, of 6.5 mm and a wire diameter, d_s, of 0.75 mm. Table 4.1 shows the different tubes that we attempted to use for the cooling channel of SMA spring [188]. We eventually chose Tube 6 because it has the best combination of inner diameter, softness, and wall thickness to ensure smooth water flow and prevent unnecessary stress on the SMA spring.

Table 4.1: Tube Parameters

Name	Inner Diameter (mm)	Outer Diameter (mm)	Wall Thickness (mm)	Softness (Shore A)
Tube 1 (High Purity White Silicone Rubber Tubing (Non-reinforced))	1.02	2.16	0.58	55
Tube 2 (Odor Resistant White Silicone Rubber Tubing)	1.57	2.41	0.43	50
Tube 3 (High Temperature NSF-51 Silicone Rubber Tubing)	1.59	3.18	0.79	50
Tube 4 (High Temperature Silicone Rubber Tubing)	1.59	3.18	0.79	35
Tube 5 (Laboratory Clear Tygon PVC Tubing)	2.38	3.18	0.41	56
Tube 6 (High Purity White Silicone Tubing)	1.98	3.18	0.61	50

Different from our previous work [135], our newly proposed mechanism involved water as the cooling medium and compressed air as the medium to remove the water for efficient resistive heating. A fluid circulation system was developed to realize the mechanism, consisting of a water reservoir, an air compressor, wye fittings, and water and air valves for

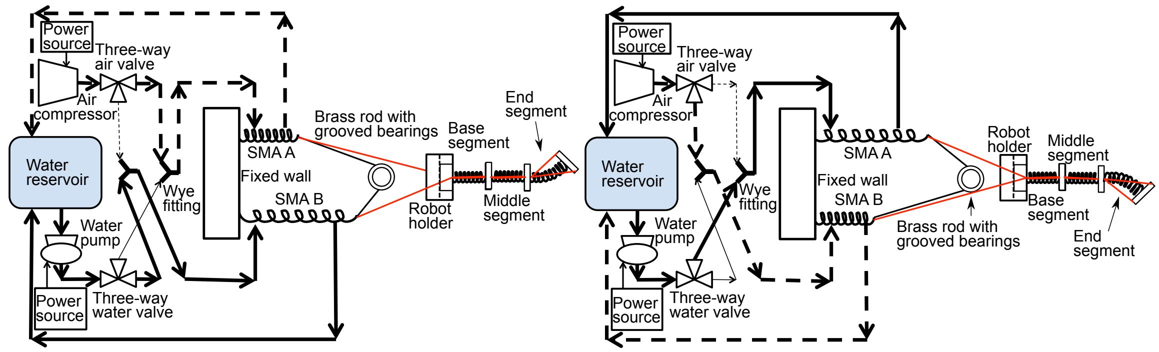

(a) (b)

Figure 4.1: Schematics showing water flow (bold solid line) and air flow (bold dashed line) during (a) upward motion and (b) downward motion of the middle segment

alternating the flow during the heating and cooling process. Each antagonistic pair of SMA springs (say, SMA A and SMA B) were responsible for only one DoF of a robot segment. Each SMA spring pair was connected directly to each other by a monofilament fishing line that was routed around a grooved bearing. Each individual SMA spring was also connected by the tendon driven mechanism to a hole terminated at a robot segment disk to bend it in one direction. Figs. 4.1(a) and 4.1(b) show the air and water flow during bending of a robot segment in two different directions. For example, in Fig. 4.1(b), air valves are opened for a short period of time (varies depending on the gauge pressure of the compressed air) to pass the compressed air at high pressure through the cooling module to force the static water out, thereby allowing water to return to the water reservoir and enabling more efficient subsequent heating. SMA B is at the same time, cooled by flowing water through its tube (water valve is opened), therefore providing minimum resistance to the upward bending of the robot.

4.3 Actuator Characterization for Optimal Robot Speed

The new actuation mechanism applied on the cooling module-integrated SMA spring had to be characterized to determine the highest robot speed that could be achieved by MINIR-II. The characterization parameters were largely based on the heat transfer model that governs the SMA spring during its actuation. It can be expressed as follows [135]:

$$\dot{T}_s - \frac{16\beta_s I^2}{\pi^2 \rho_s d_s^4 C_s} + \frac{4h_f}{\rho_s d_s C_s}(T_s - T_f) + \frac{L_s \dot{\xi}}{C_s} = 0 \tag{4.1}$$

where T_s, $\beta_s, I, \rho_s, h_f, T_f, L_s, \dot{\xi}$ and C_s are the surface temperature of SMA, SMA resistivity, current, SMA density, heat convection coefficient of fluid, fluid temperature, latent heat of transformation, rate of phase transformation, and specific heat capacity of SMA, respectively. Subscript 's' denotes the SMA spring wire and subscript 'f' denotes the fluid in the coiled silicone tube, be it air, denoted by subscript 'a' (during the heating phase) or water, denoted by 'w' (during the cooling phase). The second term in Eq. (4.1) represents the power used for resistively heating the SMA spring. The third term describes the rate of heat transfer between the SMA spring and its environment (air during the heating phase and water during the cooling phase). Heat convection coefficient, h_w, from Eq. (4.1), is defined as [183]:

$$h_f = \frac{k_f Nu}{D_h} \tag{4.2}$$

where the hydraulic diameter can be expressed as D_h = $d_t - d_s$ [183], and d_t, d_s, Nu and k_f are the silicone tube inner diameter, SMA spring wire diameter, Nusselt number, and thermal conductivity of the fluid in the cooling module, respectively. The third term describes the rate of change in latent heat energy during phase transformation of SMA between the martensite phase and austenite phase.

The experimental variables that were derived from the three heat transfer model parameters are the current, water flow rate, and pre-displacement of the SMA springs. We also investigated the effect of gauge pressure of the compressed air due to the mechanism we used in circulating the fluid. During each characterization experiment, we actuated the end segment of the robot in one DoF for $\pm 10°$ and varied only one parameter while keeping the other parameters constant. Our control parameter combination was as follows: current = 3.5 A; water flow rate = 1150 mm^3/s; pre-displacement = 50 mm; and gauge pressure =

15 psi.

Table 4.2: Heat Transfer Parameters

Parameters	Symbols	Units	Values
SMA spring wire			
Wire diameter	d_s	m	0.75×10^{-3}
Coil diameter	D_s	m	6.5×10^{-3}
Resistivity	β_s	$\mu\Omega$·m	0.44
Density	ρ_s	kg/m^3	6450 [186]
Thermal conductivity	k_s	W/(m·K)	18 [158]
Specific heat capacity	C_s	J/(kg·K)	466 (heating) -260 (cooling)
Latent heat (heating)	L_{sh}	J/kg	12188.1
Latent heat (cooling)	L_{sc}	J/kg	-4137.6
Air			
Temperature	T_a	K	300
Thermal conductivity	k_a	W/(m.K)	0.0263
Expansion coef.	β_a	1/K	3.43×10^{-3}
Kinematic viscosity	ν_a	m^2/s	15.89×10^{-6}
Thermal diffusivity	α_a	m^2/s	22.5×10^{-6}
Water			
Temperature	T_w	K	300
Prandtl number	Pr	-	5.83
Thermal conductivity	k_w	W/(m.K)	0.613
Kinematic viscosity	ν_w	m^2/s	8.6×10^{-7}

4.3.1 Effect of Current

Since current was used to vary the power, we used a motor driver in its current controller mode for heating the SMA spring. The upper limit of the current was set to be 3.8 A to prevent excessive heating in the electrical wire as well as difficulty in controlling actuation over a small range of motion in the robot joint. Four different currents were applied to the SMA springs, namely: 3.0 A, 3.25 A, 3.5 A and 3.8 A.

Eq. (4.1) provides us with the theoretical prediction of the change in the SMA temperature when it gets heated. For *free convection* (air is static in the silicone tube during the SMA heating phase), we applied the equation for Nusselt number based on [184], suitable for fluids of a large range of Raleigh number (Ra). Thus,

$$Nu = [0.60 + 0.387 \frac{Ra}{[1 + (0.56/Pr)^{9/16}]^{16/9}}^{1/6}]^2 \tag{4.3}$$

where $Ra = \frac{g\beta_a(T_s - T_a)D_h^3}{\nu_a \alpha_a}$. Pr, β_a, ν_a, and α_a are the Prandtl number, volumetric coefficient of thermal expansion, kinematic viscosity, and thermal diffusivity, respectively, of air. Using Eq. (4.3) and referring to Table 4.2, heat convection coefficient during the heating phase, h_a, can be calculated through Eq. (4.2).

4.3.2 Effect of Water Flow Rate

Forced convection happens as the water is continuously flown through the tube to cool the SMA spring. For forced convection, the following equation was implemented in our thermal model [185]:

$$Nu = (0.255 + 0.699Re^{1/2})Pr^{0.29} \tag{4.4}$$

Re is given by $Re = \frac{u_w D_h}{\nu_w}$, where u_w and ν_w are the velocity and kinematic viscosity of water, respectively. Water velocity, u_w can be related to its flow rate, q_w through $u_w = \frac{4}{\pi(d_t^2 - d_s^2)} q_w$. Therefore, in our characterization experiments, we implemented five different water flow rates: 800 mm^3/s, 1000 mm^3/s, 1150 mm^3/s, 1330 mm^3/s, and 1500 mm^3/s.

Using Eq. (4.2) and Eq. (4.4), and referring to Table 4.2, theoretical heat convection coefficient, h_w, is plotted against various tube inner diameters, d_t, that were selected in Table 4.1 for different flow rates, q_w. The results are plotted in Fig. 4.2(a). Under the ideal

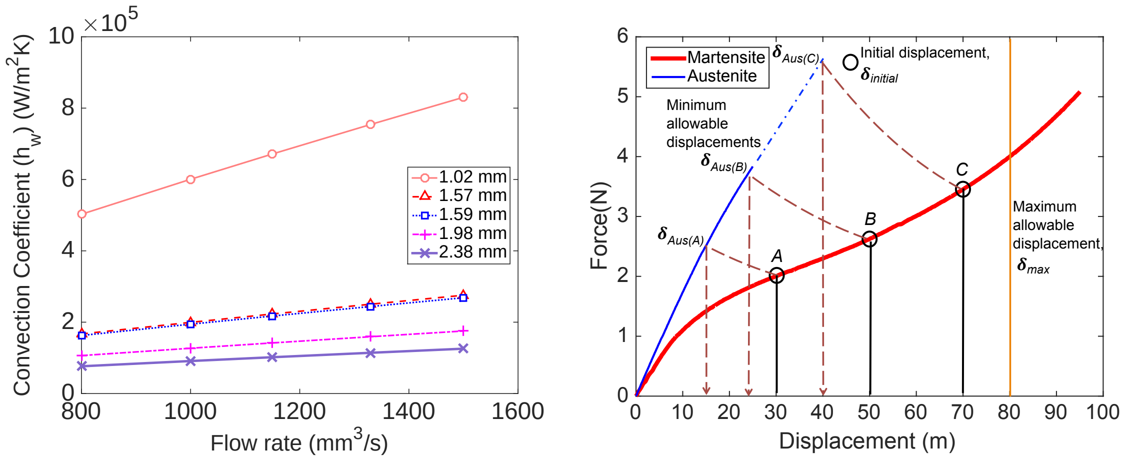

(a) (b)

Figure 4.2: (a) Predicted heat convection coefficient with variation in the tube inner diameter and water flow rate (b) Theoretical relationship to determine SMA pre-displacement, $\delta_{initial}$, to ensure coverage of the desired motion range

condition that the SMA spring wire is always in the center of the tube and there is uniform flow around the SMA spring wire, the convection coefficient increases with an increase in the water flow rate and a decrease in the tube diameter. However, a tube diameter of 1.98 mm was chosen because it is the smallest tube diameter that allows water to flow smoothly during the contraction of the SMA spring.

4.3.3 Effect of Pre-Displacement

Pre-displacements of the antagonistic SMA springs were identical to ensure that the robot joint could be actuated in either direction for the same angular displacement. The graph, shown in Fig. 4.2(b), explains how the antagonistic SMA springs in our setup theoretically behave. The characteristic martensite (red curve in Fig. 4.2(b)) and austenite (blue curve in Fig. 4.2(b)) curves were experimentally determined by stretching (within recoverable limit) the SMA spring at room temperature ($T_s \leq A_S$) and at $T_s \geq A_F$, respectively while recording its displacement and force, where A_S and A_F are the austenite start and austenite finish temperatures. The maximum SMA recovery length was experimentally determined to be 80 mm [135]. The figure shows three cases of initial SMA displacement: $\delta_{initial(A)}$, $\delta_{initial(B)}$, and $\delta_{initial(C)}$. The heated (contracting) SMA spring follows the dotted line and moves towards the austenite curve from its initial displacement while the non-heated SMA spring, getting extended, moves towards the right by following the characteristic martensite curve from the initial displacement. The path taken by the heated SMA spring is a mirror image of that by the non-heated SMA spring. The maximum range of motion in case A is dictated by the displacement of the heated spring that contracts to 15 mm ($\delta_{Aus(A)}$) while that in case C is dictated by the displacement of the non-heated spring, which is only 10 mm away from the maximum allowable displacement of SMA. To ensure the maximum range of motion in each direction, the optimal pre-displacements should be around 50 mm.

Secondly, phase transformation in the SMA spring is affected by its stress level [189] and pre-displacement can hypothetically be optimized to improve the rate of SMA temperature and its phase transformation, and thus the robot motion speed. Three SMA pre-displacements were considered in the characterization experiment, namely: 35 mm, 50 mm, and 65 mm. Using the experimentally measured force, theoretical temperature profile for each SMA pre-displacement is determined through Eq. (4.1) and compared with the experimental data in section V.

4.3.4 Effect of Gauge Pressure

We used compressed air to drive the water out so that the power supplied to the SMA can be primarily used for heating the SMA instead of heat dissipation in the surrounding water. To optimize the actuation mechanism, the air valve should be shut off as soon as the heating phase takes over. The fluid motion between the air valve opening and the outlet at the end of the coiled tube is modeled in order to predict the theoretical duration for which air valve needs to be turned on. Since the air passes through a straight tube with 1.5 m length before entering the coiled cooling module, the total pressure loss (gauge pressure) can be expressed as follows [190]:

$$P_g = \Delta P_{f_s} + \Delta P_{f_c} + \Delta P_a \tag{4.5}$$

where ΔP_{f_s}, ΔP_{f_c}, and ΔP_a are the frictional component in the straight section of the tubing, the frictional component in the coiled cooling module, and the acceleration components, respectively and can be expressed as $f_s\frac{\rho_w u_w^2 L_s}{2d_t}$, $f_c\frac{\rho_w u_w^2 L_c}{2D_h}$, and $\frac{\rho_w u_w(L_s+L_c)}{t}$. f_s and f_c are the friction factors in the straight tube and the coiled cooling module, respectively while L_s and L_c are the lengths of the straight tube and the coiled cooling module, respectively. The flow investigated in our case are considered laminar in the straight tube since the Reynolds number (Re) is less than the critical value of 2100 [191]. The critical Re used to distinguish laminar and turbulent flow in coiled cooling module can be determined from [192]: $Re_{cr} = 2100(1 + 12\sqrt{\frac{d_t}{D_s}}) = 16008$. The Re of the flow in the coiled tube for all flow rates investigated were much less than the critical value of 16008. Therefore it was confirmed that the flow throughout the entire tubing system was laminar. Friction factor in the straight tube can be expressed as $f_s = \frac{64}{Re}$ [191] whereas that in the coiled tube can be expressed as $f_c = f_s(0.556 + 0.0969(D_n))$ [192]. The Dean number is defined as $D_n = Re\sqrt{\frac{D_h}{D_s}}$. Using the water velocities experimentally measured at different gauge pressures and solving Eq. (4.5), we obtain the time required to remove water from the coiled cooling module at different gauge pressure of the compressed air through $t = \frac{\rho_w u_w(L_s+L_c)}{P_g-\Delta P_{f_c}-\Delta P_{f_s}}$.

The theoretical and experimental time required for the water to be completely removed from the cooling module were compared and an average error of 0.53 s was observed. The experimentally measured times of 3.5 s, 2.3 s, 1.8 s, 1.5 s, and 1.3 s were then hardcoded into the control program to determine the duration for which the compressed air is turned on in the characterization experiments for the five different gauge pressures of 5 psi, 10 psi, 15 psi, 20 psi and 25 psi, respectively.

4.4 Experimental Setup

4.4.1 Improved Robot Design

Our continuum robot consists of an inter-connected spring, a flexible rubber sleeve, and a robot head with channels for cautery probes, suction tube and magnetic field sensor (Robin Medical Inc., Baltimore, USA), as shown in Fig. (6.9). The inter-connected spring backbone is divided into three segments, namely base, middle and end segments, each of which consists of a disk and a spring. The design was an improved version of our MINIR-II prototype [193] as it had a larger lumen to incorporate cable for the magnetic field sensor. The design was constrained by the largest diameter of 12 mm so that the robot could fit into existing endoports used in microsurgery of brain tumor as well as the minimum lumen diameter of 4 mm for the passing of sensor cable, tendons, cautery probe wires, and suction tube. After multiple trials, the robot was determined to have optimal stiffness (defined by its ability to maintain its elasticity after at least a 90° angular displacement of the surface normal of the segment disk without breaking) with a spring wire diameter of 1.4 mm, a spring mean diameter of 5.2 mm, and 1.5 mm pitch. The robot was experimentally determined to have a bending stiffness of 8.7 N/m whereas a single segment has a bending stiffness of 96 N/m. The prototype is rapid prototyped by Shapeways using the Frosted Extreme Detail material, which has a tensile modulus of 1463 MPa and a flexural strength of 49 MPa.

The outer spring in our previous prototype [193] was replaced by a flexible sleeve that continues to separate the tendons from the environment but provides the additional advantage of a waterproof interface to protect the magnetic field sensor. The sleeve was rapid prototyped using Stratasys Object500 Connex 3 from the TangloBlackPlus FLX980 material, that can sustain approximately 200% elongation and has a tensile strength of 115-220 MPa. The latest design retains the advantages of smooth shape change and a compliant interface of our previous prototype. Tendon-driven mechanism was again employed so that the main robot body did not have to house any actuators and the heating of SMA would not

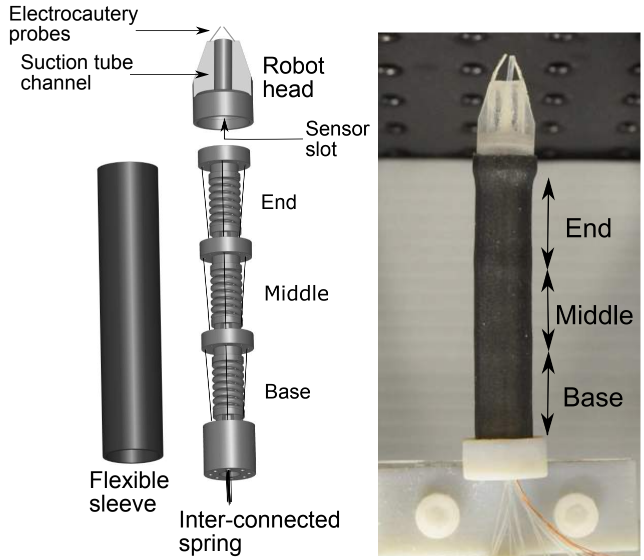

(a) (b)

Figure 4.3: (a) Schematics of the inner spring with three segments, rubber sleeve, and the robot head (b) Fully assembled MINIR-II prototype

cause distortion in the MR images. Each robot segment has two pairs of tendons terminated at its corresponding disk that would produce two-DoF bending. The central tendon routing configuration was used in the current robot to allow independent segment control [193].

4.4.2 Experiment

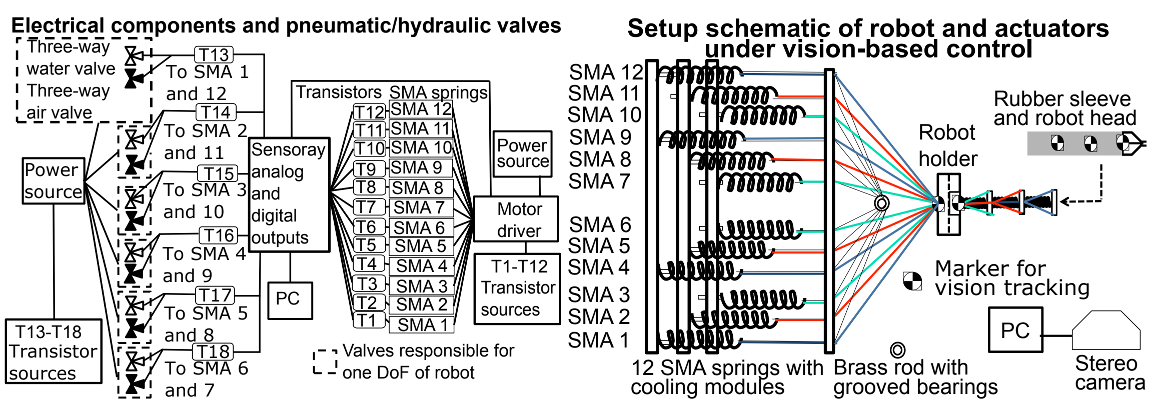

(a) (b)

Figure 4.4: (a) Electrical and pneumatic/hydraulic components involved in the experimental setup (b) Schematic of vision-based experimental setup for actuating 6 DoFs of MINIR-II

We envision that the MINIR-II would be controlled under real-time MR image feed-

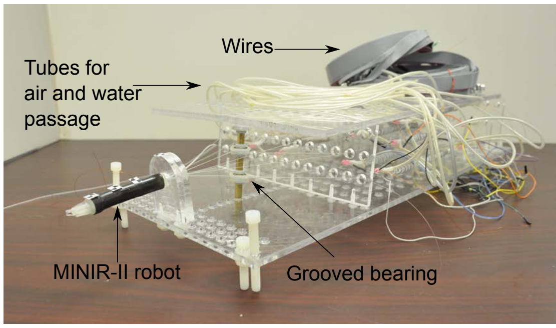

(a)

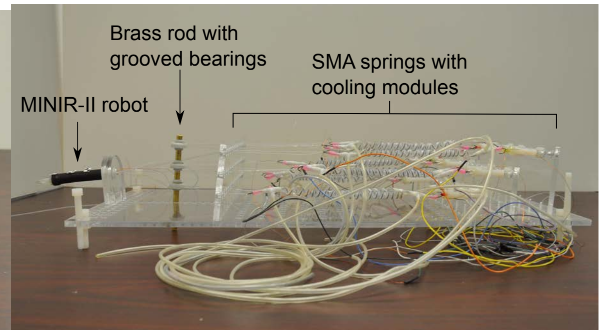

(b)

Figure 4.5: (a) Robot platform with the spring-based robot, twelve cooling module-integrated SMA springs and tubes (b) Side view of the robot platform made out of laser-cut acrylic

back. Since we were not using MR images at this point to control the robot motion, we implemented a vision-based control using a stereo camera to use the camera images as feedback to evaluate the performance of our 6 DoF robot. The schematic of the entire robotic system is shown in Fig. 4.4. The actuator platform was manufactured from laser cut acrylic plates, as shown in two different viewpoints in Figs. 4.5(a) and 4.5(b). For actuating twelve SMA springs which control three robot segments, we used six water valves and six air valves. Twelve transistors were used to determine the SMA spring actuator that would be heated by the motor driver (power source). A brass rod with three grooved plastic bearings were used, as seen in Figs. 4.5(a) and 4.5(b), to provide a direct connection between each antagonistic pair of SMA springs for each DoF. This was an important feature of the SMA actuation system for this spring-based flexible robot to prevent it from getting compressed due to the unexpected tension in the SMA springs. In this way, the non-heated SMA spring always applies zero tension on the robot segment. The entire experimental setup consists of a water reservoir, twelve three-way valves (12V DC Solenoid Valve, Electricsolenoidvalves.com, New York, USA), an actuator platform with twelve SMA spring actuators and the robot, an air compressor, an Analog/Digital Input/Output board (Model 826, Sensoray, USA), and a vision camera (MicronTracker, Claron Technology Inc., Canada).

We used vision markers of 8 mm diameter to allow accurate tracking of each robot joint.

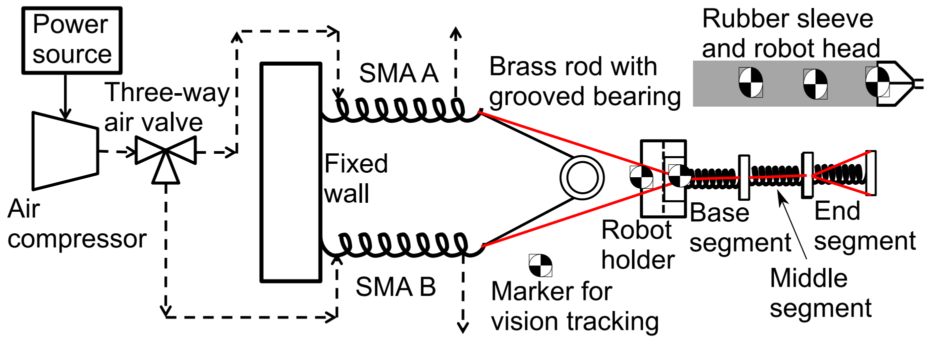

Figure 4.6: Schematic of the experimental setup that uses compressed air to force cool one pair of SMA springs for one-DoF motion of the end segment

The four markers (in the same plane) were respectively attached to the base of the robot, the end of the base segment, the end of the middle segment, and the robot tip. A virtual vector is formed between two adjacent markers and the angle subtended by two vectors determines the angular displacement of the corresponding robot segment. The angular displacement was considered as the vision feedback variable in this active vision control system and Proportional+Integral (PI) control was implemented to achieve set point tracking. We used the robot platform and vision-based control to perform all the characterization experiments for different control parameters as well as the experiments that compare the robot performance under forced water and forced air cooling for four motion amplitudes, namely $\pm5°$, $\pm10°$, $\pm15°$, and $\pm20°$. Two force sensors are added to the experimental setup to measure the force exerted by each of the two SMA springs that are in antagonistic configuration.

In the characterization experiments, we varied one parameter and kept the other parameters at the control state. Step inputs of $\pm10°$ were applied to the end robot segment.The same experimental setup, as shown in Fig. 4.5, was used during the forced air cooling experiment, except that the water reservoir and valves used for flowing water were removed. Compressed air (high speed air), maintained at gauge pressure of 25 psi, instead act as the cooling medium during the experiment. The schematic for the forced air cooling setup is shown in Fig. 4.6.

4.5 Results and Discussion

In all the characterization experiments, a target amplitude of 10° angular displacement of the robot was implemented and the end robot segment was actuated. The raw data of angular displacement vs time is plotted in the characterization graphs while the important information from the graphs are analyzed and collected in the table under each graph. Delay time is the time it takes for the robot (not the SMA spring) to start moving after the control signal is provided to heat the SMA spring. Travel time is the time it takes for the robot to move to the target amplitude and can either be rise time or fall time. The robot frequency is defined as the reciprocal of the total time required to travel to a target amplitude (rise time) and back (fall time). The average robot speed is calculated by multiplying the distance traveled by the robot tip in a complete motion cycle, which covers one rise and one fall time, with the average robot frequency. The exact distance traveled by the robot tip is stated in each table. The parameters implemented in the experiment are clearly stated under each table. It should be noted that only the robot motion data between 30 s and 110 s is considered in the analysis. Overall, the robot speed achieved under the new actuation mechanism is more than 1 mm/s, which is within the 0.5 mm/s-5 mm/s range reported in the literature. Besides the robot displacement that was tracked by the vision camera, temperature of the SMA spring was also recorded and was discussed and compared with the model for characterization parameters such as current, water flow rate and pre-displacement.

4.5.1 Effect of Current and Water Flow Rate

As shown in Fig. 4.7(a), higher current reduces both the average delay time and travel time and the robot achieved an average robot speed of 1.3 mm/s at 3.8 A. As shown in Fig. 4.7(b), our model has produced matching temperature behavior as the experiment for each current, especially in terms of the rate of change of temperature (overall slope) and

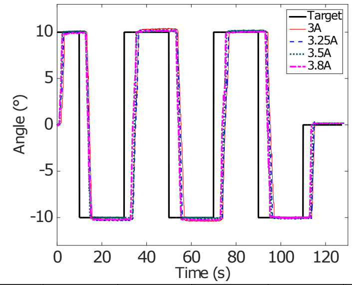

Current (A)	1st Rise (s)		1st Fall (s)		2nd Rise (s)		2nd Fall (s)		Ave robot motion time (s)		Ave robot frequency [2 x Ave travel time]$^{-1}$ (Hz)	Ave robot speed [13.3 mm x Ave freq] (mm/s)
	Delay	Travel	Delay	Travel	Delay	Travel	Delay	Travel	Delay	Travel		
3	3.7	6.4	3.9	6.8	4.1	6.8	4.2	7.0	4.0	6.8	0.074	1.0
3.25	3.9	6.5	3.5	6.1	3.9	6.6	3.8	6.2	3.8	6.4	0.079	1.1
3.5	3.7	5.8	3.3	5.5	3.5	5.8	3.5	5.8	3.5	5.7	0.088	1.2
3.8	2.7	5.3	3.0	5.4	3.0	5.4	3.0	5.1	2.9	5.3	0.095	1.3

Parameters: 1150 mm³/s, 50 mm, 15 psi, 10° Amplitude

(a)

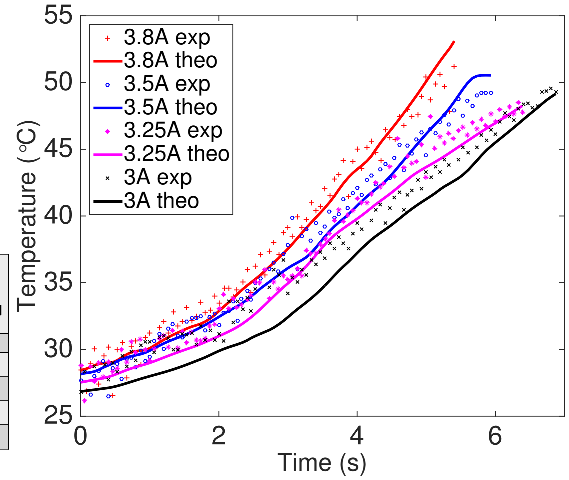

(b)

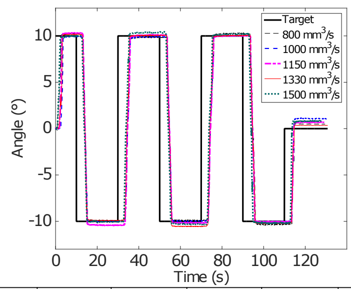

Flow rate (mm³/s)	1st Rise (s)		1st Fall (s)		2nd Rise (s)		2nd Fall (s)		Ave robot motion time (s)		Ave robot frequency [2 x Ave travel time]$^{-1}$ (Hz)	Ave robot speed [13.3 mm x Ave freq] (mm/s)
	Delay	Travel	Delay	Travel	Delay	Travel	Delay	Travel	Delay	Travel		
800	3.5	6.0	3.6	5.9	3.5	6.1	3.6	6.1	3.6	6.0	0.083	1.1
1000	3.4	6.0	3.7	6.0	3.5	5.9	3.7	5.9	3.6	5.9	0.084	1.1
1150	3.5	5.9	3.7	5.8	3.3	6.0	3.7	5.9	3.5	5.9	0.085	1.1
1330	3.3	5.5	3.5	5.8	3.3	5.7	3.6	5.8	3.4	5.7	0.089	1.2
1500	2.7	5.3	3	5.4	3.0	5.4	3.0	4.9	2.9	5.3	0.095	1.3

Parameters: 3.5 A, 50 mm, 15 psi, 10° Amplitude

(c)

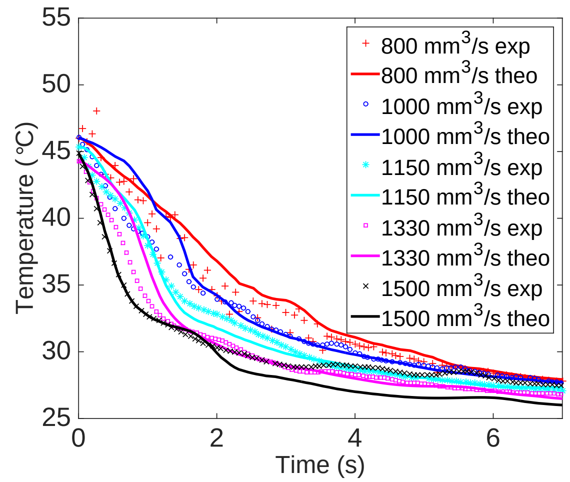

(d)

Figure 4.7: Robot motion in response to step input at various (a) currents and (b) water flow rates. Temperature change in response to step input at various (c) currents and (d) water flow rates

the final temperature.

According to analysis in Fig. 4.7(c), the average delay times and average robot speed for the water flow rates of 800 mm^3/s, 1000 mm^3/s, and 1150 mm^3/s are very similar and improved significantly under the two highest flow rates. As shown in Fig. 4.7(d), the experimental temperature profiles for the two highest flow rates are especially steep, allowing the resisting SMA spring to reach the martensite finish temperature sooner. Using the theoretical heat coefficients calculated in Fig. 4.2(a) for 1.98 mm tube diameter, which are 1.06×10^5 W/m^{2}K, 1.27×10^5 W/m^{2}K, 1.42×10^5 W/m^{2}K, 1.59×10^5 W/m^{2}K, and 1.75×10^5 W/m^{2}K for water flow rates of 800 mm^3/s, 1000 mm^3/s, 1150 mm^3/s, 1330 mm^3/s, and 1500 mm^3/s, respectively, the model proves to produce consistent temperature profiles as the experimental data. The discrepancies in the initial cooling stage and the final settling temperature for certain flow rates could be a result of the rough experimental force data used in the model and the imperfect bond between the temperature sensor and the SMA spring.

4.5.2 Effect of Pre-Displacement and Gauge Pressure

The pre-displacement characterization results, shown in Fig. 4.8(a), show that the robot average speed improves with larger SMA spring pre-displacement. This can be explained by the highest SMA heating rate and output force increase rate when it is pre-stretched by the most, as shown in Figs. 4.8(c) and 4.8(d). The delay time, however, does not show a consistent trend. According to the works of Tanaka [189], Brinson [161] and more recent works by Li *et al.* [194], higher stress in the SMA increases its transformation temperatures. Our experiment matches the theory only for the SMA spring with the smallest pre-displacement (35 mm) as it produced the shortest delay time, likely due to the SMA spring reaching its relatively lowest austenite start temperature quickest and starting to contract the soonest. One explanation for the inconsistent trend with the next two pre-displacements is that the higher heating rate of the SMA with the largest pre-displacement made up for its highest austenite start temperature. This allows the SMA with 65 mm pre-displacement to have less delay time than that with 50 mm pre-displacement. Figure 4.8(d) shows the net force exerted on the robot by the SMA springs in antagonistic configuration. The SMA with the largest pre-displacement exerted the largest force in the shortest amount time of time.

As shown in Fig. 4.8(b), clear distinction in the robot speed was observed for different gauge pressures. The highest gauge pressure led to the fastest elimination of the water in the cooling module and therefore more efficient heating was initiated earlier.

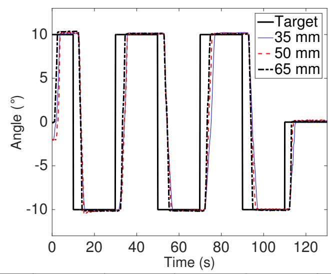

Pre-displacement (mm)	1st Rise (s)		1st Fall (s)		2nd Rise (s)		2nd Fall (s)		Ave robot motion time (s)		Ave robot frequency [2 x Ave travel time]$^{-1}$ (Hz)	Ave robot speed [13.3 mm x Ave freq] (mm/s)
	Delay	Travel	Delay	Travel	Delay	Travel	Delay	Travel	Delay	Travel		
35	1.5	5.6	2.7	7.1	1.8	7.1	2.6	7.3	2.1	6.8	0.074	1.0
50	2.5	5.7	3.0	6.3	2.2	5.7	3.1	6.2	2.7	6.0	0.084	1.1
65	2.3	4.5	2.9	5.4	2.2	4.8	2.9	4.9	2.6	5.0	0.102	1.4

Parameters: 3.5 A, 1150 mm^3/s, 15 psi, 10^o Amplitude

(a)

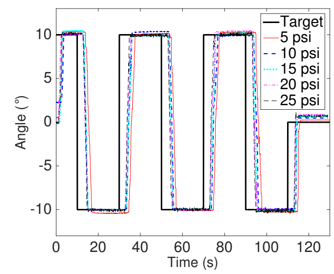

Gauge Pressure (Psi)	1st Rise (s)		1st Fall (s)		2nd Rise (s)		2nd Fall (s)		Ave robot motion time (s)		Ave robot frequency [2 x Ave travel time]$^{-1}$ (Hz)	Ave robot speed [13.3 mm x Ave freq] (mm/s)
	Delay	Travel	Delay	Travel	Delay	Travel	Delay	Travel	Delay	Travel		
5	2.7	7.5	4.6	7.0	4.7	7.5	4.8	7.7	4.2	7.4	0.067	0.9
10	3.4	5.9	3.8	5.8	3.8	6.8	3.8	6.0	3.7	6.1	0.082	1.1
15	3.5	5.7	3.7	5.5	3.4	5.7	3.7	5.7	3.6	5.7	0.088	1.2
20	4.5	5.3	3	5.4	3.0	5.4	2.9	5.3	3.4	5.3	0.094	1.3
25	3	4.7	3.2	5.1	2.9	5.1	3.0	4.8	3.0	4.9	0.10	1.3

Parameters: 3.5 A, 1150 mm^3/s, 50 mm, 10^o Amplitude

(b)

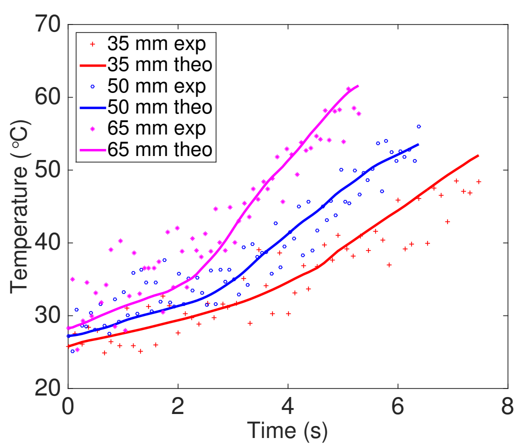

(c)

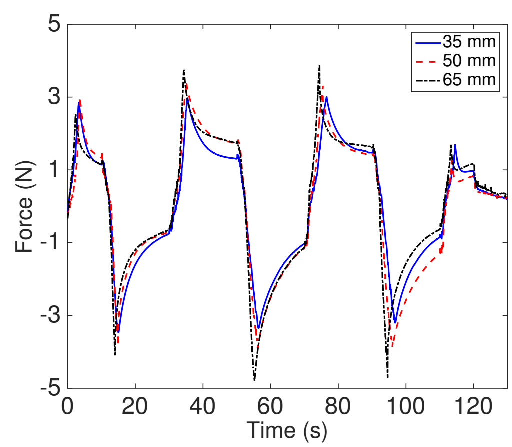

(d)

Figure 4.8: (a) Robot motion in response to step input at various SMA pre-displacements and (b) gauge pressures (c) Temperature change during one heating phase due to different pre-displacements (d) Net force acting on the robot in response to step inputs at various pre-displacements

4.5.3 Comparison between Two Cooling Media: Water and Air

Table 4.3: Performance comparison between water (our proposed mechanism) and air for different motion amplitudes

Cooling medium	Average Robot Speed (mm/s)			
	5°	10°	15°	20°
Water	0.82	1.28	1.42	1.73
Air	0.34	0.53	0.68	0.80

We investigated the effect of different cooling media on the robot speed at four motion amplitudes. The average robot speed when water was the cooling medium consistently more than doubled that when high speed compressed air was used, as shown in Table 4.3. There is however only slight difference in the delay time. The robot speed also improves under both cooling media when the motion amplitude becomes larger and it reaches 1.73 mm/s under forced water cooling at amplitude of 20°. This is due to the non-linear SMA heating behavior with smaller initial heating slope.

4.6 Summary

We developed an SMA spring-actuated robotic system with active water cooling to enable real-time control of SMA spring actuators. Due to the limitation in actuation bandwidth of the SMA material, we implemented a new actuation mechanism to operate the previously developed cooling module-integrated SMA springs. Water was used as the coolant during the cooling phase and compressed air as the medium to force out water during the heating phase. We modeled the thermal behavior of the SMA spring that was operated under the new mechanism at different currents, water flow rates, and SMA pre-displacements. Gauge pressure of the compressed air was another important control parameter to optimize the robot speed. Experimental characterization was performed to determine the effect of each parameter on the robot speed and experimental data was used to verify the model. Comparison between water and air as the cooling media also demonstrated that water consistently provided superior performance in terms of the robot speed. Our new actuation mechanism had been shown to allow the robot to consistently achieve average robot speed of more than 1mm/s, which is within the speed range reported in literature for neurosurgical robots. The results from the current work served as important foundation for the tuning of the control parameters to adjust the robot speed in an actual surgical procedure.

CHAPTER 5

STIFFNESS MODULATED SPRING-BASED FLEXIBLE ROBOT

5.1 Background and Research Objective

It is generally agreed that robots with high flexibility are safer for accessing a deep-seated brain tumor. However, these flexible robots may lack the stiffness and strength advantages that rigid tools provide [195]. There are a number of occasions that a rigid/stiffened robot shaft can be advantageous for. For instance, a stiffened robot backbone would allow the robot to be inserted and smoothly advanced forward without undesired buckling and bending. A stiffened backbone would provide a more stable support structure for the actuated segment, which in most cases would be the end segment, especially for large bending angles. When a proximal segment is being actuated, the distal segment can be stiffened to avoid undesirable deformation from external disturbances that would change the pointing angle of the end effector.

Thus, robots with tunable stiffness have been explored for the next generation of manipulation devices [196, 197]. Structural stiffening has been applied mainly though angle locking and curve length locking. Many works [198, 199, 200, 201] proposed similar discrete angle locking concept, where an actively steerable distal guide is controlled using cables that run through the rest of the flexible proximal portion. Once the distal guide is steered into a certain direction and all the cables are pulled, the segments are compressed together, allowing the passive proximal portion to follow the curve trajectory formed by the distal guide. The normal force between the segments prevents the segments from sliding over one another, thus locking the overall shape of the robotic endoscope. Curve length locking mechanism has been employed to create an outer sheath that switches between rigid and flexible mode [202]. It is a different shape locking method that connects sliders and stoppers pneumatically to fix inner and outer bending curves of the flexible sheath.

Stiffness tunable materials, such as magnetorheological [203] fluid, have also been mainly in rehabilitation robotics to develop grippers and exoskeleton that changes actuation force at the end effectors. When a magnetic field is applied, the magnetorheological fluid, which is a suspension of microparticles, changes its rheological properties to provide a gripping surface with different compliance level appropriate for items of a variety of shape and hardness. Solder-based phase change materials (PCMs) [204] have been used to thermally lock and unlock the joint of a centimeter-scale robot to allow locomotion. The thermoplastic polymer such as thermophastic shape memory alloy polymer has also been used to provide rigidity control in medical catheters [205] and endoscopes [206]. The thermophastic polymer transitions between a rigid state and a compliant state as it is cooled below and heated above its glass transition temperature. Loeve $et\ al.$ passed fluids of different temperatures through the channels in their ”plastolock” which can be shaped into a rod or an overtube to change the compliance of the endoscope. In the area of microelectronics, shape memory polymer (SMP) was embedded in an elastomer layer that also contains an elastic Joule heating element made out of gallium indium alloy. As the SMP is heated beyond its glass transition temperature by the flexible microcoil heater, the elastomer composite softens and deforms reversibly. The transition temperature of 62° is probably too high for in-body applications but the combination of smart actuators and liquid embedded technology have high potential in making stiffness tunable microscale flexible surgical robots.

Granular jamming has recently been used as the stiffness tuning mechanism in various soft robots. A volume of granular materials such as coffee or dry sand can transition between a compliant state and a solid (jammed) state by removing and applying a vacuum condition to the volume. A thin-walled flexible tubular manipulator [207] was developed using ”layer jamming” that makes use of friction between the spiral plastic layers forming the thin wall. Under a maximum 101kPa vacuum pressure, the manipulator can resist a maximum force of 5 N. The stiffness tunable property, along with Its compact size and hollow geometry, makes the manipulator suitable to be used in minimally invasive surgical applications.

The STIFF-FLOP surgical manipulator [208, 209] is an elastomeric cylinder/tube that has three equiradially-spaced pneumatic chambers [210, 211] that allow elongation and omnidirectional bending and a central granular jamming chamber. The undesired radial expansion in every direction is restricted by a novel braided sheath configured in bellows shape that allows free bending and elongation motion. The stiffening capability to resist lateral force is maximum when the robot module is in the straight configuration and decreases when the bending angle of the robot module increases.

Biologically inspired [212] by the structural organization and mechanical principles of eukaryote flagellum, a 6-mm diameter dexterous manipulator is constructed using interlocking polymer fibers. It has an open lumen of 4 mm diameter that allows the passage of a variety of surgical instruments. The friction between fibers can be tuned to modulate the robot stiffness in certain degrees of freedom. More recently, Kang et al. [213] developed an interesting and novel continuum robot that consists of the leading units (disc) and follower units (disc) with shape lockers for each segment. The follower unit is controlled by distinct rods from the leading unit's rod and has shape lockers to hold the rod that is connected to the leading unit. Thus, once the leading unit forms the desired shape, the follower unit locks the rod and maintain the shape, therefore providing the stability for tool manipulation in a surgical procedure.

There are many other research [214] that have made use of smart materials, including magneto-rheological fluid [215] and electro-rheological fluid [216], polymers [204, 206, 217, 218, 219], composites [220], jamming [197, 207, 221, 222, 223, 224, 225, 226, 227, 228], locking [202, 212], and modular mechanism [209].

The importance of a stable tool operation has to be underscored in the robotic neurosurgery due to the critical structures that the robot may come into contact with. Following our previous work on the fully 3-D printed plastic spring-based MINIR-II robot in Chapter 2 [193], we proposed a new robot design for selective actuation and stiffening of individual robot segment using shape memory alloy (SMA), a smart actuator that responses to temperature changes. We replaced the plastic spring segments of MINIR-II with the SMA springs and rapid prototyped customized rod-shaped disks to come up with a local stiffness tunable MINIR-II. The stiffening of the non-actuated robot segments would provide the necessary rigidity to a flexible robot and therefore stability to the brain tumor removal procedure. Inspired by the work of Choi $et\ al.$ [229], we presented a local stiffness model of the SMA spring backbone using the beam model. Different from Choi $et\ al.$ who derived the stiffness model of a spring from a beam that has equivalent axial stiffness as the spring, we developed a modified beam model for each of our robot segment that consists of an SMA spring and a rigid rod. The modified model does not make the assumption of equivalent axial stiffness and instead contains spring-related parameters such as flexural rigidity and shear rigidity of the SMA spring based on Wahl's spring theory [123]. We explored different combinations of tendon tensioning and segment stiffening to investigate the resultant stiffness of the robot segment and intend to verify the practicality of the robot in a gelatin phantom under MRI. Part of the work described in this chapter was done in collaboration with the former post-doc in the lab, Dr. Yeongjin Kim.

5.2 Robot Design

The MINIR-II has an inner inter-connected SMA spring backbone that is divided into three segments (see Fig. 5.1(a)) for the multiple DoFs required in a neurosurgical procedure [193]. Each segment consists of a 3-D printed disk and a Nitinol SMA spring (Flexmet, Belgium), as shown in Fig. 5.1(b) and there is a continuous lumen throughout the robot length. Induced by heating and cooling, SMA transforms between two phases called austenite and martensite, which have different material properties. At high temperature, SMA exists in the austenite phase, usually with a body-centered cubic crystal structure. It only deforms by slipping of the lattice structure (bonds between atoms are broken) and therefore has a higher Young's modulus. At lower temperature, SMA exists in the martensite phase, usually with a face-centered cubic crystal structure. It deforms by detwinning (rearrangement of atoms without breaking the bonds) and therefore has a lower Young's modulus. The SMA springs allow the robot to have segments with independently modulated stiffness. As shown in Fig. 5.1(b), together with the outer plastic spring which acts as a flexible shell, the entire robot is assembled into a compact robotic device. The robot is designed to have the workspace to cover deep brain tumors which have an average diameter of less than 40 mm [111] and each segment should achieve a bending angle of at least 45°. It is important to note that the bending angle is relative to the orientation (surface normal vector) of the prior disk. Hence the change in bending angle causes twice the change in the surface normal of the subsequent disk. For example, a bending angle of 45° results in a 90° orientation change of the subsequent disk as illustrated in Fig. 1(c). The diameter was selected so that the entire robot can fit inside an existing endoport (11-13 mm) used in microsurgical resection of deep-seated brain tumor [112, 113]. The lumen through the center of the robot has to be at least 4 mm to have enough room for the electrocautery wires, and suction and irrigation tubes. Therefore, the MINIR-II robot has a 65 mm length, an outer diameter of 12.6 mm, and a lumen diameter of 4.1 mm to cover the required workspace, fit in the existing endoport, and to house the required wires and cables with the electrocautery probe embedded at the tip of the end segment of the robot.

The inner inter-connected spring backbone is the main structure of the robot and offers high flexibility and dexterity since it is able to change its compliant body into shapes that interact more gently with the brain environment. The spring length change may influence the stiffness modeling of our spring segments. To minimize the influence, we used SMA springs which have been heated to fully austenite phase so that the springs are fully contracted. Then, they are naturally cooled to the room temperature martensite phase, after which no intentional stretching is applied to the springs. Therefore, the SMA springs that form the inner backbone of the robot have minimal gaps between the spring coils. When the SMA spring is heated during an application to modulate its stiffness, the robot length changes from 70.49 mm to 70.36 mm. The 0.18% reduction is considered negligible, as shown in Fig. 5.1(b). Each thin disc between the segments contains multiple holes on its periphery for termination of the tendon wires and is vital for maintaining the robot shape as well as providing the moment arm for respective segment motion. The outer spring is covered with a layer of vinyl wrap that prevents contact between the SMA spring robot segments and the brain tissue. The surface temperature of the robot was measured to be less than 35° over a period of 5 minutes that the SMA spring backbone was maintained at 47°, the austenite finish temperature. This is lower than the body temperature and is siginficantly lower than the brain necrosis temperature of approximately 44°C [230].

The tendon routing process in a multi-segment continuum robot is complex and actuation of one robot segment can cause deflection of the other robot segments. As the number of segments in the robot increases, it is even more critical to have motion decoupling between the various segments. We explored two different tendon routing configurations as shown in Fig. 5.2. Figure 5.2(a) led to significant coupling between the robot segments due to the straight tendon routing along the outer rim of the disks. In the configuration shown in Fig. 5.2(b), the tendons were routed along the central axis of the inner inter-connected spring and start branching out to the respective robot segment at the base of the corresponding segment. For instance, a tendon starts branching out at Disk 3 and are terminated at Disk 4 for end segment actuation as shown in Fig. 5.2(c). This tendon routing configuration minimizes coupling between segments and potentially allows independent segment control of the robot segments. This is also one of the unique features that differentiate the MINIR-II robot from other tendon-driven continuum robots [115, 116, 120]. In the previous works, a coupled motion existed due to the motion of three tendons routed similar to the configuration in Fig. 5.2(a). The effectiveness of the centrally routed tendon configuration would be assessed in section V for bending angles of up to 45° in the actuated segment. Funda-

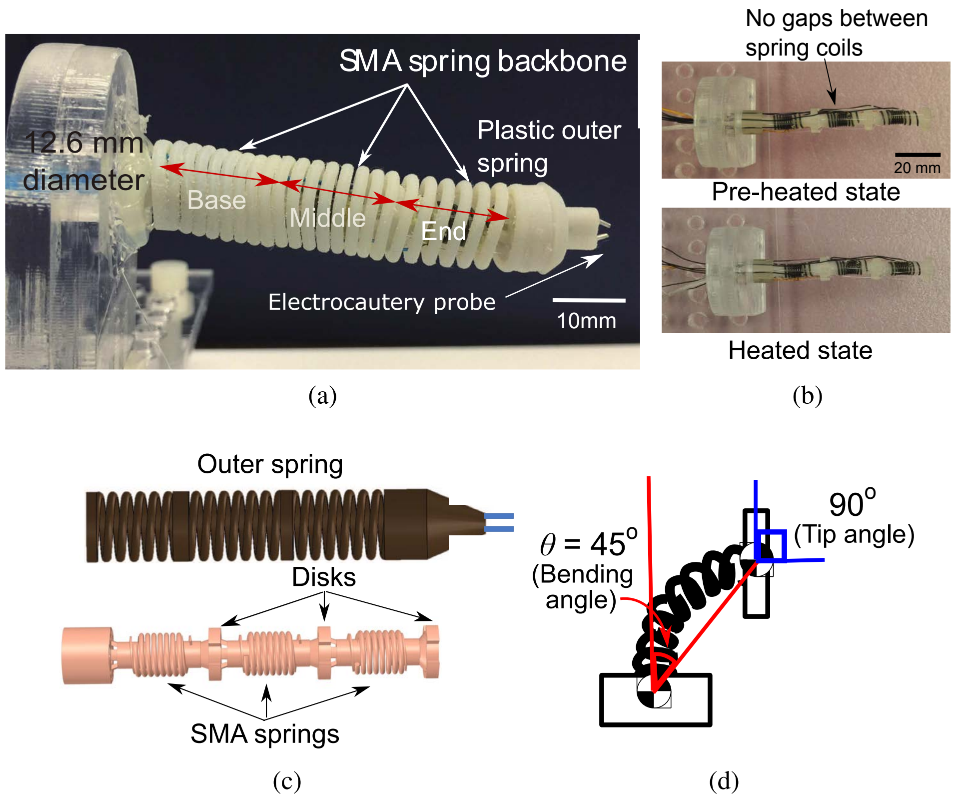

Figure 5.1: (a) Spring-based continuum robot with three segments (b) Pictures showing the length of SMA spring before it was heated and during heating (c) Complete CAD model of the continuum robot with outer spring and inner inter-connected spring (d) Illustration showing that the surface normal of the end segment disk has an orientation change of 90° that is twice the bending angle of 45°

mentally our design allows for independent control of even larger range of motion but due to material properties and the pitch of the SMA backbone spring, bending angles beyond 45° are yet to be investigated and in any case, beyond the scope of our requirement. As the angle increases beyond 45°, we can expect more coupling due to geometrical non-linearity and possibly also the lack of sheath around the tendons.

The tendon routing configuration shown in Fig. 5.2(b), not only has the potential to allow independent segment control but also independent segment locking using tendons. Many continuum robots that have a flexible backbone [23] are actuated by tendon driven mechanism using an external actuator due to the limited space in the robots. These robots usually have low stiffness and are not desirable due to the lack of stability required in many

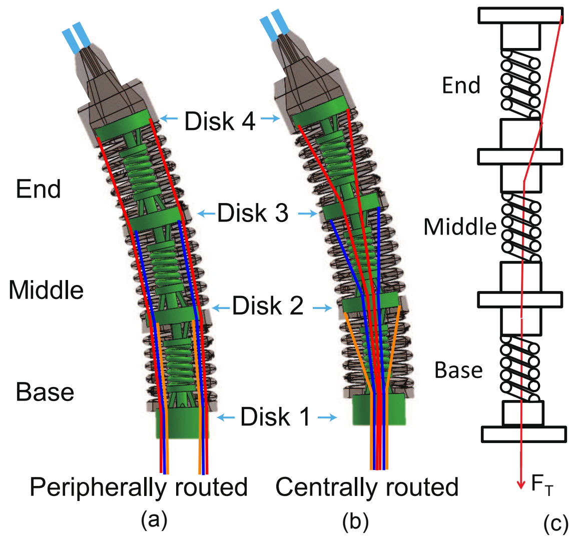

Figure 5.2: Different configurations of tendon routing mechanism in the robot: (a) Peripherally routed tendon configuration (b) Centrally routed tendon configuration for independent segment control (c) Illustration of end segment actuation for motion in one direction, a tendon starts branching out at Disk 3 and is terminated at Disk 4.

surgical procedures. In a case illustrated in Fig. 5.3(b), where there is undesirable deformation of the end segment due to bending of the middle segment, it is difficult to achieve independent stiffening of a specific robot segment (i.e. end segment) without affecting the desired motion of an actuated segment (i.e. middle segment). Continuum robots that adopt peripherally routed tendon configuration can only have their entire robot body stiffened by tensioning all the tendons, as shown in Fig. 5.3(a). On the other hand, by tensioning a specific pair of tendons in a centrally routed tendon configuration, we can lock one segment without interfering with the motion or compliance of the other segments.

As shown in Fig. 5.4, SMA springs are utilized as the inner spring backbone in our robot and the stiffness of an individual segment can be actively controlled by changing the temperature of the corresponding SMA spring backbone which has an attached resistance temperature detector (RTD, Alpha Technics, CA, USA). Thus, combining independent segment locking by tendon tensioning and independent SMA backbone stiffening will provide more rigidity to a specific segment without interfering with the motion of the other segments. As shown in Fig. 5.5, using our design, we intend to increase the stiffness of only

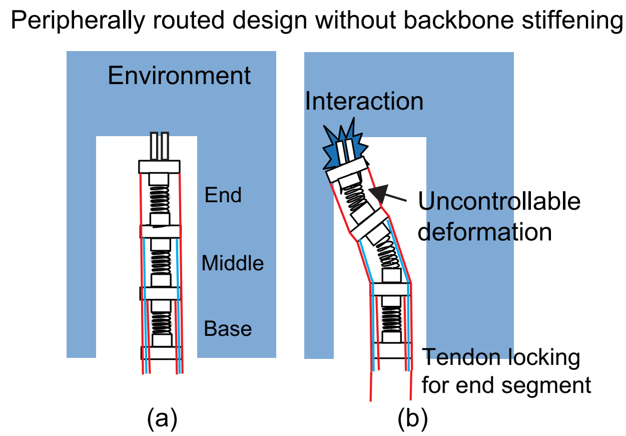

Figure 5.3: (a) Home configuration of the robot with regular spring backbone and peripherally routed tendon configuration (b) Middle segment actuation causes undesirable deformation of the end segment with the environment. Note: The outer spring is not shown in these schematics.

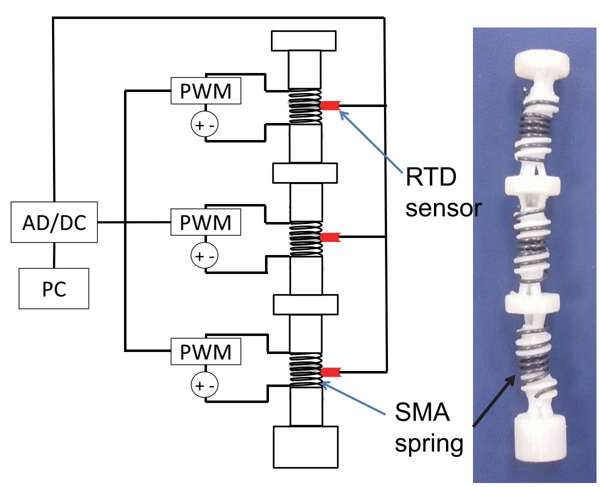

Figure 5.4: Design of active local stiffness control with SMA spring backbone. Stiffness of a segment is controlled by controlling the temperature changes of the corresponding SMA spring backbone. Note: The outer spring is not shown in this schematic

the end segment to eliminate the undesirable deformation while still allowing the desired motion in the middle segment. In Fig. 5.6, by selectively stiffening the non-actuated segments through tendon locking and SMA stiffening, ideally, only the actuated segment will bend while the other segments stay rigid. In this way, a more robust motion of the actuated segment will be generated.

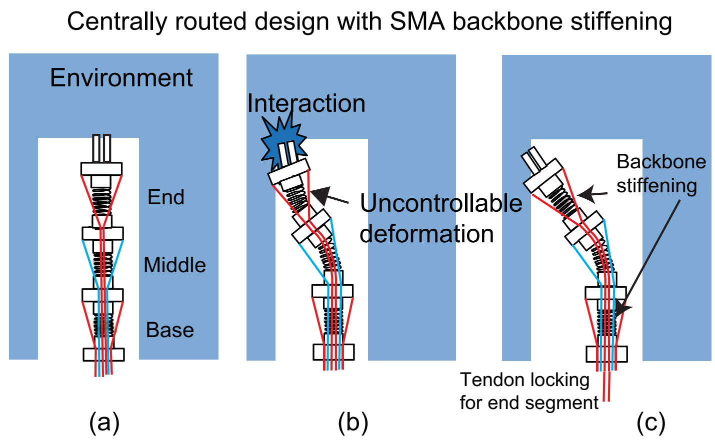

Figure 5.5: (a) Home configuration of the robot with the SMA spring backbone and centrally routed tendon configuration (b) Middle segment actuation results undesirable deformation of the end segment with the environment (c) SMA backbone stiffening and independent segment locking of the end segment resolve the undesirable deformation without interfering with the motion of the middle segment. Note: the outer spring is not shown in these schematics.

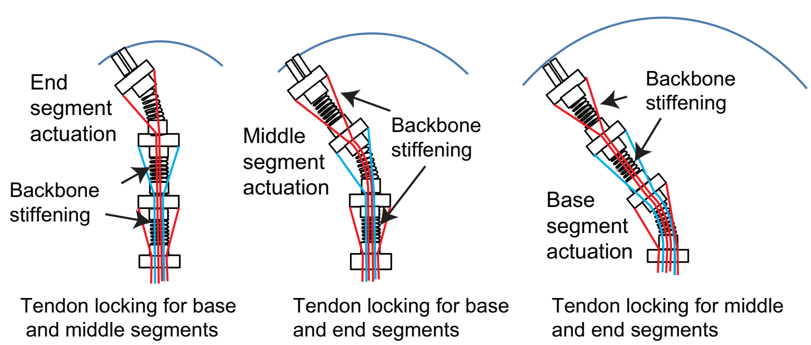

Figure 5.6: Only the actuated segment would bend by selectively stiffening the other two segments through tendon locking and SMA backbone stiffening. Note: The outer spring is not shown in these schematics

5.3 SMA Spring Bending Stiffness Model

To model the relationship between the resistive force and the lateral deflection of a robot segment, consisting of a spring and a rod, we use a modified cantilever beam model [123] that takes into account the flexural rigidity as well as shear rigidity of the SMA spring when a point load is exerted at the tip of the robot segment. This model is still based on the assumption that the slope or bending angle of the spring lateral deflection is small. The model does not utilize the actual complex loading condition of the robot in an actual neurosurgical application. Instead, more importantly, it is used to exhibit how the stiffness of the robot segment can be modulated when the elastic modulus of the SMA spring changes due to temperature variation.

Figure 5.7 shows a single round-wire SMA spring backbone with mean spring diameter, D, and spring wire diameter, d, loaded by a resistive force, F_k. Since the shear modulus of the SMA backbone determines the relationship between lateral deflection and the resistive force and there is an order of magnitude difference in the modulus value of the outer and inner springs, we ignore the stiffness contribution of the outer spring in our model. When the resistive point force is applied to cause lateral displacement, y, at the tip of the rod, both an internal moment, M, and an internal shear force, V, act at the end of the spring. As we need to determine the individual contributions to lateral displacement, y, at the tip of the rod, we separate a segment into two distinct components (a spring and a rod). Using static analysis, the internal moment and the shear force can be determined as follows:

$$M = F_k l_r \tag{5.1}$$

$$V = F_k \tag{5.2}$$

where l_r is the length of the rod. The moment, M, causes a spring deflection, $\delta_{s_{(Moment)}}$, that can be obtained from the beam model. The shear force leads to a spring deflection, $\delta_{s_{(Shear)}}$, that consists of two components: one component due to the deflection of the beam model and the other component due to deformation of individual spring coils. Note that the flexural rigidity of a beam, normally represented by EI (E: Young's modulus, I: Moment of inertia), is replaced by the flexural rigidity of a spring, β [123].

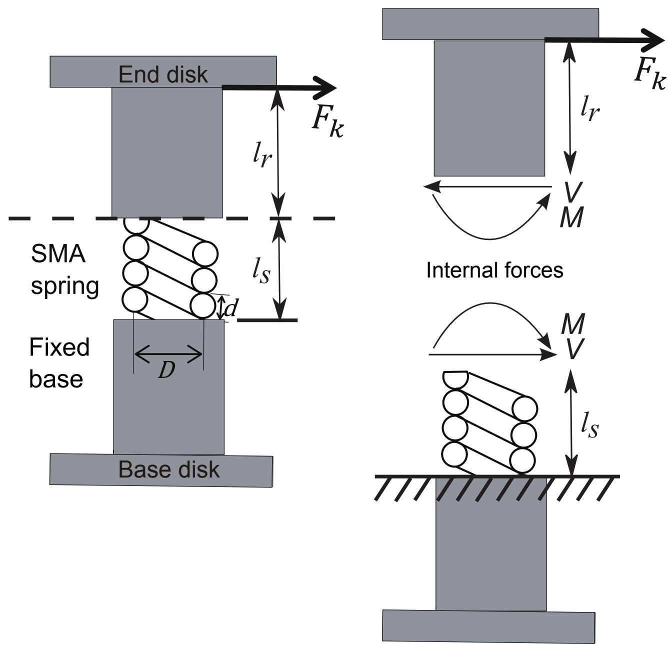

Figure 5.7: Static analysis of the robot segment modeled as a beam where V and M are the internal forces

The spring deflection at its tip, δ_s, can therefore be expressed as the sum of the deflection due to the moment and the deflection due to the shear force.

$$\begin{aligned}\delta_s &= \delta_{s_{(Moment)}} + \delta_{s_{(Shear)}} \\ &= \frac{Ml_s^2}{2\beta} + (\frac{Vl_s^3}{3\beta} + \frac{F_k l_s}{\gamma}) \\ &= \frac{F_k}{6\beta}(3l_r l_s^2 + 2l_s^3) + \frac{F_k l_s}{\gamma} \qquad (5.3)\end{aligned}$$

where l_s and γ are the length and the shear rigidity of the spring, respectively. β and γ are given by [123]:

$$\beta = \frac{2l_s E_s I_s G_s}{\pi n R(2G_s + E_s)}; \gamma = \frac{l_s E_s I_s}{\pi n R^3} \tag{5.4}$$

where E_s, I_s, G_s, R, and n are the Young's modulus, area moment of inertia, shear modulus, mean spring coil radius, and the number of active coils of the SMA spring, respectively. The area moment of inertia of the spring is given by:

$$I_s = \frac{\pi r^4}{4} \tag{5.5}$$

where r is the wire radius of the SMA spring. Substituting β and γ into Eq. (5.3), we obtain:

$$\delta_s = F_k\{\frac{\pi n R(2G_s + E_s)(3l_r l_s + 2l_s^2) + 12\pi n R^3 G_s}{12 E_s I_s G_s}\} \tag{5.6}$$

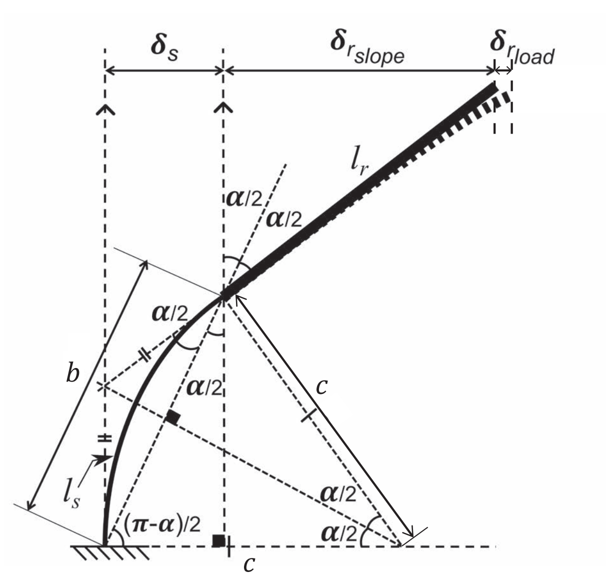

Figure 5.8: Kinematic relationship to determine the deflection of the rod

Furthermore, the shear modulus and the Young's modulus of the SMA spring can be determined by the SMA temperature which relates with martensite volume fraction, ξ.

Martensite volume fraction determines the shear modulus, G_s and Young's modulus, E_s, of the SMA spring through the following relationship:

$$G_s(\xi) = G_M + \xi(G_A - G_M) \tag{5.7}$$

$$E_s = 2G_s(1 + \nu) \tag{5.8}$$

where G_A, G_M, and ν are the shear moduli in austenite phase and martensite phase, and the Poisson's ratio, respectively. In our case, $\nu = 0.3$. The martensite volume fraction of SMA ranges from 0 (fully austenite) to 1 (fully martensite), depending on the temperature of the SMA. Martensite volume fraction is expressed as [161]:

$$\xi(T) = \frac{\xi_0}{2}\left\{cos\left[\frac{\pi}{A_f - A_s}\left(T - A_s - \frac{\sqrt{3}\tau}{C_A}\right)\right] + 1\right\} \tag{5.9}$$

where C_A is a material parameter. A_s, A_f, ξ_0, and τ are the austenite start temperature, austenite finish temperature, initial martensite volume fraction, and direct shear stress, respectively. As an approximation, the torsion moment due to the lateral force, F_k and the shear stress due to the torsion moment are given by [123]:

$$M_t = F_k(l_r + \frac{l_s}{2}) \tag{5.10}$$

$$\tau = \frac{16F_k(l_r + \frac{l_s}{2})}{\pi d^3}\frac{4a - 1}{4a - 4} \tag{5.11}$$

where a=D/d, is the spring index. In our case, $a = 6.6$. The theoretical model in this study was computed with parameters found in the work of Cheng and Desai [135] ($G_A = 29.57$ GPa, $G_M = 14.12$ GPa, $C_A = 12.81$ MPa/$°C$).

We then determine the slope at the tip of the spring, α (refer to Fig. 5.8) using the assumption that the spring has a constant curvature throughout its length. In the actual system, there are no gaps between the coils because the SMA backbone is heated to a temperature above the austenite finish temperature and cooled down before every experiment. We assume that the arc length of the spring does not change during the lateral bending. As shown in Fig. 5.8, δ_s is related to chord b through the following equation:

$$\delta_s = b \; sin(\alpha/2) \tag{5.12}$$

Chord b can be obtained from the geometrical relationship:

$$b = 2c \; sin(\alpha/2) \tag{5.13}$$

where c is the radius of curvature of the SMA spring. The relationship between the arc length of the spring and the radius of curvature can be defined as:

$$c = \frac{l_s}{\alpha} \tag{5.14}$$

Substituting Eq. (5.14) into Eq. (5.13), we get:

$$b = \frac{2l_s}{\alpha}[sin(\alpha/2)] \tag{5.15}$$

We then substitute Eq. (5.15) into Eq. (5.12) to obtain an equation for δ_s that is a function of the arc length of the spring and the slope at its tip, α, expressed as follows:

$$\delta_s = \frac{2l_s}{\alpha} sin^2(\alpha/2) \tag{5.16}$$

Using Newton's method, we can solve for α by equating Eq. (5.6) and Eq. (5.16). α is then used to calculate the deflection of the rod due to the slope of the SMA spring. Lateral rod deflection consists of two terms: the deflection due to the slope of the spring and the deflection due to the resistive force at the tip of the rod. It can thus be written as:

$$\begin{aligned} \delta_r &= \delta_{r_{slope}} + \delta_{r_{load}} \\ \delta_r &= l_r sin\alpha + \frac{F_k l_r^3}{3E_r I_r} \end{aligned} \tag{5.17}$$

where E_r and I_r are the Young's modulus and area moment of inertia of the rod, respectively. The total deflection, y, is therefore the sum of δ_s, expressed in Eq. (5.6), and δ_r, expressed in Eq. (5.17). Thus:

$$\begin{aligned} y =& \delta_s + \delta_r \\ =& F_k \{ \frac{\pi n R(2G_s + E_s)(3l_r l_s + 2l_s^2) + 12\pi n R^3 G_s}{12 E_s I_s G_s} \} \\ &+ l_r sin\alpha + \frac{F_k l_r^3}{3E_r I_r} \end{aligned} \tag{5.18}$$

The total deflection, y, can also be expressed as:

$$y = \frac{2l_s}{\alpha} sin^2(\alpha/2) + l_r sin\alpha + \frac{F_k l_r^3}{3E_r I_r} \tag{5.19}$$

where α has to be solved numerically by equating Eq. (5.6) and Eq. (5.16). Note that using small angle assumption, the horizontal displacement due to the resistive force, $\delta_{r_{load}}$, can be approximated to be the same as the arc length caused by the deflection due to the loading at the tip of the rod.

5.4 Resistive Force Analysis from Tendon Locking

To achieve certain stiffness in the robot segment through tendon locking, we need to make sure the robot actuators can apply a sufficient amount of force to lock the tendons. Since the stiffness model relates the lateral resistive force and the lateral displacement at the robot tip, it can be related to the amount of force required by the robot actuators through the relationship between the resistive force and the tendon tension. In this section, we develop a model for the resistive force as a function of the tendon tension during tendon locking. Due to the centrally routed tendon configuration, shown in Fig. 5.2(b), there is a fundamental difference in the kinematic relationship between the bending shape and the tendon wire length. As shown in Fig. 5.9, two opposite tendons (l_1 and l_3) lie in plane B_x. Likewise, the other two tendons (l_2 and l_4) are in plane B_z. When the robot bends by an angle, α, lying on the bending plane, α can be divided as α_x and α_z.

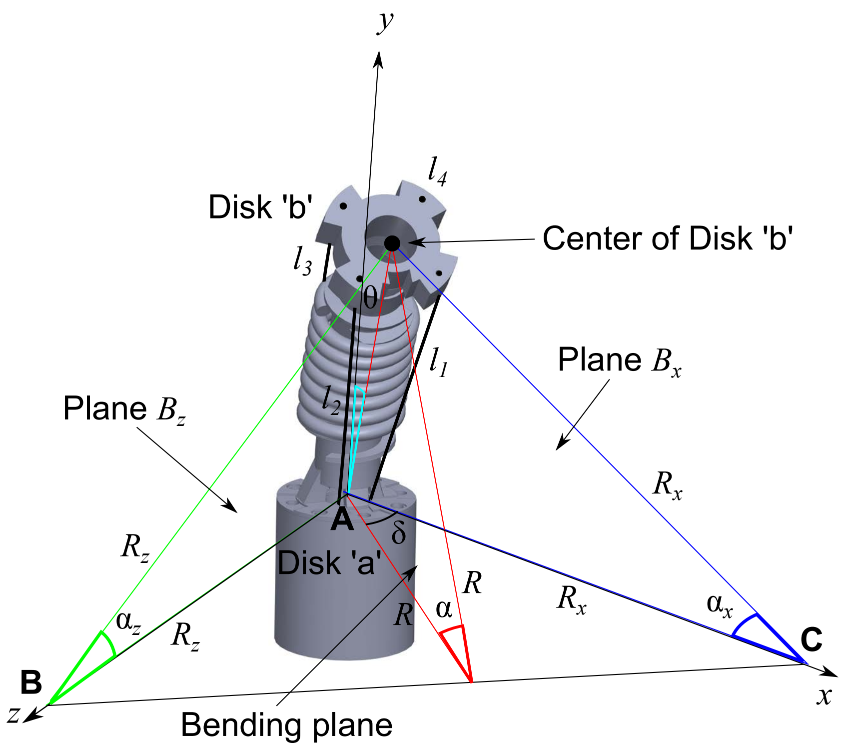

Figure 5.9: Relationship between the radius of bending arc, c, and the radius of bending arc to the x-axis and z-axis. The radius of bending arc, c, and the angle, δ, can be determined by c_x and c_z

In plane B_x, we can determine the moment arm length, H and W, by the given tendon wire length, l_3, shown in Fig 5.10. When the locking mechanism is applied on the segment, only single tendon (l_3) is affected by the lateral resistive force, F_k. The moment arm length, H and W, can be expressed as:

$$H = l_3 cos\sigma_x \tag{5.20}$$

$$W = l_{DE} + l_3 sin\sigma_x \tag{5.21}$$

where l_{DE} is the distance from D to E and σ_x is the angle shown in Fig. 5.10. The tension force F_T on the tendon can be divided into $(F_T)_x$ and $(F_T)_y$, as shown in Fig. 5.10. $(F_T)_x$ and $(F_T)_y$ are given by:

$$(F_T)_x = F_T sin\sigma_x \tag{5.22}$$

$$(F_T)_y = F_T cos\sigma_x \tag{5.23}$$

The relationship between the tension force, F_T, and the resistive force, F_k, can be expressed as:

$$\sum M^E = (F_T)_x H - (F_T)_y W + F_k H = 0 \tag{5.24}$$

$$F_k = \frac{(cos\sigma_x(l_{DE} + l_3 sin\sigma_x) - sin\beta_x l_3 cos\sigma_x)}{l_3 cos\sigma_x} F_T \tag{5.25}$$

where l_{DE}, l_3, and σ_x are determined experimentally (see Section. VI).

5.5 Independent Segment Control

Our novel tendon routing configuration allows improved control over the motion of each robot segment. To verify the independent segment control, we attached the three-segment MINIR-II to a fixed wall, as shown in Figs. 5.11(a), 5.11(b), and 5.11(c). Vision markers were attached to the disks of all segments and a vision camera called MicronTracker (ClaroNav, Toronto, Canada) was used to track the three-dimensional position of the markers at 20 Hz and an accuracy of 0.20 mm. We tracked the position of each marker while a tendon was being pulled to actuate a single segment by the heated SMA spring actuator. In this particular experiment, the heating of SMA spring actuators was performed by manually turning on and off the power supply. Figs. 5.12(a), 5.12(b) and 5.12(c) show that Disk 4,

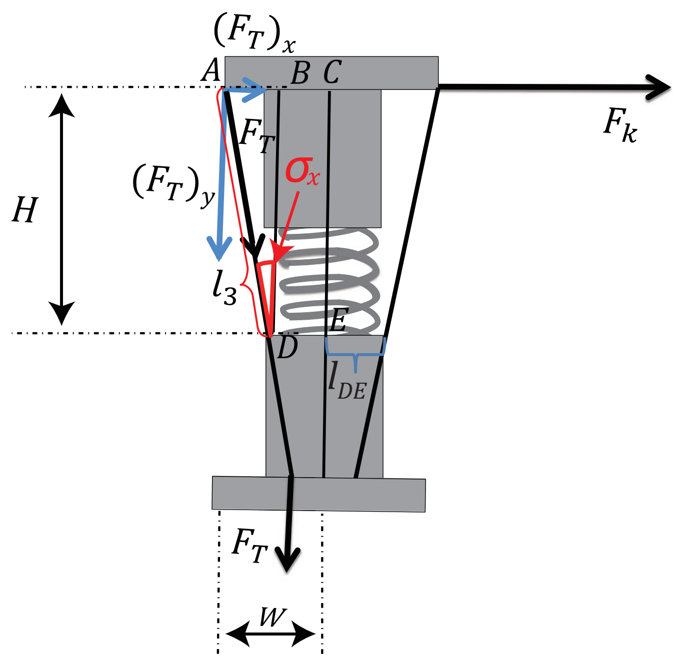

Figure 5.10: A spring model in which F_k is the resistive force generated by the lateral motion while tension, F_T, is applied on the tendon, l_3.

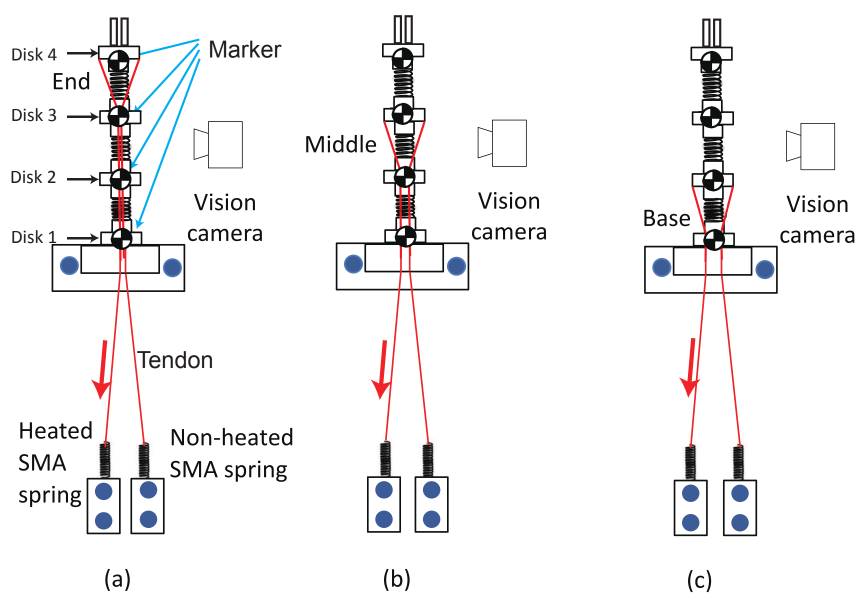

Figure 5.11: Experimental setup schematics for investigating the independent segment motion by actuating (a) only end segment, (b) only middle segment, and (c) only base segment

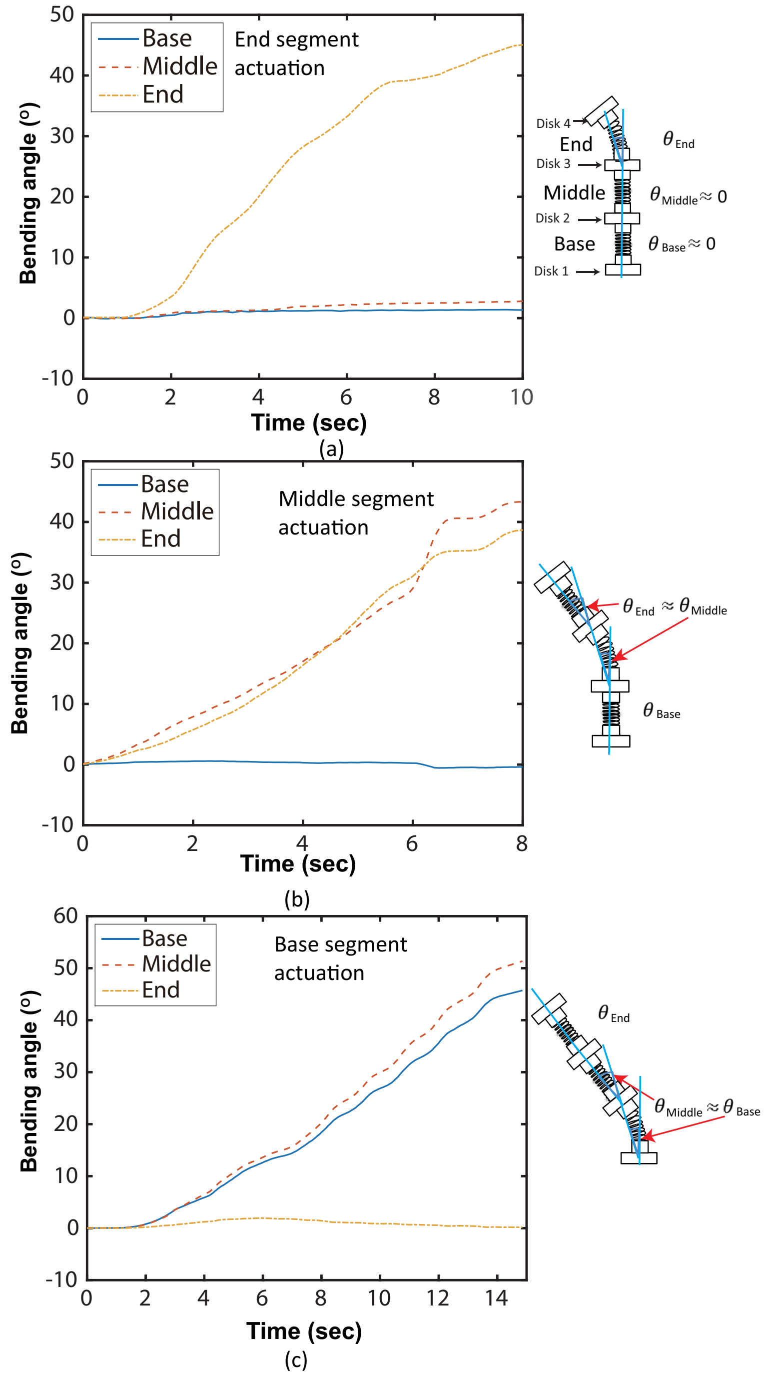

Figure 5.12: Experimental results of the independent segment motion for (a) only end segment actuation, (b) only middle segment actuation, and (c) only base segment actuation

Disk 3, and Disk 2 were bent at various angles during actuation of the end, middle and base segments, respectively. During the same period, minimal angle changes were observed in the segments proximal to the actuated segment. When the end segment was moved, as shown in Fig. 5.12(a), the average changes in the angles for the base and middle segments were 0.97°, and 1.61°, respectively. While the middle segment was bent, as shown in Fig. 5.12(b), the average angle change of the base segment was 0.18°. While the base segment was bent, as shown in Fig. 5.12(c), the average angle change of the end segment was 0.87°. The actuated segment and its neighboring distal segment have nearly identical bending angles, as shown in Figs. 5.12(b) and 5.12(c). This supports the assumption that each SMA spring robot segment bends with a constant curvature throughout its length, which leads theoretically to identical bending angles between the actuated segment and its neighboring distal segment, as seen in Fig. 5.8. The larger discrepancies towards the end of the experiments could be a result of magnification of the error at larger bending angles due to the imperfect parallel alignment between the vision markers on the robot segment disks and the vision camera. Through these experiments, we verified independent segment control in our robot. It is important to note that this makes independent segment locking possible. By using independently controllable tendon routing configuration, locking the tendons connected to a target segment can stiffen the target segment without interfering with the motion of the other segments. This also leads to better detection and localization of contact along a multi-segment continuum robot which was previously studied by Bajo and Simaan [116]. If each tendon is connected to a force sensor for measurement of the tension force (interaction force during an operation), we can distinguish the specific segment interacting with the surgical environment.

5.6 Local Stiffness Characterization

Local stiffness tuning is important because the robot should be able to stiffen some of its segments to achieve desired motion in the surgical environment or accomplish specific surgical tasks which need structural rigidity. By combining independent segment locking with stiffness tuning of the SMA backbone, we can adjust the stiffness of the specific segment without interfering with the motion of the other segments. In this paper, we performed the characterization experiments on the robot segment by moving its tip using the MP-285 micromanipulator (Sutter Instrument, California, USA). The wire diameter, height, mean diameter, the number of coils, and shear modulus of the outer plastic spring used in the experiment were 1.50 mm, 66.50 mm, 12.6 mm, 3, and 831.66 MPa, respectively. We assume that the force at the tip when the robot is bent at small angle is approximated to be the same as the force when the tendon is perpendicular to the MLP-10 force sensor (Transducer Techniques, LLC, California, USA) for all experiments. The stiffness values discussed in this section are the slopes of graphs that relate resistive force to lateral displacement and represent the average stiffness of the robot segment consisting of an SMA spring and a rigid rod.

5.6.1 Local Stiffness Changes by SMA Backbone Stiffening and Tendon Locking

To experimentally determine the local stiffness changes in a single robot segment by SMA backbone stiffening, tendon locking, and the combination of both, we performed four experiments (Cases I, II, III, and IV) as shown in Fig. 5.13(a). In the following characterization experiments, we used a cotton thread to connect the end disk to a force sensor attached to a micromanipulator. The elasticity of the thread allowed small lateral displacement of the micromanipulator without bending the robot by any significant angle. This ensures that the force measured by the force sensor is always the resistive force that acts perpendicular to the robot end disk. The cotton thread was chosen because its flexibility allowed it to stay taut without causing lateral deflection of the end disk when the experiments were being set up. To ensure that the cotton thread did not break and that the robot end disk was always perpendicular to the micromanipulator, only a small deflection of 5 mm was commanded in the experiments for characterization purpose. In all four cases, the SMA spring backbone

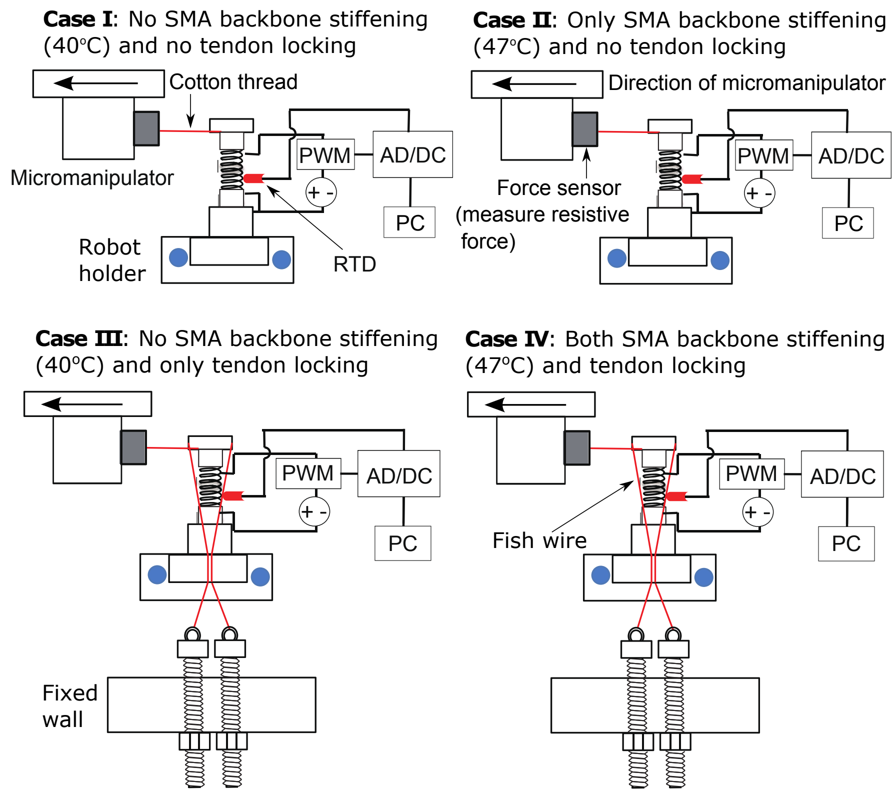

(a)

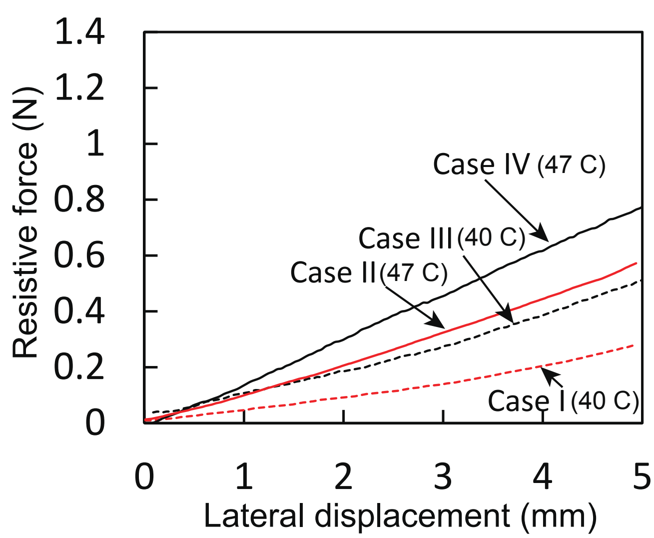

(b)

Figure 5.13: (a) Schematic representation of the experimental setups for the four different cases to investigate the effect of tendon locking and SMA stiffening on the local stiffness (b) Changes in resistive force when the single robot segment tip moves by a lateral displacement of 5 mm in the four different cases

was heated to a temperature above austenite finish temperature and cooled down before every experiment to ensure a stress-free condition and that there were no gaps between the spring coils. Fish wires (OmniFlex 8lb, Zebco, USA) of 0.011" diameter were used as the tendons to connect the end disk to a screw attached to a fixed wall in Cases III and IV. The tautness of the wires can be adjusted by changing the position of the screw in and out of the fixed wall. By visual inspection, we ensured that the tendons were taut. During the experiments, the micromanipulator was moved by 5 mm and the resistive force was measured.

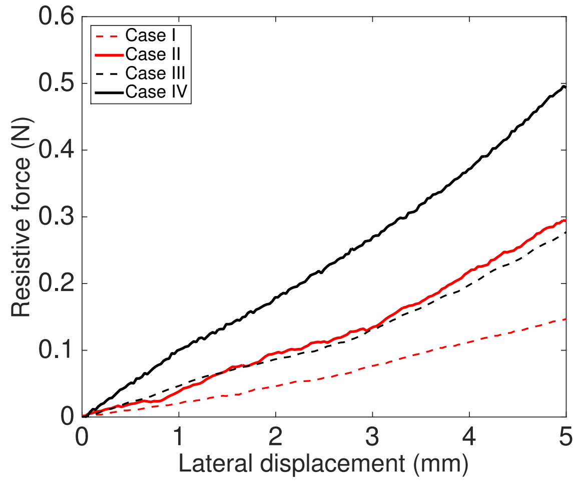

Figure 5.14: Changes in resistive force when the tip of the three-segment robot moves by a lateral displacement of 5 mm in the four aforementioned cases

For Case I and Case II, shown in Fig. 5.13(a), we carried out the lateral deflection experiment when the temperature of SMA spring backbone was 40°C and 47°C, so that we can ensure the SMA spring backbone was in the non-stiffened state (fully martensite) and the stiffened state (fully austenite). The resistive force of the stiffened SMA spring-based robot segment is almost twice that of the non-stiffened SMA spring-based robot segment, as shown in Fig. 5.13(b). To measure the resistive force generated at the robot tip by only tendon locking, we carried out an experiment as shown in Case III in Fig. 5.13(a). The end of the one-segment robot was moved laterally by the micromanipulator while the SMA spring backbone was maintained at 40°C (fully martensite) and the tendons connecting the

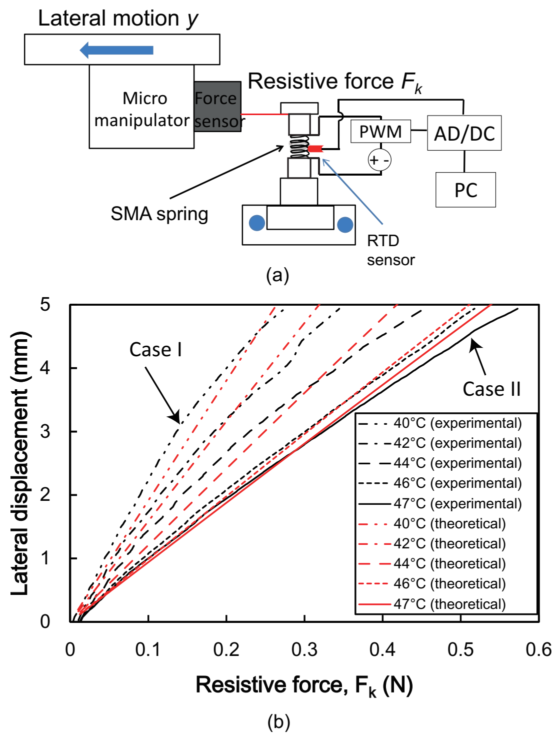

Figure 5.15: (a) Experimental setup schematic of stiffened and non-stiffened SMA spring-based robot segment (b) Variation of resistive force during SMA heating (from Case I (40°C) to Case II (47°C) for various intermediate temperatures and a fixed lateral displacement of 5 mm

end disk of the robot to a wall was taut. As shown in Fig. 5.13(b), the resistive force in Case III is larger than that of Case I, but smaller than that of Case II. In case IV shown in Fig. 5.13(a), the SMA spring backbone was stiffened and tendon connecting the end disk of the robot to the wall was taut. As the micromanipulator was moved laterally, the resistive force was measured.

The results, shown in Fig. 5.13(b), show the influence of various combinations of the tendon locking and SMA backbone stiffening on the rigidity of the one-segment robot. The combination of tendon locking and stiffened SMA spring backbone resulted in the greatest stiffness (1.5×10^{-4} N/m). The stiffened SMA spring backbone configuration came second with 1.1×10^{-4} N/m, followed by the tendon locking configuration with 1.05×10^{-4} N/m. The stiffness of the robot segment in case IV is merely 5.1×10^{-5} N/m. If the tension force that is applied to the tendon is large enough to withstand the interaction force between the

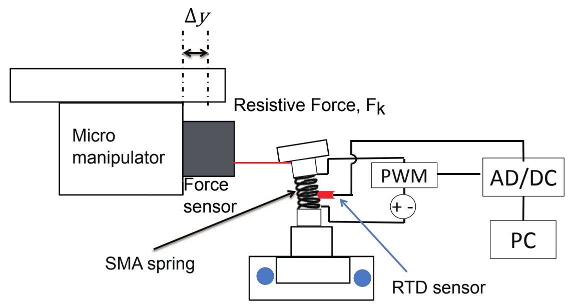

(a)

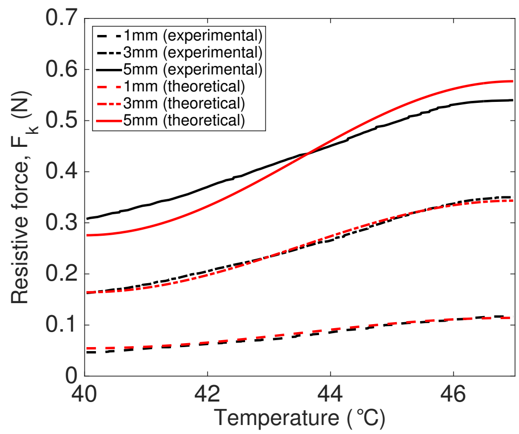

(b)

Figure 5.16: (a) Schematic of the experimental setup and (b) variation of resistive force with temperature for different lateral displacements

robot and the environment, the tool rigidity can be enhanced by using a combination of tendon locking and stiffened SMA spring backbone.

We also performed the stiffness modulation experiment for the complete robot with three segments under identical conditions (Case I, II, III, and IV). The end disk of the three-segmented robot was connected to the force sensor using the cotton thread. All three SMA spring segments were heated simultaneously in case II while the tendons connected to the all the segments were taut in case III. In case IV, all robot segments were heated and the tendons connected to all robot segments were taut. The results shown in Fig. 5.14 confirm that the tip forces of the three-segmented robot are smaller than those of a single robot segment for all conditions. Similar to the single robot segment, the combination of tendon locking and SMA backbone stiffening leads to the highest stiffness of the three-segmented robot (9.5x10^{-5} N/m), followed by SMA backbone stiffening only (5.8x10^{-5}

N/m), tendon locking only (5.3x10^{-5} N/m), and finally the case without either backbone stiffening and tendon locking (3x10^{-5} N/m).

5.6.2 Active Stiffness Tuning of SMA Spring Backbone

For active stiffness tuning, we characterized the stiffness of the SMA spring backbone by fixed lateral deflection experiments over a range of temperatures between 40°C (Case I) and 47°C (Case II), as shown Fig. 5.15(a). The lateral motion at the end of the one-segment robot was provided by the micromanipulator. The RTDs attached on the SMA spring robot segments were used to obtain their real-time temperature while a proportional-integral-derivative (PID) controller was used to control and maintain the temperature. While we maintained the temperature of the SMA spring backbone at certain values, the robot tip was moved laterally by 5 mm. The resistive force, F_k, exerted by the SMA spring backbone of the robot, was measured by the force sensor. The characterization results of the SMA springs from the lateral deflection experiment are shown in Fig. 5.15(b). The wire diameter, mean diameter, and the number of the SMA spring coils used in the experiment were 0.78 mm, 5.8 mm and 2.8, respectively. The resistive force, F_k is known from the experiment. Total lateral deflection (lateral displacement), y, is calculated from Eq. (5.18). The experimental lateral deflection and theoretical lateral deflection do not have significant differences (R^2-value = 0.9866 for $(y)_{T=40°C}$, R^2-value = 0.9917 for $(y)_{T=42°C}$, R^2-value = 0.9873 for $(y)_{T=44°C}$, R^2-value = 0.9982 for $(y)_{T=46°C}$, and R^2-value = 0.9978 for $(y)_{T=47°C}$). The discrepancies in the shape of the plots are likely due to the non-linear behavior of the SMA spring that is anchored at one end in response to bending. The assumptions we made in the model that the arc length of the spring remains constant and that the bending angle is small such that the resistive force is always normal to the tip of the robot segment would also contribute to errors at larger bending angles. However, the model captures the important trend of SMA spring robot segment stiffness behavior and predicts within good R^2-values the slopes of the plots across different SMA temperatures.

We also performed the temperature variation experiment, as shown in Fig. 5.16(a). We maintained certain lateral displacements of 1 mm, 3 mm, and 5 mm while the SMA was heated from 40°C to 47°C. This experiment allows us to better understand the resistive force changes at different temperatures of the SMA spring. Total lateral deflection, y, is known from the experiment. F_k (theoretical value) is calculated by using Eqs. (5.3), (5.16), and (5.19). Figure 5.16(b) shows the variation of the resistive force with temperature at three specific lateral displacements of the micromanipulator. The resistive force of the SMA spring-based robot increased as the temperature of the SMA spring backbone increased. Theoretical resistive force for 1 mm, 3 mm, and 5 mm displacements matched with the experimental data well (R^2-values = 0.9924 for $(F_k)_{y=1mm}$, R^2-values = 0.9939 for $(F_k)_{y=3mm}$, and R^2-values = 0.9963 for $(F_k)_{y=5mm}$). The fact that the relatively biggest difference occurs with the largest lateral displacement of 5 mm could be due to the two assumptions that there is constant spring length and that the resistive force is always normal to the robot end disk.

5.6.3 Relationship between Tension and Resistive Force

To experimentally determine the relationship between the resistive force and the tension needed for tendon locking, we performed an experiment, as shown in Fig. 5.17(a). An additional force sensor was added to measure the tension force in the tendon that was connected to the end disk of the robot. We kept the initial tension in the tendon to be 0.04 N, so that the tendon was initially taut. While the end of the robot was moved laterally by the micromanipulator, both the tension in the tendon and the resistive force were being measured. The results for the experiment are shown in Fig. 5.17(b). It can be observed that the tension applied was 5.02 times the exerted resistive force for 5 mm lateral displacement of the micromanipulator. Therefore, considering the safety of the device, we need to ensure that our actuators are able to generate and withstand approximately 6 times the amount of force we need at the robot tip. The theoretical resistive force data from Eq. (5.25) discussed in Section IV matches the experimental data well (R^2-value = 0.9931).

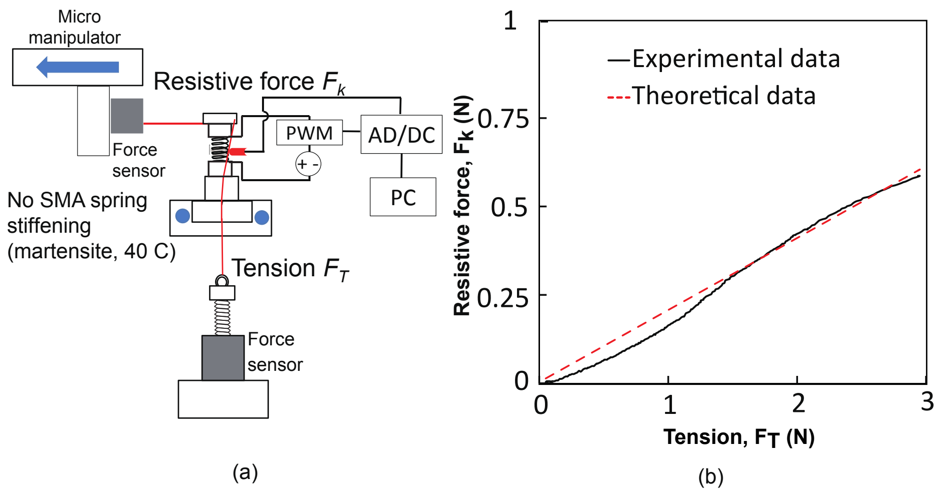

Figure 5.17: (a) Schematic of experimental setup and (b) variation of the resistive force, F_k and tendon tension, F_T

5.7 Motion Capability Evaluation and MRI Compatibility Verification

As shown in Fig. 6.19, we developed an MRI-compatible robotic platform consisting of Nitinol SMA spring actuators (Flexmet, Belgium) with integrated water cooling modules and attached the 3-segment MINIR-II robot to the robot holder on the platform. The entire system is composed of the robotic platform, water reservoir, air compressor, and a computer with an analog-to-digital-converter (ADC) board. More details about the robotic platform can be found in the work by Cheng and Desai [188]. The robot head was designed to have a specific slot for the EndoScout® sensor (Robin Medical, Inc., Baltimore, MD, USA), as shown in Fig. 8.21(e). We inserted the robot part of the platform into a gelatin (Knox, USA) slab and performed a robot motion experiment in the gelatin slab to verify motion capability and MRI compatibility of the robot in a brain simulated environment. Figure 8.21(a) shows the experimental setup of the MRI compatibility test. A head coil was placed over the robot/gelatin slab at the center of the MRI scanner. In the MRI scanner, we used an on-off control (visual inspection of robot motion) when heating the SMA spring actuators. Before actuating the robot, we took 50 MR images, to evaluate the degree of image distortion caused by the robot and determine the signal-to-noise ratio (SNR) changes of MR images during MRI scanning. We then heated one SMA spring actuator to bend the end segment of the robot to the right before actively cooling it down and heating the antagonistic SMA spring actuator to bend the end robot segment to the left. During the actuation process, an additional 50 MRI images were taken. During this test, we performed the resistive heating and active cooling of SMA spring actuators, but SMA backbone stiffening was not activated. It can be seen from Fig. 8.21(b) that the motion of the robot end segment in the gelatin phantom did not cause any significant shape change in the non-stiffened proximal segments. The increase in stiffness would further improve stability of the robot during a procedure. The SNR was calculated as a ratio of the mean value of an area of pixels at the center of the image (black box) and the standard deviation of an area of pixels at the lower-right corner of the image (red box) as shown in Fig. 8.21[231]. The average and standard deviation of SNR of the 50 images with non-actuated MINIR-II was 25.98 ± 0.60. The MR image of robot under the non-actuated state can be seen in Fig. 8.21(b) and Figure 8.21(c) shows the actuated state where the end segment has been moved to the right and then to the left. During the actuation of the robot, the average and standard deviation of SNR of the 50 images was 25.95 ± 0.76, resulting in a 0.8% SNR drop (See Fig. 8.21 (d)). It is confirmed that there was minimal distortion caused by the actuation of the robot. Furthermore, we also performed additional test where only SMA backbone stiffening (heating) was activated. To enhance quality of the MR images, we used a body coil, instead of the head coil. To heat the inner SMA spring backbone, it needs to be insulated from the gelatin. Thus, the three segmented robot with the only inner SMA spring backbone was wrapped in a vinyl wrap during the SMA backbone stiffening (heating) as shown in Fig. 8.21 (e). As a result, the SNRs of each image for non-stiffened backbone (See Fig. 8.21 (f)) and stiffened backbone (See Fig. 8.21 (g)) are 243.93 and 235.20, respectively. Minimal distortion (3.6% SNR drop) by the SMA backbone stiffening (heating) was observed.

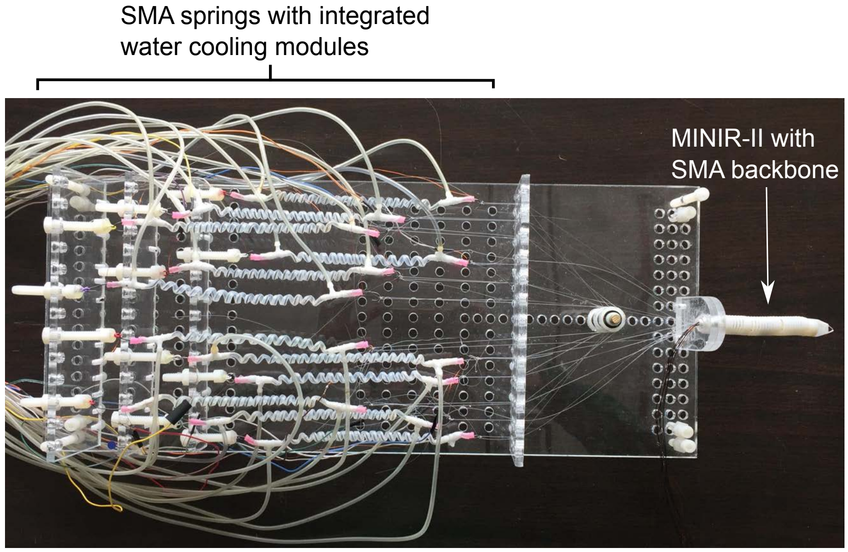

Figure 5.18: Experimental platform built to hold and actuate the MINIR-II in the MRI compatibility test

5.8 Summary

We developed a spring-based continuum robot that has an inner inter-connected SMA spring backbone with multiple segments and an outer plastic spring, whereby the stiffness of the inner inter-connected spring could be tuned based on the temperature of the SMA spring. The robot used a tendon driven mechanism with a unique tendon routing configuration to avoid coupling between the robot segments and achieve independent segment locking. Advanced motion capabilities can be achieved by using independent segment locking and SMA spring backbone stiffening. Compared to the interlaced robot proposed by Kang et al. [213], the MINIR-II robot has a relatively simple structure of a continuous spring and still provides similar function of robot stiffening and tool stability. The MINIR-II robot is different from the interlaced robot such that we focused our effort on achieving independent stiffening of the non-actuated robot segment in MINIR-II while the interlaced robot's main strength is to achieve tool stability through pose control in any configuration using follow-the-leader deployment. The MINIR-II robot can control the stiffness of each segment easily at any time during the surgery through temperature variation of the

SMA spring backbone while the interlaced robot may need more complex steps to change and maintain a desired pose.The resistive force generated from SMA spring-based segment was analyzed in terms of its stiffness. We performed experiments to verify our SMA spring stiffness model and determine the relationship between the resistive force and the tension in the connecting tendons. We also verified that structural rigidity of MINIR-II is greatly improved by using a combination of tendon locking and SMA spring backbone stiffening. We tested the motion capability of the robot in a gelatin phantom and verified its MRI-compatibility. In the next chapters, we planned to address the problem of deployment of the robot, including the manufacture of a customized head frame that allows trajectory adjustment and insertion of the robot. We also planned to integrate ultrasonic motor actuators with the MINIR-II robot.

(a)

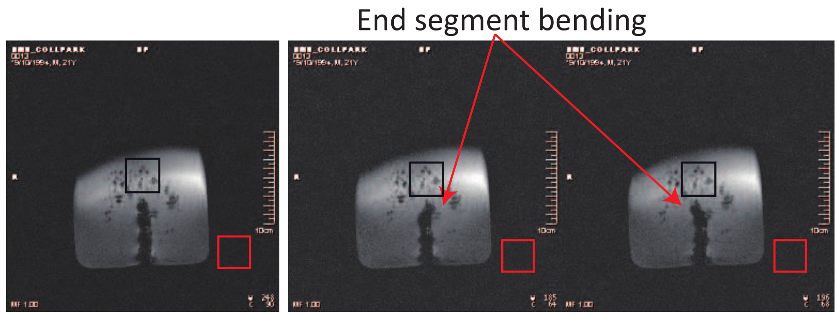

(b)

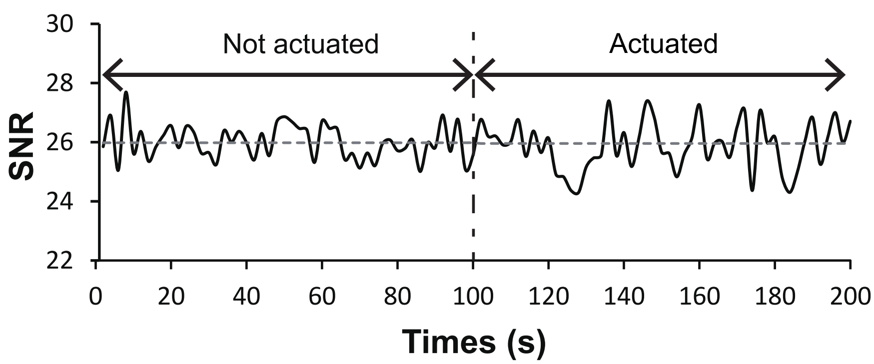

(c)

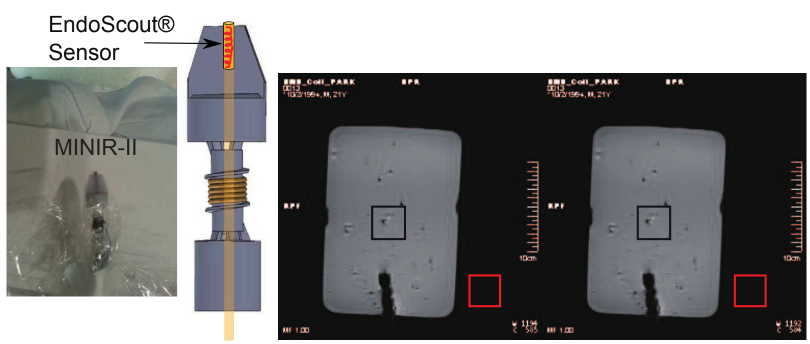

(d) (e)

Figure 5.19: (a) Experimental setup during MRI compatibility test; MR images of MINIR-II in a gelatin slab: (b) MR images of the MINIR-II in the non-actuated state and actuated states (c) SNR changes when the MINIR-II was in the non-actuated state and the actuated state (d) Actual picture and schematic of the MINIR-II with integrated EndoScout® sensor; (e) MR images of MINIR-II in a gelatin slab without SMA backbone stiffening (left) and with SMA backbone stiffening (right)

CHAPTER 6

REMOTE ACTUATION: FLEXIBLE BOWDEN CABLE TRANSMISSION

6.1 Transition from SMA Springs to Ultrasonic Motors

In the previous chapters, we used SMA springs as the actuators and developed a new actuation mechanism to operate the cooling module-integrated SMA springs to allow real-time control of the robot. After evaluating the robot extensively using the SMA springs, we were ready to switch the actuators to the more precise and reliable piezo/ultrasonic motors. Among the many piezoelectric/ultrasonic motors available on the market, ultrasonic motors from Shinsei Corporation were chosen due to its unparalleled supplied torque (maximum torque of 1.0 Nm and nominal torque of 0.5 Nm), an integrated optical encoder, and its simple rotary configuration that can be integrated easily into a robotic system. However, consideration had to be given to the practical integration of the ultrasonic motors in the robotic system and its implementation in a high magnetic field environment to minimize artifacts on the MRI images caused by electrical noise from the actuators and their drivers. As elaborated in Chapter 1 and 2, it has been found in previous literature that ultrasonic motors, despite being non-magnetic and MRI compatible, create artifacts on MR images when placed too close to the MR isocenter [3, 232] or during MR scanning [97]. Their drivers are usually placed in a Faraday cage [76, 79] and customized drivers were also developed to minimize the SNR drop caused by the interference from the driving waveforms to the MR imaging [80]. Our approach was to develop a remotely-actuated setup where the actuation unit was placed around 2-3 m from the robot end effector with novel transmission modules placed in between to connect them.

6.2 Background on Remotely-Actuated Surgical Robotic Systems

Given the limited workspace and choice of actuators, cable-driven mechanism is promising for intraoperative surgical procedures in the MRI. In a broader sense, tendon, tendon sheath or Bowden cable driven robots are used for a wide variety of applications such as neural rehabilitation [129, 233, 234], steerable needles-based surgical robots [235, 236], rescue missions [237], underwater actuation and sensing [238, 239], and dexterous manipulation in manufacturing environment [240].

Narrowing the scope to MRI-compatible surgical robotic systems, cable-driven mechanism has been used to perform needle insertion for prostate intervention [241, 242]. The cable-driven mechanism allows the actuators to be placed outside the MR room, thus keeping the robotic device in the MR machine compact. A needle guide is connected by several cables to a template grid. The angulation of the needle guide, achieved by pulling of the cables from the control room, adjusts the needle trajectory.

Remote actuation mechanism was used to position the needle gripper in the second prototype of the patient-mounted light puncture robot (LPR v2) which was developed to perform MRI-guided percutaneous needle insertion for abdominal and thoracic procedures [243]. The first prototype of the LPR uses pneumatic actuators [244] that are placed on a bed-mounted frame, creating a bulky setup which limits the patient size that it can operate on. Sterilization issue was also reported as the most important limitation of the robot. In the LPR v2, ultrasonic motors are placed far from the MR imaging field and Bowden cables are used to transmit the force from the motors to the various joints needed to position the needle guide and adjust the insertion depth.

An MRI-compatible patient-mounted parallel platform (ROBOCATH) employs tendon-driven mechanism to control four DoFs, that include two rotational joints and two prismatic joints, to position and orient surgical catheters for intercardiac interventions [245, 246, 247]. A state feedback linear parameter varying (LPV) controller was designed and shown to be superior to the previously-used proportional-integral-derivative (PID) controller in terms of shorter settling time especially at larger target amplitude. DC motors used as the actuators for the robot are placed outside the MRI room and transmit power through a transmission system that is composed of closed chains of plastic ropes and pulleys.

Transmission is needed if the actuation system is to be placed far from the MRI isocenter. Chinzei $et\ al.$ [68] used two long rigid arms as transmission in the transperineal intraprostatic intervention procedure. A versatile robot [248] has its four DoFs controlled from outside the MRI gantry via timing-belts. Tsekos $et\ al.$ [96] used telescopic acrylic shafts to connect the ultrasonic motors with their robotic positioning setup. Recently, a multiplexed power transmission [249] was integrated in a prostate intervention robotic assistive system to actuate a 4-DoF needle manipulator sequentially.

There are a few MRI-guided commercial systems that have compact profile, especially the laser ablation surgical systems such as the NeuroBlate® and Visualase® systems. With the exception of the NICHE, NeuroBlate® and Visualase®, which have their initial configuration aligned with the incision trajectory, most of the meso-scale robots have relatively big actuator setups where the robots are directly attached to. This means that in their current states, they cannot be directly mounted at the incision site and therefore require registration between the incision site and the robot.

In this chapter, we proposed an MRI-compatible Bowden cable transmission with quick connect modules, a skull-mounted platform and a slightly modified meso-scale MINIR-II robot. Electric linear motors were used temporarily as the actuators to test the Bowden cable transmission. These linear motors would be replaced by ultrasonic motors in the actual setup in the Chapter 7 and Chapter 8. Two important aspects of the neurosurgical procedure, including the identification of robot entry point and the trajectory planning, are beyond the scope of the current work.

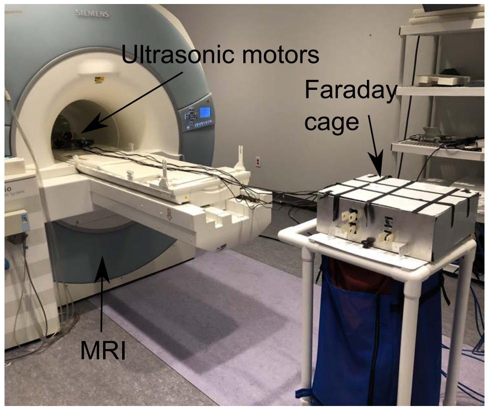

(a)

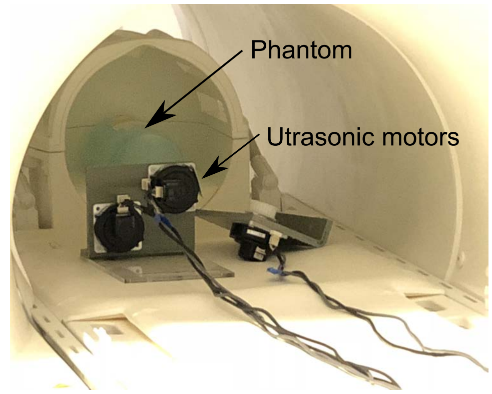

(b)

Figure 6.1: (a) The experimental setup to evaluate the effect the number and location of ultrasonic motors and drivers on the MR images (b) Close-up view of the ultrasonic motors in the MR isocenter

6.3 Effect of Ultrasonic Motors and Drivers on Signal-to-Noise Ratio (SNR)

The effect of the number and position of the ultrasonic motors (USR60-E3NT, Shinsei Corporation) and drivers (D6060S, Shinsei Corporation) on the SNR of MR images was investigated. We performed the experiment in a 3-Tesla 60 cm bore Siemens Magnetom Trio system, as shown in Fig. 6.1(a). In the first set of experiments, different number of motors (one, two and three) were placed at the isocenter of the MR machine, as shown in Fig. 6.1(b). In the second set of experiments, all three motors were placed at different locations: at the MR isocenter, 2 m from the isocenter and inside a Faraday cage. In each experiment, the MP-RAGE (three-dimensional, T1-weighted, gradient-echo) scanning sequence was implemented for four minutes, during which the motor(s) were actuated continuously. The results can be divided into quanlitative and quantitative features. Qualitatively, it was noticed that the drivers could not be placed any closer than 2 m from the MR isocenter or 1 m from the MR bore entrance, beyond which the drivers and motors stopped working properly. The motors, on the other hand, work fine even when placed at the MR isocenter, given that the drivers are placed beyond the aforementioned critical distance. The quantitative experimental results, as shown in Fig. 6.2(a), show that the SNR value drops more with increasing number of motors. As shown in Fig. 6.2(b), the SNR also increases significantly by 28% when the motors were placed at 2 m from the isocenter compared to at the isocenter. The MR quality improves only slightly with an increase of approximately 6% when the motors are placed at 2m outside the Faraday cage compared to inside the Faraday cage. Based on these results, it was decided that a remotely-actuated setup, consisting of a transmission module located between the actuation module (Faraday cage) and the robot, would be designed to operate the MINIR-II robot.

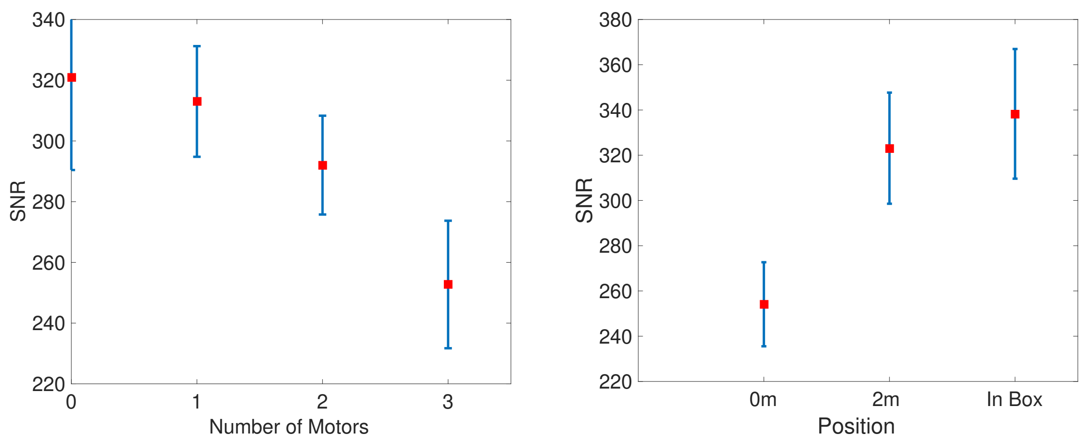

(a) (b)

Figure 6.2: The changes in SNR when (a) different number of motors were actuated simultaneously and (b) the motors were placed in different positions

6.4 Design of the Robotic System

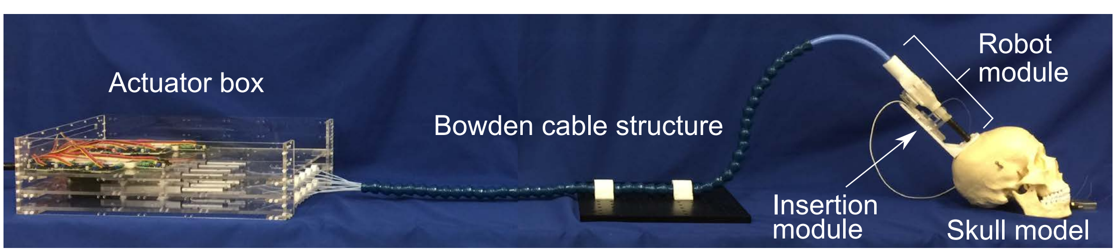

Figure 6.3: The complete cable-driven remotely-actuated neurosurgical robotic system

6.4.1 System Requirements

The ultimate goal of the work was to develop a remotely-actuated neurosurgical system with a head mounted insertion module to advance the meso-scale spring-based MINIR-II robot that was previously developed [193]. This system would not require registration of a standalone robot with respect to the incision site through a stereotactic frame. Once the incision hole has been determined, the insertion module can be mounted on the skull at the incision hole with a trajectory towards the brain tumor. The robot that is attached to the insertion module would have the same trajectory that allows straight penetration towards the brain tumor through a channel called neuroendoport. When the robot is attached to the insertion module, slight adjustment of the robot trajectory may be needed but this issue is beyond the scope of this work.

There are several important system requirements that were considered in the design of the system, as shown in Fig. 6.3.

1) The transmission cables should be robust to small disturbances and do not need to be in straight configuration to maintain its tautness.

2) The actuation system and the transmission cables for the remotely-actuated robot should be robust and reusable while the section of the robot module that enters the brain should be disposable.

3) The robot module and the head mounted insertion module, when placed on a person's skull, should fit in a standard MRI-bore that has approximately 300 mm room above an average person's head.

4) The robot module and the head mounted insertion module should be compact and lightweight.

5) The insertion module should lower the robot by at least 61 mm, which is the total length of the three-segmented MINIR-II robot.

6) The entire system has to be MRI-compatible.

6.4.2 Key Design Components

Based on the system requirements, the broad design concept that was implemented in this work can be divided into several pieces as follows:

1) An insertion module that advances the robot module towards a defined trajectory determined by the incision site

2) A robot module that has a disposable part including the MINIR-II robot and a reusable part that leads to the transmission cables

3) A Bowden cable transmission structure that connects the robot module to its actuation system and an actuator box that contains all the actuators and control boards

All of these components can be seen in Fig. 6.3.

Assuming the incision site (robot entry site) has been determined and an endoport has been inserted into the brain that leads directly to a deep seated brain tumor, the rest of the surgical procedure would be as follows:

a) The insertion module is screwed onto the patient's skull at the incision site

b) The disposable and reusable parts are put together easily to form the robot module that would then be secured on the insertion module.

c) A linear actuator on the insertion module would advance the robot module towards the target brain tumor along the neuroendoport.

d) After the procedure is complete, the linear actuator would raise the robot module which would then be taken off the insertion module.

e) The disposable part of the robot module would be removed.

Head-mounted insertion module

The head mounted insertion module, as seen in Fig. 6.4, consists of a base that would be screw-mounted on the skull at the robot entry site and a flat vertical plate on which a piezoelectric linear actuator (SLC-2490, SmarAct, Germany) is attached. The piezoelectric

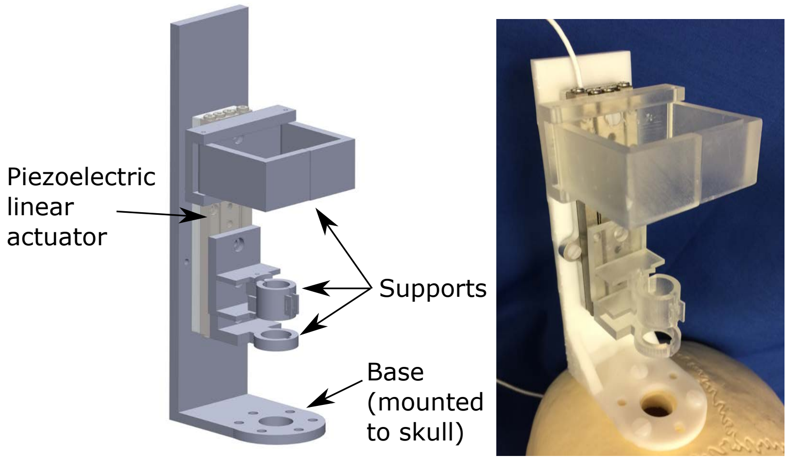

(a) (b)

Figure 6.4: (a) Schematic and (b) actual photo of the insertion module

linear actuator was selected due to its precision (resolution of 1nm), small weight (108 g), travel range of 63 mm, and a maximum lift force of 1.5 N, all of which satisfy the aforementioned system requirements. There were three support holders on the linear actuator that are used to hold the robot module securely. The insertion module had a lean and compact profile which is 136 mm in height and 180 g in total mass (including the piezoelectric linear actuator).

Robot module

The robot module, as seen in Fig. 6.5, was designed to be a compact quick connect body that consists of the disposable part and the reusable part. To allow quick connection and disconnection between the disposable and reusable part, we opted for a snap-together connection method. The disposable part consists of the MINIR-II robot and half of the quick connect modules. The reusable part consists of the other half of the quick connect modules which was connected to the transmission cables that lead to the remotely placed actuators.

The half side of the quick connect modules (shown in Fig. 6.5) that belongs to the reusable part is named the proximal module whereas the half that connects to the robot is named the distal module. Each module has a rectangular shape sized at 42 mm by 31 mm.

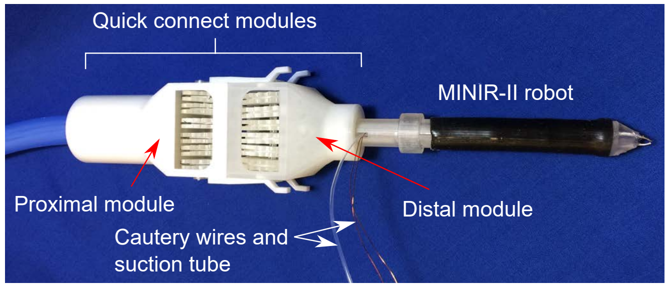

Figure 6.5: Robot module that consists of the reusable part and the disposable part (sleeve of the robot is not shown)

The proximal module has a 35 mm long column on one end to secure the transmission cables and locking clips on the other end to provide a snap-together mechanism to attach to the distal module. The distal module has two windows on each side, into which the locking clips from the proximal module lock into. It also has a threaded connector where the robot can be screwed into. Inside each of the proximal and distal module, there are six 3-D printed spur gears and six plastic bearings with glass balls (Model B623B1G, igus®, Germany) lined up on a 3-D printed cylindrical rod of 3 mm in diameter, as shown in Fig. 6.6. The bearings have an inner diameter of 3 mm and outer diameter of 10 mm and the smallest bearings without metals that we are aware of. Two neighboring bearings (or gears) are separated by a separation disk of 1 mm width to keep the quick connect modules compact while making sure the neighboring gears do not interfere with one another. This gap distance of 1 mm was determined after several trials and errors in 3-D prototyping and testing.

The design of the gear was made to ensure that the number of gears is minimal for the compactness of the quick connect modules. It is important that the rotation of each gear is sufficient to induce the desired range of motion in each robot segment, which is set to be 45°in each direction for each DoF or at least 10 mm in robot tendon displacement. The theoretical and experimental relationship between the bending angle and tendon displacement of a standalone MINIR-II robot can be found in the work by Kim and Desai [193]. In the current prototype, each gear is responsible for one DoF of a robot segment. Modifica-

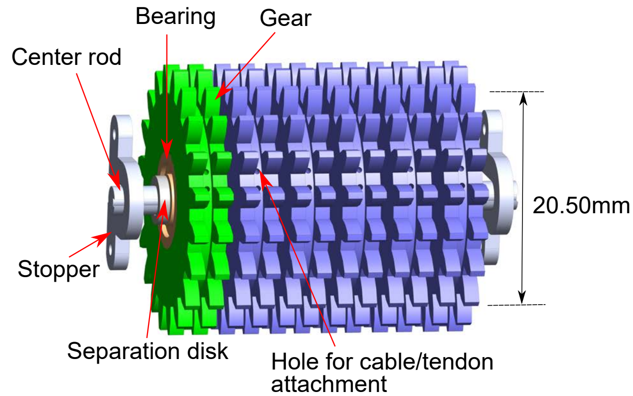

Figure 6.6: Gear and bearing setup along the center rod that is fixed in place by a two stoppers on each end. The rectangular box indicates one single gear.

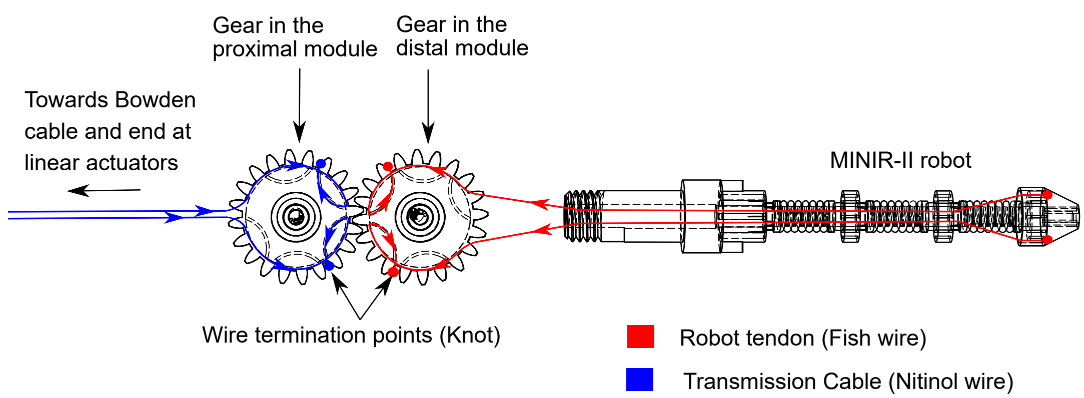

Figure 6.7: Routing of transmission cable and robot tendon around the gears in the proximal and distal module. (Arrows show the direction of routing the tendon/cable which ends in cable/tendon knots)

tions in terms of design of a standard spur gear and routing of transmission cables or robot tendons were done to ensure the robot could achieve its desired range of motion.

As shown in Figs. 6.6 and 6.7, each gear, with a diameter of 20.50 mm (not considering the teeth pitch), has two circular rows of teeth instead of one in a regular gear. The resulting gap between the two rows of teeth and the curved channels of 0.6 mm diameter built on the circular gear surface into the gear body (see Fig. 6.7) to allow the attachment of cable or tendon. The routing of the cable or tendon is shown in Fig. 6.7, where the rectangular outer bodies of the proximal and distal modules are hidden. This exposes the configuration of the gear pairs that mesh when the proximal and distal modules are snapped together. The

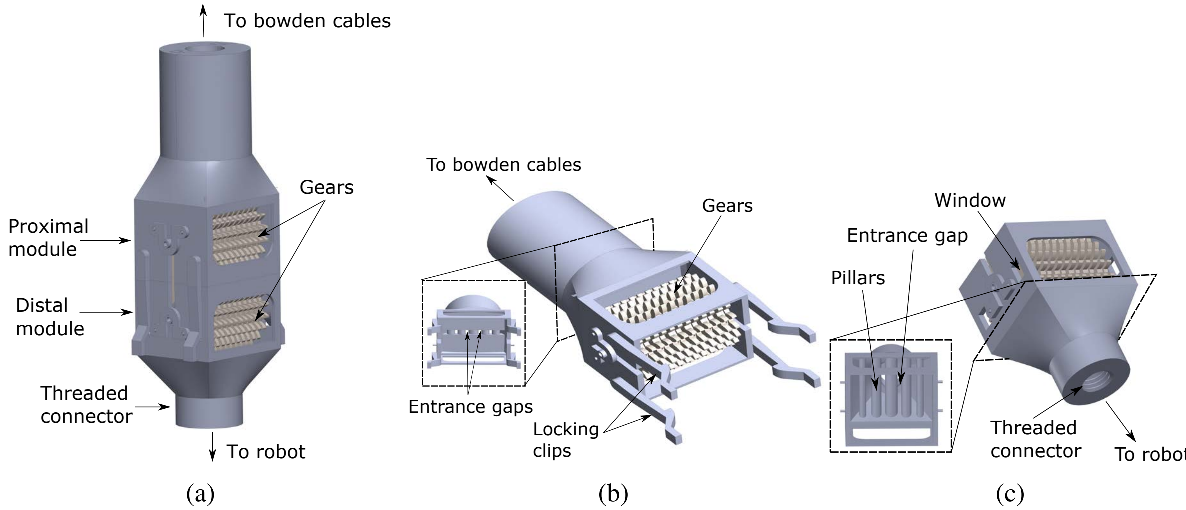

Figure 6.8: (a) The full assembly of the quick connect modules (b) Proximal module with locking clips (c) Distal module on which the robot is directly attached

arrows show the direction of routing the transmission cables and robot tendons in the gears. By routing the cables/tendons through narrow channels in the gear, no space is wasted for cables/tendons termination. The configuration of the cables/tendons shown in Fig. 6.7 would allow each gear to rotate by at least 90°with a safe estimation. In the ideal case, the cable/tendon displacement associated with 90°gear rotation is approximately 16 mm, which is significantly more than what is required.

The ways the cables and tendons exit the proximal and distal modules are caused by the difference in structural design of the entrance gaps in the modules, as indicated in the insets of Fig. 6.13(b) and 6.13(c). In the proximal module, there are tiny entrance gaps created for the passage of Nitinol superelastic wires, which are used as the transmission cables. The gaps are created in the center of the body mainly to prevent the expansion of the superelastic wires, which would try to stay straight when routed along the circumferences of the gear surface. This design also potentially offers almost up to 180°of rotation for the gears in the proximal module. The potential contact edges around the entrance gaps are smoothened to minimize friction. On the other hand, the entrance gaps in the distal module are formed by pillars and they do not have to be tiny holes since the tendons that connect the gears and the robot segment disks are monofilament fish wires which would rest properly around the

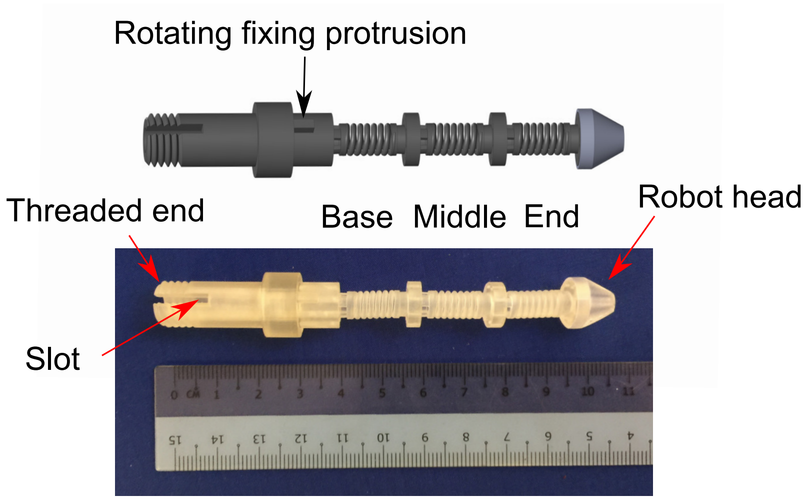

Figure 6.9: Schematic and actual picture of the modified MINIR-II robot with threaded end, rotation fixing protrusion and a slot for passage of electrocauterization wires, suction and irrigation tubes (sleeve is not shown)

circumference of the gear surfaces with just a little tension. The larger entrance gaps also reduces potential contact friction during tendon motion. In both modules, each entrance gap is created in front of the each gear to ensure the gears do not experience any axial force along the center rod axis.

The design of the MINIR-II robot [193], with the outermost diameter of 13 mm, has been modified so that it can attach well with the proximal module to form the disposable part of the system. It has a threaded male end that screws into the threaded female end of the distal module and a slot near the threaded end to provide passageway for the electrocauterization wires and suction tube. There is a protrusion, as seen in Fig. 6.9, that would prevent the robot from rotating about its own axis when combined with the robot support holder on the linear actuator. The robot head has slots for the electrocautery probe, the suction tube, and the MRI-compatible magnetic field sensor (not used in this work).

The complete robot module including both the disposable and reusable parts has a total length of 222 mm, less than the 300 mm room above the patient head in a closed-MRI bore. It is weighed at a mere 70 g. When combined with the insertion module, the total mass that would be placed on a patient's skull is 250 g. Except the plastic bearings, the entire robot module is 3-D printed, tremendously reducing the cost of manufacturing the disposable part. The robot module is entirely plastic, except the transmission cables that are made of Nitinol, which is MRI-compatible as well.

Bowden cable transmission structure

To address the first criterion in the system requirement listed in section II(A), a Bowden cable design was the the only best option since it does not require the transmission cables to be straight when they are in tension. This is important to provide the flexibility for the surgeon to place the robot module at the incision site on a patient's skull without constantly adjusting the position of the actuator box. However, a regular Bowden cable would not be feasible since material compatibility issues prevent the use of steel, meaning cables are usually made from high tensile polymers and flexible shafts from phosphor bronze.

The Bowden cable structure in our system is an approximately three feet long and 1/2" diameter nylon Loc-Line modular hose system, as shown in Fig. 6.10, consisting of twelve superelastic Nitinol wires (Confluent Medical Technologies, USA) of 0.2290 mm diameter, each of which is inserted into a Teflon tube. Twelve wires are needed to actuate six degrees of freedom (DoFs) of the three-segmented MINIR-II robot. Each Teflon tube and a Nitinol wire already act as one Bowden cable but it can only be used in applications that transmit small force since the teflon sheath does not have enough stiffness to allow efficient transmission of force in the cables. The modular hose provides a stiff path and a strict configuration for the entire collection of twelve Bowden cables, allowing all the cables to experience similar amount of friction for less complex control and more importantly enabling effective transmission of larger force. There is a 20 cm silicone rubber tubing with durometer 50 A, 9 mm inner diameter and 13 mm outer diameter at the distal end of the modular hose structure to act as a flexible sleeve that enables the insertion and retraction of the robot module without displacing the transmission cables during those procedures.

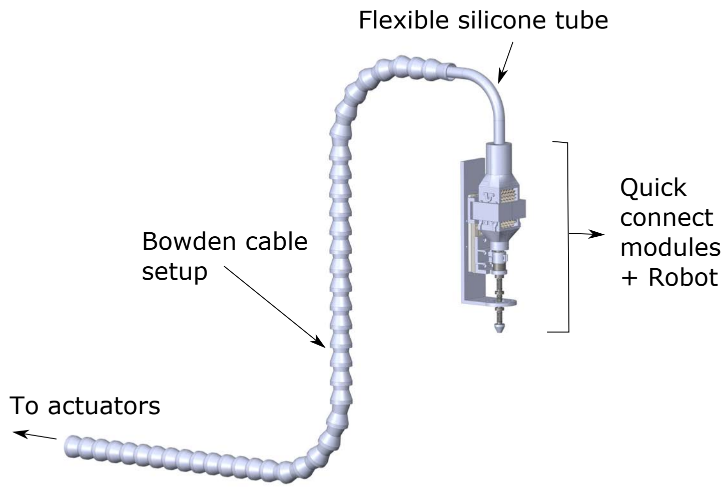

Figure 6.10: Potential configurations of the bowden cable setup: bowden cable is bent by 90°at two locations

6.5 Friction Model of the Bowden Cable Transmission

A Bowden cable that consists of the Teflon sheath and a Nitinol wire (cable) is used to remotely control the position of the target end of the cable by its control end, where the length of the cable in the sheath is unchanged. The input tension on the control end, denoted by T_1 is usually different from the output load on the target end, denoted by T_2, due to the friction between the cable and the sheath. The friction model can be derived by studying an infinitesimal element of the cable at position x with a length of dx, where x is the natural coordinate along the cable from the target end to the control end, as shown in Fig. 6.11. Assuming that the radius of curvature of the cable at x is $R(x)$, one can obtain the normal force from the sheath to this element by:

$$N(x) = \frac{T(x)}{R(x)}dx = T(x)d\theta$$

where $T(x)$ is the tension on the cable at x and $d\theta = dx/R(x)$ is the bending angle of this element. If the cable is moving at a constant speed in the sheath, the friction force on this element of length dx is [250, 251]:

$$f(x) = dT = \mu N(x)\mathrm{sgn}(\dot{x}) = \mu T(x)\mathrm{sgn}(\dot{x})d\theta \quad (6.1)$$

where dT is the increment of $T(x)$, $\mathrm{sgn}(\dot{x})$ is the sign function of the speed $\dot{x}$, and μ is Coulomb friction coefficient. From Eq. (6.1), the cable tension can be calculated as:

$$T(x) = T_2 e^{\mu\theta(x)\mathrm{sgn}(\dot{x})} \quad (6.2)$$

where $\theta(x) = \int_0^x d\theta$ is the angle measured from the tangential direction of the sheath at the target end to that at position x. The tension on the control end is given by:

$$T_1 = T_2 e^{\mu\theta\mathrm{sgn}(\dot{x})} \quad (6.3)$$

The assumption that the speed of the cable in the sheath is constant may not hold generally. However, this analysis can be a good approximation method in practice since the mass of the cable is too small to change the solution of $T(x)$, and it can be used in the experimental estimation of the friction coefficient, μ.

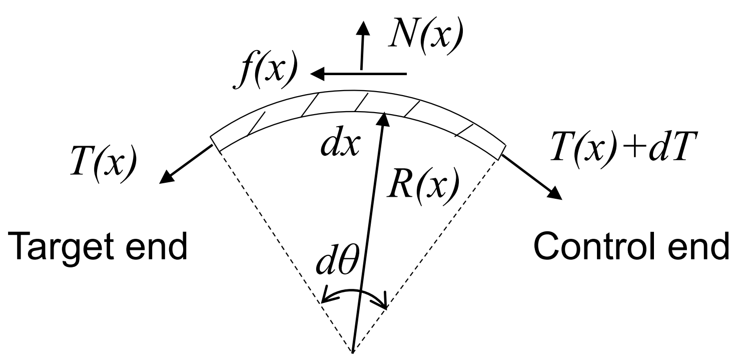

Figure 6.11: Infinitesimal element analysis of the cable

The experimental setup, as seen in Fig. 6.12(a), consists of an input motion module, an output load module and the Bowden cable structure for which the friction coefficient, μ, is estimated. The input motion module includes a rotary DC motor (Model 110966, Maxon

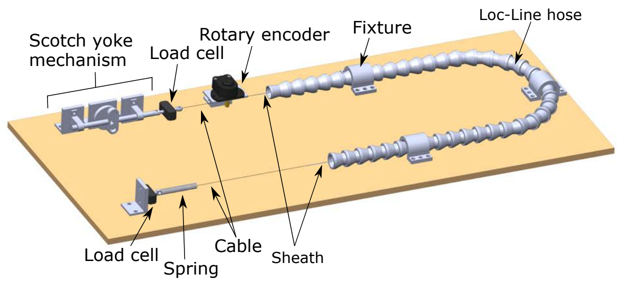

(a)

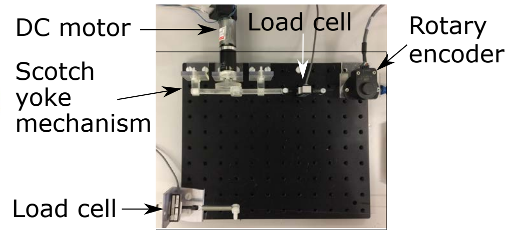

(b)

Figure 6.12: (a) Schematic of the experimental setup to estimate friction coefficient in the Bowden cable which has a semicircle bending shape (b) Actual experimental setup with the input control module (top side) and the output module (bottom side) (the Bowden cable structure is not shown)

Motor, Switzerland), a Scotch yoke mechanism, a load cell (Model MLP-10, Transducer Techniques, USA) and a rotary encoder, and the output load module includes a load cell and a spring of stiffness 131 N/m. The shape of the Bowden cable is fixed by a Loc-Line hose, and its control end and target end are connected to the load cell in the input motion module and the spring in the output load module, respectively, as shown in Fig. 6.12. When the DC motor is controlled by a servo controller to rotate at a constant speed, the constant rotational speed is converted to a sinusoidal translational speed of the reciprocal part in the Scotch yoke mechanism, and the cable also moves in a sinusoidal way along the natural coordinate. The amplitude of the sinusoidal motion is determined by the distance of the pin that engages with the horizontal slider from the center of the disk and was set to be 12 mm, which is within the range of cable displacement required for the actual application to actuate the MINIR-II robot.The pretension provided by the spring makes the tendon always remain in tension in its back and forth motion, considering no compression can be applied to a cable. The spring stiffness was chosen to allow the force measured to range less than 10 N during the $\pm$12 mm cable displacement, which is again what is expected in the actual application. In the experiment, the input tension T_1 measured by the load cell in the input motion module and the output load T_2 measured by the load cell in the output load module are sampled in different conditions, and they are used to estimate the friction coefficient μ.

In the experiments, if the angle of the target end of the cable with respect to the control end is fixed at π, there are three other variables that could generate different test conditions. The variables are the shape of the cable, the rotating speed of the DC motor and the pre-tension in the spring. We performed experiments using various combinations of the three variables, all of which are listed in Table 6.1. The plot of the relationship of the input force, T_1, and the output force, T_2, is shown in Fig. 6.14 for Trial 2. The flat part of the plot is the dead zone of the motion under friction, and the two inclined curves indicate the motion under dynamic friction, which can be described by Eq. (6.3). When the cable moves to the control end, $\dot{x}$ is positive and the ratio

$$\frac{T_1}{T_2} = e^{-\mu\pi}$$

is the slope of the right inclined curve in Fig. friction. When the cable moves to the target end, $\dot{x}$ is negative and the ratio

$$\frac{T_1}{T_2} = e^{\mu\pi}$$

is the slope of the left inclined curve. One can fit the data for the inclined curves by two linear functions with the constraint $k_1 k_2 = 1$, where k_1 and k_2 are slopes of the two functions, and the friction coefficient can be estimated by:

$$\mu = \frac{\log(k_1)}{\pi} = 0.051$$

For different test conditions using different values of variables, the estimation of μ was conducted and is listed in Table. 6.1. The estimated value of μ does not change significantly for different conditions, indicating that μ is insensitive to the three variables and the relationship in Eq. (6.3) is valid.

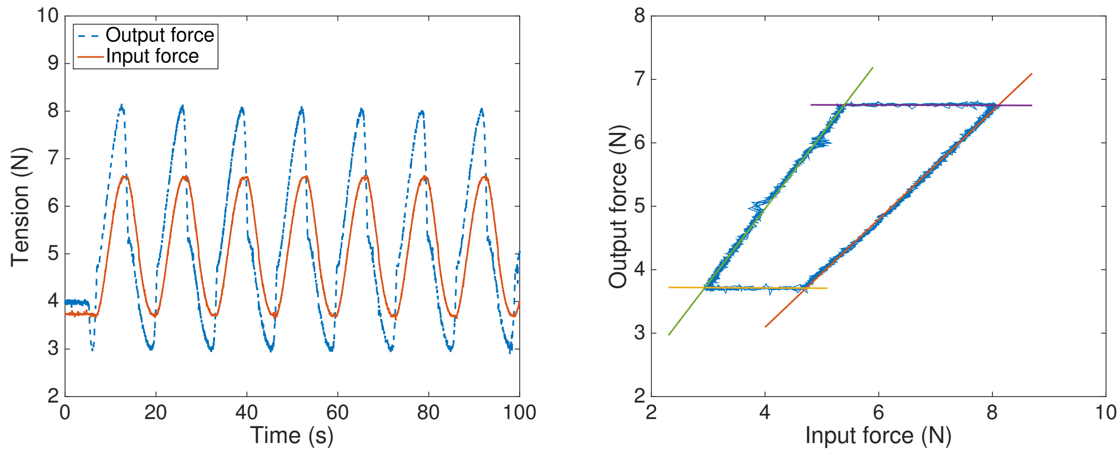

(a) (b)

Figure 6.13: (a) Changes in the output and input tension in response to the sinusoidal cable displacement caused by the scotch yoke mechanism (b) Hysteresis due to friction observed during the characterization experiment. Four straight lines associated with the sliding and pre-sliding phases of the cable motion are identified.

Table 6.1: Friction coefficient estimated for different test conditions - pretension, cable shape, and motor rotation speed

Trial	Pretension (N)	Cable shape	Rotation speed (RPM)	Estimated μ
1	1.8	semicircle	4.5	0.053
2	3.8	semicircle	4.5	0.051
3	1.5	rectangular	4.5	0.050
4	2.1	rectangular	4.5	0.053
5	2.7	rectangular	2.5	0.055

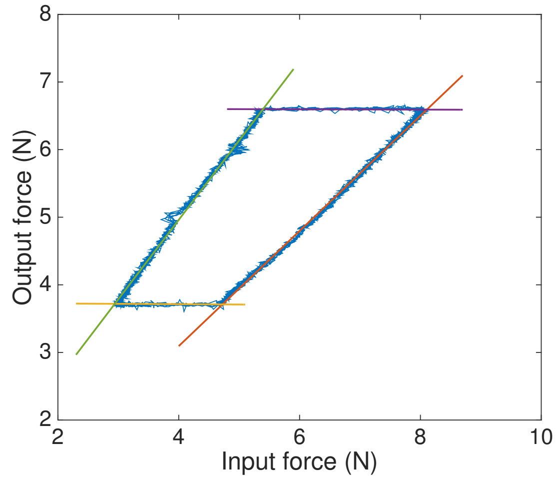

Figure 6.14: Hysteresis due to friction observed during the characterization experiment. Four straight lines associated with the sliding and pre-sliding phases of the cable motion are identified.

6.6 Experimental Setups

Evaluation of the robot was performed in two important aspects: bending angles of the robot segments and end effector forces of the robot segments. In the current work, only the middle segment and the end segment were actuated and had their performance evaluated. The actuators used in this work are linear actuators that are not MRI compatible and therefore will not be implemented in the final prototype. However, they are inexpensive actuator option to evaluate the effectiveness of this remotely-actuated system. The base segment is expected to largely maintain its straight configuration in the actual application and would only be actuated in rare circumstances when some residual tumor shifts to a location far from the initially planned trajectory of the neuroendoport. However, in our future work, the base segment would also be equipped with its own set of actuators.

6.6.1 Relationship between Cable Displacement and Robot Segment Displacement

The tendon displacement and robot segment bending angle was investigated using the same setup shown in Fig. 6.15(a), except that the force sensors at the tip of the linear actuator and near the robot segment were removed. Markers were attached to the segment disks of the

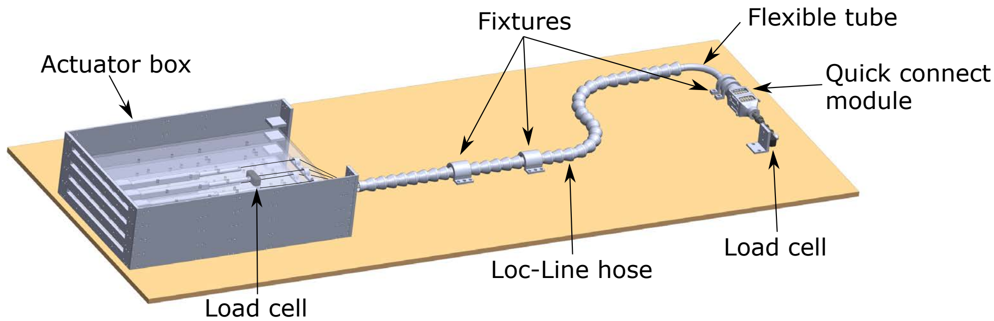

(a)

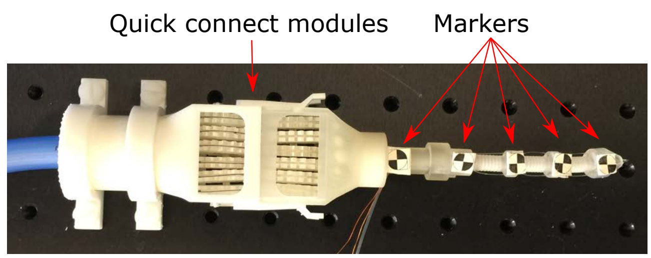

(b)

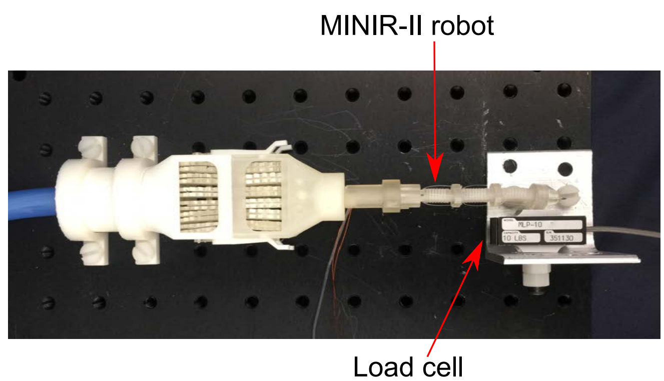

(c)

Figure 6.15: (a) Schematic of the experimental setup to investigate the relationship between tension of the cable by the actuator and output force at the robot segment). The same setup is used for the displacement characterization experiments. (b) Photo of the robot module with markers attached at its segment disks during the displacement characterization experiment. (c) Photo of the robot module during the force characterization experiment

robot instead, as shown in Fig. 6.15(b). A virtual vector is formed between the two markers and the angle subtended by the two vectors is the bending angle of a particular robot segment. The markers were constantly being tracked by the stereoscopic Microntracker (ClaroNav, Inc., Canada). The linear actuators have been calibrated to obtain the relationship between the voltage supplied and its displacement, which was found to be linear with an R^2 value of 0.96. Since each robot segment was controlled by one pair of linear actuators, the extension of one linear actuator is accompanied simultaneously by the retraction of its antagonistic paired actuator. The linear actuators were displaced by up to 10 mm with 2 mm interval and the corresponding bending angles of the actuated robot segment was recorded.

6.6.2 Relationship between Input Force and Output Force

In the experiment to investigate the relationship between input tendon tension and output end effector force, a three-level actuator box was constructed out of acrylic plates. It contains eight linear actuators (Model L16-P, Actuonix, Canada), equally divided between the base level and middle level of the box. A load cell was attached to the extending rod of the linear actuator, as shown in Fig. 6.15, to measure the tendon tension supplied to the system. On the other hand, the robot segment (either the middle or end segment) that is under investigation is placed against another load cell (see Fig. 6.15(c)) that measured the end effector force when the robot segment is in the straight configuration. The actuator box was taped to the table surface using a strong double-sided tape while the Bowden cable structure and the quick connect modules were fixed on the table using plastic fixtures. These steps were taken to ensure that the force exerted by the actuators would be transmitted to the robot segment effectively. During the experiment, the linear actuator was allowed to retract to actuate the robot segment until the robot segment shows sign of buckling in its spring backbone.

6.6.3 System Evaluation

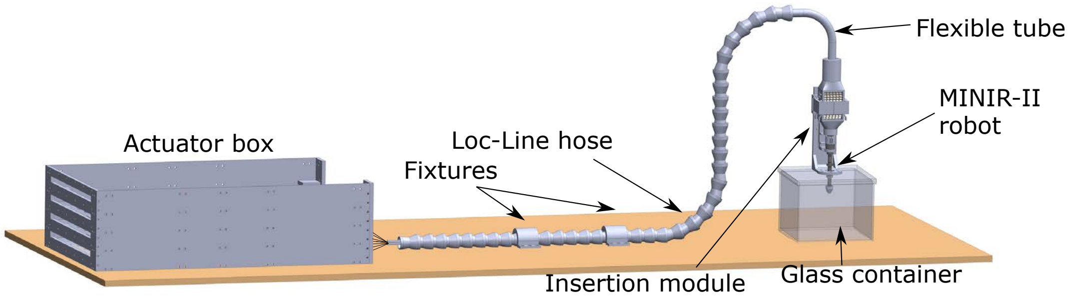

(a)

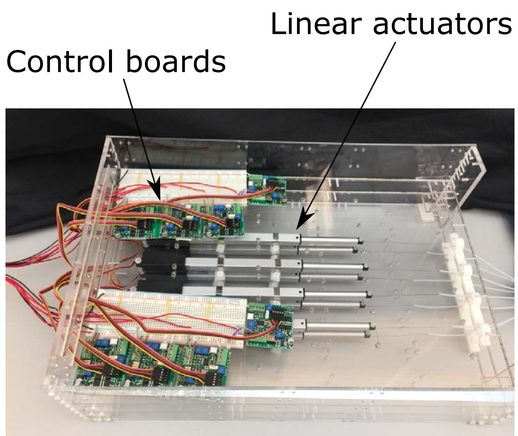

(b)

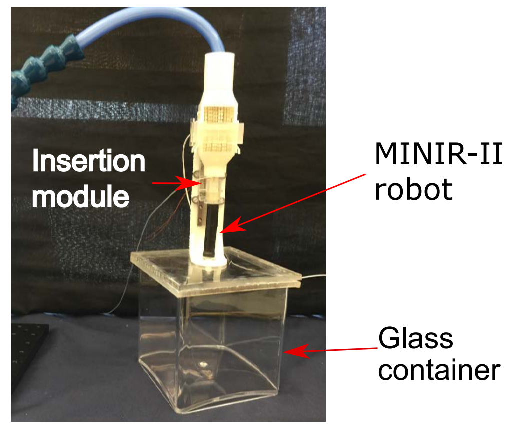

(c)

Figure 6.16: (a) Schematic of the experimental setup to investigate functionality of the robotic system (b) Photo of the robot module secured to the insertion module (c) Photo of the actuator box

The entire robotic system was put together for functionality and motion capability evaluation, as shown in Fig. 6.16. It consists of the actuator box with eight linear actuators, eight controller boards, a standing Bowden cable structure, robot module that was secured to the insertion module, a glass vase filled with phantom brain tissue and phantom brain tumor, and other components that are not shown in Fig. 6.16 such as a computer with a 16-bit data acquisition board (Model 826, Sensoray, USA), a power supply, and the modular control system (MSC, SmarAct, Germany) for the piezoelectric linear actuator. The phantom tissues are made of gelatin (Knox, Kraft Foods Global Inc., USA) of 2% by weight. The robot module was lowered and raised by the piezoelectric linear actuator through the graphical user interface provided by SmarAct and the end segment was moved back and forth in the gelatin.

6.7 Results and Discussion

6.7.1 Relationship between Cable Displacement and Robot Segment Displacement

As shown in Fig.6.17(a), the step inputs in displacement of the cable caused by the linear actuator resulted in stable bending angle changes in the robot segments. The delay between the time when actuation command was given and the initiation of the robot motion was on average 0.5 s which is negligible. Fig. 6.17(b) shows that the bending angle varies fairly linearly with the tendon displacement and becomes nonlinear at larger angles beyond 20°.

The kinematics of the standalone MINIR-II robot has been derived in the previous work [193]. Using small angle approximation, the bending angle and the tendon displacement form a linear relationship. At larger bending deflection, there is an approximately 10% nonlinearity in the relationship. Our experimental data follows a similar trend. However, a more detailed model that investigates the effect of the Bowden cable setup and gear boxes on the bending angle-tendon displacement relationship will be

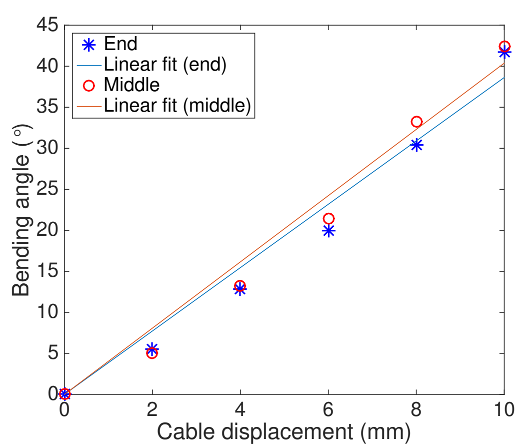

Figure 6.17: Experimental relationship between tendon displacement and bending angle of the robot segment

6.7.2 Relationship between Input Force and Output Force

The force at the end effector was plotted against the tendon tension applied for both the end segment and the middle segment in Figs. 6.18(a) and 6.18(b). The input and output forces form a linear relationship with an R^2 value of 0.9715 and 0.9837 for the end segment and middle segment, respectively, when the robot is in the straight configuration. As investigated in the previous section, the input and output forces for the Bowden cable structure have a linear relationship. The model developed in our previous work [193] also shows that the end effector force has a linear relationship with the cable tension when the robot is in its straight configuration. Assuming a linear frictional effect from the gears in the quick connect modules, the experimental results agrees with our expectation. A detailed theoretical modeling of the friction loss when the cables pass through the gears and the quick connect modules will be part of our future work.

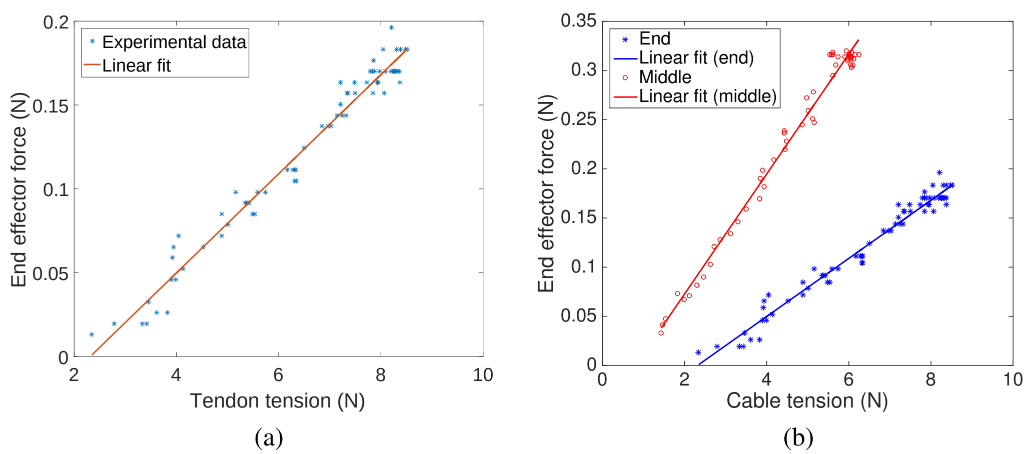

Figure 6.18: Relationship between tendon tension and the end effector force at the (a) end segment and (b) middle segment of the robot

6.7.3 Implementation of the Robotic System

Two different procedures were investigated in this section: the insertion and penetration of the robot through the ”burr hole” of 15 mm diameter we made in the cover of the glass

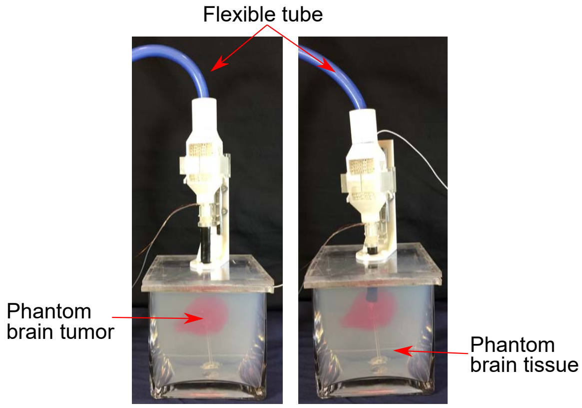

(a)

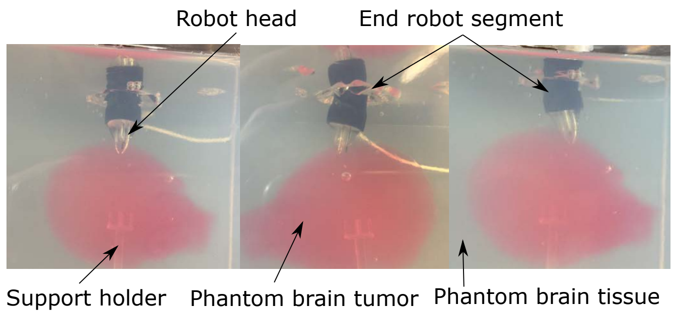

(b)

Figure 6.19: (a) Before and after insertion of the robot into the gelatin (b) The end robot segment in three different configurations during its 2-DoF motion

container and the motion capability of the robot end segment in two DoFs. The lowering of the piezoelectric linear actuator successfully inserted the robot along a straight trajectory into the phantom brain tissue and towards the phantom brain tumor (colored red), as shown in Fig. 6.19(a). The end segment of the robot was bent back and forth in both pitch and yaw directions, as shown in Fig. 6.19(b).

6.8 Summary

A new remotely actuated robotic system was developed for the spring-based MINIR-II neurosurgical robot using a fully MRI-compatible Bowden cable structure and 3-D printed quick connect modules. An insertion module was developed as a platform that could be head mounted and a piezoelectric linear actuator was integrated to provide the linear motion during insertion and retraction. A friction model was utilized to simulate the friction behavior in the Bowden cable structure and characterization experiment making use of the scotch yoke mechanism was performed to verify the model that hypothesizes a small friction loss in the Bowden cable. Experiments to investigate the relationship between the input cable tension and output end effector force as well as that between cable displacement and robot segment bending angle were performed with satisfactory results. This work showed the successful development of a remotely-actuated neurosurgical robotic system with a compact quick connect robot module and a light-weight head mounted platform. However, large force transmission loss was found in this flexible transmission design, therefore prompting a much improved design. Electric linear actuators that were used in this work would be replaced with ultrasonic motors in the next chapter.

CHAPTER 7

REMOTE ACTUATION: RIGID TRANSMISSION 1

7.1 Introduction

In Chapter 6, we developed an MRI-compatible Bowden cable transmission mechanism [252] to actuate the MINIR-II robot. Based on the preliminary evaluation and the drawbacks observed such as backlash and excessive friction in the flexible tube, we developed a more robust transmission using the combination of timing belts, kevlar wires, and gear-pulley combinations. We integrated a switching mechanism to reduce the number of motors required and a novel quick-connect mechanism. The twelve linear electric motors were replaced by three ultrasonic motors. Only the skull-mounted head frame was preserved from our previous design. Part of the work described in this chapter was done in collaboration with the former post-doc in the lab, Dr. Xuefeng Wang.

7.2 Objectives and Overview of the Robotic System

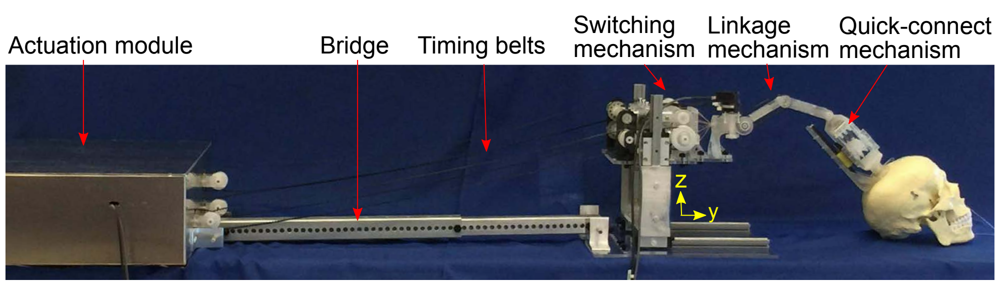

Figure 7.1: The complete neurosurgical robotic system consisting of actuation module, transmission module (switching, linkage, and quick-connect mechanism), and robot module (inside the skull model).

7.2.1 Design criteria

The ultimate goal of this work was to develop a robust remotely-actuated neurosurgical system to advance and actuate the tendon-driven six-DoF MINIR-II robot [253]. To reliably actuate the robot, which would be head mounted on a patient's skull, in the closed-bore MRI using ultrasonic motors, a transmission and actuation system have to be designed for it. The design criteria can be classified into five aspects: force transmission efficiency, mobility, convenience, MRI-compatibility and complexity of the overall system.

1. Force transmission efficiency: The relative motion between the tendons and the movable section of the Bowden cable transmission structure in our previous design [252] led to significant loss in force transmission efficiency. A transmission mechanism that is movable during robot insertion and retraction and remains rigid during robot actuation has to be designed. **2. Mobility**: The placement of the robot at the predetermined incision site on the patient's skull requires the development of a positioning mechanism that has high mobility. Additionally, we have to pass twelve tendons through the positioning mechanism to reach and actuate the 6-DoF robot at the distal end. Thoughtful design is needed in the transmission to reduce the coupling between the routing path of the tendons and the highly mobile positioning mechanism. **3. MRI-compatibility**: Only non-magnetic materials are used to construct the robotic system to prevent any safety hazard in the MRI room. Electronic devices can result in artifacts in MR images and need to be isolated electromagnetically. Previous research [3] also shows that placing actuators at least 1 m from the MRI isocenter is an effective solution. **4. Convenience**: To improve the process flow during setting up of the robotic system, the actuation module should be easily decoupled from the positioning/transmission mechanism. A quick-connect mechanism is needed to allow easy disassembly and replacement of the disposable and patient specific robot so that the robotic system can be reused. With the use of a skull-mounted head frame to which the robot is attached to, the robot's initial trajectory is already aligned with the incision direction, thus skipping the pre-operative step that would register a standalone robot trajectory to the surgical site. **5. Complexity**: High complexity, due to the large number of actuators to operate the six-DoF robot and position the robot in 3D space, reduces robustness and increase size and cost. Thus, some DoFs in positioning the robot are manually operated and a switching mechanism is designed to reduce the number of actuators required.

7.2.2 Overview of the Robotic System

The MRI-compatible neurosurgical robotic system consists of three modules: the actuation module, followed by the transmission module and finally the robot module, as shown in Fig. 7.1. The overall operation of the robotic system can be described as follows. At first, user commands are provided into the computer located in the MRI control room. The A/D data acquisition board (Model 826, Sensoray Co., Inc.) in the computer sends out analog signals carrying the commands through the signal cables that passes the penetration panel in the wall between the MRI room and the control room. The signal cables reach the actuation module where the ultrasonic motors and their drivers are. Rotations of different motors controlled by the commands are transmitted to the transmission module before being converted into robot motion.

The actuation module contains three ultrasonic motors (USR60-E3NT, Shinsei Corporation, Japan), four drivers (D6060S), and a 24 V battery (Tenergy 24V 10kmAh NiMH battery,). Four 9-pin brass D-sub connectors (Molex, LLC) are attached to the back of the box to receive the signal cables while three timing-belt pulleys are attached to the front of the box to transmit the motor motion outside the box. The motor rotation is transmitted to the transmission module using long-span timing belts, which can be easily mounted on and removed from the transmission module. The actuation module also features a bridge, as shown in Fig. 7.1, that physically connects the Faraday cage and the rest of the robotic system. The bridge, which can be extended to 1.5 meters, consists of two square cross section bars of different diameters with dense through holes along the longitudinal axis on their sides. The bridge is extended and fixed when the timing belts are in a reasonable amount of tension that prevents tooth jumping in the pulleys. It can be removed from both the Faraday cage and the transmission module during transportation of the robotic system.

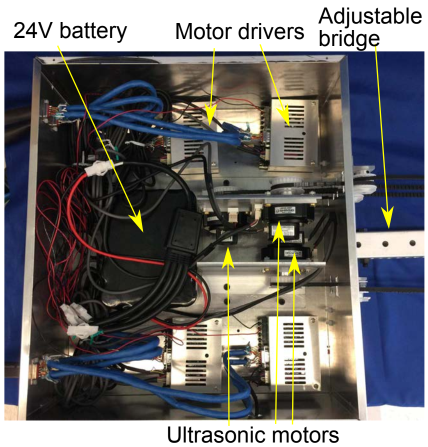

(a)

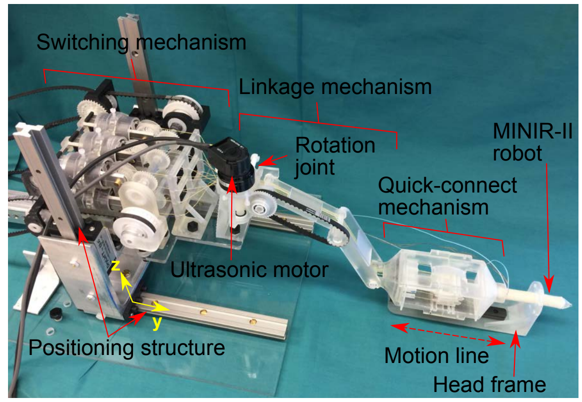

(b)

Figure 7.2: (a) Actuation module and (b) transmission module shown together with the positioning structure and the head frame.

The transmission module has five main functions: bridging the actuation module and the robot module, positioning the robot module in 3-D space around the incision site, selecting the robot segment to be actuated, enabling efficient force transmission, and enabling quick connection and disconnection of the disposable part of the robot module. To implement all these functionalities, the transmission module consists of four important mechanisms/parts: the positioning structure, the switching mechanism, the linkage mechanism, and the quick-connect mechanism, as shown in Fig. 7.2(b). The positioning structure caters to the different incision locations around the skull. It holds a plate on which the switching mechanism is placed. Through manual adjustment, the switching mechanism, together with the rest of the transmission and robot module, can be moved in y- and z-axis independently (refer to Fig. 7.1). There is also a rotation joint at the base of the linkage mechanism to adjust the motion plane of the linkage mechanism, as shown in Fig. 7.2(b). The detailed design of the other three components of the transmission module will be discussed in Section III.

The robot module consists of the MINIR-II robot and a skull-mounted head frame with a rail and carriage. The maximum height that the linkage mechanism and the head frame can reach is 25 cm, which is enough to fit in the room above a person's skull in a standard wide-bore MRI. The detailed information about the MINIR-II robot can be found in [253]. As a summary, it is a tendon driven flexible robot, whose backbone comprised of three interconnected spring segments. Each spring has two actuation DoFs controlled by two pairs of orthogonally oriented fish wires (referred to as ”tendons” in the rest of the paper), respectively. The robot is designed to meet several criteria, including a workspace to cover brain tumors of up to 40 mm diameter, a bending angle of at least 90° in each segment, an outer diameter than can fit inside a trans-sulcal endoport such as the NICO BrainPath®, and a lumen that can incorporate multiple instruments including bipolar cautery probes, suction tube, and irrigation tube. In the MINIR-II robot, tendons for a distal segment are passed along the central axis of the proximal segments to minimize segment coupling [253]. The coupling effect is further minimized through the addition of sheath (Teflon tubing) for each tendon inside the robot to prevent tendon tangling. The robot module is placed on a rail attached to the skull-mounted head frame [252] and will be inserted and retracted by an ultrasonic motor at the base of the linkage mechanism. The rail is designed to allow insertion and retraction of the robot along its motion trajectory for about 65 mm.

7.3 Design of the Transmission Module

7.3.1 Quick-Connect Mechanism

In the quick-connect mechanism, twelve tendons from the robot and twelve Kevlar strings (referred to as ”cables” in the rest of the paper) from the transmission module need to be connected simultaneously and be free to move individually once connected to drive the robot. This quick-connect can be described as a two-level structure: a single connector at the low level and the chassis to integrate twelve connectors at the high level.

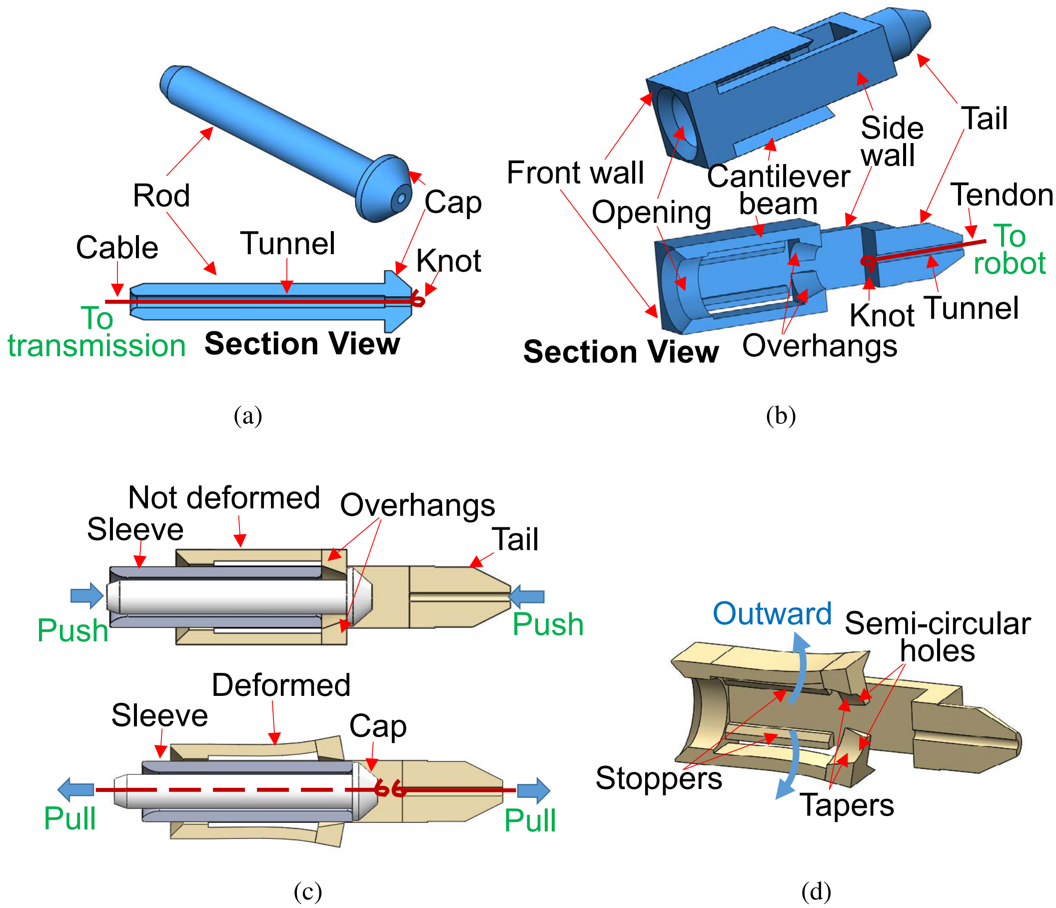

Figure 7.3: The (a) male part and (b) female part of the single connector. (c) Schematics showing quick connection (top) and disconnection (bottom) of the single connector. (d) Detailed schematic of how the cantilever of the female part gets deformed during the disconnection.

Design and principle of a single connector

Each connector consists of a male part and a female part, and is responsible for one segment motion direction in one DoF. The cable from the transmission is attached to the male part while the tendon from the robot is attached to the female part. The male part is a rod with a conical cap and a tunnel along its long axis, as shown in Fig. 8.8(a). The female part has a conical tail with a tunnel that allows the passage of the tendon from the robot which then terminates with a knot, as show in Fig. 8.8(b). The cantilevers, facing each other, have their fixed ends attached to the front wall. Their free ends have overhangs that form a circular entrance. Stoppers are built on the side walls just underneath the cantilever beams to stop the inward deformation caused by the pulling force, as shown in Fig. 8.8(d). The connection principle of the male and female parts is similar to the snap fit connection. Once inserted, the back of the male part pushes against the retaining sides of the overhangs when it is being pulled by the transmission to actuate a robot segment. To disassemble the connector, a rigid sleeve is inserted into the female part until it pushes the overhangs and keeps the cantilever beams open. Together with the sleeve, the male part is removed from the female part when the cable is pulled, as shown in Fig. 8.8(c).

Housing of the quick-connect mechanism and the connection/disconnection procedure

The quick-connect chassis consists of a proximal housing and a distal housing. The twelve cables and twelve tendons are arranged into a 4 columns x 3 rows matrix in the proximal housing and distal housing, respectively. The 4 columns represents the two DoFs of each segment while the 3 rows represent the 3 different robot segments. The proximal housing has a base plate, a connection plate, and a disconnection plate, arranged in the descending order of their proximity to the male connectors, as shown in Fig. 7.4. The initial configuration of the twelve connectors in both proximal and distal housings are shown in Fig. 7.4(a). The plate stoppers are used to hold the disconnection plate and the position plate in place. When making the quick connection, the distal housing is aligned with the proximal housing

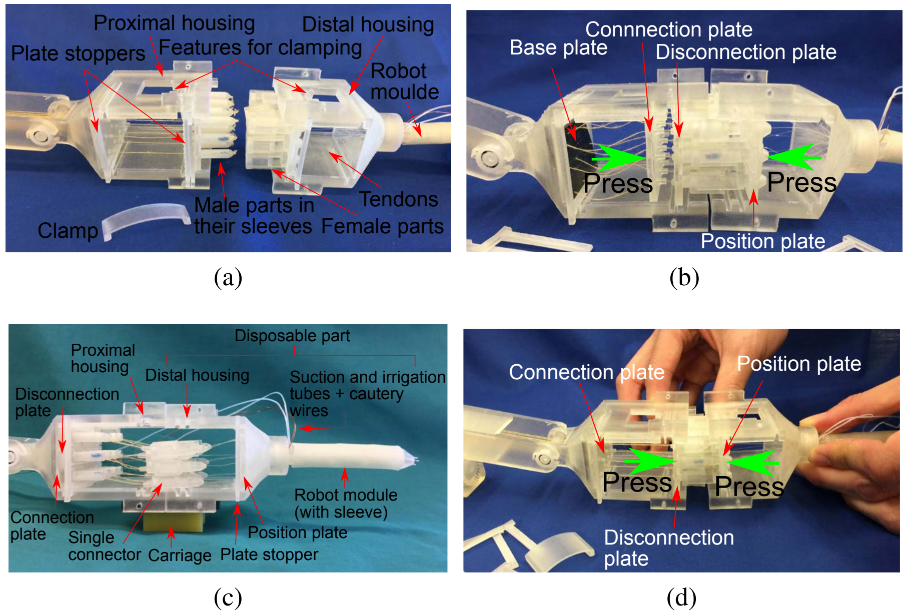

Figure 7.4: (a) The proximal and distal quick-connect housing before connection. (b) Press the connection plate and the position plate together during connection. (c) The connected quick-connect mechanism. (3) Press the disconnection plate and the position plate together during disconnection.

to allow the male parts (and the twelve sleeves) to be inserted into the female parts smoothly without deforming the cantilever beams. The plate stoppers are removed, after which the connection plate and the position plate are pressed together to insert the male parts through the overhangs (Fig. 7.4(b)). The quick connection of twelve connectors is then simultaneously formed. The proximal and distal housings are then clamped together using a clip on the top side of the housings, thus providing an initial slack in the cables/tendons.

The disconnection starts by pressing together the disconnection plate and the position plate, allowing the sleeves to deform the cantilevers in the female part (Fig. 7.4(d)). While the distal housing is being pulled away from the proximal housing, the disconnection plate in the proximal housing continues to be pressed against the male parts to provide a tension force that simultaneously disconnect twelve male parts out from their corresponding female parts.

7.3.2 Linkage Mechanism

Design of the linkage mechanism

The linkage mechanism is a movable mechanism to insert and retract the robot along a slider without displacing the cables that pass through it. Once the robot is inserted, it has to maintain its structural shape to prevent unnecessary loss in force transmission. Thus, a rigid crank-slider mechanism with one DoF actuated by an ultrasonic motor (USR30-E3NT, Shinsei Corporation, Japan) is used.

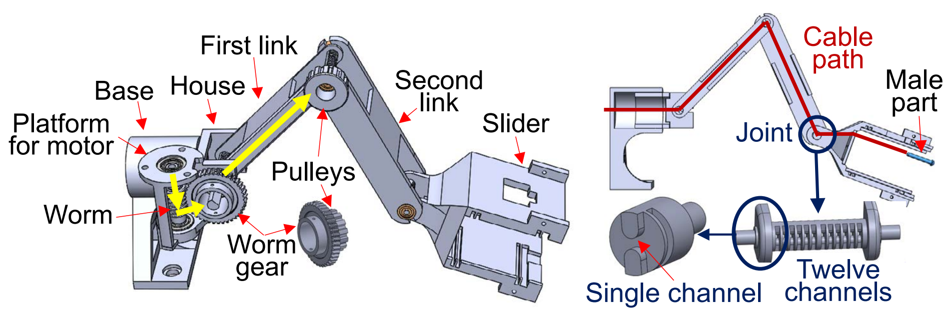

(a) (b)

Figure 7.5: (a) Schematic of the linkage mechanism with part of the quick-connect mechanism (slider) (Yellow line shows the actuation path to deform the linkage mechanism during insertion and retraction of the robot). (b) Schematics of the two links and the important channels in each joint that allow passage of cables.

The mechanism consists of a base, two links and a slider, as shown in Fig. 8.11(a). The motion line of the slider is fixed by the head frame that is mounted on the skull at the incision opening. At the base, there is a house for the first revolute joint, a platform to hold the motor and a pair of worm and worm gear to act as the transmission of the motor. The motor and worm gear combination prevents the linkage mechanism from changing shape once the robot is inserted to its target depth, allowing efficient force transmission in the tendons. Another toothed pulley is fixed to the joint between the two links and connected to the first pulley through a timing belt. Thus, the second link is rotated directly by the motor and the motion of the motor translate into forward and backward motion of the slider. The proximity of this particular ultrasonic motor to the MRI isocenter may require it to not be turned on during live MRI imaging.

The cables go through twelve channels in the center of the joint shafts of the linkage mechanism, as shown in Fig. 8.11(b) to make sure the tendon displacement is minimal during insertion and retraction of the robot.

7.3.3 Switching Mechanism

Overview and power flow of the switching mechanism

The switching mechanism reduces the required number of motors by allowing 2-DoF control of only one robot segment at one time. In most cases, only the end segment needs to be actuated to sweep across the entire brain tumor. Therefore, the critical function of the robot is preserved even when the reduced number of motors. There are two driving motors to control the two DoFs of each robot segment and another selector motor to choose the robot segment to control. The switching mechanism, as shown in Fig. 7.6(a), consists of the driving part (two receiving pulleys) and the selection part (one receiving pulley) with both receiving power from the motors via three timing belts. The two receiving pulleys for the driving part are connected to another two driving pulleys via short timing belts. To achieve satisfactory tension in these belts, we went through multiple trials and errors to finalize the distance between the centers of every pair of pulleys. In the driving part, there are six drive units, each of which controls one DoF of the robot. The pair of cables originating from one drive unit should be connected to the pair of tendons responsible for a particular degree-of-freedom (DoF) in a robot segment. The two pairs of Kevlar strings originating from the top and bottom drive units in the same column should be connected to the two DoFs of the same robot segment. The selection part consists of six cams that would engage a pair of drive units (in the same column of the switching framework) with their corresponding drive gears on the power train at one time, allowing 3-D motion of a particular robot segment. When a new pair of drive units are engaged, the previously engaged drive units are disengaged from the power train and their motion are locked to fix the bending position of the previously actuated robot segment. By engaging (unlocking) and disengaging (locking) the different pairs of drive units, all three robot segments can be controlled by three motors to approximate the performance with six motors. In this way, the number of ultrasonic motors required is halved without making compromise on the critical functionalities of the robotic system.

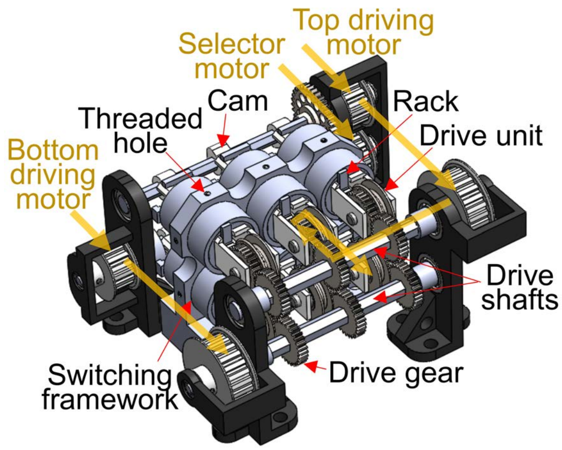

(a)

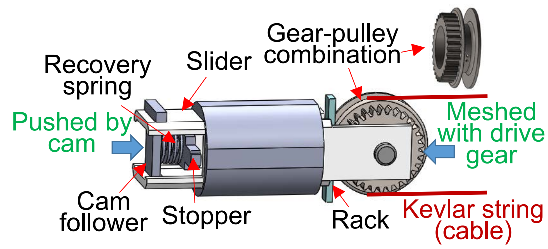

(b)

Figure 7.6: (a) Schematic of the switching mechanism that receives timing belts from the motors (Yellow line shows the power flow) (b) Schematic of the singe drive unit that contains mainly a slider and a gear-pulley combination

Drive part of the switching mechanism

As shown in Fig. 7.6(b), each drive unit is composed of a square cross-section aluminum slider, a gear-pulley combination and a recovery compression spring. A Kevlar string is wound on the pulley, resulting in two antagonistic cables being passed towards the robot. The recovery spring is installed between a plate (cam follower) at the tail of the slider and a stopper that is fixed on the switching framework. During contact between the cam and its cam follower, the gear-pulley combination moves away from a rack fixed on the framework to mesh with a drive gear located on the drive shaft. When the cam moves away from its cam follower, the recovery spring pulls the slider back, allowing the gear-pulley combination to mesh with the rack, thus locking the position of a robot segment.

Selection part of the switching mechanism

Cams in the selection part are used to push drive units forward and guide them back with recovery force from the springs. Each gear-pulley combination of the drive unit should always be meshed with either the drive gear or the rack. In our design, the profile of a cam consists of two arcs. One arc makes up the majority of the cam profile while the other one creates the protrusion of the cam. The radial difference between the two arcs, as indicated by the length difference between the two tangent lines to the two arcs, is 1.5 times the tooth height of the gear, as shown in Fig. 7.7(b). The cam angle, ω, can be defined as the angle between the vector at which the cam nose is pointing at and the global horizontal line. The entire selection part consists of two rows of cams, arranged behind the cam follower of every drive unit, as shown in Fig. 7.7(a). Since only one selector motor is used to activate 2 DoFs of one robot segment, one motor operation needs to be able to activate two cams to push their respective drive units forwards. This is achieved by connecting the selector motor via a timing belt with the bottom cam shaft, which is in turn connected to the top cam shaft through a pair of meshed gears. The top and bottom cams in a particular column are made to have cam angles of the same magnitude but opposite signs, as shown in Fig. 7.7.

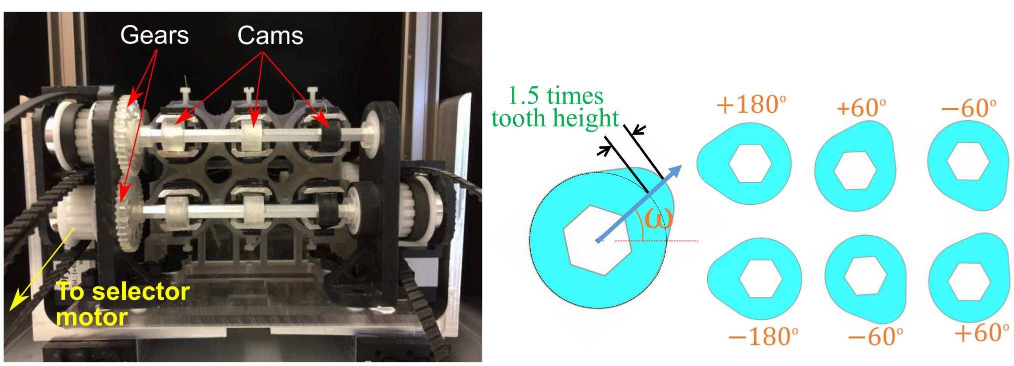

(a) (b)

Figure 7.7: (a) Rear view of the switching mechanism showing the positions of the cams (Yellow line shows the power flow from the selector motor to the cams) (b) Schematic showing the cam and the three different orientations for engagement of each of the three robot segments

Table 7.1: Mechanical properties of the robotic system

Backlash (mm)	1st stage coefficient ($^\circ/mm$)	2nd stage coefficient ($^\circ/mm$)	Linearity (R^2)	Accuracy (%)
±1.66	0.497±0.08	6.065±0.03	0.998	1.33

7.4 Results and Discussion

7.4.1 Preliminary Mechanical Properties Characterization

Preliminary characterization experiments were performed to measure the mechanical properties of the robotic system. The extreme backlash for 6 DoFs was determined to be ±1.66 mm, which mainly comes from the accumulated slack of belts and cables. We will reduce backlash by modifying the transmission desgn in our future work. There was a bilinear relationship between the output bending angle and input tendon displacement. The 1^{st} linear stage, covering 0-10°of bending angles, is dominated by uncertainties such as coil compression, structural deformation, and tendon slack. The 2^{nd} stage, covering all bending angles beyond 10°, is dominated by the bending stiffness of the spring segment, thus leading to a significantly larger bending angle per mm of tendon displacement, compared to the first stage. The experimental relationship between bending angle and tendon displacement in both stages are fit with linear functions. The first stage has a linear coefficient of 0.497 °/mm with a repeatability of 0.08 °/mm and the second stage has a linear coefficient of 6.065 °/mm with a repeatability of 0.03 °/mm. The linearity of the second stage is characterized by an R-squared value of 0.998. Comparison between the theoretical model for the MINIR-II robot [253] and the experimental data in the 2^{nd} stage leads to an accuracy error of 1.33%. As we are planning to integrate Fiber Brag Grating (FBG) sensors along the robot body, we will also implement a robust feedback with feedforward controller, with the feedback component especially important to compensate for the uncertainties in the first stage of the robot motion.

7.4.2 Evaluation of Motion Range and Switching Mechanism Effectiveness

Each robot segment was actuated independently and bent between its two extrema, as shown in Fig. 7.8. The work ranges of the actuated segments and motion coupling effects were determined through a vision-tracking experiment, in which vision markers attached to the robot segments were tracked by the MicronTracker (Claron Technology Inc., Canada). The results are summarized in Table II. All segments could move nearly from $-90°$ to $90°$. The results also show the effectiveness of the switching mechanism in decoupling actuated robot segment from the other segments, as shown in Fig. 7.8(d). The base segment was engaged and bent to the negative direction in the first stage before the middle segment was engaged and bent to the positive direction in the second stage. Then, the end segment was actuated through two cycles to simulate the tumor removal procedure. In the last stage, the end, middle and base segments were moved back to their home configuration in order. Throughout this robot segment switching process, the drive units of the two non-actuated robot segments were locked to the racks very effectively and not engaged with the drive shaft, as proven by the minimal changes in the positions of non-actuated robot segments. The slight motion of 10° in the base segment as the middle segment was actuated is attributed to the imperfect tendon routing in the flexible robot and not the ineffectiveness of the switching mechanism. During actuation of different robot segments, there was no shape change in the linkage mechanism which was being locked in place by the block force of the ultrasonic motor, suggesting no relative motion between the linkage mechanism and the tendons. This indicates an improvement in the force transmission efficiency compared to our previous flexible transmission system [252].

7.4.3 Evaluation on Motion Capability

We inserted the MINIR-II robot into a brain-like phantom model made of 2% gelatin (Knox, USA), which has similar stiffness of around 1 kPa as that of the human brain. The phantom contains a tumor-like phantom in the center of it, as shown in Fig. 7.9(a).

Table 7.2: Work ranges and coupling variations of three robot segments

Actuated segment	Range (°)	Base variations (°)	Mid variations (°)	End variations (°)
Base	-89.4-89.4	N/A	4.2	0.9
Middle	-89.6-87.9	2.5	N/A	0.5
End	-82.1-83.5	0.3	0.2	N/A

The middle and end segment of the robot were actuated independently from the home configuration, as shown in Fig. 7.9(b), to verify its motion capability. In a separate experiment, the middle segment was actuated and locked in place before the end segment was actuated back and forth, as shown in Figs. 7.9(c-d). The videos for these experiments are attached as supplementary files.

7.4.4 Evaluation on MRI Compatibility

The MRI compatibility of the robotic system was verified by setting it up in a 7-Tesla MRI, as shown in Fig. 8.21(a). Two static MR images of the robot were taken before and after the robotic system was powered on. The powering on of the robotic system led to an SNR drop of 3.56% from 39.9 to 38.47. The image quality is further qualitatively evaluated by comparing the images acquired during the robot actuation process when the motor drivers were sending out signals to the motors for both DoFs of the end segment. A T2-weighted dynamic brain imaging sequence was performed to take 64 images at 2 frames per second and the robot end segment was bent to different configurations (it was being bent out of plane in the MR images shown in Figs. 8.21(b-d)). The robot motion caused the displacement of gelatin phantom, resulting in the white space around the robot. There is no visible artifact or observable degradation throughout the dynamic MR scanning procedure.

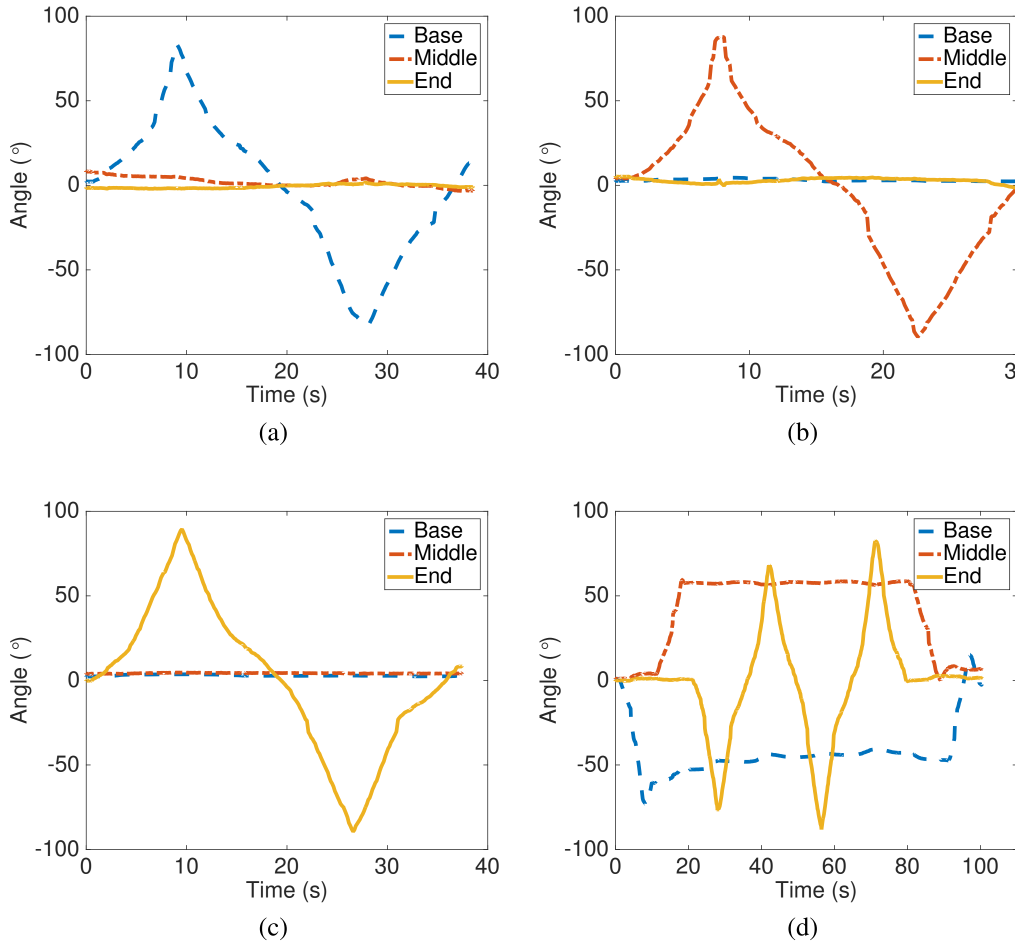

Figure 7.8: Angle change of all robot segments during actuation of the (a) base segment, (b) middle segment, and (c) end segment. (d) Angle change during sequential motion test of all robot segments.

7.5 Summary

A remotely actuated robotic system, consisting of an actuation module, a transmission module, and the MINIR-II robot, was developed. The novelties include using a switching mechanism to reduce the number of actuators required to replicate the functionalities of a 6-DoF robot, a quick-connect mechanism for assembly and disassembly of twelve tendons, and a linkage mechanism that improves force transmission efficiency. Preliminary evaluation showed a system that had sufficient working range, capability to move in the brain environment, and was MRI-compatible. The second linear stage of the input-output relationship closely matches the theoretical model. However, the system had its weakness

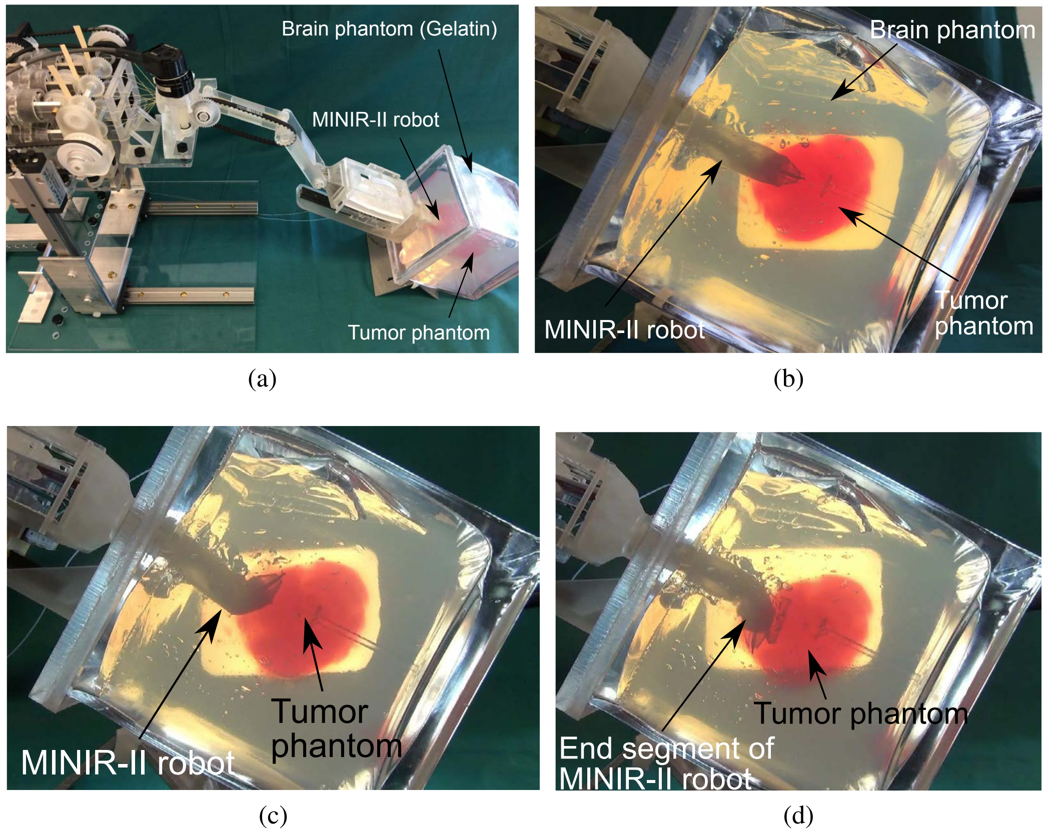

(a) (b) (c) (d)

Figure 7.9: (a) Experimental setup to test robot motion in brain phantom. Robot configuration (b) when it was not actuated, (c) when its end segment was actuated up, and (d) when its end segment was actuated down.

in backlash and unmodeled uncertainties for small bending angles. In the next chapter, we would make significant design changes to improve robustness of the transmission, which would in turn improve the open-loop control of the robot. We would also investigate the hysteresis behavior of the robotic system.

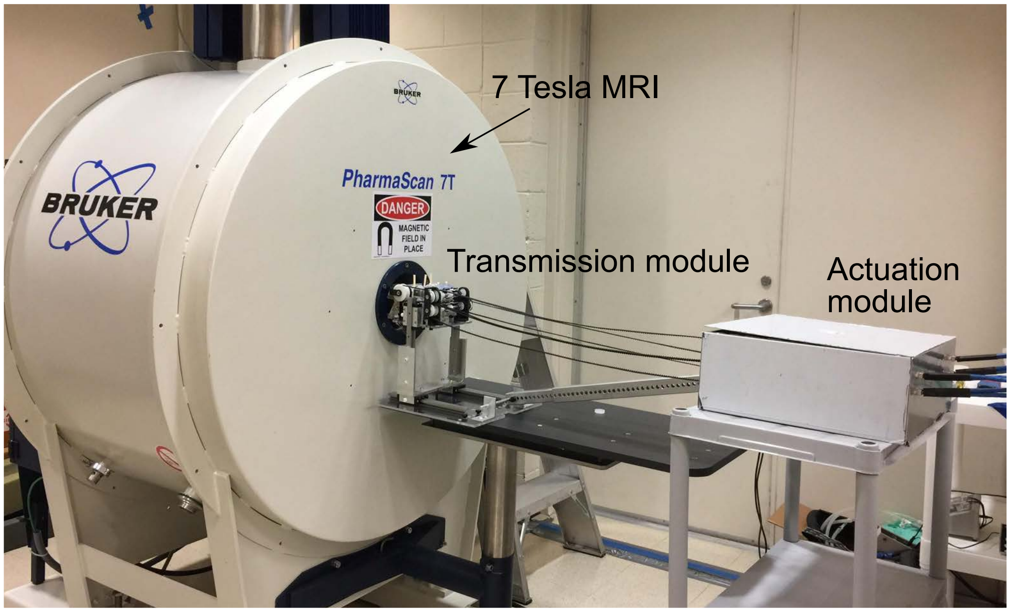

(a)

(b)

(c)

(d)

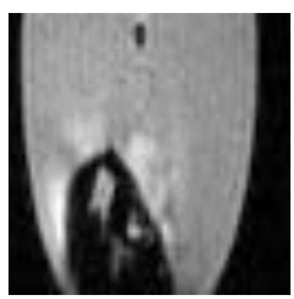

(e)

Figure 7.10: (a) The entire robotic setup in the MRI room. Dynamic MR images showing the robot end segment at the (b) 30th frame (c) 40th frame (d) 50th frame, and (e) 60th frame throughout the 32s actuation process.

CHAPTER 8

REMOTE ACTUATION: RIGID TRANSMISSION 2

8.1 Introduction

In this chapter, we introduced a remotely-actuated design that has the same setup configuration as Chapter 7 [254] but made significant design modifications to all three mechanisms in the transmission module, namely the switching mechanism, linkage mechanism, and quick connect mechanism. Hysteresis performance of the robotic system was also modeled and analyzed. Part of the work described in this chapter was done in collaboration with the former post-doc in the lab, Dr. Xuefeng Wang.

8.2 Overview of the neurosurgical robotic system and its operation

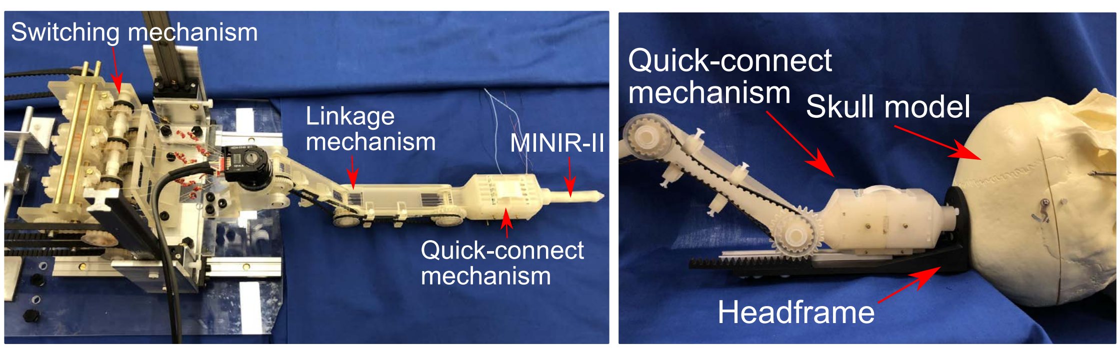

(a) (b)

Figure 8.1: (a) Transmission system consisting of switching mechanism, linkage mechanism, and quick-connect mechanism (b) Configuration of the robot when it is placed on the headframe and inserted into the skull

8.2.1 Design Changes

The neurosurgical robotic system consists of three modules: the actuation module, followed by the transmission module and finally the robot module. The power flow in the

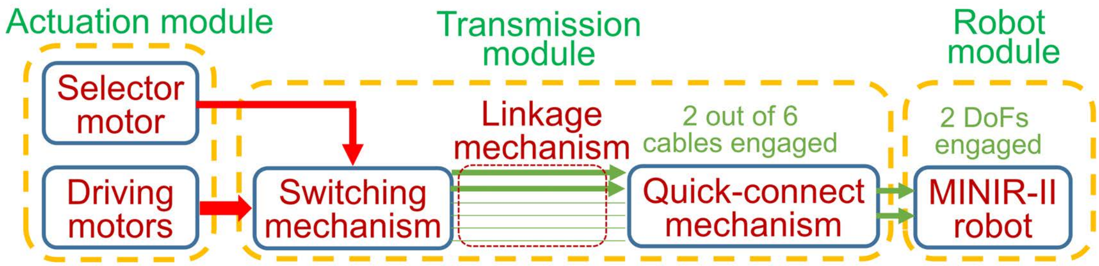

Figure 8.2: Power flow in the transmission module

transmission is summarized in Fig. 8.2. The motion of the selector motor that transmits to the switching mechanism engages two out of six pairs of Kevlar strings (referred to as cables in the rest of the paper) into the power train that is powered by two driving motors. These cables pass through the linkage mechanism and end in the proximal connector of the quick-connect mechanism. When the proximal and distal connectors are connected, pulling forces in those cables are transmitted to fish wires (referred to as tendons in the rest of the paper) in the robot module and finally converted to the bending forces of the robot.

During preliminary evaluation of our previous design [254], backlash was identified as one of the most concerning issues, which was observed in both timing belts and cables in the transmission. In this setup, a floated tensioner was therefore designed and used to tight the long-span belt to reduce the backlash in the timing belt, as shown in Fig. 8.3. There are two idlers and two timing-belt pulleys between the two walls of the tensioner. The timing-belt passes the left idler and is lifted up by the guide pulley. It then passes around the tension pulley on the top and the right idler on the bottom. Except for the tension pulley, other three pulleys have the fixed shafts. By moving the shaft of the tension pulley leftwards or rightwards, one can loose or tight the belt, respectively. The same bridge in [254] was placed between the box and the transmission module to counter the potential internal reaction force in the robotic system.

The cable backlash, on the other hand, comes from the transmission structure. Another issue is the robustness of the switching mechanism. Since the disengaging direction of the engaged unit is the same to the tension direction of cables on it, the unit will not return

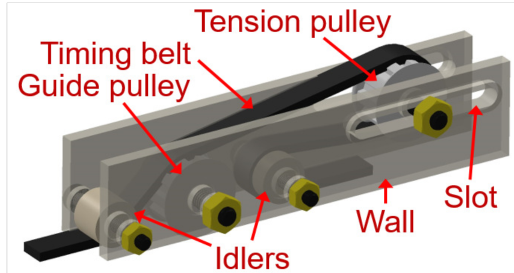

Figure 8.3: Schematic of the timing belt tensioner

to the disengaged position by the recovery spring when there is large tension in cables. Meanwhile, the unit movement also generates unexpected variations in the robot motion. Therefore, the direction of the unit movement is orthogonal to that of cables in the new switching mechanism, where side-surface teeth are designed here to implement the function.

The linkage mechanism is also improved in the new design to reduce the required force for the insertion of the robot. Considering there is no rotation of the robot during its insertion, a decoupled mechanism is developed for the belt drive so that we can directly actuate the distal joint of the the linkage system without affect the intermediate joints.

In the previous quick-connect mechanism [254], the male-female configuration ensures that there is no relative motion and no friction loss in its power train. However, the configuration couples the tension in the transmission cable and robot tendon once the two quick-connect halves are connected. Since tightening the cables will pre-compress the robot spring coils and may damage the robot as soon as the quick connection happens, we left significant slack in the transmission cables. By doing so, we introduced significant backlash in the transmission cables. In this work, gear pairs are adopted to decouple the tension in the quick-connect mechanism of the new design, which enable us to tighten the cables without causing pre-compression of the robot spring coils upon quick connection and thus reduce the backlash.

Based on the above improvements, we have developed a new transmission module, as shown in Fig. 8.1(a). The details about the design and development of each transmission mechanism are described in Section III.

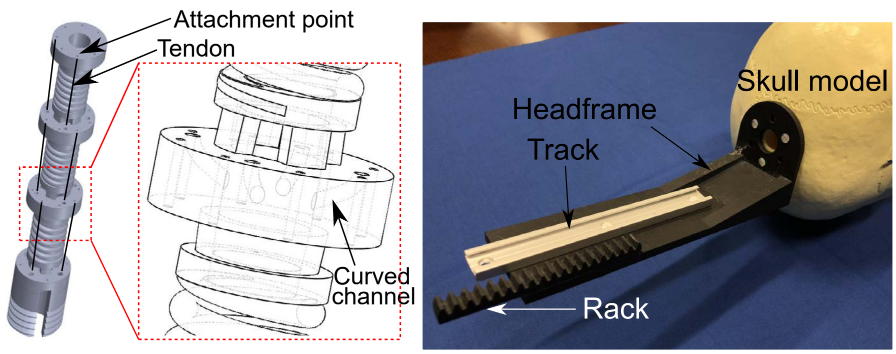

(a) (b)

Figure 8.4: (a) MINIR-II updated with curved channels for improved tendon routing and tendons spaced out by 30°for consecutive segments (b) Headframe with track and rack for facilitating the insertion and retraction of MINIR-II

The robot module is the MINIR-II prototype equipped with surgical instruments including a suction tube, an irrigation tube, and a bipolar electrocautery probe. The three-segmented backbone is 3-D printed in one single part file and requires no further assembly after the additive manufacturing process except tendon routing. In the MINIR-II robot, tendons are routed along a curved channel in the segment disk, as shown in Fig. 8.4(a) before passing along the central axis of the proximal segments [32], thus decoupling segment motion. Teflon tubings of 0.5 mm inner dimeter are used as the sheath for each tendon inside the robot, significantly reduces the twisting effect among tendons and thus the coupling between segments.

The new headframe, as shown in Fig. 8.4(b) can be mounted on the skull model using three screws equally spaced apart from one another. It has a track that allows the carriage on the robot module to slide along as well as a rack that mates with the gear on the linkage mechanism during insertion and retraction of the robot.

8.2.2 Preparation workflow to set up the robotic system

As shown in Fig. 8.5, the pathway and the incision site are first determined by the surgeons based on the pre-operative MR images to allow the robot access to the brain tumor. Once the patient is on the patient bed with his or her head fixed, a burr hole with a diameter of 15mm, together with three securing holes of 2.3 mm diameter spaced equiradially at

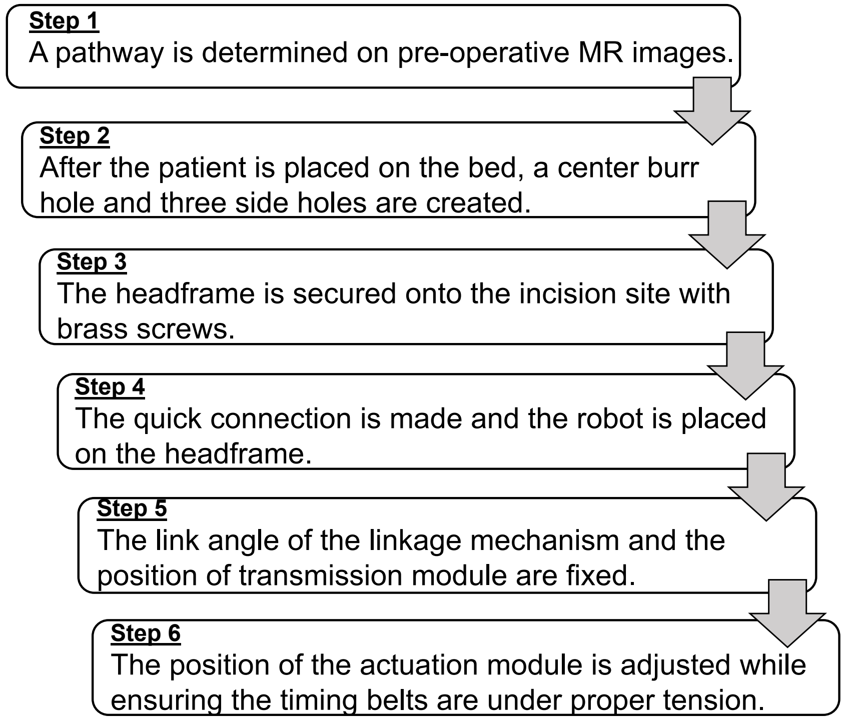

Figure 8.5: Power flow in the transmission module

30 mm diameter around the burr hole, are made. The head skull is then secured onto the incision site using three 40/4x1/2 diameter brass screws (no tapping is required). The quick connection is made to attach the robot module onto the transmission module. The entire transmission module is moved close to the patient's head. The robot module is placed onto the slider on the head frame, aligning the robot trajectory with the incision direction. Based on the initial position and the required insertion distance of the robot, the desired position of the switching mechanism and the initial link angles in the linkage mechanism can be determined. After adjusting and fixing the position of the transmission module, the actuation module and the connecting bridge are moved to their proper positions and the timing belts are installed between the actuation module and the transmission. The robotic system is ready to be used.

8.3 Design of New Transmission Module

8.3.1 Switching Mechanism

Overall structure of the switching mechanism

The switching mechanism in the transmission module interfaces with the timing belts from the actuation module and provides two major functions: selecting function and driving function. It basically selects the robot segment to be engaged and then transmits the driving force from the motor to bend the selected robot segment. Six driver units arranged in two rows and three columns are used to transmit power from the two driving motors to six DoFs of the robot, where each row is powered by a driving motor through a driving shaft, as shown in Fig. 8.6. Each driver unit is responsible for actuating a pair of cables to control the bidirectional motion of one DoF of the robot. The 6-DoF motion consists of vertical and horizontal bending of the end, middle and base segments and the arrangement of the driver units for the six DoFs are shown in Table 8.1. In each row, there are a square rail on the bottom and two round rails on the top to allow the driver units to slide laterally. The lateral sliding motions are controlled by rotation of the two cam shafts. The top cam shaft for the top row of the driver units is directly powered by the selector motor via the timing belt, while the bottom cam shaft for the bottom row of the driver units is rotated by the top cam shaft through three meshed gears on the right wall, as shown in Fig. 8.6(b). Driver units and the corresponding DoFs of the robot can be engaged or disengaged from the power train (driving shafts and the input pulley) by rotating the cam shafts.

Driving function of the switching mechanism

A driver unit consists of an input pulley that is fixed on the driving shaft, a sliding block for engaging and disengaging the unit with the driving shaft and a output disk that is connected with two cables to control one-DoF motion of the robot, as shown in Fig. 8.7. The output disk is installed on a shaft with a bearing and has teeth arranged in a circular shape on both

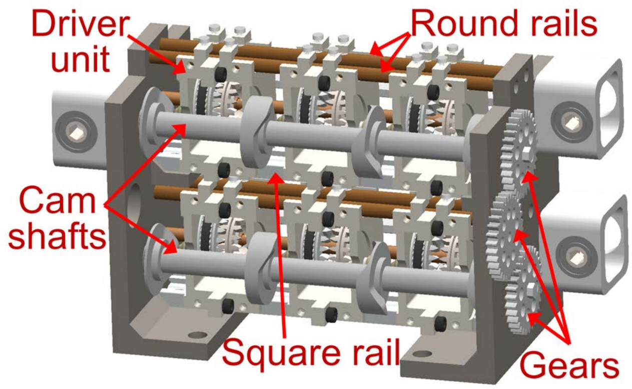

(a)

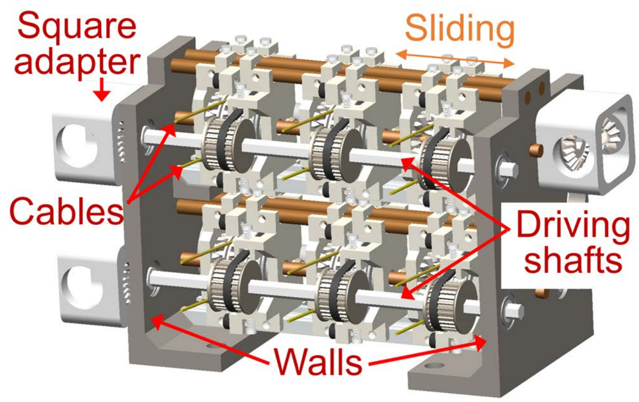

(b)

Figure 8.6: (a) Back side and (b) front side of the overall structure of the switching mechanism

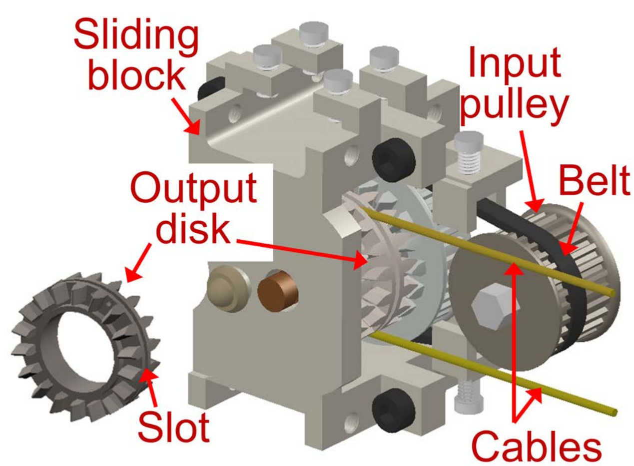

Figure 8.7: Schematic of a driver unit

Table 8.1: Arrangement* of driver units for six DoFs of the MINIR-II robot

Row	Left column	Middle column	Right column
Top	1^{st} DoF (end seg)	1^{st} DoF (mid seg)	1^{st} DoF (base seg)
Bottom	2^{nd} DoF (end seg)	2^{nd} DoF (mid seg)	2^{nd} DoF (base seg)

*Viewed from the actuation module towards the transmission module.

sides. The two cables are wounded around a slot in the middle of the disk. The output disk can rotate freely but cannot move laterally. When the disk rotates, one cable is drawn in and the other is released to bend a robot segment in one direction. The sliding block has two pieces: the engaging part and the ground part, as shown in Fig. 8.8(a). They are connected together through snaps and screws. All these components were 3-D printed on a high-resolution multijet 3-D printer (ProJet 5600, 3D Systems).

In the engaging part, as shown in Fig. 8.8(a), an engaging pulley is installed through a bearing and driven by the input pulley using a short timing belt. There are circularly arranged teeth on a side of the engaging pulley facing the output disk. In the ground part, there are also the same teeth that can be meshed with the teeth on the other side of the output disk. The sliding block has two cam followers on its two sides, as shown in Fig. 8.8(b), which are pushed by cams to make the block slide. When the sliding block is pushed to the left side (Fig. 8.8(b)), the disk is grounded by meshing with the teeth on the ground part. The output disk is disengaged from the power train (input pulley) and therefore the corresponding DoF of the robot will not move. When the sliding block is pushed to the right side, the output disk is meshed with the engaging pulley instead of the ground part so that it can be rotated by the driving pulley to actuate the corresponding DoF of the robot. In this case the driver unit is engaged into the power train. The gap size between the separate teeth (Fig. 8.8(b)) is around half of the teeth length so that there is no slip of the disk when it is switched between the two cases. It can be observed that there are two channels in the engaging part of the sliding block, where a bolt is screwed on each channel, as shown in Fig. 8.8(a). The channels are used to guide the direction of the belt so that it will not drop off from the pulley when the block is moved laterally. The screws are used to generate pretension on the belt to reduce backlash.

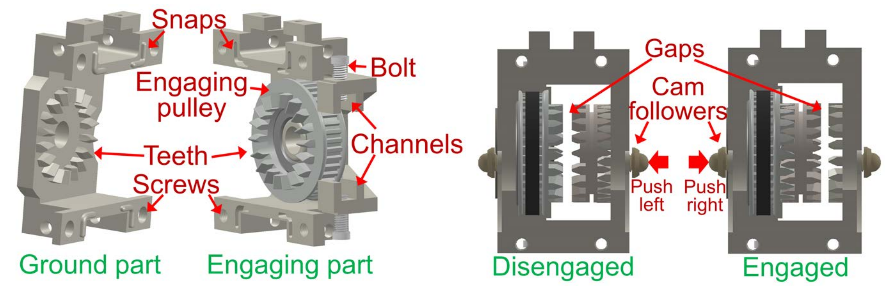

(a) (b)

Figure 8.8: (a) Schematic of the sliding block (b) Engaged and disengaged modes of a driver unit

Selecting function of the switching mechanism

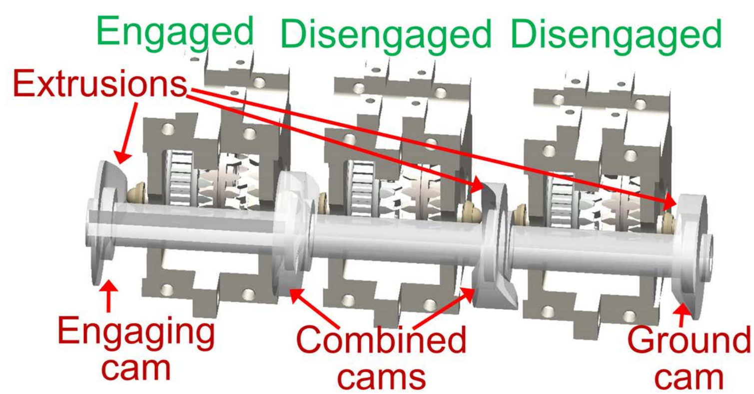

Figure 8.9: Cam shaft for a row of driver units. The leftmost driver unit is pushed rightward by the extrusion of its engaging cam while other two driver units are pushed leftward by those of their ground cams.

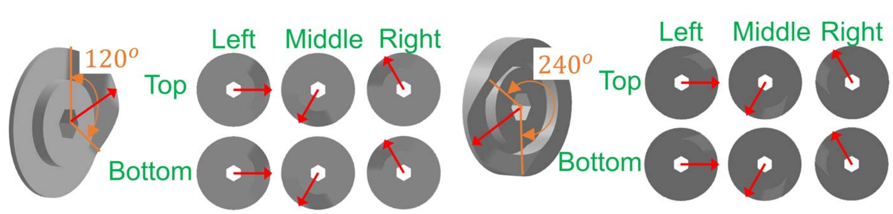

(a) (b)

Figure 8.10: Phase arrangement of all 2×3 (a) engaging cams and (b) ground cams

Driver units are switched between engaged and disengaged modes by the cam shafts. There are a pair of cams for each driver unit, including an engaging cam on the left and a ground cam on the right. The sliding block of each driver unit is pushed rightward to be engaged by the extrusion on the engaging cam and leftward to be disengaged by the extrusion on the ground cam, as shown in Fig. 8.9. In each cam shaft, there are three pairs of engaging cams and ground cams for three driver units, while two adjacent engaging and ground cams in the middle of the shaft are combined as an entire piece. When a driver unit is engaged, the two other driver units should be disengaged. Thus, for one complete revolution of the cam shaft, the extrusion region of each engaging cam covers 120° and the three engaging cams have extrusion regions that do not overlap one another. The extrusion region of a ground cam is complementary to that of the corresponding engaging cam, as shown in Fig. 8.10. Due to the gear transmission between the top and bottom cam shafts, their rotating angles of the two cam shafts and the movement of a pair of driver units in each column can be synchronized. Therefore, driver units in a column, i.e. two DoFs of a robot segment, can be engaged into the power train together simultaneously. After the engaged segment is moved to a desired bending position, rotating the cam shafts by 120° in either clockwise or counterclockwise direction will disengage the segment and in turn engage one of the other two segments. The position of the first engaged robot segment will be maintained.

8.3.2 Linkage Mechanism

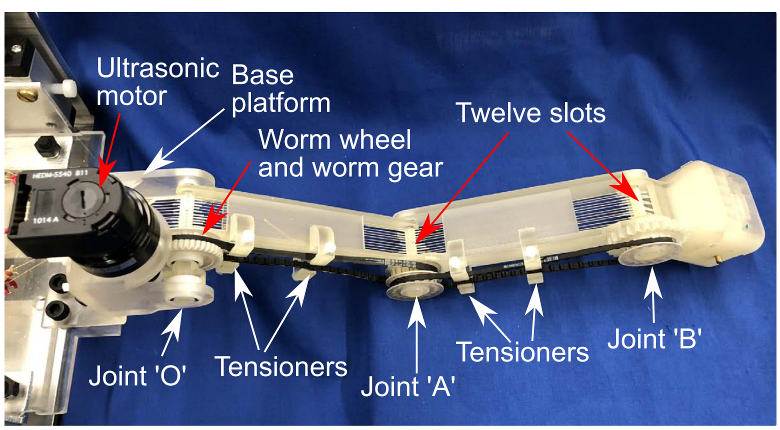

Figure 8.11: Linkage mechanism featuring the ultrasonic motor and the proximal quick connector

The linkage mechanism consists of two links, each of which has a 124 mm length. As shown in Fig. 8.11, the mechanism consists of a base, two links, and the proximal quick connector, as shown in Fig. 8.11. The motion line of the slider is fixed by the head frame that is mounted on the skull at the incision opening. At the base, there is a platform to hold the motor and a pair of worm gear and worm wheel (with a gear ratio of 40) to act as the transmission of the motor. The motor and worm gear combination prevents the linkage mechanism from changing shape once the robot is inserted to its target depth, allowing efficient force transmission in the tendons during actuation of the robot segments. A custom-made worm wheel-toothed pulley part is installed at joint 'O' to transfer force from motor rotation to the timing belt pulley. Two timing belts are used to transfer the torque from the joint 'O' to joint 'B', as shown in Fig. 8.11. A dual-channel toothed pulley is installed at joint 'A' and is decoupled from its joint rotation using bearings. A toothed pulley-gear part is designed to be installed at joint 'B' and is decoupled as well from its joint rotation. The gear is intended to meet with the rack attached to the top of the headframe. In this way, the ultrasonic motor shaft rotation directly generates a linear force along the surface of the headframe to move the robot module forward and backward. The cables go through twelve channels in the center of the joint shafts of the linkage mechanism to make sure the tendon displacement is minimal during insertion and retraction of the robot.

Friction of the cables that pass through the channels in the joint shafts is proportional to the exponential of the wrapping angle, which is the total changing angle of cable directions in the linkage mechanism. When the linkage mechanism varies from an initial configuration to a final configuration for manipulating the robot, the wrapping angle may change. To minimize the friction, the maximum wrapping angle in the overall working range should be minimized. For an arbitrary linkage configuration, the wrapping angle, w, which is the sum of all joint angles shown in Fig. 8.12, can be expressed as:

$$w = (\pi - \alpha) + |\beta| + |\gamma| = \theta + \beta + |\beta| + \gamma + |\gamma| \tag{8.1}$$

where γ, α and β are angles of joints 'O', 'A' and 'B'. θ is a constant angle between the motion line and the horizontal direction, and is fixed after the incision site is determined. The angles in the linkage mechanism are related as follows:

$$\alpha + \beta + \gamma + \theta = \pi \tag{8.2}$$

Based on our analysis [254], we know that both $\gamma + |\gamma|$ and $\beta + |\beta|$ are non-increasing terms and the maximum wrapping angle occurs at the initial linkage configuration. Knowing the insertion depth, l_{insert}, we can calculate the initial angle of α, α_0, from:

$$l_{insert} = 2l(1 - sin\frac{\alpha_0}{2}) \tag{8.3}$$

At this stage, β and γ are left to be determined to achieve the linkage mechanism configuration with the minimum initial wrapping angle. We can define κ as: $\kappa = \pi - \alpha_0 - \theta = \beta + \gamma$ based on Eq. (8.2). If $\kappa < 0$, the minimized initial wrapping angle is $w = \theta$ by choosing $\beta < 0$ and $\gamma < 0$. If $\kappa > 0$, the minimized initial wrapping angle is $w = \theta + 2\kappa$ by choosing $\beta > 0$ and $\gamma > 0$.

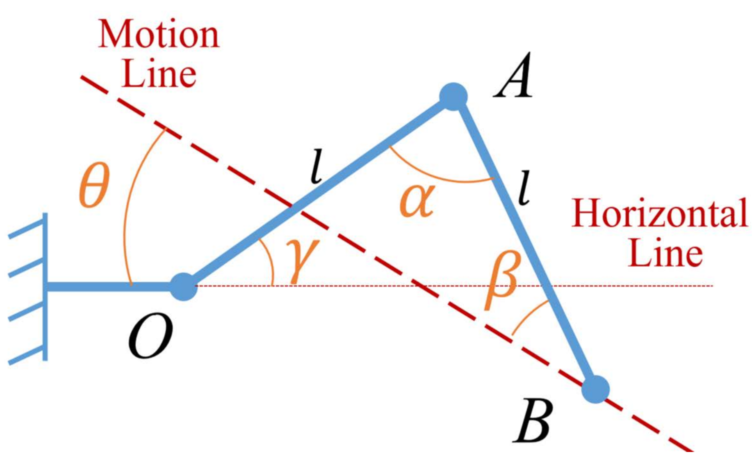

Figure 8.12: Angles of a linkage configuration

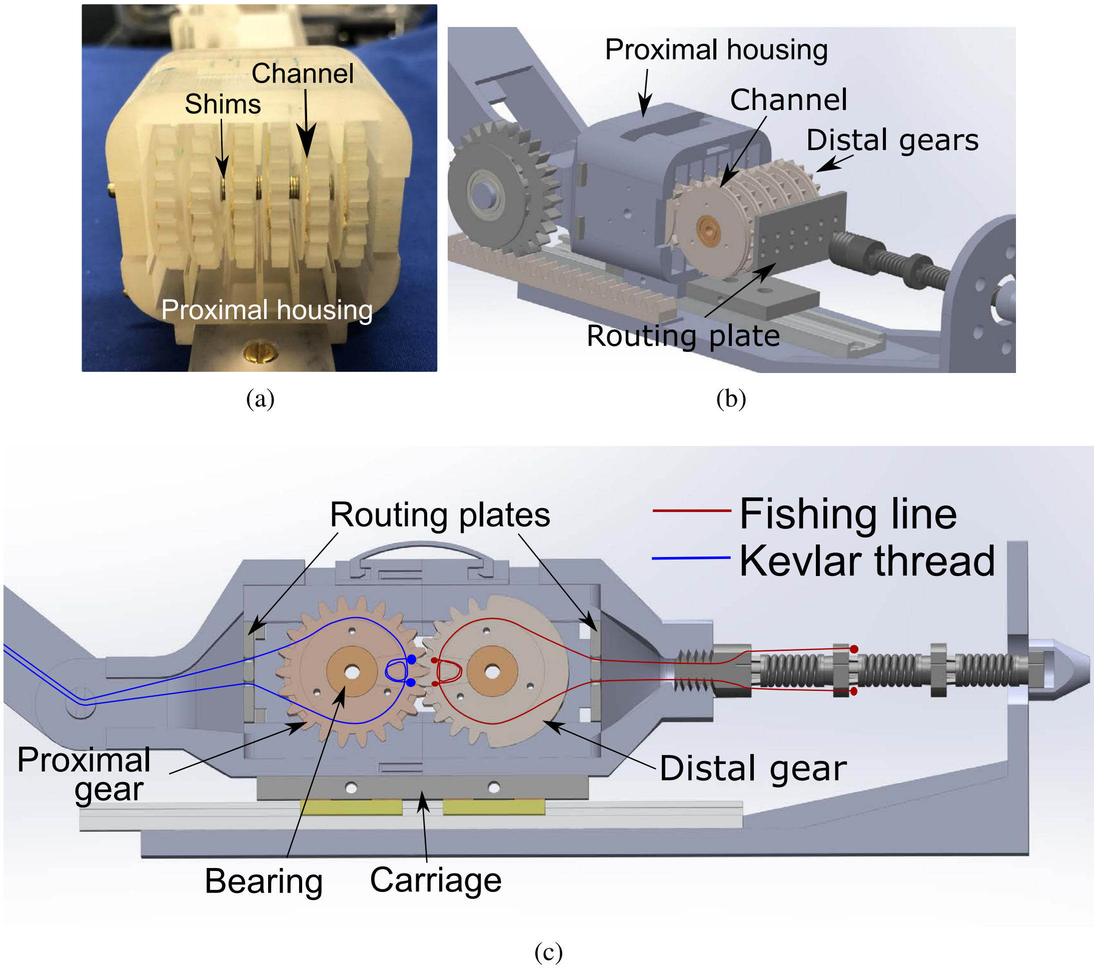

Figure 8.13: (a) A close view on the quick-connector showing shims separating the bearings and the side channel where the tendons are routed (b) CAD schematic that shows gears, bearings, and the routing plate inside each of the quick connector housing (c) Cross-sectional view of the quick connector showing the cable (Kevlar thread) and tendon (fishing line) routes inside the quick connector and how the proximal and distal gears mate

8.3.3 Quick-Connect Mechanism

The quick-connect mechanism, of which the exploded view is shown in Fig. 8.13(a), consists of a proximal connector and a distal connector, each with six modified spur gears. The distal connector, together with the robot module, is disposable after each procedure. Each gear is 3-D printed with a circular channel that is of 20.5 mm diameter for tendon routing and attachment, as shown in Fig. 8.13(b). Cables and tendons enter the proximal and distal connectors, and pass through the routing plates before getting routed on the circular channels. In the distal gears, higher walls are designed on two sides of each tendon channel to ensure that the tendons would not be hooked on the gear teeth whenever it becomes slack (e,g. tendon that is not being actively pulled becomes slack due to flexibility of the robot segment). The gear diameter is determined to ensure that there is no overlapping of tendons on the gear channels and that 90° bending angle in the robot segment can b achieved by less than 90° gear rotation. The routes for both tendons in the distal quick connector and cables in the proximal quick connector are highlighted in red and blue in Fig. 8.13(c). The structural design and feature arrangement in both proximal and distal connectors are exactly the same, except the proximal connector is attached to the linkage mechanism while the distal connector to the robot module. The gears, alongside their bearings, are lined up along a brass bar with shims separating the gears. Behind the gear array inside each connector, there is a routing plate with twelve holes that changes the tendon directions so that the tendons would always be in the same plane as their target gears.

During assembly of the distal connector, a tiny amount of pre-slack is retained for each gear, allowing robot motion in each DoF to be smooth especially when changing direction. This amount of backlash can be characterized due to its repeatability and will be compensated in our controller. The gears also allow power transmission in the longitudinal directions of the cables and tendons to be decoupled. A reset pin is inserted through the housing of each connector and all the gears to ensure that the gears are configured in an orientation that is ready to mate with its opposite side during the quick connection. The quick connection is formed by simply bringing together the two sets of gears before the two housings are firmly connected together by a clip on the top and a carriage on the bottom.

8.4 Hysteresis Modeling

8.4.1 Generalized Play Operator

Hysteresis is a common phenomenon in a tendon-driven system and needs to be modeled and compensated to allow more precise control of the robotic system. The generalized play operator, as shown in Fig. 8.14(a), for the hysteresis condition can be defined by [255]:

$$
\begin{aligned}
y_i(x(t)) &= F\big[x_i, y_{i_0}\big](t) \\
&= max\big\{\gamma_R\big(x(t) - r_b\big), min\big(\gamma_L(x(t) + r_b), y_i(t - T)\big)\big\}
\end{aligned}
\tag{8.4}
$$

where x, y, r_b, and T are the system input, system output, backlash amplitude in the hysteresis loop, and the sampling time interval. γ_L and γ_R are the two envelope functions that represent the pathways along which the input decrease and increase, respectively, during the periodic process. The initial condition can be expressed as:

$$
y_i(0) = max\big\{\gamma_R\big(x(0) - r_b\big), min\big(\gamma_L(x(0) + r_b), y_{i_0}\big)\big\}
\tag{8.5}
$$

where y_{i_0} is usually initialized to zero.

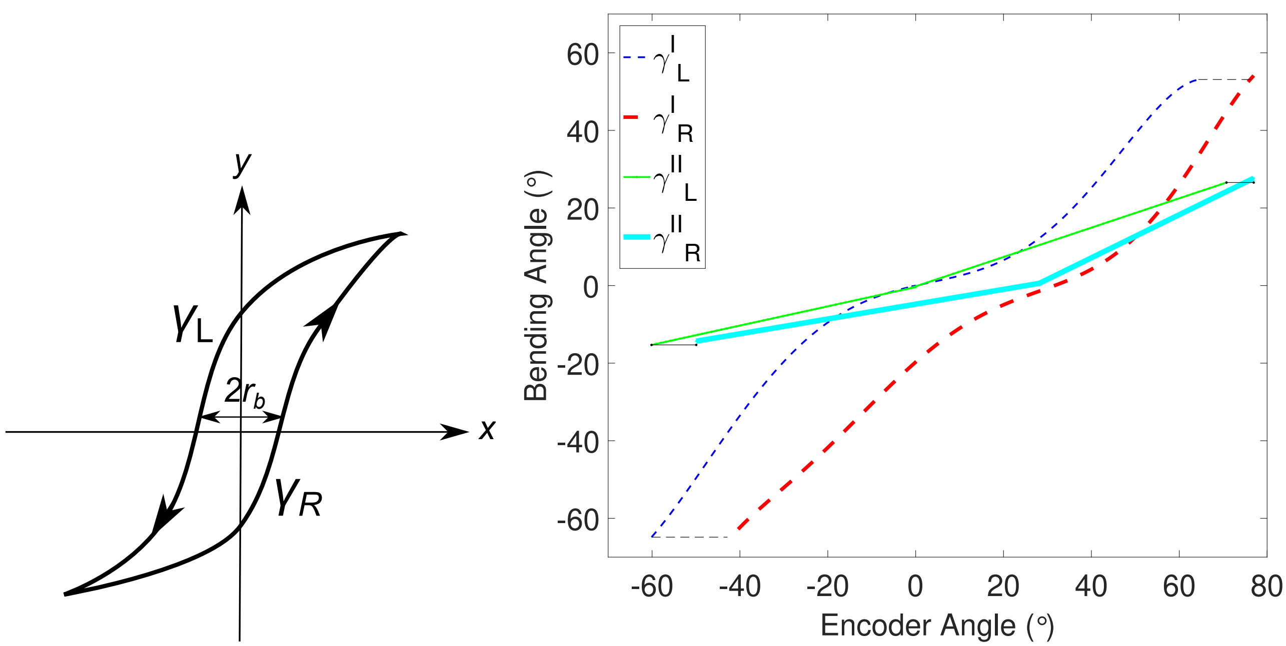

(a) (b)

Figure 8.14: (a) Input-output relationship of a generalized play operator (b)A sample of two generalized play operators for 1^{st} DoF of the end segment

8.4.2 Prandtl-Ishlinski Model

In our case, the input x is the motor encoder angle while output y is the robot segment bending angle. A generalized Prandtl-Ishlinski (PI) model is used to describe the hysteresis relationship between them. It is the result of superposition of two generalized play operators and can be expressed as:

$$y(x(t)) = y^{\mathrm{I}}(x(t)) + y^{\mathrm{II}}(x(t)) \tag{8.6}$$

Each play operator consists of a left and a right envelope functions, as shown in Fig. 8.14(b). The first proposed play operator makes use of polynomial envelope functions to reconstruct the nonlinear bending behavior of the robot with respect to the motor input. It can be expressed as:

$$y^{\mathrm{I}}(x(t)) = \max\left\{\gamma_R^{\mathrm{I}}\big(x(t) - r_b\big),\ \min\{\gamma_L^{\mathrm{I}}\big(x(t) + r_b\big),\ y^{\mathrm{I}}\big(x(t-T)\big)\}\right\} \tag{8.7}$$

where

$$\gamma_R^{\mathrm{I}} = a_{R,3}^{\mathrm{I}} x^3 + a_{R,2}^{\mathrm{I}} x^2 + a_{R,1}^{\mathrm{I}} x^1 + a_{R,0}^{\mathrm{I}} x^0$$

$$\gamma_L^{\mathrm{I}} = a_{L,3}^{\mathrm{I}} x^3 + a_{L,2}^{\mathrm{I}} x^2 + a_{L,1}^{\mathrm{I}} x^1 + a_{L,0}^{\mathrm{I}} x^0$$

It should be noted that the proposed polynomial envelope function is not unique and was decided based on the nature of hysteresis of the tendon-driven system. The second play operator is used to represent the top and bottom transient stages, especially in the engaging corners, between the two nonlinear curves. It can be expressed as:

$$y^{\mathrm{II}}(x(t)) = \max\left\{\gamma_R^{\mathrm{II}}\big(x(t) - r_b\big),\ \min\{\gamma_L^{\mathrm{II}}\big(x(t) + r_b\big),\ y^{\mathrm{II}}\big(x(t-T)\big)\}\right\} \tag{8.8}$$

where the envelope functions are:

$$\gamma_R^{\mathrm{II}} = \begin{cases} k_{R,1}x & x < 0 \\ k_{R,2}x & x \geq 0 \end{cases}$$

$$\gamma_L^{\mathrm{II}} = \begin{cases} k_{L,1}x & x < 0 \\ k_{L,2}x & x \geq 0 \end{cases}$$

8.5 Experiments, Results, and Discussions

Experiments are conducted to characterize and evaluate the performance of the robot. As shown in Fig. 8.15, the trakSTAR electromagnetic tracking sensors (Model 180, NDI Medical, LLC) were installed at each segment disk of the robot as well as at the transmission driving pulley. The mid-range transmitter was placed more than 20 cm from each of the sensors. The position and orientation data of all sensors as well as the encoder data from the motors were recorded in real time.

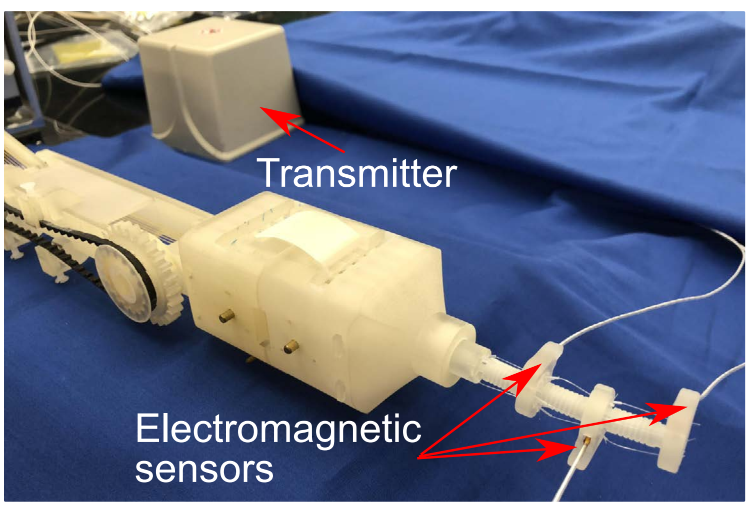

Figure 8.15: Experimental setup to verify that there is minimal coupling between robot segments

In the first set of experiments, each robot segment was actuated individually in both DoFs. The results shown in Fig. 8.16(a-c) showed that there is minimal segment coupling

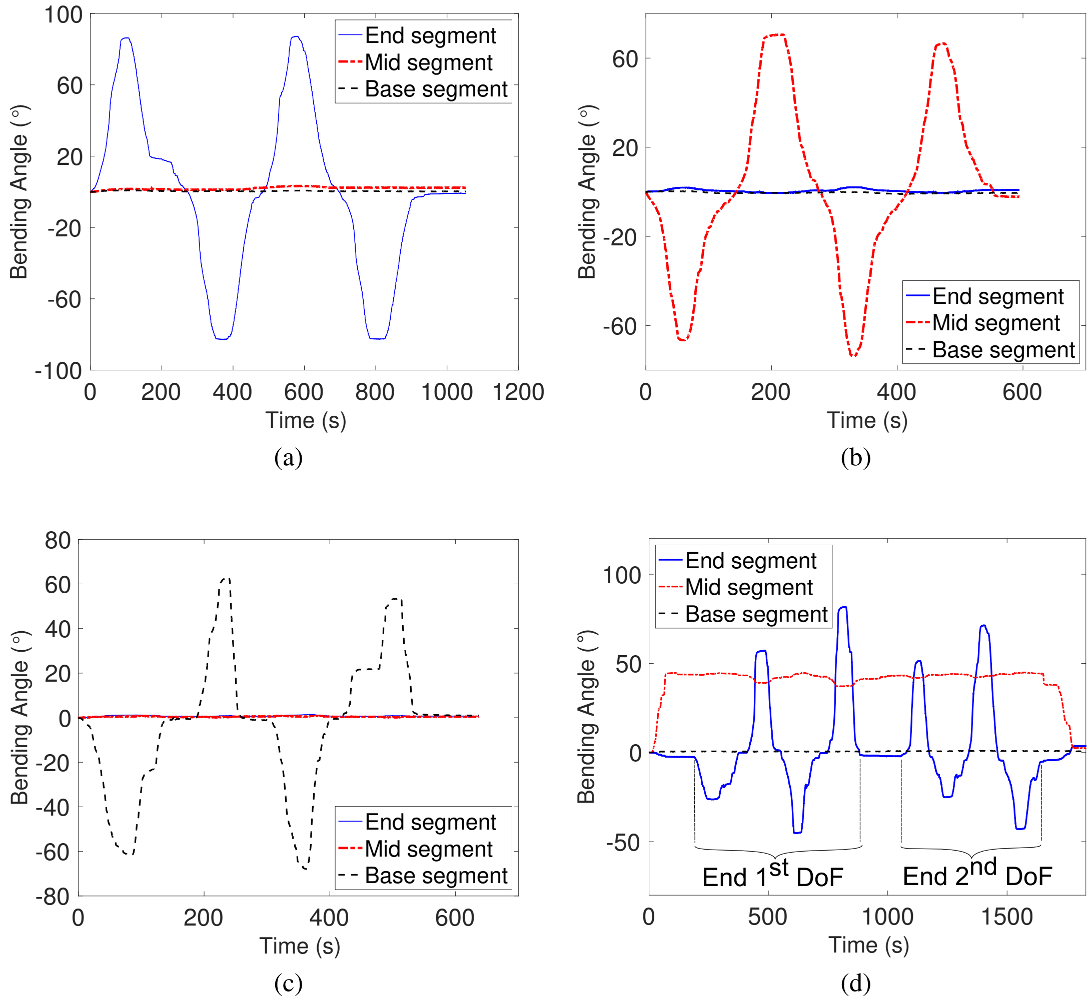

Figure 8.16: Bending angles of all segments when (a) end segment only, (b) middle segment only, and (c) base segment only were actuated through two cycles. (d) Bending angle of all segments when two robot segments were commanded to move consecutively

with the maximum bending angles of the non-actuated segments being 3.30° when the end segment was actuated, 2.14° when the middle segment was actuated, and 1.42° when the base segment was actuated. We also commanded more complicated motion involving the middle and end segments, the result of which is shown in Fig. 8.16(d). During this experiment, five events took place in the following order: (i) The middle segment was actuated and locked in place. (ii) The end segment was activated. (iii) The 1^{st} DoF of the end segment was actuated through two cycles. (iv) The 2^{nd} DoF of the end segment was actuated through two cycles and locked in place. (v) The middle segment was reactivated and

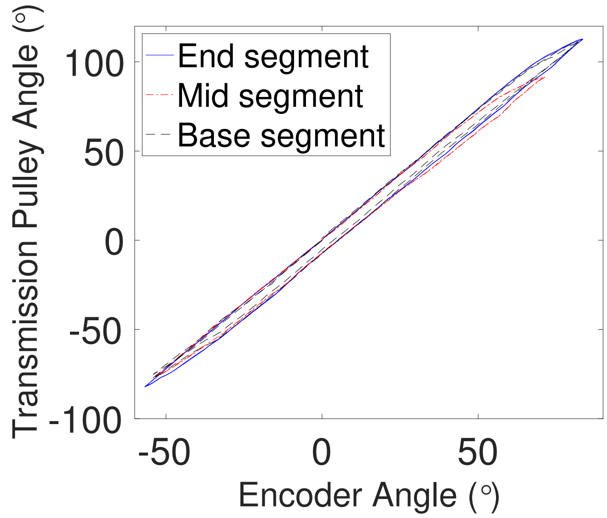

(a)

Figure 8.17: Hysteresis in the timing belt between the actuation module and the transmission module for the 1^{st} DoFs of all three segments

moved back to its home configuration. The switch between different segments happened smoothly without any effect on bending angles of any segment, as seen in Fig. 8.16(d). We also observed that there was completely no coupling in the switching mechanism, ensuring that only one robot segment was engaged at any time. The coupling in the robot segment, on the other hand, could not be eliminated entirely due to the inherent flexible nature of the spring backbone. However, the addition of the curved channels in the segment disk, the use of the teflon tubes inside the robot, and the central tendon routing configuration [32] have successfully minimized the segment coupling effect. As seen in Fig. 8.16(d), the maximum angle variation in the base segment was 1.03° throughout the entire timeline, which is negligibly small considering the large range of complex motion the two distal segments were going through. The two more noticeable variations in the middle segment with respect to its initial bending angle of 45° were 5.6° at 473s and 7.4° at 815s and they happened when the end segment was bent in almost the same direction as that of the middle segment.

In the second set of experiments, we intended to investigate the hysteresis effect in the robotic system. Each robot segment was actuated for multiple cycles between a predetermined range and the data were divided into a training dataset and a test dataset. We

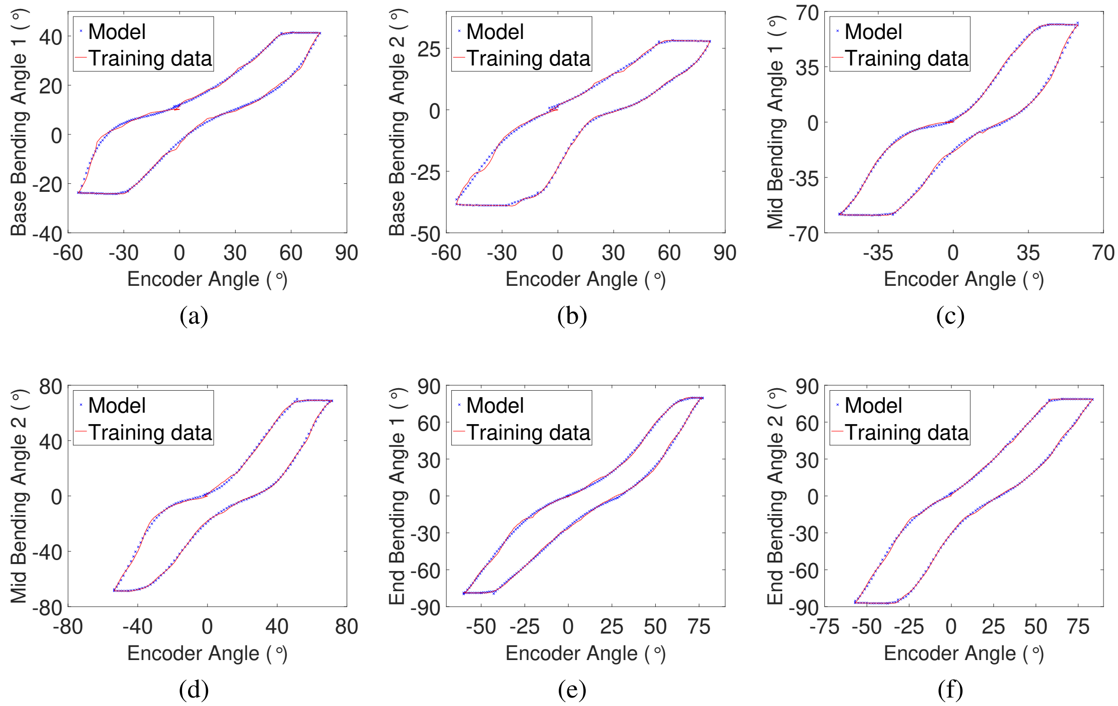

Figure 8.18: Complete cycles of training data is used to develop the PI model

Table 8.2: Parameters for PI models

Segment/DoF	r_b	$a^{I}_{L,3}$	$a^{I}_{L,2}$	$a^{I}_{L,1}$	$a^{I}_{L,0}$	$a^{I}_{R,3}$	$a^{I}_{R,2}$	$a^{I}_{R,1}$	$a^{I}_{R,0}$	$k_{L,1}$	$k_{L,2}$	$k_{R,1}$	$k_{R,2}$
End 1	14.1	0.0004	-0.0042	0.2582	-0.0213	0.0005	0.00004	0.4054	-1.4227	0.2480	0.3782	0.5555	0.1909
End 2	14.1	0.0004	0.0072	0.6040	2.154	0.0005	0.0012	0.5214	-0.3845	0.2543	0.2236	0.2666	0.2189
Middle 1	10.7	0.0006	0.0285	0.3583	0.7316	0.001	0.0014	0.2635	-1.5372	0.1941	0.3343	0.4350	0.1844
Middle 2	12.7	0.0006	0.024	0.2858	1.5165	0.0008	0.0091	0.3282	-0.8319	0.2721	0.1495	0.1925	0.2054
Base 1	15.8	0	0.0057	0.1535	11.7221	0.0002	-0.0005	0.1286	10.65	0.1787	0.1302	0.1860	0.1483
Base 2	16.8	0.0001	0.0045	0.1217	1.2114	0.0004	0.0053	-0.0122	0.2738	0.2995	0.1633	0.2250	0.2650

noticed that the new tensioner design significantly eliminated much of the hysteresis in the timing belt system between the actuation module and the transmission module. As shown in Fig. 8.17, the maximum backlash for base, middle, and end segments were on average $\pm 2.1^{\circ}$ of encoder angle. The majority of hysteresis in the robotic system was found in the transmission module and the robot module.

In order to more accurately control the robot, we modeled the hysteresis of the robotic system using the PI model, as described in Section IV. To identify the PI model for each DoF of the robot, parameters in the operators are estimated by fitting the hysteresis model onto the training data, as shown in Fig. 8.18. The parameters were obtained for all six DoFs of the robot and shown in Table 8.2. The test data were then used to verify the hysteresis model, as shown in Fig. 8.19. The R^2-values for the base segment 1^{st} DoF, base segment

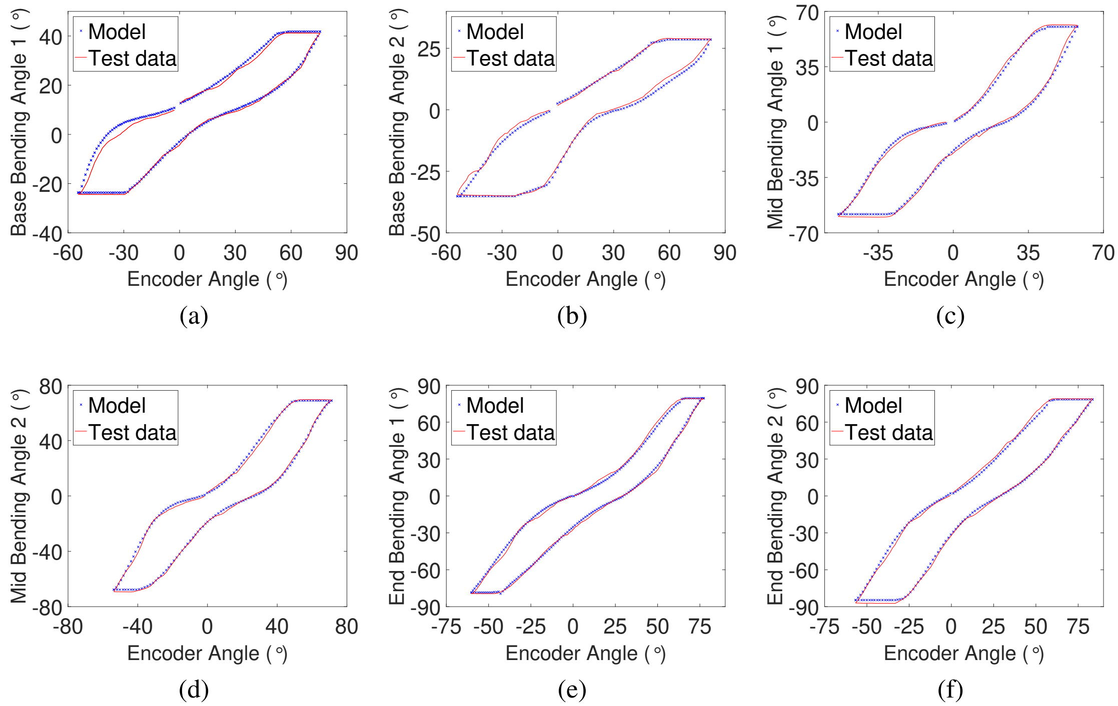

Figure 8.19: Comparison between the hysteresis model and the test data

2^{nd} DoF, middle segment 1^{st} DoF, middle segment 2^{nd} DoF, end segment 1^{st} DoF, and end segment 2^{nd} DoF are 0.9966, 0.9940, 0.9989, 0.9981, 0.9986, and 0.9991 respectively. The high R^2-values confirm the model accuracy in predicting the motion of the robotic system. Based on [256], the inverse PI model that makes use of exact same parameters of the forward model, which were already identified, can be developed. It will then be used as a feedforward controller to compensate for the hysteresis nonlinearities in this tendon-driven system.

In the final experiment, we simulated the actual procedure, as shown in Fig. 8.20, based on the process flow described in Section II(C), by first making an incision (a center hole of around 15 mm diameter and three other side holes of 2.3 mm diameter) at the predetermined incision site on a human cadaver head. The headframe was then attached to the skull by three 4-40 x1/2 brass screws. At this point, the motion line of the robot was determined to be horizontal ($\theta = 0$) and the insertion depth of the robot, l_{insert} was set as 50 mm. Using Eq. (8.3), α_0 was calculated as 106°. Therefore, $\kappa = 74° > 0$ and we configured

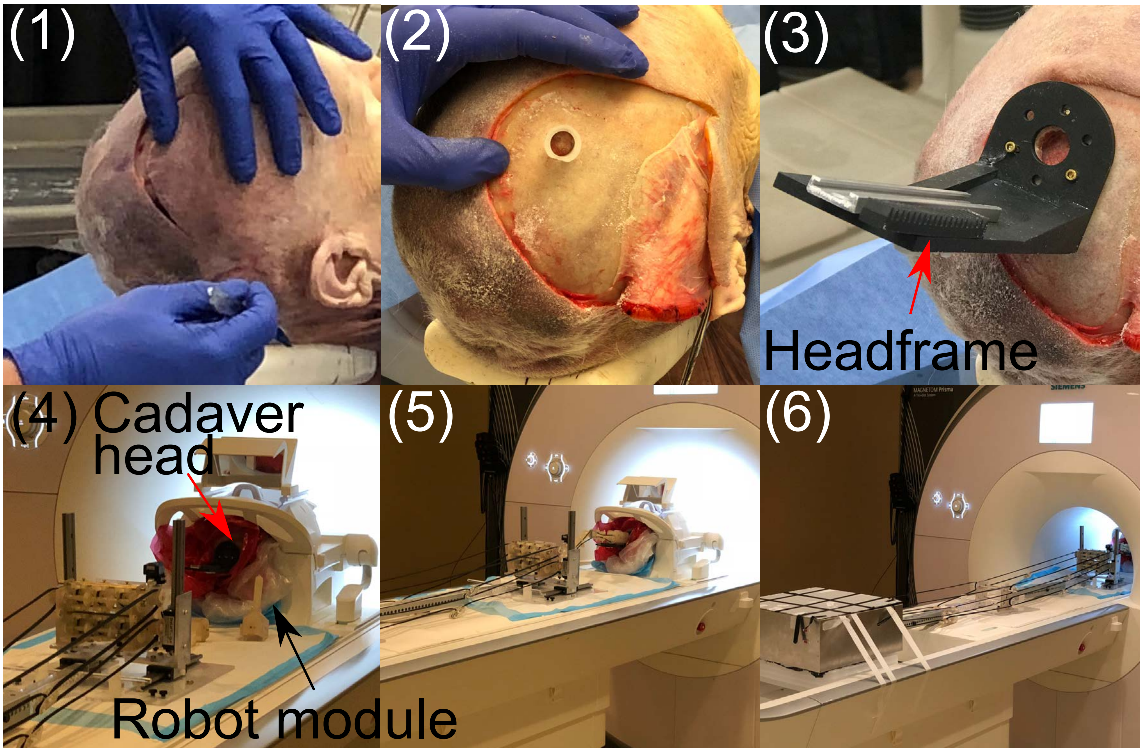

Figure 8.20: Steps taken when preparing the cadaver sample and setting up the robotic system

the linkage mechanism such that the motion line passed through Joint 'O' in Fig. 8.12 to achieve positive β and γ. This linkage mechanism configuration is shown in Fig. 8.21(a). The robot module was then placed on the headframe and inserted into the brain before its segments were actuated inside the brain. The robot's capability to move inside the human brain environment is confirmed by the MR images taken during the procedure, one of which is shown in Fig. 8.21(b).

High resolution 3-D static MR images, as shown in Fig. 8.22 and Fig. 8.23, were also taken through the MP-RAGE (three-dimensional, T1-weighted, gradient-echo) scanning sequence in both the sagittal plane and the coronal plane when the robot end segment was actuated two different DoFs, respectively. The parameters involved in the 3-D MR scan was as follows: TE=2.32ms, TR=2300ms, FoV=240mm, Slice number=192, Voxel size=0.9x0.9x0.9mm, Flip angle=8°, Inversion pulse=900ms, and Bandwidth=200Hz/pixel. A dynamic MR scan was performed for 5 min and 57 seconds, during which the system was powered off, powered on, executed one complete actuation cycle, and eventually powered off. The status of the robot throughout the dynamic scanning was shown in Fig. 8.24. The dynamic MR scan parameters are as follows: TE=1.72ms, TR=12ms, FoV=220mm, Frame number=260, Base resolution=160, Voxel size=1.4x1.4x4.0mm, and Flip angle=10°. As shown in Fig. 8.25, the mean SNR throughout the procedure was 12.84 with a standard deviation of 0.89 and less than 2% SNR change across every procedure status change.

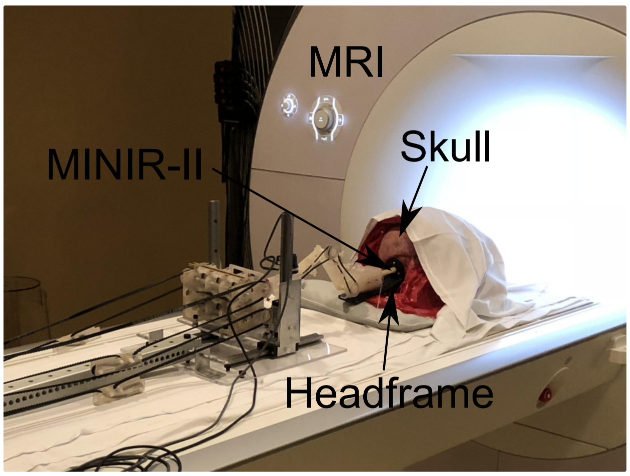

(a)

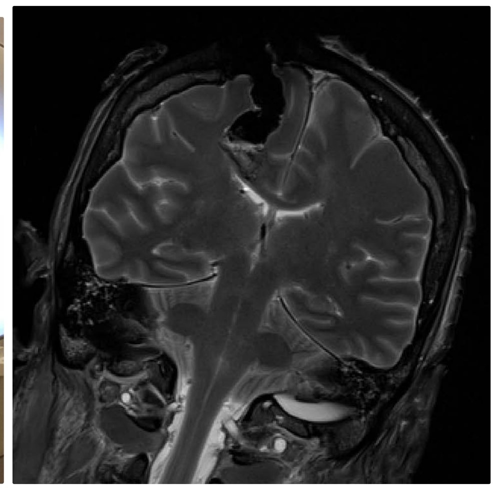

(b)

Figure 8.21: (a) Experimental setup to evaluate the motion capability of the MINIR-II in human cadaver brain (b) MR image showing the end robot segment motion in the brain

8.6 Summary

A cable-driven robotic system was developed to actuate the 6-DoF MINIR-II neurosurgical robot in the MRI environment. It was an improved version of a previous robotic system with major design innovation being done on the transmission module to reduce the backlash in the long timing belt and increase robustness of the switching mechanism, linkage mechanism, and quick-connect mechanism. Performance of the robotic system, in terms of the coupling in the switching mechanism, segment coupling, and hysteresis behavior, was experimentally determined. Hysteresis, majority of which determined to originate from the transmission module, had been simulated using the PI model with a non-linear and a linear play operator. The robotic system was also set up in an MRI patient bed and a surgical

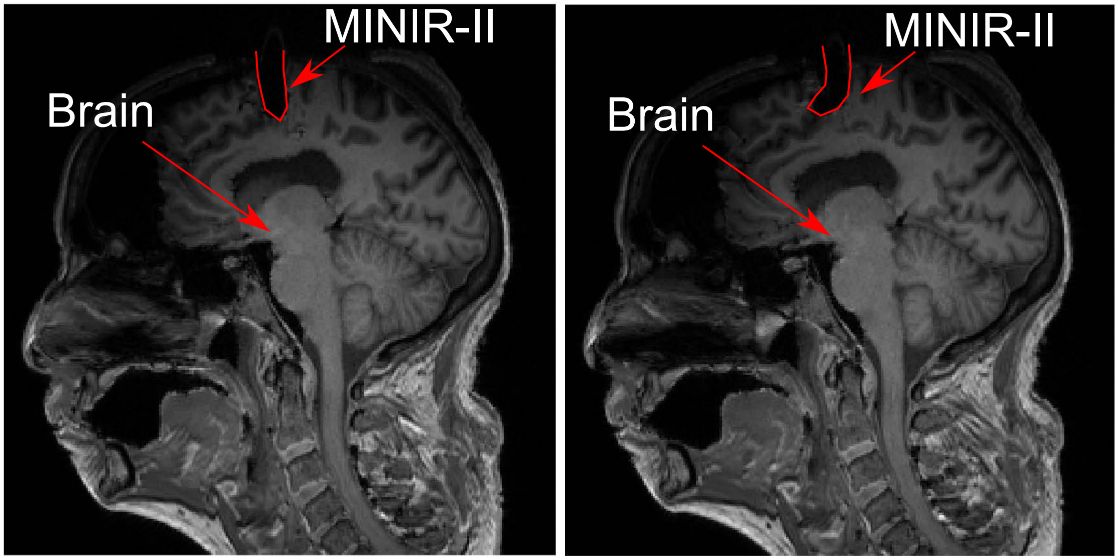

(a) (b)

Figure 8.22: The static MR images in the sagittal plane of the robot when (a) it was in the straight configuration and (b) its 1^{st} DoF of the end segment was actuated

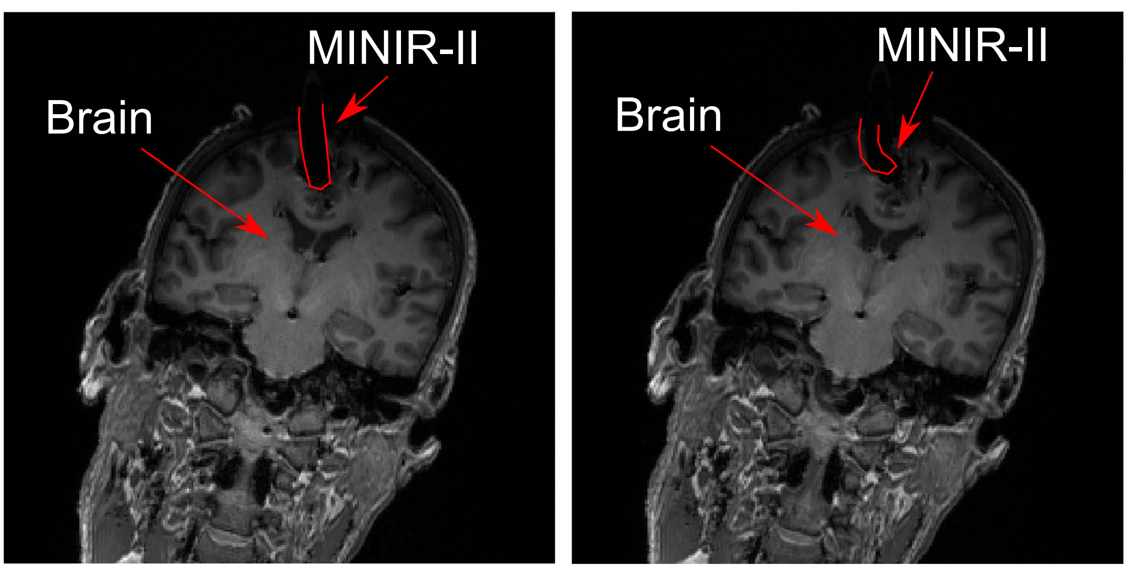

(a) (b)

Figure 8.23: The static MR images in the coronal plane of the robot when (a) it was in the straight configuration and (b) its 2^{nd} DoF of the end segment was actuated

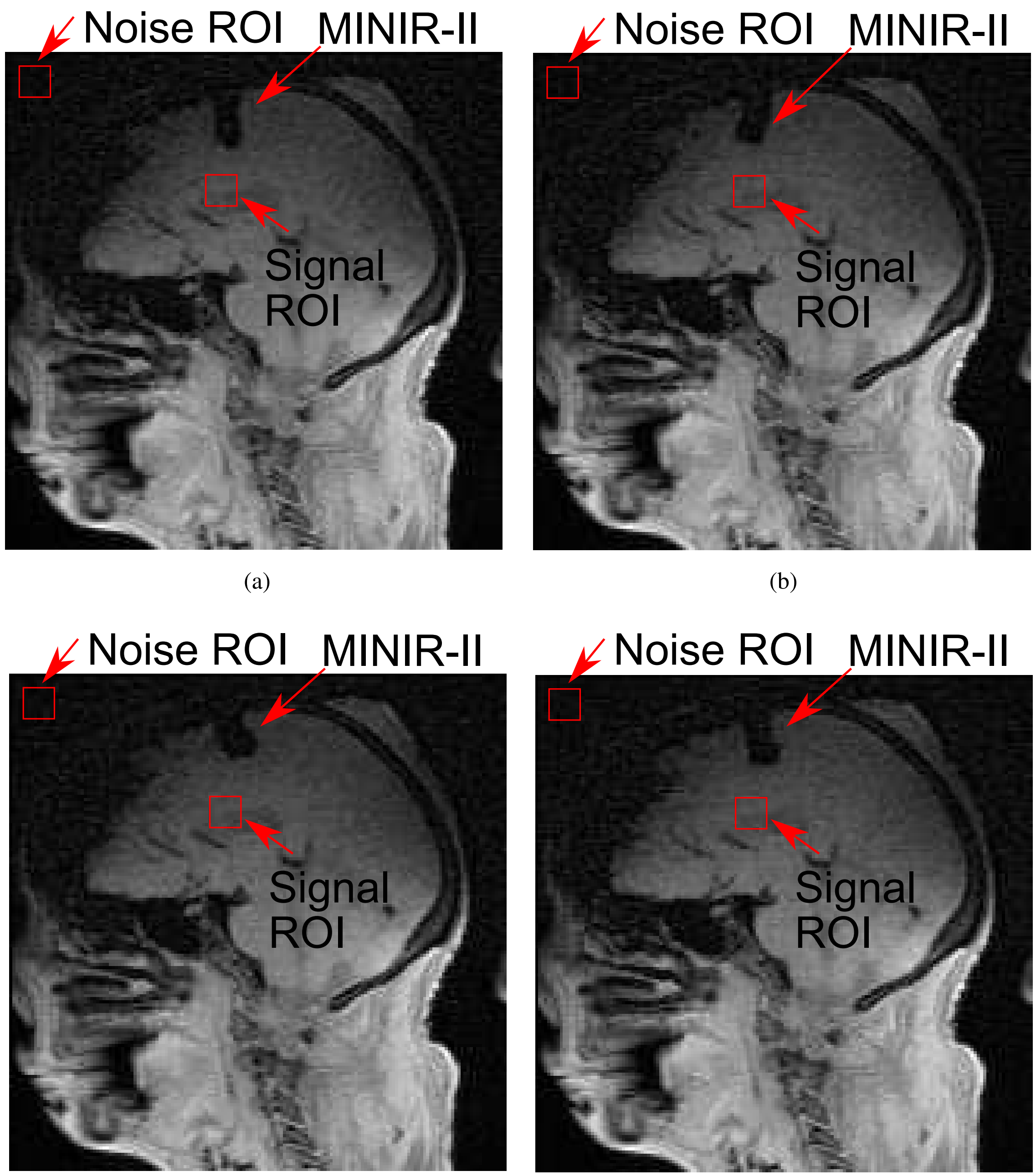

(a) (b)

(c) (d)

Figure 8.24: The dynamic MR images (a) before the system was powered on, (b) after the system was powered on and robot was actuated to the left, (c) when the robot was actuated to the right, and (d) after the robot was back to the home configuration and the system was powered off

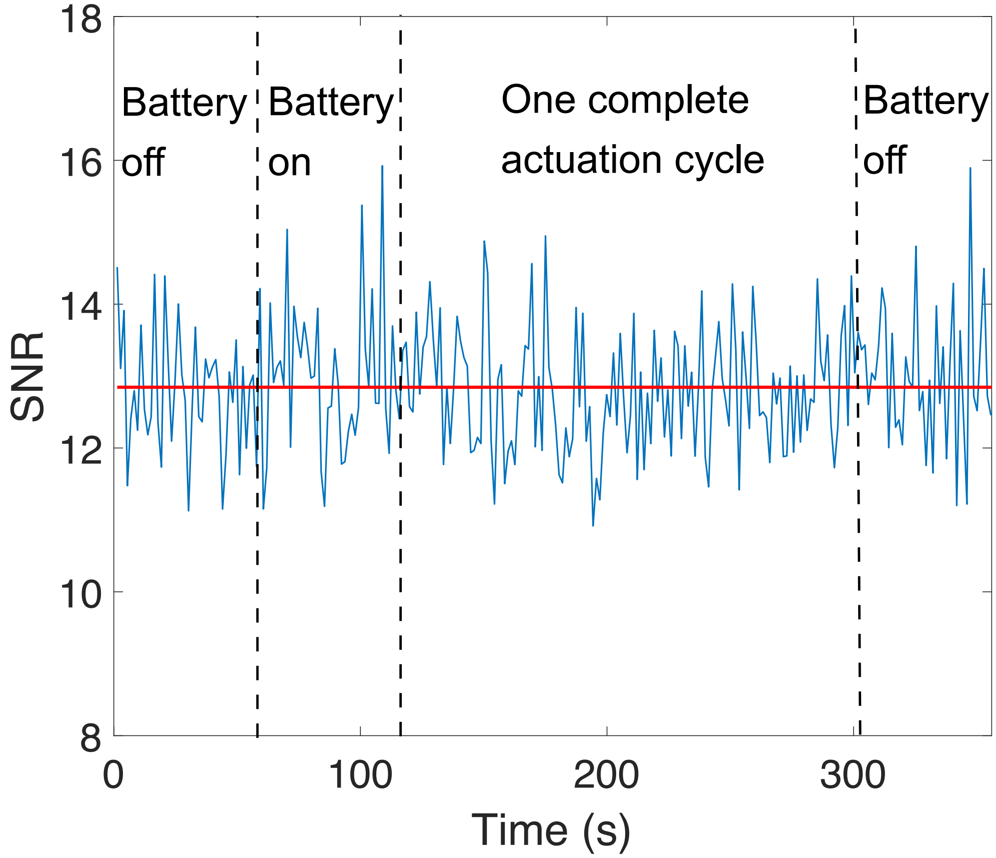

Figure 8.25: Changes in SNR during a dynamic scan of the robot in the cadaver before, during and after robot actuation

procedure, involving insertion and bending of the robot segment inside a human cadaver brain, was simulated.

CHAPTER 9

CONCLUSIONS AND FUTURE WORK

9.1 Conclusions

The work was motivated by the need to improve existing neurosurgical procedures which mostly utilize straight rigid surgical instruments or/and are planned and performed based on pre-operative images. We faced some unique challenges in the process of developing this MRI-compatible robotic system with flexible robot end effector, such as MRI-compatible flexible robot design, MRI-compatible SMA actuator and its limitations, stiffness modulation in a flexible robot, and MRI-compatible ultrasonic actuator and its limitations. Some of the other challenges related to MRI-guided robotics, including different types of MRI sequencing techniques, tumor resection methods, and path planning of the flexible robot, are out of the scope of this work. Based on the results, we have the following conclusions:

1) 3-D printing allows the development of personalized surgical robot with even complicated shape and geometry. In our work, a three-segment spring-based robot was 3-D printed as a single piece without any post-printing assembly to connect the different segments. 3-D printing is also a good manufacturing method to construct MRI-compatible robots. One limitation would be material degradation, which is not an issue for a disposable robot like MINIR-II.

2) Segment motion decoupling could be addressed from the design perspective so that minimum number of actuators needs to be used to actuate an individual segment. In our work, the central tendon routing configuration, the use of teflon tube as the sheaths and the built-in channel in each segment disk are an integrated way of achieving minimal segment coupling. The central tendon routing makes sure the tendon generates close to zero moment arm to the proximal segments; the teflon tubes prevents tangling of the tendons within the

robot; the built-in channels minimize friction between the tendon and the robot segment disc.

3) A compact cooling strategy for SMA spring was very difficult to achieve. Even though our method of passing water and air alternately through a cooling module-integrated SMA spring improves the actuation bandwidth of the robot and maintains the compactness of the actuator, the construction of the actuator by threading silicone tubing across the spring coils is labor intensive. There is also potential for holes in the silicone tubing to develop during the threading process, causing water leakage. It may not be appropriate for mass production unless an automated method of threading the tubing across the spring coils is developed.

4) The phenomenological model and heat transfer model for antagonistic cooling module-integrated SMA springs were developed and verified with high accuracy, confirming their potential to be used in a model-based controller.

5) Ultrasonic motors are completely compatible in the MRI bore but their drivers have to placed at least 3 m from the the 3-Tesla 70 cm Siemens Magnetom MRI bore, 2.5 m from the 3-Tesla 60 mm Siemens MRI bore, and 1.5 m from the 7-Tesla 14 cm Bruker MRI bore. The critical distance depends on the MRI bore size and its magnetic strength.

7) The MRI-compatible Bowden cable transmission that we developed would be a novel design for a robotic system that does not insert and retract the end effector robot, such as a needle positioning system. The insertion and retraction of the robot requires us to include another section of flexible tube at the end of the Bowden cable, thus leading to the loss of transmission force.

8) Increasing the number of motors increases the SNR loss in the MR images. Therefore, the development of a switching mechanism to reduce the number of motors while maintaining the critical functions of the robot is justified.

9) The engagement direction of the switching mechanism should not be the same as the cable motion direction to ensure that switching mechanism and the robot actuation is de-

coupled.

10) Gear-based quick-connect mechanism allows the two tendon-based systems, namely the cable transmission from the switching mechanism to the proximal quick-connector and the tendon transmission from the distal quick-connector to the flexible robot, to be decoupled and tightened individually to its desired level. The cable transmission system should be taut while the tendon transmission system should have a tiny amount of pre-slack to prevent the flexible spring segment from buckling during its two-direction bending.

9.2 Contributions

The main contributions of the dissertation can be summarized as follows:

1) Design of a 3-D printed spring-based flexible robot

- A three-segment spring-based robot was 3-D printed in one-single piece with the tendon-routing being the only post-processing work.

- Central tendon routing configuration was implemented to decouple motion between robot segments, thus solving the age-old problem for flexible robot from the design standpoint.

2) Development of the cooling module-integrated SMA spring actuator

- A cooling strategy making use of soft silicone tubing was implemented on the SMA spring. The helical shape of the spring makes developing a compact cooling method for it challenging. Threading of silicone tubing over each spring coil allows us to maintain the compactness of the SMA actuator while increase its actuation bandwidth.

- The mechanical model and heat transfer model cooling module-integrated SMA spring was developed with extensive characterization and then verified with experiments.

3) Development and characterization of an actuation mechanism for the cooling module-integrated SMA springs

- An actuation mechanism involving the flow exchange between the water and compressed air was developed and characterized to achieve robot motion speed comparable to existing neurosurgical robots.

4) Design and modeling of a stiffness modulated flexible robot

- An SMA spring-based robot was develop to allow real-time stiffness modulation of individual robot segment to achieve more stable robot operation.

- A modified cantilever model was developed to investigate the effect of spring stiffening and tendon locking on the overall robot stiffness.

5) Development of MRI-compatible remote actuation setups and a mathematical hysteresis model for the cable-driven system

- To the best of our knowledge, the first MRI-compatible Bowden cable transmission was developed.

- While tradeoffs, including the freedom to easily manipulate the transmission, had to be made to switch from flexible transmission to rigid transmission, novel transmission modules, namely the switching mechanism, the linkage mechanism, and the quick-connect mechanism were developed.

- A Prandtl-Ishlinski model with a nonlinear and a linear play operator was used to model the hysteresis behavior of the robotic system, which has repeatable behavior, with high R^2 values.

9.3 Future Work

A few future work following the development of our more recent robotic system are as follows:

1) An inverse hysteresis model should be derived to be used as a feedforward compensation to provide more accurate open-loop control of the robot.

2) A user interface should be developed to allow more intuitive control of the robot by the clinicians. Currently, every command to the motor drivers is given through keyboard. Either a joystick with graphical user interface (GUI), a haptics interface with handles, or a virtual reality platform should be developed to allow the clinicians to adapt to the robotic

surgery with less steep of a learning curve.

3) Currently, the motor encoder provides an indirect sensing mechanism that has to be combined with the hysteresis model to provide us the predicted robot position. An intrinsic sensing mechanism using the MRI-compatible fiber bragg grating (FBG) sensors needs to be integrated into the robot. The potential challenges that could be encountered are the attachment of the fiber on the spring surface of the robot and the large curvature that needs to be formed during robot bending.

4) The design of the stiffness modulated flexible robot should be improved to allow the robot to be more symmetric geometrically to improve the smoothness of its motion. Changes can be done to the way the SMA springs are attached to the segment discs. More direct measure of the stiffness in the robot could be developed using FBG sensors to replace the indirect temperature sensing.

APPENDIX A

PERMISSIONS

1. © [2015] IEEE. Portions reprinted, with permission, from [Shing Shin Cheng and Jaydev P. Desai, ”Towards High Frequency Actuation of SMA Spring for the Neurosurgical Robot-MINIR-II”, *Robotics and Automation (ICRA)*, 2015 IEEE International Conference on, pp. 2580-2585, IEEE, 2015]

2. Portions reprinted by permission from Springer Nature: [Springer Nature] [In *Robotics Research* (pp. 187-200), Springer] [”Towards Real-Time SMA Control for a Neurosurgical Robot: MINIR-II”, Shing Shin Cheng, Yeongjin Kim, and Jaydev P. Desai] [Copyright © 2018]

3. Shing Shin Cheng, Yeongjin Kim, and Jaydev P. Desai. ”Modeling and Characterization of Shape Memory Alloy Springs with Water Cooling Strategy in a Neurosurgical Robot.” *Journal of Intelligent Material Systems and Structures* 28, no. 16 (2017): 2167-2183. Copyright © [2017] (SAGE). Reprinted by permission of SAGE Publications. `https://doi.org/10.1177/1045389X16685443`

4. © [2017] IEEE. Reprinted, with permission, from [Yeongjin Kim, Shing Shin Cheng, and Jaydev P. Desai, ”Toward the Development of a Flexible Mesoscale MRI-Compatible Neurosurgical Continuum Robot”, IEEE *Transactions on Robotics*, Volume: 33, Issue: 6, Dec. 2017]

5. © [2017] IEEE. Reprinted, with permission, from [Shing Shin Cheng, Yeongjin Kim, and Jaydev P. Desai, ”New Actuation Mechanism for Actively Cooled SMA Springs in a Neurosurgical Robot”, IEEE *Transactions on Robotics*, Volume: 33, Issue: 4, Aug. 2017]

6. © [2017] IEEE. Reprinted, with permission, from [Shing Shin Cheng, Xuefeng Wang, and Jaydev P. Desai, ”Design and analysis of a Remotely-Actuated Cable-Driven Neurosurgical Robot”, *Intelligent Robots and Systems (IROS)*, 2017 IEEE/RSJ International Conference on, pp. 1685-1690, IEEE, 2017]

7. © [2018] IEEE. Reprinted, with permission, from [Yeongjin Kim, Shing Shin Cheng, and Jaydev P. Desai, ”Active Stiffness Tuning of a Spring-Based Continuum Robot for MRI-Guided Neurosurgery”, IEEE *Transactions on Robotics*, Volume: 34, Issue: 1, Feb. 2018]

8. © [2018] IEEE. Reprinted, with permission, from [Xuefeng Wang, Shing Shin Cheng, and Jaydev P. Desai, ”Design, Analysis, and Evaluation of a Remotely Actuated MRI-Compatible Neurosurgical Robot”, IEEE *Robotics and Automation Letters*, Volume: 3, Issue: 3, July 2018]

BIBLIOGRAPHY

[1] JS Loeffler, RA Patchell, and Sawaya R. *Treatment of metastatic cancer.* Lippincott Raven, pensylvania,Philadelphia, 1997.

[2] Jason D Wright, Alessandra Kostolias, Cande V Ananth, William M Burke, Ana I Tergas, Eri Prendergast, Scott D Ramsey, Alfred I Neugut, and Dawn L Hershman. Comparative effectiveness of robotically assisted compared with laparoscopic adnexal surgery for benign gynecologic disease. *Obstetrics and gynecology*, 124(5):886, 2014.

[3] Oliver John North. Medical robotics for use in MRI guided endoscopy. 2013.

[4] Yik San Kwoh, Joahin Hou, Edmond A Jonckheere, and Samad Hayati. A robot with improved absolute positioning accuracy for ct guided stereotactic brain surgery. *IEEE Transactions on Biomedical Engineering*, 35(2):153–160, 1988.

[5] James M Drake, Michael Joy, Andrew Goldenberg, and David Kreindler. Computer- and robot-assisted resection of thalamic astrocytomas in children. *Neurosurgery*, 29(1):27–33, 1991.

[6] Dominique Glauser, Pierre Flury, and CW Burckhardt. Mechanical concept of the neurosurgical robot 'minerva'. *Robotica*, 11(6):567–575, 1993.

[7] D Glauser, H Fankhauser, M Epitaux, J-L Hefti, and A Jaccottet. Neurosurgical robot minerva: first results and current developments. *Journal of image guided surgery*, 1(5):266–272, 1995.

[8] Akio Morita, Shigeo Sora, Mamoru Mitsuishi, Shinichi Warisawa, Katopo Suruman, Daisuke Asai, Junpei Arata, Shoichi Baba, Hidechika Takahashi, Ryo Mochizuki, et al. Microsurgical robotic system for the deep surgical field: development of a prototype and feasibility studies in animal and cadaveric models. *Journal of neurosurgery*, 103(2):320–327, 2005.

[9] Qing Hang Li, Lucia Zamorano, Abhilash Pandya, Ramiro Perez, Jianxing Gong, and Fernando Diaz. The application accuracy of the neuromate robot—a quantitative comparison with frameless and frame-based surgical localization systems. *Computer Aided Surgery*, 7(2):90–98, 2002.

[10] Kevin Cleary and Charles Nguyen. State of the art in surgical robotics: clinical applications and technology challenges. *Computer Aided Surgery*, 6(6):312–328, 2001.

[11] Daniel von Langsdorff, Philippe Paquis, and Denys Fontaine. In vivo measurement of the frame-based application accuracy of the neuromate neurosurgical robot. *Journal of neurosurgery*, 122(1):191–194, 2015.

[12] B Davies, Stephen Starkie, Simon J Harris, E Agterhuis, Volker Paul, and Ludwig M Auer. Neurobot: a special-purpose robot for neurosurgery. In *Robotics and Automation, 2000. Proceedings. ICRA'00. IEEE International Conference on*, volume 4, pages 4103–4108. IEEE, 2000.

[13] Kazuhiro Hongo, Shigeaki Kobayashi, Yukinari Kakizawa, Jun-ichi Koyama, Tetsuya Goto, Hiroshi Okudera, Kazutoshi Kan, Masakatsu G Fujie, Hiroshi Iseki, and Kintomo Takakura. Neurobot: telecontrolled micromanipulator system for minimally invasive microneurosurgery—preliminary results. *Neurosurgery*, 51(4):985–988, 2002.

[14] H Takasuna, T Goto, Y Kakizawa, T Miyahara, J Koyama, Y Tanaka, T Kawai, and K Hongo. Use of a micromanipulator system (neurobot) in endoscopic neurosurgery. *Journal of Clinical Neuroscience*, 19(11):1553–1557, 2012.

[15] Seyed-Ahmad Ahmadi, Tassilo Klein, Nassir Navab, Ran Roth, Reuben R Shamir, Leo Joskowicz, Elena DeMomi, Giancarlo Ferrigno, Luca Antiga, and Roberto Israel Foroni. Advanced planning and intra-operative validation for robot-assisted keyhole neurosurgery in robocast. In *Advanced Robotics, 2009. ICAR 2009. International Conference on*, pages 1–7. IEEE, 2009.

[16] Mirko Daniele Comparetti, Alberto Vaccarella, Danilo De Lorenzo, Giancarlo Ferrigno, and Elena De Momi. Multi-robotic approach for keyhole neurosurgery: the ROBOCAST project. In *Joint Workshop on New Technologies for Computer/Robot Assisted Surgery*, 2011.

[17] L Frasson, SY Ko, A Turner, T Parittotokkaporn, Julian F Vincent, and F Rodriguez y Baena. STING: a soft-tissue intervention and neurosurgical guide to access deep brain lesions through curved trajectories. *Proceedings of the Institution of Mechanical Engineers, Part H: Journal of Engineering in Medicine*, 224(6):775–788, 2010.

[18] Michel Lefranc, Cyrille Capel, Anne-Sophie Pruvot-Occean, Anthony Fichten, Christine Desenclos, Patrick Toussaint, Daniel Le Gars, and Johann Peltier. Frameless robotic stereotactic biopsies: a consecutive series of 100 cases. *Journal of neurosurgery*, 122(2):342–352, 2015.

[19] Sumeet Vadera, Alvin Chan, Thomas Lo, Amandip Gill, Anna Morenkova, Nicolas M Phielipp, Neal Hermanowicz, and Frank PK Hsu. Frameless stereotactic robot-assisted subthalamic nucleus deep brain stimulation: case report. *World neurosurgery*, 97:762–e11, 2017.

[20] David YA Dadey, Ashwin A Kamath, Eric C Leuthardt, and Matthew D Smyth. Laser interstitial thermal therapy for subependymal giant cell astrocytoma: technical case report. *Neurosurgical focus*, 41(4):E9, 2016.

[21] B Jerbic, G Nikolic, D Chudy, M Svaco, and B Sekoranja. Robotic application in neurosurgery using intelligent visual and haptic interaction. *International journal of simulation modelling*, 14(1):71–84, 2015.

[22] Domagoj Dlaka, Marko Švaco, Darko Chudy, Bojan Jerbić, Bojan Šekoranja, Filip Šuligoj, Josip Vidaković, Fadi Almahariq, and Dominik Romić. Brain biopsy performed with the RONNA G3 system: a case study on using a novel robotic navigation device for stereotactic neurosurgery. *The International Journal of Medical Robotics and Computer Assisted Surgery*, 14(1), 2018.

[23] Ian D Walker. Continuous backbone continuum robot manipulators. *ISRN Robotics*, 2013, 2013.

[24] David Canes, Amy C Lehman, Shane M Farritor, Dmitry Oleynikov, and Mihir M Desai. The future of notes instrumentation: flexible robotics and in vivo minirobots. *Journal of endourology*, 23(5):787–792, 2009.

[25] Jessica Burgner-Kahrs, D Caleb Rucker, and Howie Choset. Continuum robots for medical applications: A survey. *IEEE Transactions on Robotics*, 31(6):1261–1280, 2015.

[26] Tian En Timothy Seah, Thanh Nho Do, Nobuyoshi Takeshita, Khek Yu Ho, and Soo Jay Phee. Future of flexible robotic endoscopy systems. *arXiv preprint arXiv:1703.05569*, 2017.

[27] Koji Ikuta, Keiichi Yamamoto, and Keiji Sasaki. Development of remote microsurgery robot and new surgical procedure for deep and narrow space. In *Robotics and Automation, 2003. Proceedings. ICRA'03. IEEE International Conference on*, volume 1, pages 1103–1108. IEEE, 2003.

[28] Johnathan A Engh, G Podnar, D Kondziolka, and Cameron N Riviere. Toward effective needle steering in brain tissue. In *Engineering in Medicine and Biology Society, 2006. EMBS'06. 28th Annual International Conference of the IEEE*, pages 559–562. IEEE, 2006.

[29] Hao Su, Gang Li, D Caleb Rucker, Robert J Webster III, and Gregory S Fischer. A concentric tube continuum robot with piezoelectric actuation for MRI-guided closed-loop targeting. *Annals of biomedical engineering*, 44(10):2863–2873, 2016.

[30] Patrick Sears and Pierre Dupont. A steerable needle technology using curved concentric tubes. In *Intelligent Robots and Systems, 2006 IEEE/RSJ International Conference on*, pages 2850–2856. IEEE, 2006.

[31] Mingyen Ho, Yeongjin Kim, Shing Shin Cheng, Rao Gullapalli, and Jaydev P Desai. Design, development, and evaluation of an MRI-guided SMA spring-actuated neurosurgical robot. *The International journal of robotics research*, 34(8):1147–1163, 2015.

[32] Yeongjin Kim, Shing Shin Cheng, and Jaydev P Desai. Towards the development of a flexible meso-scale MRI-compatible neurosurgical continuum robot. *IEEE Transactions on Robotics*, 2017.

[33] Takeyoshi Ota, Amir Degani, David Schwartzman, Brett Zubiate, Jeremy McGarvey, Howie Choset, and Marco A Zenati. A highly articulated robotic surgical system for minimally invasive surgery. *The Annals of thoracic surgery*, 87(4):1253–1256, 2009.

[34] Jun Sheng and Jaydev P Desai. Towards a SMA-actuated neurosurgical intracerebral hemorrhage evacuation (NICHE) robot. In *Intelligent Robots and Systems (IROS), 2015 IEEE/RSJ International Conference on*, pages 3805–3810. IEEE, 2015.

[35] Atsushi Yamada, Shigeyuki Naka, Shigehiro Morikawa, and Tohru Tani. MR compatible continuum robot based on closed elastica with bending and twisting. In *Intelligent Robots and Systems (IROS 2014), 2014 IEEE/RSJ International Conference on*, pages 3187–3192. IEEE, 2014.

[36] Andria A Remirez and Robert J Webster. A new continuum robot with crossed elastic strips: Extensible sections with only one actuator per section. In *ASME 2015 Dynamic Systems and Control Conference*, pages V003T43A004–V003T43A004. American Society of Mechanical Engineers, 2015.

[37] Peter A York, Philip J Swaney, Hunter B Gilbert, and Robert J Webster. A wrist for needle-sized surgical robots. In *Robotics and Automation (ICRA), 2015 IEEE International Conference on*, pages 1776–1781. IEEE, 2015.

[38] Philip J Swaney, Peter A York, Hunter B Gilbert, Jessica Burgner-Kahrs, and Robert J Webster. Design, fabrication, and testing of a needle-sized wrist for surgical instruments. *Journal of medical devices*, 11(1):014501, 2017.

[39] Anzhu Gao, Ryan J Murphy, Hao Liu, Iulian I Iordachita, and Mehran Armand. Mechanical model of dexterous continuum manipulators with compliant joints and tendon/external force interactions. *IEEE/ASME Transactions on Mechatronics*, 22(1):465–475, 2017.

[40] Mohsen Khadem, Carlos Rossa, Nawaid Usmani, Ron Sloboda, and Mahdi Tavakoli. Robotics-assisted needle steering around anatomical obstacles using notched steerable needles. *IEEE Journal of Biomedical and Health Informatics*, 2017.

[41] Nabil Simaan, Russell Taylor, and Paul Flint. High dexterity snake-like robotic slaves for minimally invasive telesurgery of the upper airway. In *Medical Image Computing and Computer-Assisted Intervention–MICCAI 2004*, pages 17–24. Springer, 2004.

[42] Stephen Okazawa, Richelle Ebrahimi, Jason Chuang, Septimiu E Salcudean, and Robert Rohling. Hand-held steerable needle device. *Mechatronics, IEEE/ASME Transactions on*, 10(3):285–296, 2005.

[43] Robert J Webster III, Joseph M Romano, and Noah J Cowan. Kinematics and calibration of active cannulas. In *Robotics and Automation, 2008. ICRA 2008. IEEE International Conference on*, pages 3888–3895. IEEE, 2008.

[44] Robert J Webster III, Joseph M Romano, and Noah J Cowan. Mechanics of precurved-tube continuum robots. *IEEE Transactions on Robotics*, 25(1):67–78, 2009.

[45] Evan J Butler, Robert Hammond-Oakley, Szymon Chawarski, Andrew H Gosline, Patrick Codd, Tomer Anor, Joseph R Madsen, Pierre E Dupont, and Jesse Lock. Robotic neuro-emdoscope with concentric tube augmentation. In *Intelligent Robots and Systems (IROS), 2012 IEEE/RSJ International Conference on*, pages 2941–2946. IEEE, 2012.

[46] Arthur W Mahoney, Hunter B Gilbert, and Robert J Webster III. A review of concentric tube robots: modeling, control, design, planning, and sensing. *Encyclopedia of Medical Robotics, Minimally Invasive Surgical Robotics*, 2016.

[47] MP Chapman, T Yokota, T Ota, S Tully, D Schwartzman, B Zubiate, C Wright, H Choset, and M Zenati. A highly articulated robotic system (cardioarm) is safer than a rigid system for intrapericardial intervention in a porcine model. In *IEEE ICRA Full Day Workshop. IEEE, Anchorage*, 2010.

[48] Flex robotic system: Expanding the reach of surgery. *Medrobotics*, 2017.

[49] J Zuo, G Yan, and Z Gao. A micro creeping robot for colonoscopy based on the earthworm. *Journal of Medical Engineering & Technology*, 29(1):1–7, 2005.

[50] Michael DM Kutzer, Sean M Segreti, Christopher Y Brown, Mehran Armand, Russell H Taylor, and Simon C Mears. Design of a new cable-driven manipulator with a large open lumen: Preliminary applications in the minimally-invasive removal of osteolysis. In *Robotics and Automation (ICRA), 2011 IEEE International Conference on*, pages 2913–2920. IEEE, 2011.

[51] Anzhu Gao, John P Carey, Ryan J Murphy, Iulian Iordachita, Russell H Taylor, and Mehran Armand. Progress toward robotic surgery of the lateral skull base: Integration of a dexterous continuum manipulator and flexible ring curette. In *Robotics and Automation (ICRA), 2016 IEEE International Conference on*, pages 4429–4435. IEEE, 2016.

[52] Dong-Geol Choi, Byung-Ju Yi, and Whee-Kuk Kim. Design of a spring backbone micro endoscope. In *Intelligent Robots and Systems, 2007. IROS 2007. IEEE/RSJ International Conference on*, pages 1815–1821. IEEE, 2007.

[53] Minho Hwang, Hyunsoo Chung, and Dong-Soo Kwon. A portable endoscopic tool handler (PETH) with its ex-vivo ESD trials. In *Ubiquitous Robots and Ambient Intelligence (URAI), 2014 11th International Conference on*, pages 85–87. IEEE, 2014.

[54] Baldwin Po Man Yeung and Terence Gourlay. A technical review of flexible endoscopic multitasking platforms. *International journal of surgery*, 10(7):345–354, 2012.

[55] J Andres Astudillo, Emanuel Sporn, Sharon Bachman, Brent Miedema, and Klaus Thaler. Transgastric cholecystectomy using a prototype endoscope with 2 deflecting working channels (with video). *Gastrointestinal endoscopy*, 69(2):297–302, 2009.

[56] Christopher C Thompson, Marvin Ryou, Nathaniel J Soper, Eric S Hungess, Richard I Rothstein, and Lee L Swanstrom. Evaluation of a manually driven, multitasking platform for complex endoluminal and natural orifice transluminal endoscopic surgery applications (with video). *Gastrointestinal endoscopy*, 70(1):121–125, 2009.

[57] Bernard Dallemagne and Jacques Marescaux. The anubis project. *Minimally Invasive Therapy & Allied Technologies*, 19(5):257–261, 2010.

[58] Naoki Suzuki, Asaki Hattori, Kazuo Tanoue, Satoshi Ieiri, Kozo Konishi, Morimasa Tomikawa, Hajime Kenmotsu, and Makoto Hashizume. Scorpion shaped endoscopic surgical robot for NOTES and SPS with augmented reality functions. In *Medical Imaging and Augmented Reality*, pages 541–550. Springer, 2010.

[59] Georges-Pascal Haber, Riccardo Autorino, Humberto Laydner, Bo Yang, Michael A White, Shahab Hillyer, Fatih Altunrende, Rakesh Khanna, Gregory Spana, Isac Wahib, et al. SPIDER surgical system for urologic procedures with laparoendoscopic single-site surgery: from initial laboratory experience to first clinical application. *European urology*, 61(2):415–422, 2012.

[60] KR Julian Chun, Boris Schmidt, Bülent Köktürk, Roland Tilz, Alexander Fürnkranz, Melanie Konstantinidou, Erik Wissner, Andreas Metzner, Feifan Ouyang, and Karl-Heinz Kuck. Catheter ablation–new developments in robotics. *Herz Kardiovaskuläre Erkrankungen*, 33(8):586–589, 2008.

[61] Jean Bismuth, Elika Kashef, Nicholas Cheshire, and Alan B Lumsden. Feasibility and safety of remote endovascular catheter navigation in a porcine model. *Journal of Endovascular Therapy*, 18(2):243–249, 2011.

[62] Celia V Riga, Nicholas JW Cheshire, Mohamad S Hamady, and Colin D Bicknell. The role of robotic endovascular catheters in fenestrated stent grafting. *Journal of vascular surgery*, 51(4):810–820, 2010.

[63] CV Riga, A Rolls, R Rippel, C Shah, M Hamady, C Bicknell, and N Cheshire. Advantages and limitations of robotic endovacular catheters for carotid artery stenting. *The Journal of cardiovascular surgery*, 53(6):747–753, 2012.

[64] Christopher J Nycz, Radian Gondokaryono, Paulo Carvalho, Nirav Patel, Marek Wartenberg, Julie G Pilitsis, and Gregory S Fischer. Mechanical validation of an MRI compatible stereotactic neurosurgery robot in preparation for pre-clinical trials.

In *Intelligent Robots and Systems (IROS), 2017 IEEE/RSJ International Conference on*, pages 1677–1684. IEEE, 2017.

[65] Garnette R Sutherland, Stefan Wolfsberger, Sanju Lama, and Kourosh Zarei-nia. The evolution of neuroArm. *Neurosurgery*, 72:A27–A32, 2013.

[66] Ken Masamune, Etsuko Kobayashi, Yoshitaka Masutani, Makoto Suzuki, Takeyoshi Dohi, Hiroshi Iseki, and Kintomo Takakura. Development of an MRI-compatible needle insertion manipulator for stereotactic neurosurgery. *Journal of Image Guided Surgery*, 1(4):242–248, 1995.

[67] Werner A Kaiser, Harald Fischer, Jeorg Vagner, and Manfred Selig. Robotic system for biopsy and therapy of breast lesions in a high-field whole-body magnetic resonance tomography unit. *Investigative Radiology*, 35(8):513–519, 2000.

[68] Kiyoyuki Chinzei, Nobuhiko Hata, Ferenc A Jolesz, and Ron Kikinis. Surgical assist robot for the active navigation in the intraoperative MRI: Hardware design issues. In *Intelligent Robots and Systems, 2000.(IROS 2000). Proceedings. 2000 IEEE/RSJ International Conference on*, volume 1, pages 727–732. IEEE, 2000.

[69] Roland Moser, Roger Gassert, Etienne Burdet, Laurent Sache, HR Woodtli, J Erni, Willy Maeder, and Hannes Bleuler. An MR compatible robot technology. In *Robotics and Automation, 2003. Proceedings. ICRA'03. IEEE International Conference on*, volume 1, pages 670–675. IEEE, 2003.

[70] G Ganesh, Roger Gassert, Etienne Burdet, and Hannes Bleuler. Dynamics and control of an MRI compatible master-slave system with hydrostatic transmission. In *Robotics and Automation, 2004. Proceedings. ICRA'04. 2004 IEEE International Conference on*, volume 2, pages 1288–1294. IEEE, 2004.

[71] Blake T Larson, Arthur G Erdman, Nikolaos V Tsekos, Essa Yacoub, Panagiotis V Tsekos, and Ioannis G Koutlas. Design of an MRI-compatible robotic stereotactic device for minimally invasive interventions in the breast. *Journal of Biomechanical Engineering*, 126(4):458–465, 2004.

[72] Haytham Elhawary, Aleksander Zivanovic, Marc Rea, Brian Davies, Collin Besant, Donald McRobbie, Nandita de Souza, Ian Young, and Michael Lampérth. The feasibility of MR-image guided prostate biopsy using piezoceramic motors inside or near to the magnet isocentre. *Medical Image Computing and Computer-Assisted Intervention–MICCAI 2006*, pages 519–526, 2006.

[73] Haytham Elhawary, Aleksandar Zivanovic, Marc Rea, Brian L Davies, Collin Besant, I Young, and MU Lamperth. A modular approach to MRI-compatible robotics. *IEEE Engineering in medicine and biology magazine*, 27(3):35–41, 2008.

[74] Gregory S Fischer, Iulian Iordachita, Csaba Csoma, Junichi Tokuda, Simon P DiMaio, Clare M Tempany, Nobuhiko Hata, and Gabor Fichtinger. MRI-compatible pneumatic robot for transperineal prostate needle placement. *IEEE/ASME transactions on mechatronics*, 13(3):295–305, 2008.

[75] Bo Yang, Steven Roys, U-Xuan Tan, Mathew Philip, Howard Richard, Rao P Gullapalli, and Jaydev P Desai. Design, development, and evaluation of a master–slave surgical system for breast biopsy under continuous MRI. *The International journal of robotics research*, 33(4):616–630, 2014.

[76] Axel Krieger, Iulian Iordachita, Sang-Eun Song, Nathan B Cho, Peter Guion, Gabor Fichtinger, and Louis L Whitcomb. Development and preliminary evaluation of an actuated MRI-compatible robotic device for MRI-guided prostate intervention. In *Robotics and Automation, 2010 IEEE International Conference on*, pages 1066–1073, 2010.

[77] Andrew A Goldenberg, John Trachtenberg, Yang Yi, Robert Weersink, Marshall S Sussman, Masoom Haider, Liang Ma, and Walter Kucharczyk. Robot-assisted MRI-guided prostatic interventions. *Robotica*, 28(2):215–234, 2010.

[78] Gang Li, Hao Su, Gregory A Cole, Weijian Shang, Kevin Harrington, Alex Camilo, Julie G Pilitsis, and Gregory S Fischer. Robotic system for MRI-guided stereotactic neurosurgery. *IEEE Transactions on Biomedical Engineering*, 62(4):1077–1088, 2015.

[79] Hao Su, Diana C Cardona, Weijian Shang, Alexander Camilo, Gregory A Cole, D Caleb Rucker, Robert J Webster, and Gregory S Fischer. A MRI-guided concentric tube continuum robot with piezoelectric actuation: a feasibility study. In *Robotics and Automation (ICRA), 2012 IEEE International Conference on*, pages 1939–1945. IEEE, 2012.

[80] Gregory S Fischer, Gregory Cole, and Hao Su. Approaches to creating and controlling motion in MRI. In *Engineering in Medicine and Biology Society, EMBC, 2011 Annual International Conference of the IEEE*, pages 6687–6690. IEEE, 2011.

[81] Daeyoung Kim, Etsuko Kobayashi, Takeyoshi Dohi, and Ichiro Sakuma. A new, compact MR-compatible surgical manipulator for minimally invasive liver surgery. In *Medical Image Computing and Computer-Assisted Intervention?MICCAI 2002*, pages 99–106. Springer, 2002.

[82] Dan Stoianovici, Danny Song, Doru Petrisor, Daniel Ursu, Dumitru Mazilu, Michael Mutener, Michael Schar, and Alexandru Patriciu. MRI stealth robot for prostate interventions. *Minimally Invasive Therapy & Allied Technologies*, 16(4):241–248, 2007.

[83] Dan Stoianovici, Chunwoo Kim, Govindarajan Srimathveeravalli, Peter Sebrecht, Doru Petrisor, Jonathan Coleman, Stephen B Solomon, and Hedvig Hricak. MRI-safe robot for endorectal prostate biopsy. *IEEE/ASME Transactions on Mechatronics*, 19(4):1289–1299, 2014.

[84] Marco Salerno, Ketao Zhang, Arianna Menciassi, and Jian S Dai. A novel 4-DOFs origami enabled, sma actuated, robotic end-effector for minimally invasive surgery.

In *Robotics and Automation (ICRA), 2014 IEEE International Conference on*, pages 2844–2849. IEEE, 2014.

[85] Mingyen Ho, Alan B McMillan, J Marc Simard, Rao Gullapalli, and Jaydev P Desai. Toward a meso-scale SMA-actuated MRI-compatible neurosurgical robot. *Robotics, IEEE Transactions on*, 28(1):213–222, 2012.

[86] Elise Taillant, Juan-Carlos Avila-Vilchis, Christophe Allegrini, Ivan Bricault, and Philippe Cinquin. CT and MR compatible light puncture robot: Architectural design and first experiments. In *International Conference on Medical Image Computing and Computer-Assisted Intervention*, pages 145–152. Springer, 2004.

[87] Taylor Fisher, Abbi Hamed, Panagiotis Vartholomeos, Ken Masamune, Guoyi Tang, Hongliang Ren, and Zion TH Tse. Intraoperative magnetic resonance imaging–conditional robotic devices for therapy and diagnosis. *Proceedings of the Institution of Mechanical Engineers, Part H: Journal of Engineering in Medicine*, 228(3):303–318, 2014.

[88] National Electrical Manufacturers Association et al. Determination of signal-to-noise ratio (SNR) in diagnostic magnetic resonance imaging. *NEMA Standards Publication MS 1-2008 (R2014)*, 2014.

[89] Richard W Briggs, Iona Dy-Liacco, Matthew P Malcolm, Hyunsook Lee, Kyung K Peck, Kaundinya S Gopinath, Nathan C Himes, David A Soltysik, Paul Browne, and Roger Tran-Son-Tay. A pneumatic vibrotactile stimulation device for fMRI. *Magnetic resonance in medicine*, 51(3):640–643, 2004.

[90] Anne-Catherin Zappe, Thorsten Maucher, Karlheinz Meier, and Christian Scheiber. Evaluation of a pneumatically driven tactile stimulator device for vision substitution during fMRI studies. *Magnetic resonance in Medicine*, 51(4):828–834, 2004.

[91] SP DiMaio, GS Fischer, SJ Haker, N Hata, I Iordachita, CM Tempany, R Kikinis, and G Fichtinger. A system for MRI-guided prostate interventions. In *Biomedical Robotics and Biomechatronics, 2006. BioRob 2006. The First IEEE/RAS-EMBS International Conference on*, pages 68–73. IEEE, 2006.

[92] Tianxue Zhang, David Navarro-Alarcon, Kwun Wang Ng, Man Kiu Chow, Yun-hui Liu, and Hayley Louise Chung. A novel palm-shape breast deformation robot for MRI-guided biopsy. In *Robotics and Biomimetics (ROBIO), 2016 IEEE International Conference on*, pages 527–532. IEEE, 2016.

[93] Bo Yang, U-Xuan Tan, AB. McMillan, R. Gullapalli, and J.P. Desai. Design and control of a 1-DOF MRI-compatible pneumatically actuated robot with long transmission lines. *Mechatronics, IEEE/ASME Transactions on*, 16(6):1040–1048, Dec 2011.

[94] Hiroyuki Sajima, Hiroki Kamiuchi, Kenta Kuwana, Takeyoshi Dohi, and Ken Masamune. MR-safe pneumatic rotation stepping actuator. *Journal of Robotics and Mechatronics*, 24(5):820–827, 2012.

[95] Yue Chen, Christopher D Mershon, and Zion Tsz Ho Tse. A 10-mm MR-conditional unidirectional pneumatic stepper motor. *IEEE/ASME Transactions on Mechatronics*, 20(2):782–788, 2015.

[96] Nikolaos V Tsekos, Essa Yacoub, Panagiotis V Tsekos, and Ioannis G Koutlas. Design of an MRI-compatible robotic stereotactic device for minimally invasive interventions in the breast. *J. Biomechanical Eng.*, 126(4):458–465, 2004.

[97] Gregory S Fischer, Axel Krieger, Iulian Iordachita, Csaba Csoma, Louis L Whitcomb, and Gabor Fichtinger. MRI compatibility of robot actuation techniques–a comparative study. In *International Conference on Medical Image Computing and Computer-Assisted Intervention*, pages 509–517. Springer, 2008.

[98] Akio Yamamoto, Keigo Ichiyanagi, Toshiro Higuchi, Hiroshi Imamizu, Roger Gassert, Martin Ingold, Laurent Sache, and Hannes Bleuler. Evaluation of MR-compatibility of electrostatic linear motor. In *Robotics and Automation, 2005. ICRA 2005. Proceedings of the 2005 IEEE International Conference on*, pages 3658–3663. IEEE, 2005.

[99] John Vogan, Andreas Wingert, J-S Plante, Steven Dubowsky, Moustapha Hafez, Daniel Kacher, and Ferenc Jolesz. Manipulation in MRI devices using electrostrictive polymer actuators: With an application to reconfigurable imaging coils. In *Robotics and Automation, 2004. Proceedings. ICRA'04. 2004 IEEE International Conference on*, volume 3, pages 2498–2504. IEEE, 2004.

[100] A Khanicheh, A Muto, C Triantafyllou, B Weinberg, L Astrakas, A Tzika, and C Mavroidis. MR compatible ERF driven hand rehabilitation device. In *Rehabilitation Robotics, 2005. ICORR 2005. 9th International Conference on*, pages 7–12. IEEE, 2005.

[101] William J Buehler, JV Gilfrich, and RC Wiley. Effect of low-temperature phase changes on the mechanical properties of alloys near composition TiNi. *Journal of applied physics*, 34(5):1475–1477, 1963.

[102] Inderjit Chopra and Jayant Sirohi. *Smart structures theory*, volume 35. Cambridge University Press, 2013.

[103] Koji Ikuta, Masahiro Tsukamoto, and Shigeo Hirose. Shape memory alloy servo actuator system with electric resistance feedback and application for active endoscope. In *Robotics and Automation, 1988. Proceedings., 1988 IEEE International Conference on*, pages 427–430. Ieee, 1988.

[104] Yoshihiko Nakamura, A Matsui, T Saito, and K Yoshimoto. Shape-memory-alloy active forceps for laparoscopic surgery. In *Robotics and Automation, 1995. Proceedings., 1995 IEEE International Conference on*, volume 3, pages 2320–2327. IEEE, 1995.

[105] Elif Ayvali, Mingyen Ho, and Jaydev P Desai. A novel discretely actuated steerable probe for percutaneous procedures. In *Experimental Robotics*, pages 115–123. Springer, 2014.

[106] Andrea Holton, Edward Walsh, Andreas Anayiotos, Gerald Pohost, and Ramakrishna Venugopalan. Comparative MRI compatibility of 316l stainless steel alloy and nickel–titanium alloy stents: Original article technical. *Journal of Cardiovascular Magnetic Resonance*, 4(4):423–430, 2002.

[107] Jun Sheng and Jaydev P Desai. Design, modeling and characterization of a novel meso-scale SMA-actuated torsion actuator. *Smart Materials and Structures*, 24(10):105005, 2015.

[108] Javed Khader Eliyas, Ryan Glynn, Charles G Kulwin, Richard Rovin, Ronald Young, Juan Alzate, Gustavo Pradilla, Mitesh V Shah, Amin Kassam, Ivan Ciric, et al. Minimally invasive transsulcal resection of intraventricular and periventricular lesions through a tubular retractor system: multicentric experience and results. *World neurosurgery*, 90:556–564, 2016.

[109] Mingyen Ho, Michael Koltz, J Marc Simard, Rao Gullapalli, and Jaydev P Desai. Towards a MR image-guided SMA-actuated neurosurgical robot. In *Robotics and Automation (ICRA), 2011 IEEE International Conference on*, pages 1153–1158, Shanghai, China, 9-13 May, 2011. IEEE, NY.

[110] Mingyen Ho and Jaydev P Desai. Towards the development of a SMA-actuated MRI-compatible tendon-driven neurosurgical robot. In *Robotics and Automation (ICRA), 2012 IEEE International Conference on*, pages 683–688, Minneapolis, Minnesota, 14-18 May, 2012. IEEE, NY.

[111] D Linzer, SM Ling, H Villalobos, W Raub Jr, X Wu, J Ting, A Berti, Howard Landy, and AM Markoe. Gamma knife radiosurgery for large volume brain tumors: An analysis of acute and chronic toxicity. *Stereotactic and functional neurosurgery*, 70(Suppl. 1):11–18, 1998.

[112] Dale Ding, Robert M Starke, R Webster Crowley, and Kenneth C Liu. Endoport-assisted microsurgical resection of cerebral cavernous malformations. *Journal of Clinical Neuroscience*, 22(6):1025–1029, 2015.

[113] Kwang-Wook Jo, Hyung Jin Shin, Do-Hyun Nam, Jung-Il Lee, Kwan Park, Jong Hyun Kim, and Doo-Sik Kong. Efficacy of endoport-guided endoscopic resection for deep-seated brain lesions. *Neurosurgical review*, 34(4):457–463, 2011.

[114] Matthew C Murphy, John Huston III, Clifford R Jack Jr, Kevin J Glaser, Matthew L Senjem, Jun Chen, Armando Manduca, Joel P Felmlee, and Richard L Ehman. Measuring the characteristic topography of brain stiffness with magnetic resonance elastography. *PLoS One*, 8(12):e81668, 2013.

[115] IA Gravagne and ID. Walker. Kinematic transformations for remotely-actuated planar continuum robots. In *Robotics and Automation, 2000. Proceedings. ICRA '00.*, volume 1, pages 19–26 vol.1, 2000.

[116] A. Bajo and N. Simaan. Kinematics-based detection and localization of contacts along multisegment continuum robots. *IEEE Transactions on Robotics*, 28(2):291–302, Apr 2012.

[117] Mircea Ivanescu, Decebal Popescu, and Nirvana Popescu. A decoupled sliding mode control for a continuum arm. *Advanced Robotics*, 29(13):831–845, 2015.

[118] Shigeo Hirose and Shugen Ma. Coupled tendon-driven multijoint manipulator. In *Robotics and Automation, 1991. Proceedings., 1991 IEEE International Conference on*, pages 1268–1275. IEEE, 1991.

[119] Benjamin L Conrad and Michael R Zinn. Interleaved continuum-rigid manipulation approach: Development and functional evaluation of a clinical scale manipulator. In *Intelligent Robots and Systems (IROS 2014), 2014 IEEE/RSJ International Conference on*, pages 4290–4296. IEEE, 2014.

[120] B. A. Jones and I. D. Walker. Kinematics for multisection continuum robot. *IEEE Transactions on Robotics*, 22(1):43–57, Feb 2006.

[121] Demeter G Fertis. *Advanced mechanics of structures*. CRC Press, 1996.

[122] Kai Xu and Nabil Simaan. An investigation of the intrinsic force sensing capabilities of continuum robots. *Robotics, IEEE Transactions on*, 24(3):576–587, 2008.

[123] Arthur Munzenmaier Wahl. *Mechanical springs*. Penton Publishing Company, 1944.

[124] Othon K Rediniotis and Dimitris C Lagoudas. Shape memory alloy actuators as locomotor muscles. *Progress in Astronautics and Aeronautics*, 195:483–500, 2001.

[125] Hiroyuki Tamai and Yoshikazu Kitagawa. Pseudoelastic behavior of shape memory alloy wire and its application to seismic resistance member for building. *Computational materials science*, 25(1-2):218–227, 2002.

[126] M. A. Qidwai D. C. Lagoudas, D. Moorthy and J. N. Reddy. Modeling of the thermomechanical response of active laminates with SMA strips using the layerwise finite element method. *Intelligent Material Systems and Structures*, 8(88):476, 1997.

[127] Thompson Danniella M; Griffin O H Jr. Finite element predictions of active buckling control of stiffened panels. *Intelligent Material Systems and Structures*, 4(7):243, 1993.

[128] P. Krulevitch, AP. Lee, P.B. Ramsey, J.C. Trevino, J. Hamilton, and M.A Northrup. Thin film shape memory alloy microactuators. *Microelectromechanical Systems, Journal of*, 5(4):270–282, Dec 1996.

[129] Yeongjin Kim, Shing Shin Cheng, Aleksandrs Ecins, Cornelia Fermüller, Kelly P Westlake, and Jaydev P Desai. Towards a robotic hand rehabilitation exoskeleton for stroke therapy. In *ASME 2014 Dynamic Systems and Control Conference*, pages V001T04A006–V001T04A006. American Society of Mechanical Engineers, 2014.

[130] KL Ng and QP Sun. Stress-induced phase transformation and detwinning in NiTi polycrystalline shape memory alloy tubes. *Mechanics of Materials*, 38(1-2):41–56, 2006.

[131] Mohammad H Elahinia, Mahdi Hashemi, Majid Tabesh, and Sarit B Bhaduri. Manufacturing and processing of NiTi implants: a review. *Progress in Materials Science*, 57(5):911–946, 2012.

[132] A Bhattacharyya, DC Lagoudas, Yand Wang, and VK Kinra. On the role of thermoelectric heat transfer in the design of SMA actuators: theoretical modeling and experiment. *Smart Materials and Structures*, 4(4):252, 1995.

[133] SR White and JB Berman. Thermomechanical response of SMA composite beams with embedded nitinol wires in an epoxy matrix. *Journal of intelligent material systems and structures*, 9(5):391–400, 1998.

[134] Toshiyuki Takagi, J Tani, S Suzuki, and M Matsumoto. Electromagneto thermostructural analysis of an ARSME plate. *Transactions of the Japan Society of Mechanical Engineering, Ser. C*, pages 2966–2973, 1998.

[135] Shing Shin Cheng and Jaydev P. Desai. Towards high frequency actuation of SMA spring for the neurosurgical robot-MINIR-II. In *Proceedings of the IEEE International Conference on Robotics and Automation (ICRA 2015)*, pages 2580–2585, May 2015.

[136] Jinhao Qiu, Junji Tani, Daisuke Osanai, Yuta Urushiyama, and David Lewinnek. High-speed response of SMA actuators. *International Journal of Applied Electromagnetics and Mechanics*, 12(1, 2):87–100, 2000.

[137] Roy Featherstone and Yee Harn Teh. Improving the speed of shape memory alloy actuators by faster electrical heating. In *Proceedings of the Ninth International Symposium on Experimental Robotics*, 2004.

[138] Chee Siong Loh, Hiroshi Yokoi, and Tamio Arai. Natural heat-sinking control method for high-speed actuation of the SMA. *International Journal of Advanced Robotic Systems*, 3(4), 2006.

[139] RB Gorbet, KA Morris, and RCC Chau. Mechanism of bandwidth improvement in passively cooled SMA position actuators. *Smart Materials and Structures*, 18(9):095013, 2009.

[140] Brian Selden, Kyujin Cho, and H Harry Asada. Segmented shape memory alloy actuators using hysteresis loop control. *Smart materials and structures*, 15(2):642, 2006.

[141] T Luchetti, A Zanella, M Biasiotto, and A Saccagno. Electrically actuated antiglare rear-view mirror based on a shape memory alloy actuator. *Journal of materials engineering and performance*, 18(5-6):717–724, 2009.

[142] M Leary, F Schiavone, and A Subic. Lagging for control of shape memory alloy actuator response time. *Materials & Design*, 31(4):2124–2128, 2010.

[143] S Huang, Martin Leary, T Ataalla, K Probst, and A Subic. Optimisation of Ni-Ti shape memory alloy response time by transient heat transfer analysis. *Materials & Design*, 35:655–663, 2012.

[144] A. York N. Lewis and S. Seelecke. Experimental characterization of self-sensing SMA actuators under controlled convective cooling. *Smart Materials and Structures*, 22, 2013.

[145] Guo-xin Hu Li-xiang Zhang and Zhi guo Wang. Study on liquid jet cooling and heating of the moving SMA actuator. *International Journal of Thermal Sciences*, 47:306–314, 2008.

[146] Yun Luo, Toshiyuki Takagi, Shigenao Maruyama, and Makoto Yamada. A shape memory alloy actuator using peltier modules and R-phase transition. *Journal of Intelligent Material Systems and Structures*, 11(7):503–511, 2000.

[147] Andrew Russell R and Gorbet RB. Improving the response of SMA actuators. In *1995 IEEE International Conference*, 1995.

[148] A. Pathak, D. Brei, and J. Luntz. Experimental characterization of the convective heat transfer from shape memory alloy (SMA) wire to various ambient environments. In *Student's papers*, page 12 pp, Ascona, Switzerland, October 6-9, 2008 2008. Pathak,A.; Mechanical Engineering, University of Michigan, 2250 GG Brown, Ann Arbor, MI 48109-2126, USA, apathak@umich.edu.

[149] Yonas Tadesse, Nicholas Thayer, and Shashank Priya. Tailoring the response time of shape memory alloy wires through active cooling and pre-stress. *Journal of Intelligent Material Systems and Structures*, 21(1):19–40, 2010.

[150] A Lara-Quintanilla and HEN Bersee. Active cooling and strain-ratios to increase the actuation frequency of SMA wires. *Shape Memory and Superelasticity*, 1(4):460–467, 2015.

[151] Sung-Hyuk Song, Jang-Yeob Lee, Hugo Rodrigue, Ik-Seong Choi, Yeon June Kang, and Sung-Hoon Ahn. 35 hz shape memory alloy actuator with bending-twisting mode. *Scientific reports*, 6, 2016.

[152] M.D. Comparetti, E. De Momi, A. Vaccarella, M. Riechmann, and G. Ferrigno. Optically tracked multi-robot system for keyhole neurosurgery. In *Robotics and Automation (ICRA), 2011 IEEE International Conference on*, pages 661–666, May 2011.

[153] Deon F. Louw, Tim Fielding, Paul B. McBeth, Dennis Gregoris, Perry Newhook, and Garnette R. Sutherland. Surgical robotics: A review and neurosurgical prototype development. *Neurosurgery*, 54(3), 2004.

[154] M. Zimmermann, R. Krishnan, A. Raabe, and V. Seifert. Robot-assisted navigated endoscopic ventriculostomy: implementation of a new technology and first clinical results. *Acta Neurochirurgica*, 146(7):697–704, 2004.

[155] Danilo De Lorenzo, Elena De Momi, Ilya Dyagilev, Rudy Manganelli, Alessandro Formaglio, Domenico Prattichizzo, Moshe Shoham, and Giancarlo Ferrigno. Force feedback in a piezoelectric linear actuator for neurosurgery. *The International Journal of Medical Robotics and Computer Assisted Surgery*, 7(3):268–275, 2011.

[156] Isuru S Godage, Andria A Remirez, Raul Wirz, Kyle D Weaver, Jessica Burgner-Kahrs, and Robert J Webster III. Robotic intracerebral hemorrhage evacuation: An in-scanner approach with concentric tube robots. In *Intelligent Robots and Systems (IROS), 2015 IEEE/RSJ International Conference on*, pages 1447–1452. IEEE, 2015.

[157] Norio Fukami. *Endoscopic Submucosal Dissection: Principles and Practice*. Springer, 2015.

[158] Mascaro-Stephen A. Ertel, Joel D. Dynamic thermomechanical modeling of a wet shape memory alloy actuator. *Journal of Dynamic Systems, Measurement, and Control*, 132:45–57, 2010.

[159] Tanaka K. A thermomechanical sketch of shape memory effect: One-dimensional tensile behavior. *Res. Mechanica*, 18(3):251–263, 1986.

[160] C. Liang and C. A. Rogers. One-dimensional thermomechanical constitutive relations for shape memory materials. *Journal of Intelligent Material Systems and Structures*, 1(2):207–234, 1990.

[161] L.C. Brinson. One-dimensional constitutive behavior of shape memory alloys: Thermomechanical derivation with non-constant material functions and redefined martensite internal variable. *Journal of Intelligent Material Systems and Structures*, 4(2):229–242, 1993.

[162] J.G. Boyd and D.C. Lagoudas. A thermodynamical constitutive model for shape memory materials. part i. the monolithic shape memory alloy. *International Journal of Plasticity*, 12(6):805 – 842, 1996.

[163] M. Frémond. Shape memory alloy. In *Shape Memory Alloys*, volume 351 of *International Centre for Mechanical Sciences*, pages 1–68. Springer Vienna, 1996.

[164] Kikuaki Tanaka Hisaaki Tobushi. Deformation of a shape memory alloy helical spring (analysis based on stress-strain-temperature relation). *JSME International Journal*, 34(1), 1991.

[165] C. Liang and C. A. Rogers. Design of shape memory alloy springs with applications in vibration control. *Journal of Intelligent Material Systems and Structures*, 4(2):229–242, 1997.

[166] Ricardo A A Aguiar, Marcelo A Savi, and Pedro M C L Pacheco. Experimental and numerical investigations of shape memory alloy helical springs. *Smart Materials and Structures*, 19(2):025008, 2010.

[167] Alireza Hadi, Aghil Yousefi-Koma, Majid M. Moghaddam, Mohammad Elahinia, and Asadollah Ghazavi. Developing a novel SMA-actuated robotic module. *Sensors and Actuators A: Physical*, 162(1):72 – 81, 2010.

[168] Haolei Huang Jianzuo Ma and Jin Huang. Characteristics analysis and testing of SMA spring actuator. *Advances in Materials Science and Engineering*, 2013, 2013.

[169] Sung-Min An, Junghyun Ryu, Maenghyo Cho, and Kyu-Jin Cho. Engineering design framework for a shape memory alloy coil spring actuator using a static two-state model. *Smart Materials and Structures*, 21(5):055009, 2012.

[170] Ho M. and J. P. Desai. Modeling, characterization and control of antagonistic sma springs for use in a neurosurgical robot. In *Proceeding of IEEE International Conference on Robotics and Automation*, pages 2488–2493, 2013.

[171] Ricardo Alexandre Amar de Aguiar, Waldyr Cardoso de Castro Leão Neto, Marcelo Amorim Savi, and Pedro Manuel Calas Lopes Pacheco. Shape memory alloy helical springs performance: Modeling and experimental analysis. *Materials Science Forum*, 758(2013):147–156, 2013.

[172] Pierre-Yves Manach and Denis Favier. Shear and tensile thermomechanical behavior of near equiatomic NiTi alloy. *Materials Science and Engineering: A*, 222(1):45–57, 1997.

[173] H. J. Wagner C. M. Jackson and R. J. Wasilewski. 55-nitinol-the alloy with a memory: Its physical metallurgy, properties and applications. Report, NASA-SP 5110, 1972.

[174] James M McNaney, Valentina Imbeni, Youngjean Jung, Panayiotis Papadopoulos, and RO Ritchie. An experimental study of the superelastic effect in a shape-memory nitinol alloy under biaxial loading. *Mechanics of Materials*, 35(10):969–986, 2003.

[175] P Thamburaja and L Anand. Superelastic behavior in tension–torsion of an initially-textured Ti-Ni shape-memory alloy. *International Journal of Plasticity*, 18(11):1607–1617, 2002.

[176] Shane J Yates and Alexander L Kalamkarov. Experimental study of helical shape memory alloy actuators: effects of design and operating parameters on thermal transients and stroke. *Metals*, 3(1):123–149, 2013.

[177] Vagner Candido de Sousa and Carlos De Marqui Jr. Effect of pseudoelastic hysteresis of shape memory alloy springs on the aeroelastic behavior of a typical airfoil section. *Journal of Intelligent Material Systems and Structures*, 27(1):117–133, 2016.

[178] Joseph Edward Shigley. Mechanical engineering design. 1972. McGraw-Hill, NY.

[179] Francesco Bucchi, Mohammad Elahinia, Paola Forte, and Francesco Frendo. A passive magneto-thermo-mechanical coupling actuated by SMA springs and MR fluid. *International Journal of Structural Stability and Dynamics*, 14(08):1440031, 2014.

[180] Vagner Candido de Sousa, Carlos De Marqui Junior, and Mohammad H Elahinia. Effect of constitutive model parameters on the aeroelastic behavior of an airfoil with shape memory alloy springs. *Journal of Vibration and Control*, 2016.

[181] N Ma, G Song, and HJ Lee. Position control of shape memory alloy actuators with internal electrical resistance feedback using neural networks. *Smart materials and structures*, 13(4):777, 2004.

[182] A Bhattacharyya, L Sweeney, and M G Faulkner. Experimental characterization of free convection during thermal phase transformations in shape memory alloy wires. *Smart Materials and Structures*, 11(3):411, 2002.

[183] Frank P. Incropera. *Fundamentals of Heat and Mass Transfer*. John Wiley & Sons, 2006.

[184] Stuart W. Churchill and Humbert H.S. Chu. Correlating equations for laminar and turbulent free convection from a horizontal cylinder. *International Journal of Heat and Mass Transfer*, 18(9):1049 – 1053, 1975.

[185] R.M Fand and K.K Keswani. The influence of property variation on forced convection heat transfer to liquids. *International Journal of Heat and Mass Transfer*, 15(8):1515 – 1536, 1972.

[186] Technical Characteristics of FLEXINOL Actuator Wires. Technical note, Dynalloy, November 2011.

[187] Stephen A Mascaro and H Harry Asada. Wet shape memory alloy actuators for active vasculated robotic flesh. In *Robotics and Automation, 2003. Proceedings. ICRA'03. IEEE International Conference on*, volume 1, pages 282–287. IEEE, 2003.

[188] Shing Shin Cheng, Yeongjin Kim, and Jaydev P. Desai. Towards real-time SMA control for a neurosurgical robot: MINIR-II. In *Proceedings of the International Symposium on Robotics Research (ISRR 2015)*, 2015 (in press).

[189] K Tanafxiaka. A thermomechanical sketch of shape memory effect: One- dimensional tensile behavior. *Res. Mechanica*, 18(3):251–263, 1986.

[190] Bharath Rao. Coiled tubing hydraulics modeling. Technical note, CTES.

[191] NW Ryan and MM Johnson. Transistion from laminar to turbulent flow in pipes. *AIChE Journal*, 5(4):433–435, 1959.

[192] PS Srinivasan, SS Nandapurkar, and FA Holland. Friction factors for coils. *Trans. Inst. Chem. Eng*, 48(4-6):T156–T161, 1970.

[193] Yeongjin Kim and Jaydev P Desai. Design and kinematic analysis of a neurosurgical spring-based continuum robot using SMA spring actuators. In *Intelligent Robots and Systems (IROS), 2015 IEEE/RSJ International Conference on*, pages 1428–1433. IEEE, 2015.

[194] Yan Li, Lishan Cui, Ping Shi, and Dazhi Yang. Phase transformation behaviors of prestrained TiNi shape memory alloy fibers under the constraint of a hard substrate. *Materials Letters*, 49(3):224–227, 2001.

[195] Arjo Loeve, Paul Breedveld, and Jenny Dankelman. Scopes too flexible... and too stiff. *Pulse, IEEE*, 1(3):26–41, 2010.

[196] Matteo Cianchetti, Tommaso Ranzani, Giada Gerboni, Thrishantha Nanayakkara, Kaspar Althoefer, Prokar Dasgupta, and Arianna Menciassi. Soft robotics technologies to address shortcomings in today's minimally invasive surgery: the STIFF-FLOP approach. *Soft Robotics*, 1(2):122–131, 2014.

[197] Yong-Jae Kim, Shanbao Cheng, Sangbae Kim, and Karl Iagnemma. Design of a tubular snake-like manipulator with stiffening capability by layer jamming. In *Intelligent Robots and Systems (IROS), 2012 IEEE/RSJ International Conference on*, pages 4251–4256. IEEE, 2012.

[198] Gottumukkala S Raju, Douglas K Rex, Richard A Kozarek, Ijaz Ahmed, Douglas Brining, and Pankaj Jay Pasricha. A novel shape-locking guide for prevention of sigmoid looping during colonoscopy. *Gastrointestinal endoscopy*, 59(3):416–419, 2004.

[199] Vahid Saadat, Richard C Ewers, and Eugene G Chen. Shape lockable apparatus and method for advancing an instrument through unsupported anatomy, September 14 2004. US Patent 6,790,173.

[200] Joseph M Tartaglia, Wade A Keller, Amir Belson, and Arthur R Ratchford. Endoscope with adjacently positioned guiding apparatus, January 10 2006. US Patent 6,984,203.

[201] Amir Degani, Howie Choset, Alon Wolf, and Marco A Zenati. Highly articulated robotic probe for minimally invasive surgery. In *Robotics and Automation, 2006. ICRA 2006. Proceedings 2006 IEEE International Conference on*, pages 4167–4172. IEEE, 2006.

[202] Akihiko Yagi, Kiyoshi Matsumiya, Ken Masamune, Hongen Liao, and Takeyoshi Dohi. Rigid-flexible outer sheath model using slider linkage locking mechanism and air pressure for endoscopic surgery. *Medical Image Computing and Computer-Assisted Intervention–MICCAI 2006*, pages 503–510, 2006.

[203] Anders Pettersson, S Davis, JO Gray, TJ Dodd, and Tomas Ohlsson. Design of a magnetorheological robot gripper for handling of delicate food products with varying shapes. *Journal of Food Engineering*, 98(3):332–338, 2010.

[204] Maria J Telleria, Malik Hansen, Don Campbell, Amelia Servi, and Martin L Culpepper. Modeling and implementation of solder-activated joints for single-actuator, centimeter-scale robotic mechanisms. In *Robotics and Automation (ICRA), 2010 IEEE International Conference on*, pages 1681–1686. IEEE, 2010.

[205] Stephen Griffin. Selectively flexible catheter and method of use, November 9 2010. US Patent 7,828,790.

[206] Arjo J Loeve, Johannes H Bosma, Paul Breedveld, Dimitra Dodou, and Jenny Dankelman. Polymer rigidity control for endoscopic shaft-guide plastolock - a feasibility study. *Journal of Medical Devices*, 4(4):045001, 2010.

[207] Yong-Jae Kim, Shanbao Cheng, Sangbae Kim, and Karl Iagnemma. A novel layer jamming mechanism with tunable stiffness capability for minimally invasive surgery. *IEEE Transactions on Robotics*, 29(4):1031–1042, 2013.

[208] Matteo Cianchetti, Tommaso Ranzani, Giada Gerboni, Iris De Falco, Cecilia Laschi, and Arianna Menciassi. Stiff-flop surgical manipulator: mechanical design and experimental characterization of the single module. In *Intelligent Robots and Systems (IROS), 2013 IEEE/RSJ International Conference on*, pages 3576–3581. IEEE, 2013.

[209] Tommaso Ranzani, Matteo Cianchetti, Giada Gerboni, Iris De Falco, Gianluigi Petroni, and Arianna Menciassi. A modular soft manipulator with variable stiffness. In *3rd joint workshop on new technologies for computer/robot assisted surgery*, 2013.

[210] Benjamin Chang, Allison Chew, Nastaran Naghshineh, and Carlo Menon. A spatial bending fluidic actuator: fabrication and quasi-static characteristics. *Smart Materials and Structures*, 21(4):045008, 2012.

[211] Aline De Greef, Pierre Lambert, and Alain Delchambre. Towards flexible medical instruments: Review of flexible fluidic actuators. *Precision engineering*, 33(4):311–321, 2009.

[212] Matthew S Moses, Michael DM Kutzer, Hans Ma, and Mehran Armand. A continuum manipulator made of interlocking fibers. In *Robotics and Automation (ICRA), 2013 IEEE International Conference on*, pages 4008–4015. IEEE, 2013.

[213] Byungjeon Kang, Risto Kojcev, and Edoardo Sinibaldi. The first interlaced continuum robot, devised to intrinsically follow the leader. *PloS one*, 11(2):e0150278, 2016.

[214] Ronald Van Ham, T Sugar, Bram Vanderborght, K Hollander, and Dirk Lefeber. Review of actuators with passive adjustable compliance/controllable stiffness for robotic applications. *IEEE Robotics and Automation Magazine*, 16(3):81–94, 2009.

[215] Rehan M Ahmed, Ivan G Kalaykov, and Anani V Ananiev. Modeling of magneto rheological fluid actuator enabling safe human-robot interaction. In *Emerging Technologies and Factory Automation, 2008. ETFA 2008. IEEE International Conference on*, pages 974–979. IEEE, 2008.

[216] Gyuhae Park, Matthew T Bement, Daniel A Hartman, Ronald E Smith, and Charles R Farrar. The use of active materials for machining processes: A review. *International Journal of Machine Tools and Manufacture*, 47(15):2189–2206, 2007.

[217] Frederick H Redell, David Lichodziejewski, Justin Kleber, and Gyula Greschik. Testing of an inflation-deployed sub-Tg rigidized support structure for a planar membrane waveguide antenna. In *46th AIAA Structures, Structural Dynamics and Materials Conference*, pages 1875–1880, 2005.

[218] Nadia Cheng, Genya Ishigami, Stephan Hawthorne, Hao Chen, Malik Hansen, Maria Telleria, Robert Playter, and Karl Iagnemma. Design and analysis of a soft mobile robot composed of multiple thermally activated joints driven by a single actuator. In *Robotics and Automation (ICRA), 2010 IEEE International Conference on*, pages 5207–5212. IEEE, 2010.

[219] Hua Dong and Glenn M Walker. Adjustable stiffness tubes via thermal modulation of a low melting point polymer. *Smart Materials and Structures*, 21(4):042001, 2012.

[220] Wanliang Shan, Tong Lu, and Carmel Majidi. Soft-matter composites with electrically tunable elastic rigidity. *Smart Materials and Structures*, 22(8):085005, 2013.

[221] Allen Jiang, Tomaso Aste, Prokar Dasgupta, Kaspar Althoefer, and Thrishantha Nanayakkara. Granular jamming with hydraulic control. In *ASME 2013 International Design Engineering Technical Conferences and Computers and Information in Engineering Conference*, pages V06AT07A021–V06AT07A021. American Society of Mechanical Engineers, 2013.

[222] Allen Jiang, Kaspar Althoefer, Prokar Dasgupta, and Thrishantha Nanayakkara. The core snake, the variable stiffness laparoscopic camera. In *The Hamlyn Symposium on Medical Robotics, London, United Kingdom*, 2013.

[223] AJ Liu and SR Nagel. Nonlinear dynamics-jamming is not just cool anymore. *Nature*, 396:21, 1998.

[224] Eric Brown, Nicholas Rodenberg, John Amend, Annan Mozeika, Erik Steltz, Mitchell R Zakin, Hod Lipson, and Heinrich M Jaeger. Universal robotic gripper based on the jamming of granular material. *Proceedings of the National Academy of Sciences*, 107(44):18809–18814, 2010.

[225] Nadia G Cheng, Maxim B Lobovsky, Steven J Keating, Adam M Setapen, Katy I Gero, Anette E Hosoi, and Karl D Iagnemma. Design and analysis of a robust, low-cost, highly articulated manipulator enabled by jamming of granular media. In *Robotics and Automation (ICRA), 2012 IEEE International Conference on*, pages 4328–4333. IEEE, 2012.

[226] E Steltz, A Mozeika, J Rembisz, N Corson, and HM Jaeger. Jamming as an enabling technology for soft robotics. In *SPIE Smart Structures and Materials+ Nondestructive Evaluation and Health Monitoring*, pages 764225–764225. International Society for Optics and Photonics, 2010.

[227] Arjo J Loeve, Oscar S van de Ven, Johan G Vogel, Paul Breedveld, and Jenny Dankelman. Vacuum packed particles as flexible endoscope guides with controllable rigidity. *Granular Matter*, 12(6):543–554, 2010.

[228] Allen Jiang, Asghar Ataollahi, Kaspar Althoefer, Prokar Dasgupta, and Thrishantha Nanayakkara. A variable stiffness joint by granular jamming. In *ASME 2012 International Design Engineering Technical Conferences and Computers and Information in Engineering Conference*, pages 267–275. American Society of Mechanical Engineers, 2012.

[229] Dong-Geol Choi, Byung-Ju Yi, and Whee-Kuk Kim. Design of a spring backbone micro endoscope. In *Intelligent Robots and Systems, 2007. IROS 2007. IEEE/RSJ International Conference on*, pages 1815–1821. IEEE, 2007.

[230] Nobuhiko Matsumi. Thermal damage threshold of brain tissue. *Okayama Igakkai Zasshi (Journal of Okayama Medical Association)*, 101(11-12):1049–1061, 1989.

[231] Roger Gassert, Roland Moser, Etienne Burdet, and Hannes Bleuler. Mri/fmri-compatible robotic system with force feedback for interaction with human motion. *IEEE/ASME transactions on mechatronics*, 11(2):216–224, 2006.

[232] O Wendt, J Oellinger, TC Luth, R Felix, and U Boenick. The effects of the use of piezoelectric motors in a 1.5-tesla high-field magnetic resonance imaging system (MRI)-effekte von piezoelektrischen motoren in einem 1, 5-tesla-hochfeld-magnetresonanztomographen (MRT). *Biomedizinische Technik/Biomedical Engineering*, 45(1-2):20–25, 2000.

[233] Andreas Wege, Konstantin Kondak, and Günter Hommel. Mechanical design and motion control of a hand exoskeleton for rehabilitation. In *Mechatronics and automation, 2005 IEEE international conference*, volume 1, pages 155–159. IEEE, 2005.

[234] Ying Mao and Sunil Kumar Agrawal. Design of a cable-driven arm exoskeleton (CAREX) for neural rehabilitation. *IEEE Transactions on Robotics*, 28(4):922–931, 2012.

[235] Dylan P Losey, Peter A York, Philip J Swaney, Jessica Burgner, and Robert J Webster. A flexure-based wrist for needle-sized surgical robots. In *SPIE Medical Imaging*, pages 86711G–86711G. International Society for Optics and Photonics, 2013.

[236] Louis B Kratchman, Mohammed M Rahman, Justin R Saunders, Philip J Swaney, and Robert J Webster III. Toward robotic needle steering in lung biopsy: a tendon-actuated approach. In *SPIE Medical Imaging*, pages 79641I–79641I. International Society for Optics and Photonics, 2011.

[237] Tian Fuxiang and Wang Xingsong. The design of a tendon-sheath-driven robot. *International journal of intelligent systems technologies and applications*, 8(1-4):215–230, 2009.

[238] JR Bemfica, Claudio Melchiorri, Lorenzo Moriello, Gianluca Palli, and Umberto Scarcia. A three-fingered cable-driven gripper for underwater applications. In *Robotics and Automation (ICRA), 2014 IEEE International Conference on*, pages 2469–2474. IEEE, 2014.

[239] Per Henrik Borgstrom, Brett L Jordan, Bengt J Borgstrom, Michael J Stealey, Gaurav S Sukhatme, Maxim A Batalin, and William J Kaiser. Nims-pl: A cable-driven robot with self-calibration capabilities. *IEEE Transactions on Robotics*, 25(5):1005–1015, 2009.

[240] Changquing Li and Christopher D Rahn. Design of continuous backbone, cable-driven robots. *Journal of Mechanical Design*, 124(2):265–271, 2002.

[241] Salih Abdelaziz, Laure Esteveny, Laurent Barbé, Pierre Renaud, Bernard Bayle, and Michel de Mathelin. Development of a MR-compatible cable-driven manipulator: Design and technological issues. In *Robotics and Automation (ICRA), 2012 IEEE International Conference on*, pages 1488–1494. IEEE, 2012.

[242] Salih Abdelaziz, Laure Esteveny, Laurent Barbé, Pierre Renaud, Bernard Bayle, and Michel De Mathelin. Design of a magnetic resonance imaging-compatible cable-driven manipulator with new instrumentation and synthesis methods. *Journal of Mechanical Design*, 136(9):091006, 2014.

[243] Nikolai Hungr, Ivan Bricault, Philippe Cinquin, and Céline Fouard. Design and validation of a CT-and MRI-guided robot for percutaneous needle procedures. *IEEE Transactions on Robotics*, 32(4):973–987, 2016.

[244] Nabil Zemiti, Ivan Bricault, Celine Fouard, Benedicte Sanchez, and Philippe Cinquin. LPR: A CT and MR-compatible puncture robot to enhance accuracy and safety of image-guided interventions. *IEEE/ASME Transactions on Mechatronics*, 13(3):306–315, 2008.

[245] Amirhossein Salimi, Amin Ramezanifar, Javad Mohammadpour, K Grigoriadis, and NV Tsekos. ROBOCATH: A patient-mounted parallel robot to position and orient surgical catheters. In *ASME 2012 5th Annual Dynamic Systems and Control Conference joint with the JSME 2012 11th Motion and Vibration Conference*, pages 471–480. American Society of Mechanical Engineers, 2012.

[246] Amirhossein Salimi, Amin Ramezanifar, Javad Mohammadpour, and Karolos Grigoriadis. Gain-scheduling control of a cable-driven MRI-compatible robotic platform for intracardiac interventions. In *American Control Conference (ACC), 2013*, pages 746–751. IEEE, 2013.

[247] Amirhossein Salimi, Amin Ramezanifar, Javad Mohammadpour, Karolos M Grigoriadis, and Nikolaos V Tsekos. Design and qualification of a parallel robotic platform to assist with beating-heart intracardiac interventions. *Journal of Mechanisms and Robotics*, 6(2):021004, 2014.

[248] Mitsuhiro Oura, Yo Kobayashi, Jun Okamoto, and Masakatsu G Fujie. Development of MRI compatible versatile manipulator for minimally invasive surgery. In *Biomedical Robotics and Biomechatronics, 2006. BioRob 2006. The First IEEE/RAS-EMBS International Conference on*, pages 176–181. IEEE, 2006.

[249] Yang Wang, Sungmin Kim, Everette C Burdette, Peter Kazanzides, and Iulian Iordachita. Robotic system with multiplex power transmission for MRI-guided percutaneous interventions. In *Engineering in Medicine and Biology Society (EMBC), 2016 IEEE 38th Annual International Conference of the*, pages 5228–5232. IEEE, 2016.

[250] Chen Lin, Wang Xingsong, and Tian Fuxiang. Tendon-sheath actuated robots and transmission system. In *Mechatronics and Automation, 2009. ICMA 2009. International Conference on*, pages 3173–3178. IEEE, 2009.

[251] Soo J Phee, SC Low, Paolo Dario, and Arianna Menciassi. Tendon sheath analysis for estimation of distal end force and elongation for sensorless distal end. *Robotica*, 28(07):1073–1082, 2010.

[252] Shing Shin Cheng, Xuefeng Wang, and Jaydev P Desai. Design and analysis of a remotely-actuated neurosurgical robotic system. In *Intelligent Robots and Systems (IROS), 2017 IEEE/RSJ International Conference on*. IEEE, 2017 (Accepted).

[253] Yeongjin Kim, Shing Shin Cheng, Mahamadou Diakite, Rao P Gullapalli, J Marc Simard, and Jaydev P Desai. Toward the development of a flexible mesoscale MRI-compatible neurosurgical continuum robot. *IEEE Transactions on Robotics*, 2017.

[254] Xuefeng Wang, Shing Shin Cheng, and Jaydev P Desai. Design, analysis, and evaluation of a remotely actuated MRI-compatible neurosurgical robot. *IEEE Robotics and Automation Letters*, 3(3):2144–2151, 2018.

[255] Mohammad Al Janaideh, Subhash Rakheja, and Chun-Yi Su. A generalized prandtl–ishlinskii model for characterizing the hysteresis and saturation nonlinearities of smart actuators. *Smart Materials and Structures*, 18(4):045001, 2009.

[256] Micky Rakotondrabe. Classical prandtl-ishlinskii modeling and inverse multiplicative structure to compensate hysteresis in piezoactuators. In *American Control Conference (ACC), 2012*, pages 1646–1651. IEEE, 2012.